**Experimental Investigations of Magnesium Diboride Josephson Junctions**

A Thesis

Submitted to the Faculty

of

Drexel University

by

Steven A. Carabello

in partial fulfillment of the

requirements for the degree

of

Doctor of Philosophy

May 2016

# Acknowledgments

As with any project spanning multiple years, I received help, encouragement, and support from many sources.

The most direct help came from those who joined me in the ultra-low temperature laboratory at Drexel. I am especially thankful to have worked alongside Joey Lambert. We were a very effective team, and I am very grateful for his efforts. I also thank Dr. Roberto Ramos, for providing advice and support, pushes in the right direction, and for opening the world of condensed matter physics to me. Other students in the group, including Zechariah Thrailkill, Mariyan Stoyanov, Jerome Mlack, and Pubudu Galwaduge, made contributions without which I could not have achieved most of the results presented in this thesis.

I am also very grateful to many others at Drexel. I thank the members of my committee for their service and support, and for keeping me on track: Dr. Bose, Dr. Barsoum, Dr. Penn, and Dr. Harb. Dr. Vogeley helped this part-time commuter student in maneuvering through all aspects of the physics graduate program. Maryann Fitzpatrick and Wolfgang Nadler were always available, encouraging, and able to help with hardware or technology of any kind.

Our collaborators at Temple University and Penn State also provided fundamental support. Dr. Xiaoxing Xi inspired my investigation of magnesium diboride, and provided a great deal of support from his research group throughout my experiments. Dr. Ke Chen suggested that we explore the current-voltage characteristics for evidence of energy gap substructure, the subject of Chapter 3. And of course, no experiments could be conducted at all without experimental samples to work with. These were of extremely high quality, fabricated by Wenqing Dai and Daniel Cunnane.

I thank Sigma Xi for providing a grant in aid of research, which allowed us to purchase equipment that made many of my results possible.

My colleagues at Penn State Harrisburg also provided substantial support. Dr. Omid Ansary gave the initial impetus to complete my Ph.D., and supported me at every opportunity. My physics

colleagues also made this possible, in covering classes, giving supportive words, and reviewing drafts of this thesis. So I thank Kerwin Foster, Peggy Ankney, Roger Bussard, Wolfram Bettermann, and Susan Eskin.

The support of my family has been indispensable, and I am profoundly grateful. My wife, Elizabeth Carabello, has been a tremendous blessing in my life, with patience, kindness, and love beyond any reasonable expectation. My parents Nate and Gayle and my brother Chris have provided a lifetime of encouragement. My son Peter is now nearly two years old. He brings joy to every day, and everyone who knows him says, "He's such a good little boy."

Finally, I thank God, for creating a world of such deep beauty. For teaching me humility. For granting me peace which surpasses all understanding. And for helping me to do more than I am able under my own strength. Soli Deo gloria.

# Table of Contents

# List of Tables

# List of Figures

## Abstract

Experimental Investigations of Magnesium Diboride Josephson Junctions
Steven A. Carabello
Advisors: Shyamalendu Bose, Ph. D. and Roberto Ramos, Ph. D.

In this thesis, I present the results of experiments on Josephson tunnel junctions that incorporate magnesium diboride ($MgB_2$) as one of the superconducting electrodes. Through explorations of their current vs. voltage and conductance vs. voltage characteristics, I produced high-resolution distributions of the energy gap structure of $MgB_2$. I also explored their resonant modes by performing the first superconducting-to-normal state switching experiments on such "hybrid" junctions.

Magnesium diboride exhibits two superconducting energy gaps, $\sigma$ and $\pi$. The Josephson junctions measured for this thesis used clean $MgB_2$ thin films grown by hybrid physical-chemical vapor deposition on single-crystal silicon carbide substrates. For some films, only the $c$-axis is exposed, allowing direct tunneling to the $\pi$ gap. In others, the $a$-$b$ plane is exposed, allowing us to explore the $\sigma$ gap as well. Lead or tin were evaporated to form the superconducting counterelectrodes.

I performed high-resolution tunneling spectroscopy measurements of these junctions. Their results demonstrate that, for films with little scattering, it is not possible to model the density of states with only two superconducting energy gaps. Instead, at least four gaps are needed and a distribution is more appropriate, as anticipated by several theoretical results.

The switching of Josephson junctions from the superconducting to normal states reveals additional interesting physics. There has been some recent theoretical interest in the switching behavior of "hybrid" junctions – those consisting of one single-gap electrode and one multi-gap electrode, separated by a tunneling barrier.

I observed several features of the superconducting-to-normal switching behavior that are not yet explained by theory. However, most of my results are consistent with theories developed for conventional single-gap/single-gap Josephson junctions, suggesting that switching in these junctions is dominated by a single tunneling mode. By measuring the switching behavior across temperatures,

with and without microwave excitation, I was able to characterize the resistance, capacitance, critical current, and quality factor of these junctions. Each junction proved to be highly underdamped (quality factor $Q \gg 1$). Because my results also exhibit several signatures of quantum-mechanical behavior, similar junctions may be suitable for quantum device applications.

# Chapter 1: Introduction

This thesis presents the results of experiments I performed in the ultra-low temperature laboratory at Drexel University, using Josephson junctions that incorporate magnesium diboride ($MgB_2$). Through these experiments, I found several novel results for this type of system.

Magnesium diboride, sometimes described as the "queen of superconductivity's personality traits" [15, 16], provides an excellent platform for studying multi-gap superconductivity - a field widely applicable to a variety of superconducting materials and systems. Several of these are the subject of very active exploration today, but have a less sure theoretical foundation than for $MgB_2$.

Chapter 2 describes the procedures common to each of these experiments. This includes how we reach the very low temperatures needed, not just for superconductivity, but very low thermal noise and macroscopic quantum tunneling. To take advantage of the low thermal noise, I also needed to minimize several sources of electronic noise. Details of the devices measured for this thesis are also discussed here.

Contrary to earlier theoretical and experimental expectations, I find that it is insufficient to treat $MgB_2$ purely as a two-gap superconductor; I discuss these results in Chapter 3, which I determined from measurements of current vs. voltage and conductance vs. voltage. Additionally, I find that the switching of such a "hybrid" junction from the superconducting to the normal state is largely consistent with the theory for conventional junctions, but with some as-yet unexplained features. I discuss this in Chapter 4.

The remainder of this introduction provides some useful context for these results. First, I broadly review the history of superconductivity, highlighting results of particular relevance to this thesis. Next, I describe a variety of theoretical findings applicable to superconducting systems, with a focus on those of interest in our devices. A brief discussion of superconductivity in magnesium diboride follows. Of course, all of these provide a simplified view. Further information may be found in a variety of textbooks (e.g. [17, 18, 19, 20]) and several excellent review articles (e.g. [4, 21, 22, 23, 24]).

## 1.1 Superconductivity

### 1.1.1 Historical Background

Superconductivity was discovered by Heike Kamerlingh Onnes in 1911 [25]. These first experiments used pure mercury, which shows a superconducting transition at 4.20 K. Soon, researchers explored many materials, both to understand superconductivity more fully and to find superconducting materials more suitable for practical applications.

Prior to Onnes, measurements of conductors had shown a decrease in resistivity as temperature decreased. This is a result of a decrease in the amplitude of lattice vibrations. Some early theories suggested that the resistivity should gradually drop to zero as $T$ approaches zero. Others suggested that, after reaching a minimum value, the resistivity should grow to infinity at absolute zero. Still others predicted a residual resistance. This last is observed for many conductors, including copper (see Figure 1.1). This residual resistance depends on impurities and lattice defects, and is one reason why Onnes chose pure mercury.

Onnes was exploring resistance at low temperature both to resolve this theoretical question, and to develop thermometry useful at these low temperatures. Finding resistances experimentally indistinguishable from zero was not so much of a surprise; the surprise came in the suddenness of the transition - at a very clear "critical temperature" $T_c$.

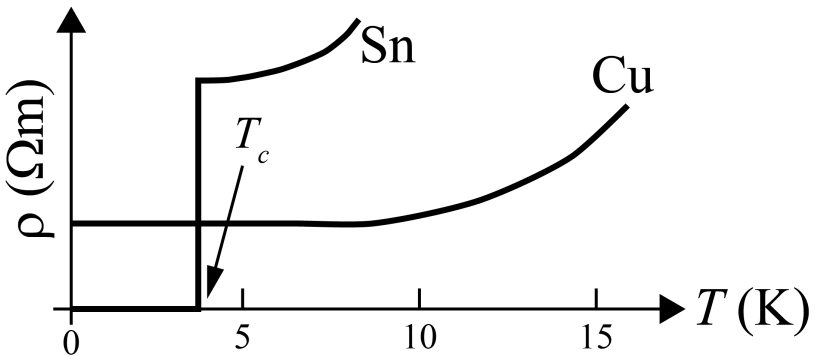


**Figure 1.1:** Schematic of the resistivities $\rho$ of copper and tin at low temperatures (adapted from [2]). Below a certain temperature (dependent on its purity), the resistivity of copper remains nearly constant; it never becomes superconducting. For superconductors such as tin, however, the resistivity suddenly drops to zero below its critical temperature $T_c$.

There were additional surprises. Superconductivity is not a rare phenomenon: 30 elements are

now known to superconduct at ambient pressure, and 23 more superconduct at high pressure [26]. The critical temperature $T_c$ varies over a very wide range; for example, 0.01 K for tungsten through 9.3 K for Niobium. Additionally, some materials do not superconduct at all; these include some of the most useful conductors, such as copper, silver, gold, and platinum.

But measurements of resistance alone are not able to distinguish whether the resistivity is simply near zero or is truly zero. Fortunately, a far more sensitive method is available and was developed by Onnes himself in 1914.

Consider a ring of superconducting material. While the system is above $T_c$, place a magnet inside the ring. Then, cool the ring below $T_c$. Finally, remove the magnet. An induced current is set up that maintains the magnetic flux through the ring; this current should decay with a time constant $\tau = \frac{L}{R}$ where $L$ and $R$ are the inductance and resistance of the ring. A schematic of this process is shown in Figure 1.2 (a).

Measurements of these induced fields show that the current, if it decays at all, does so exceptionally slowly. These "persistent currents" are so long-lived that the resistivity of a superconductor must be at most about 18 orders of magnitude smaller than that of copper at room temperature. In fact, no measurable decreases have been found for experiments as long as a year, and "under many circumstances we expect absolutely no change in field or current to occur in times less than $10^{10^{10}}$ years!" [27]

In 1933, an additional effect was observed by Meissner and Ochsenfeld [28]. If resistanceless flow were the only distinguishing feature of superconductivity, then performing a similar experiment on a solid superconducting disk should likewise form persistent currents, keeping the magnetic field inside the superconductor below $T_c$ equal to what it had been above $T_c$. Instead, the magnetic field is expelled entirely from the bulk of the superconductor, at any temperature below $T_c$, no matter what the field had been above $T_c$. So, rather than trapping any existing flux in, flux is expelled in "perfect diamagnetism" (apart from a thin surface layer through which the screening currents flow, and small vortices in "Type 2" superconductors).

By the 1950's, superconducting compounds were found with $T_c$ on the order of 20 K, including

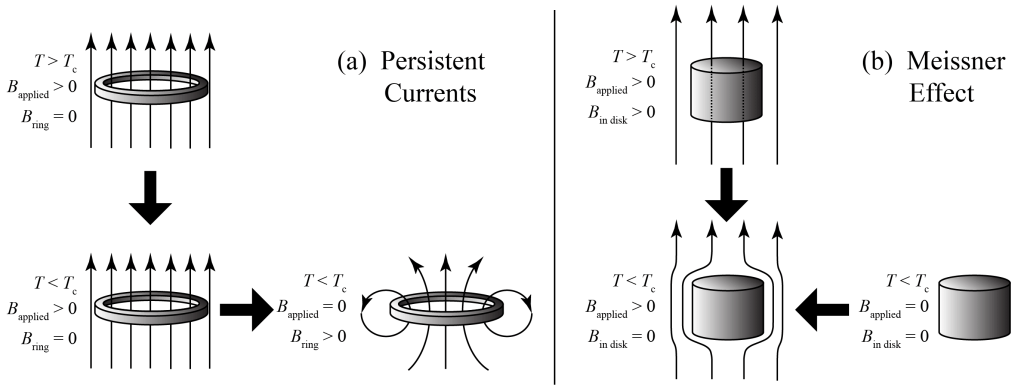


**Figure 1.2:** (a) Persistent currents: An external magnetic field is applied to a ring of a superconducting material while it has resistance ($T > T_c$). This field is then removed while the ring is superconducting ($T < T_c$). A current is induced around the superconducting ring that maintains the magnetic flux through the ring. In the absence of dissipative effects, this induced current will continue indefinitely. (b) The Meissner effect: Magnetic fields are expelled from the bulk of the superconductor, whether the fields are initially applied above or below the superconducting transition temperature $T_c$.

$Nb_3Sn$ and NbTi, widely used in superconducting magnets (such as those in MRI machines).

The theoretical understanding of superconductivity had been growing as well. A classical model was proposed in 1935 by Fritz and Heinz London [29] based on empirical evidence, rather than a microscopic understanding of the materials. The implications of quantum mechanics were increasingly appreciated during this time, and in 1948, Fritz London showed that the London equations resulted from the quantum mechanical nature of superconductivity [30, 31]. In 1950, Vitaly Ginzburg and Lev Landau further refined the theory [32] by incorporating thermodynamic as well as electromagnetic properties of superconducting materials.

These theories described the behaviors of superconductors reasonably well, but did not explain how superconductivity occurs. Then in 1957, John Bardeen, Leon Cooper, and Robert Schreiffer presented a microscopic theory known as BCS theory [33]. In conventional BCS theory, superconductivity is the result of electrons forming "Cooper pairs" as a result of the slight attraction caused by distortions in the ion lattice from the passing of an electron - phonon-mediated superconductivity. I discuss this further in Section 1.1.3.

While BCS theory did explain measurements thus far and provided a mechanism for superconductivity to occur, it only offered suggestions of what materials should or should not be superconducting.

Some attempts were made to explore materials on this basis, but there were no major advances in increasing $T_c$ as a result of these efforts. And in 1972, theorists suggested that the highest $T_c$ possible for conventional BCS superconductors is approximately 30 K [34].

Knowledge and applications of the existing materials continued to advance, with little hope of advancing $T_c$. Then in 1986, superconductivity was observed in copper-oxide materials (cuprates) [35]. The first example exhibited a $T_c$ of approximately 30 K; and within seven years, similar compounds were found with $T_c$ up to 133 K. Theorists quickly realized that these materials require an unconventional mechanism for forming electron pairs, and explanations for their behavior remain controversial. Reaching even higher values of $T_c$ for other similar compounds remains stubbornly elusive.

Although $T_c$ for these materials is attractive, relatively few practical applications have been developed for the cuprates. Mechanically, they are brittle; but a more significant issue is their short coherence length. So, in order for any polycrystalline sample to be superconducting along its length, grains must be atomically smooth. And, because the superconductivity is dominated by the copper-oxygen planes, the grains must have their crystal axes aligned.

In 2001, superconductivity was observed at 40 K in magnesium diboride [36]. Rather than the decades of theoretical uncertainty (and continuing controversy today) of the cuprates, theorists were able to successfully explain its behavior as a conventional phonon-mediated BCS superconductor within two years of this discovery. This was true in spite of the fact that several rules in the conventional wisdom of phonon-mediated superconductivity were broken [15].

The physics of magnesium diboride includes a number of features that makes its superconducting behavior substantially more complex than previously-known conventional superconductors. These include its two distinct superconducting energy gaps (see Sections 1.1.3 and 1.3, and [4]).

This thesis is focused on the exploration of superconductivity in magnesium diboride; as a result, more details are described below.

The field of superconductivity has continued to advance. For example, in 2008, superconductivity was discovered in iron-based materials (pnictides) [37] at 26 K. Due to the tendency for

magnetic fields to inhibit superconductivity, it was once thought that iron would be antithetical to superconductivity. These materials also exhibit some very interesting physics (including multi-gap superconductivity, discussed below), and their properties have not yet been fully explained theoretically. In 2016, theorists, inspired in part by magnesium diboride, suggested that two-dimensional boron may be the only 2-dimensional material to superconduct at ambient pressure without doping - and doing so at 10 - 20 K: quite high for an elemental material [38, 39].

Superconductivity remains an active and vibrant field, with ever-improving theoretical and experimental tools. The results presented in this thesis have revealed a bit more of the interesting physics in superconducting systems.

### 1.1.2 Conduction in metals

Before the discussion of superconductivity, I present a review of conduction in normal metals and the cause of electrical resistance.

Electrons, being Fermions, obey the Pauli exclusion principle. So, no two electrons may be in the same state. In a single atom at $T = 0$, electrons fill the available energy levels from low to high energy.

In a solid, the electrons are shared among the ions in the lattice. In order to obey the exclusion principle, the discrete energy levels of a single atom are smeared into bands. The Fermi level is defined as the highest energy level that can be occupied at $T = 0$; the valence band is the band containing the Fermi level.

It is often useful to visualize the charge distribution in momentum space. The Fermi surface represents all possible momentum vectors for electrons at the Fermi level. For free electrons, with a well-defined energy and able to move equally in all directions, the Fermi surface is a sphere. For some materials, the free-electron model works well and the Fermi surface is nearly spherical; for others, the Fermi surface can be substantially more complex.

In an electrical conductor, the Fermi level is adjacent to full and empty band states. But in a semiconductor, the valence band is full, with an energy gap to reach higher bands. Therefore, energy is needed to promote an electron to an available state. So, unlike conduction in conductors, electrical

conductivity in semiconductors increases with increasing temperature: thermal energy excites more electrons across the gap.

A common model for electrical conduction is of electrons as ball bearings, with the ion lattice as pegs in a board. When a voltage is applied, it seems intuitive that electrons would travel for only short distances before hitting an ion, losing the energy gained from its interaction with the electric field, resulting in a constant drift velocity and a transfer of thermal energy to the lattice. But this intuitive picture is wrong.

In an ideal crystal lattice at rest, there are no collisions whatsoever. This is a natural result of the Schrödinger equation applied to a periodic potential, but makes no sense in the particle picture.

Electrical resistance is the result of scattering, not from the lattice per se, but from imperfections in the lattice. These imperfections may be due to impurities, lattice defects, or – far more important at most temperatures – deviations of the ions in the lattice due to thermal oscillations. Low-temperature measurements demonstrate that the ions in their unperturbed positions are not the source of the scattering: the mean free path of conduction electrons may be a million times longer than the distance between adjacent ions [2].

### 1.1.3 The Superconducting Energy Gap

In order to understand superconductivity, particularly superconductivity in magnesium diboride, it is useful to gain an understanding of the superconducting energy gap and the BCS theory that provides the microscopic explanation of superconductivity.

In a superconductor, electrons near the Fermi level form pairs of opposite spin and opposite momentum. Individually, each electron is still a Fermion (thus the need for opposite spin); but the pair behaves as a Boson. So, they have a net spin of 0 and are capable of Bose-Einstein condensation into an infinite number of "Cooper pairs" (each having twice the mass and charge of a single electron) in same state, with same energy. And, a single wavefunction defines them all – a macroscopic quantum wavefunction, similar to that of superfluid.

Of course, the electrons will only do so if it is energetically favorable. Cooper considered the addition of two electrons with slightly higher energy than the Fermi energy, with equal but opposite

momenta (and opposite spin) [40]. He showed that if there was any net attraction between these electrons, however slight, then the energy of the pair was less than two times the Fermi energy. Therefore, electrons near the Fermi level will naturally form pairs and collapse to a single wavefunction $\Psi$, until only electrons too far from the Fermi level remain. So, where there had once been a continuum of available states near the Fermi level, there is now a gap: Any electron within an energy distance $\Delta$, either above or below the Fermi level, will form a Cooper pair, leaving those states unavailable for normal resistive conduction.

This energy gap is useful for the BCS density of states, as indicated in Equation 1.1, which is plotted in Figure 1.3.

$$N(E) = \Re\left\{\sqrt{\frac{E^2}{E^2 - \Delta^2}}\right\} \tag{1.1}$$

Here, $\Re$ represents the real part of the bracketed term, and $\Delta$ is the superconducting energy gap.

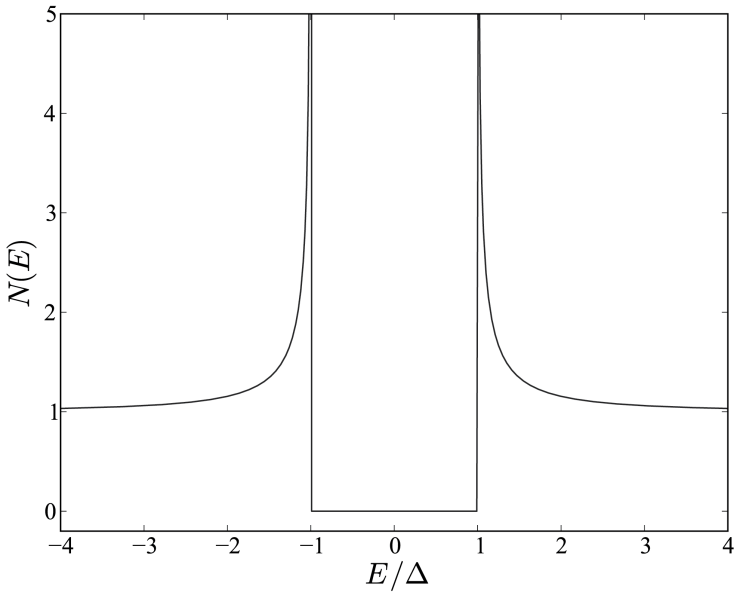


**Figure 1.3:** The BCS density of states, from Equation 1.1. Below $E = -\Delta$, all states are filled with electrons, at $T = 0$. Above $E = +\Delta$, these are all empty (hole) states, at $T = 0$. In between, there is a gap, corresponding to the tendency of electrons within this energy range to combine into Cooper pairs. Therefore, some references use $2\Delta$ as the superconducting energy gap. However, in this thesis, I refer to $\Delta$ itself as the energy gap (consistent with many other references).

This wavefunction has a ground state, but no excited state: an excitation is equivalent to breaking the Cooper pairs into individual "normal" electrons. To do so, an energy of $2\Delta$ is required. If this is greater than the thermal energy available $k_B T$, the electrons will tend to remain paired.

In this thesis, I refer to $\Delta$ as the superconducting energy gap, consistent with most references. However, because there is an energy distance $\Delta$ from the highest available electron states to the Fermi level, and another $\Delta$ from the Fermi level to the lowest available hole states, some references define $2\Delta$ as the superconducting energy gap.

What could provide this net attraction? Although the direct electron-electron interaction is repulsive and electron-ion interaction is attractive, this is not the primary concern: electrons at the Fermi level are effectively screened by the distribution of charges. Instead, it is due to interactions between electrons and the lattice.

As an electron moves through the lattice, it attracts the positive nuclei. Because of their inertia, the nuclei cannot respond immediately; instead, the center of the response lags behind by a distance inversely proportional to highest possible lattice vibration frequency, also known as the Debye frequency $\omega_D$. (See Figure 1.4.)

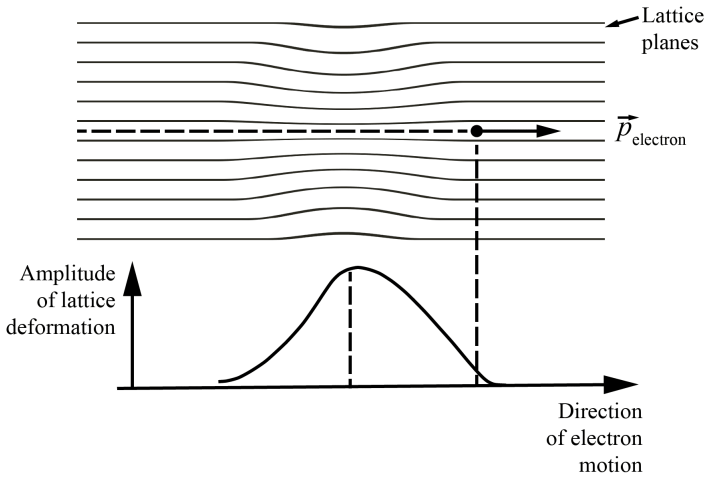


**Figure 1.4:** Schematic representation of the deformation of a crystal lattice, as the result of a passing electron, adapted from [2]. By their inertia, the nuclei lag in their response, causing a local concentration of positive charge in the wake of the passing electron.

This deformation of the lattice has a net positive charge, and is able to attract the second electron. It is also relatively large, so that the electrons in Cooper pairs may be many lattice constants apart.

This is related to the coherence length $\xi$ in a superconductor. For example, $\xi_{Pb} = 90$ nm, $\xi_{Sn} = 230$ nm, and $\xi_{Al} = 1600$ nm [41].

The highest possible phonon energy is $\hbar\omega_D$. As a result, only those electrons within a shell of thickness $\pm\hbar\omega_D$ around the Fermi surface are able to be paired. Also, phonon-mediated superconductors with a higher phonon frequency tend to have a larger superconducting energy gap and higher $T_c$.

Since lower-mass atoms oscillate at a higher frequency (all else being equal), replacing atoms in a lattice with lighter or heavier isotopes should have a clear effect on $T_c$. This isotope effect has been found in all "conventional" superconductors. Its absence in other types (such as the cuprates and pnictides) provides evidence of an unconventional pairing mechanism.

Thermal fluctuations in the lattice disrupt its ability to form localized positively charged regions in the wake of a passing electron. Therefore, unlike the energy gap in a semiconductor, the superconducting energy gap is a function of temperature, and goes to zero at $T_c$. BCS theory provides a quantitative prediction of this effect (Figure 1.5), and is a good approximation in most cases.

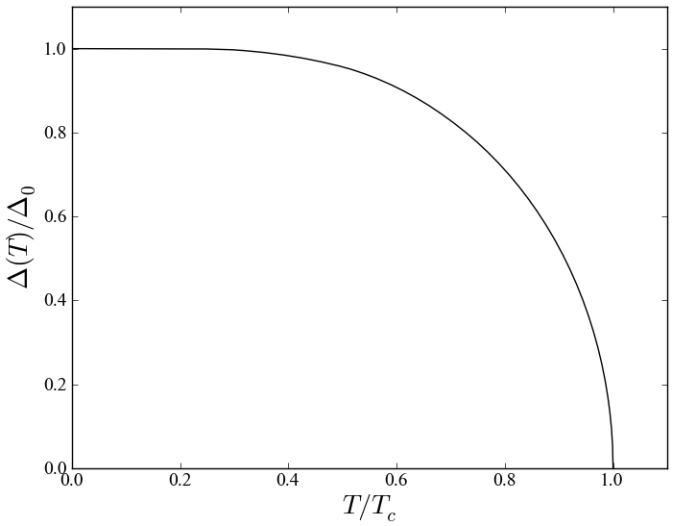


**Figure 1.5:** The dependence of the superconducting energy gap $\Delta$ on temperature, according to BCS theory.

It is interesting that vibrations, which cause an increase in resistivity as temperature increases in most cases, also cause the resistivity to drop to zero below $T_c$ for superconductors. This "phonon-

mediated superconductivity" formed the explanation for conventional BCS superconductivity [33], though any other effect providing a net attraction would also allow pairing, and thus superconductivity.

## 1.2 Josephson Junctions

By 1960, physicists were increasingly taking the concept of a macroscopic quantum-mechanical wavefunction seriously, and contemplating its implications.

For a superconducting ring with a persistent current, in order for the Cooper pairs in the entire superconductor to be described by a single wavefunction $\Psi = |\Psi|e^{i\theta}$, its phase $\theta$ must differ by $\pm 2n\pi$ around the loop. And in fact, experiments proved that the magnetic flux is quantized in increments of $\Phi_0 = \frac{h}{2e}$. Each increment in phase difference around the loop corresponds with a current around the loop.

In 1962, Brian Josephson considered a system of two superconductors, each with its own wavefunction $\Psi$ having its own phase $\theta$ [42]. If the two are coupled across a "weak link," then the phase difference $\gamma = \theta_1 - \theta_2$ across the two superconductors has a physical meaning, and acquires a physical significance.

Since the phase difference corresponds to a current in a loop of a single superconductor, Josephson supposed that the phase difference across two coupled superconductors could likewise correspond to a current. Ordinarily, the phases of two different superconductors can change independently; but if brought in close enough proximity, there is the possibility of Cooper pairs tunneling from one to the other. In this case, the phases are correlated, and the phase difference $\gamma$ acquires meaning. In a sense, the phase difference provides an asymmetry that can "tell the electrons which way to go" [43]. So, although the phase is usually irrelevant to the analysis of most physical systems, and the absolute phase cannot be measured, this phase difference is of great importance in this type of system.

The type of system originally considered by Josephson consists of two superconducting electrodes separated by a thin insulating barrier, and that is the form of the junctions considered in this thesis. These are described as "tunnel junctions." Many other geometries and materials also exhibit this

class of behavior, including point-contact junctions, nanobridges, $SNS$ junctions formed using a normal metal between the superconducting electrodes, etc. (See, e.g. [44, 21].) Their behavior may be somewhat different from those of tunnel junctions, and are not discussed in this thesis.

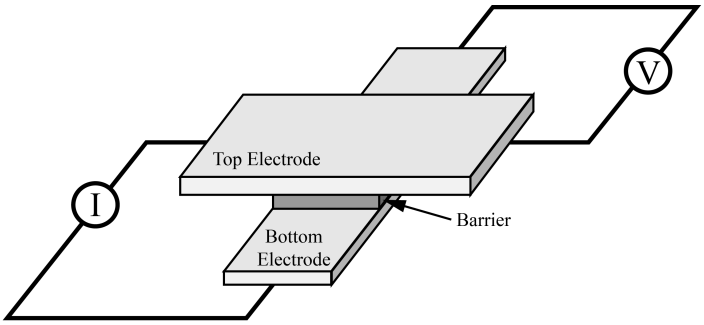


**Figure 1.6:** Schematic of a "cross-type" or "sandwich-type" junction, adapted from [3]. The superconducting bottom electrode is placed on a substrate. A thin barrier separates it from the top superconducting electrode. If this barrier is insulating, the junction is referred to as a Josephson tunnel junction. In this case, the barrier must be sufficiently thin that Cooper pairs may tunnel across the barrier.

A traditional realization of a tunnel junction is the "cross-type" or "sandwich-type" junction, similar to those used in this study (see Figure 1.6). In such a junction, one superconducting electrode is placed on a substrate. Then, a thin uniform insulating barrier is formed across it – sometimes as the result of a deposition process, or, as in the case of the junctions used in this thesis, from the formation of a native oxide. Typically, this barrier is on the order of nanometers thick. Finally, the second superconducting electrode is deposited. These electrodes are then available for electrical contact with other devices.

For tunnel junctions, for which there is a small transmission of normal electrons across the barrier, Josephson derived a sinusoidal dependence on the phase difference for the current. This is the first Josephson relation

$$I = I_0 sin\,(\gamma) \tag{1.2}$$

Below a critical current $I_0$, a current is able to flow, even in the absence of a voltage. In this sense, the behavior of a Josephson junction in the zero-voltage state is similar to that of a single superconducting sample.

Above the critical current, there is a nonzero voltage across the junction. In this sense, it is said to be in the "resistive state." However, even there, the phase difference plays a role. The second Josephson relation

$$\frac{d\gamma}{dt} = \frac{2eV}{\hbar} = \frac{2\pi}{\Phi_0}V \tag{1.3}$$

shows, somewhat surprisingly, that in the presence of a constant applied voltage, the phase difference across the junction must continuously change. And, from the first Josephson relation, an AC current must exist in the junction. As a result, this is known as the AC Josephson effect.

Experimental confirmation of the Josephson effects came shortly thereafter [45, 46], and several researchers suspected that what they had originally taken to be troublesome shorts in their junctions at low temperature were actually indications of the Josephson supercurrent. Ever since, they have been widely used in a variety of studies and practical applications.

For example, the AC Josephson effect demonstrates that external microwave signals may couple to the junction. For some types of junctions, this results in steps in the current-voltage curves, first observed by Shapiro [46], at $V_n = n\left(\frac{h}{2e}\right)f$, $n = 0, 1, 2, ....$ Because of the clarity of these steps and their clear connection to frequencies that can be determined to very high precision, Josephson junctions have been used as a voltage standard [47].

Josephson junctions are used in tunneling spectroscopy, for a variety of purposes. These include characterizing the vibrational modes of materials placed in the barrier [48] and exploring the superconducting energy gap in detail, as we have done in Chapter 3.

Since 1983 [49], Josephson junctions have also served as a test-bed for explorations of macroscopic quantum mechanics, with sizes generally on the order of microns rather than single atom or single photon systems. Studies of switching from the superconducting state to the resistive state, similar to those discussed in Chapter 4, demonstrated the presence of energy levels [50]. Later, a current-biased Josephson junction was proposed as a possible quantum bit [51], and two-qubit coupling has been demonstrated [52].

Magnetic fields play an essential role in many important characteristics of Josephson junctions,

both in theory and applications. However, since the magnetic field was kept at zero for all results presented in this thesis, I do not discuss them here.

## 1.3 Two Superconducting Energy Gaps

Not long after the BCS superconductivity papers were published, Suhl et al. [53] and Moskalenko [54, 55] presented theoretical explorations of the case where two bands cross the Fermi surface. This work was inspired by the observation that superconductivity in the transition metals is not explained well by conventional BCS theory (e.g. they do not exhibit a strong isotope effect), and that electrons in both the $s$ and $d$ bands are at their Fermi surfaces.*

In this analysis, different parts of the Fermi surface couple with different portions of the phonon spectrum, leading to different gaps. In nearly all cases, these effects are anisotropic, so a number of the early explorations of this concept highlight the anisotropy over the multi-gap nature.

Any interband coupling or impurity scattering causes the two-gap superconductor to exhibit a single critical temperature (among other common properties), usually higher than the temperature of either band alone in the absence of coupling [24].

Suhl et al. suggested that the presence of multiple gaps might explain some prior experimental results on Pb and Hg [59]. A number of later experimental results also appeared strongly suggestive of multi-gap superconductivity [60, 61, 62, 63, 64, 65].

But from the outset, there was theoretical uncertainty about the applicability of these results to real superconducting systems. When there is enough impurity or defect scattering, indications of two bands should vanish [66], and there were suggestions that this should necessarily be the case in the transition metals [67]. Although the original paper [66] was confident that pure single crystals of superconductors would exhibit a variation in the energy gap,† later researchers found reason to doubt the applicability to real samples.

*Later extensions of the BCS theory provided explanations of many of these behaviors that did not require multiple gaps. In some cases, these can be understood with a fuller understanding of the interactions between electrons and phonons in superconductors. (e.g. [56, 57, 58]) These "strong coupling" effects lead to an energy gap that has real and imaginary parts which are energy-dependent. These effects are significant for a variety of superconductors, including Pb and $MgB_2$. Therefore, they should be studied for a full understanding of the theories referenced in this thesis. However, the discussion presented here is sufficient for our experimental results.

†"...In pure single crystals of superconductors, one can very quickly show that the energy gap will be a strong function of the momentum vector on the Fermi surface, because most superconductors have fairly complicated Fermi surfaces, and it would be a miracle if the interactions were sufficiently constant to maintain a constant energy gap."[66]

The supporting experimental evidence also fell under controversy. Tunneling data was found to be consistent with a voltage divider model, rather than the intrinsic properties of the superconductors themselves [68]. And one study found that clean single-crystal niobium junctions did not exhibit suggestions of multi-gap behavior, while those that had aged or formed an oxide layer exhibited features previously taken to indicate the presence of multiple gaps in the niobium itself [69].

After that, the topic was largely abandoned. Some good evidence supporting the observation of two gaps came in 1980 [70] and 1981 [71]. With the discovery of the cuprates, there was some resumed theoretical interest [72, 73, 74, 75], but no experiments presented evidence of multiple gaps in these systems. The scattering associated with the theory of "dirty" superconductors appears to explain this result. And in 1998, the experimental results on Nb were reconsidered [76]. The arguments here in support of evidence for multi-gap superconductivity were reasonably convincing, but appear not to have been followed up on. So, for roughly 20 years, there were very few publications on the topic.

The situation changed completely after superconductivity was observed at 39 K in magnesium diboride in 2001. Its electronic structure clearly suggested two gaps, and, once fabrication of films and crystals advanced, experimental evidence soon confirmed it. This is discussed further in the following section.

Since then, multiple gaps (not just two) have since been observed in other materials, including the pnictide superconductors [21, 77]. And, theorists have reconsidered a variety of materials, including transition metals such as Pb [78, 10], and the widely-studied $NbSe_2$ [79, 80]. Improved theoretical and experimental tools are advancing this effort, and it appears to be relevant for a better understanding of many superconducting materials.

A new physical effect is also possible. In the lowest-energy state of a two-band superconductor, the superconducting phases of the two bands may be either in phase, or perfectly out of phase with each other. Leggett [81] considered fluctuations in the phase difference between the two bands, and showed that these would cause fluctuations in the Cooper pair density. This may lead to collective oscillations, known as Leggett modes. Although proposed in 1966, experimental evidence has been rather elusive, with some experimental evidence in $SmLa_{0.8}Sr_{0.2}CuO_{4-\delta}$ in 2001 [82] and in $MgB_2$

in 2007 and later [83, 84]. Other experimental results have only been suggestive.

## 1.4 Magnesium Diboride

As discussed above, magnesium diboride is a superconducting material clearly exhibiting two superconducting energy gaps. It also has the highest $T_c$ among conventional phonon-mediated BCS superconductors (at conventional pressures). Both of these properties can be understood on the basis of its physical and electronic structure.

The presence of metal-boron and boron-boron bonds produces exceptional physical and chemical properties in the entire metal boride family. Their melting points, hardness, and electrical and thermal conductivities are high, making them suitable for a range of applications [85]. However, it is the superconducting properties of magnesium diboride that are of interest in this thesis.

$MgB_2$ was a well-known material by the early 1950s. In 1957, an experiment to measure its heat capacity at low temperature had the potential to discover its superconducting nature [86]; unfortunately, given the sparse resolution of the data, this was not recognized. It was only in January 2001 that the superconducting transition of $MgB_2$ near 39 K was announced [36]. The discovery of superconductivity in $MgB_2$ was serendipitous, rather than the result of a systematic search for superconducting materials. This is typical for discoveries of superconducting materials, including the cuprates, pnictides, and fullerides.

This discovery set off such a flurry of theoretical and experimental work that, by 2003, it was already better understood than high temperature cuprate superconductors. Although it is well-explained by conventional theory, it is something special: "In fact, an agreement emerges that it is, albeit still an electron-phonon superconductor, a case of genuinely novel physics, sufficiently unusual to set it apart from all previous electron-phonon superconductors" [23].

Magnesium diboride has also proven attractive for applications. It is composed of common, inexpensive elements, eliminating that as a limiting factor in production. Since its coherence length is longer than that of the cuprates, crystallites do not need to be aligned to allow reasonable current over macroscopic scales (e.g. for wires); in fact, crystal defects may actually help by pinning flux vortices. And its normal state resistivity is much lower than most other superconductors, allowing

magnet wires to withstand quenching (the sudden loss of superconductivity).

$MgB_2$ wires have been demonstrated, and have produced a world-record 20 kA of current in a superconductor at 24 K at CERN [87]. Persistent currents have been demonstrated in solid nitrogen, eliminating the need for an expensive liquid helium bath, and allowing operation in areas where power failures are common [88]. $MgB_2$ coils have even been proposed for magnetic shielding to protect crews in interplanetary spacecraft [89].

As indicated in Figure 1.7, $MgB_2$ is made up of parallel hexagonal boron lattices, intercalated by magnesium. In this sense, it appears similar to intercalated graphite. However, in this case, the magnesium donates an electron to the boron planes, causing the layers to be held together by ionic bonding. The $c$-axis is defined as the direction perpendicular to the boron plane. The $a-b$ plane is parallel to the boron lattice.

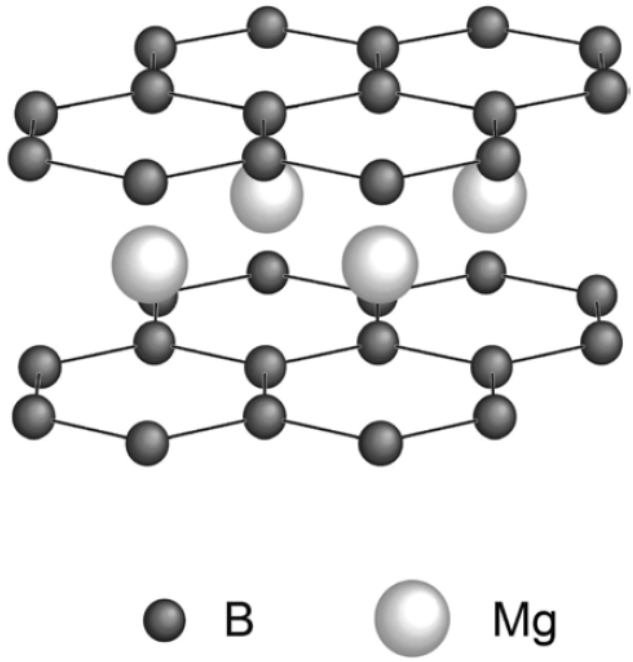


**Figure 1.7:** The crystal structure of $MgB_2$ (from [4]). Parallel hexagonal Boron lattices are intercalated by magnesium, which donates an electron to the boron planes. The $c$-axis is perpendicular to the boron planes; the $a-b$ plane is parallel to the Boron lattice. (Reproduced with permission from [4] ©IOP Publishing.)

The boron atoms are held together by strong $\sigma$ bonds formed from 2s and $p_{x,y}$ orbitals, localized in the boron planes, and by $\pi$ bonds formed from the $p_z$ orbitals, perpendicular to the planes [90].

Electrons at the Fermi level occupy both the $\sigma$ and $\pi$ orbitals – neither is completely filled. As noted in reference [5], "$MgB_2$ may be unique with partially occupied $\sigma$-bonding states in a layer structure."

These strong $\sigma$ bonds coupled with the light boron atoms produce a high phonon frequency, and thus a high energy. Certain resonant modes are able to couple strongly with the electrons, allowing these electrons to be bound into Cooper pairs with a high energy gap. These are responsible for the high $T_c$ of magnesium diboride.

The $\pi$-bonding states are also partially filled, and permit conduction of electrons. However, they form much weaker Cooper pairs. Therefore, it is logical that $MgB_2$ would exhibit two separate superconducting energy gaps.

By substituting different boron isotopes in the lattice, it became clear that phonons provide the pairing mechanism for superconductivity in $MgB_2$ [91, 92]. However, the much weaker isotope effect for magnesium [91] showed that vibrations of the boron atoms are largely responsible for its superconductivity. So, $MgB_2$ is accepted as a phonon-mediated BCS superconductor (rather than requiring an unconventional pairing mechanism). In this sense, it is "conventional;" however, the presence of two gaps allows new and interesting physics to be observed.

Considering its Fermi surface can help to illustrate its features. The $\sigma$ orbitals are largely confined to the $a-b$ plane. So, rather than the spherical surface for free electrons, the Fermi surface produced by these orbitals forms cylinders, with no available endpoints along the $c$-axis. These are indicated in orange at the corners of the zone shown in Figure 1.8(a). There are two sheets, one for electron states, and the other for hole states.

The $\pi$ orbitals, perpendicular to the $a-b$ plane, have a more complex three-dimensional character. This produces the tunnel-like structures shown in blue and green in Figure 1.8(a). There are again two sheets for electron and hole states.

These $\sigma$ bands, with strong bonds and strong coupling with the electrons, are the primary reason for the high $T_c$ of $MgB_2$. The $\pi$ bands also contribute, but to a lesser extent.

Impurity scattering will tend to equalize the gaps within each type of band, but not much between

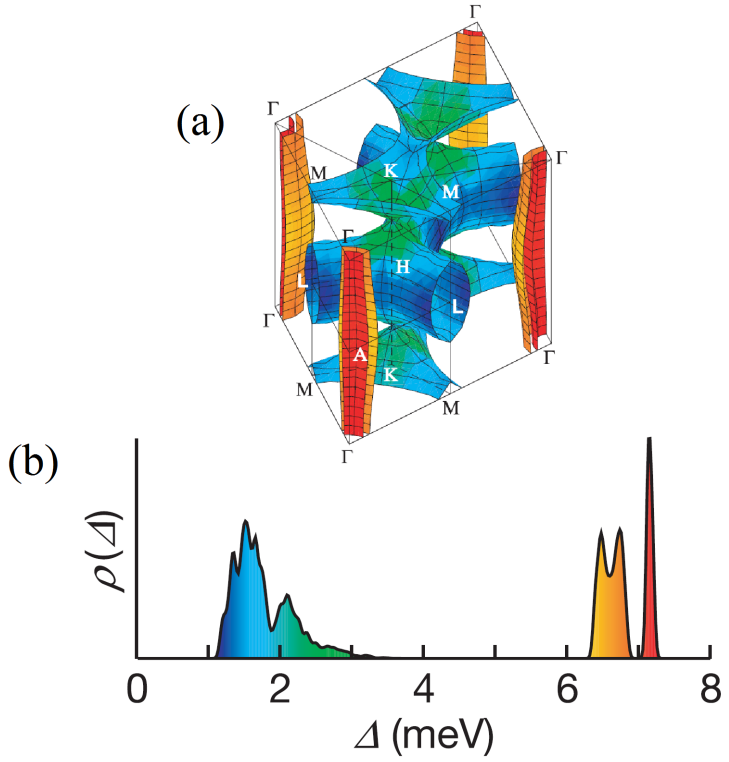


**Figure 1.8:** (a) Fermi surface of magnesium diboride, colored according to the value of the superconducting energy gap at that portion of the surface. The two $\sigma$ bands form cylinders in orange at the corners, and are associated with the higher energy gap. The $\pi$ bands are indicated in blue and green, and are responsible for the lower energy gap. (b) Local density of states for magnesium diboride. (Reprinted by permission from Macmillan Publishers Ltd: Nature 418(6899):758-760, copyright 2002. [5])

them [23]. This leads to the two distinct superconducting energy gaps, commonly referred to as $\Delta_\sigma$ and $\Delta_\pi$, reflecting their origin.

Thanks to these differing structures, superconductivity in $MgB_2$ is highly anisotropic. This led some of the early experiments to produce conflicting results. But the overall picture of two separate gaps soon became clear, both in theory and experiment.

The nature and energy values of the two gaps are fairly consistent across the theoretical predictions. However, the study of Reference [5] was the first to display a "local gap distribution" for $MgB_2$: $\rho(r,\Delta) = \Sigma_k |\psi_k(\vec{r})|^2 \delta(\Delta - \Delta_k)$, where $\psi_k(\vec{r})$ is the electron wavefunction with crystal momentum $\vec{k}$. Figure 1.8(b) comes as a result of integrating this local distribution: each portion of the Fermi surface provides its own unique contribution to the energy gap structure.

These results were controversial. Not only are there competing theoretical results, the papers [5, 93] were explicitly questioned as to their legitimacy. Reference [94] claims, among other objections, that this "distribution of gaps *within* the $\sigma$ and the $\pi$ sheets" should not be observable in real samples, due to the need for unreasonably small scattering rates. In response [95], it is agreed that scattering will indeed tend to average out these features, though that is not an essential flaw in the theory. In addition, "we hope that perhaps clever experiments in the future may observe these variations in appropriate samples."

To resolve the question of the presence of two gaps, and of any substructure within them, it seems logical to measure the gap structure on the Fermi surface directly. As shown in Chapter 3, the conductance of a Josephson tunnel junction bears a direct relationship with the density of states and thus, the energy gap.

However, the situation is more complex than it may appear. The results of any tunneling spectroscopy measurement will be sample-dependent: thanks to the structure of the Fermi surface, not all parts of Fermi surface are directly accessible to tunneling in any given sample. Even those parts that are accessible will not appear in proportion to their theoretical influence on superconductivity.

So, the first experimental indications of two-gap superconductivity in magnesium diboride came not from electronic measurements, but from measurements of the specific heat [96]. With better-

characterized crystals, tunneling spectroscopy did reveal two gaps soon enough [97].

Observing substructure was a greater challenge, requiring the development of high-quality thin films. This work was performed by our collaborators at Penn State and Temple University. Their measurements [98] and ours [99] demonstrate that these substructures within each energy gap are observable in real samples.

In Chapter 3, I present the results of our experiments, which show these features with high resolution (Figure 3.18).

# Chapter 2: Experiment Overview

The goal of our experiments is two-fold: to study the useful electronic properties of the superconductor magnesium diboride through its energy gaps, and to determine the application potential of Josephson junction devices based on $MgB_2$ for switching and quantum state applications.

To do so, a current must pass through the junction, and the voltage across it must be measured. We need very low levels of thermal and electric noise in order to achieve the high resolution we desire: for some measurements, current fluctuations must be kept substantially under $\sim$10 nA. To achieve this, we operated at very low temperatures ($\sim$20 mK), and used several methods to minimize electronic noise.

Each part of the experimental process presents its own challenges, as outlined in sections 2.1 and 2.2. The general principles and some components used in all of our experiments are discussed in section 2.3.

We conducted two different categories of experiment: current and conductance vs. voltage (Chapter 3), and superconducting-to-normal switching (Chapter 4). Because these are substantially different experiments, further details are also addressed in Sections 3.2 and 4.2.

## 2.1 Helium Dilution Refrigeration

Helium dilution refrigeration is the conventional technique for achieving temperatures on the order of 100 mK. It has several advantages over other methods of cooling. For example, although Bose-Einstein condensates at nanoKelvin temperatures have been generated via laser cooling of magnetically-confined atoms, these methods work on a countable number of atoms, rather than the large mass of copper, aluminum, and electronic components that make up our system's cold finger, samples, sample boxes, and filtering. Additionally, electric currents running through the wiring, including at the base temperature portion, provide a continuous source of heating. The helium dilution refrigerator is the only continuous-cycle method currently available to provide sufficient cooling

power at these temperatures [100]. It is also a well-established technique, with the first continuously operating dilution refrigerators reported in 1966 [101, 102].

However, it does have several disadvantages for some of our higher-temperature experiments. Because the system is designed to operate below 1 K, it is difficult to maintain stable temperatures above 4K, and the thermometer closest to the sample is calibrated for 6K and below. So, although in principle temperatures up to ∼40 K would be of interest when studying $MgB_2$, we only have data up to 6 K.

Also, each round of experiments typically requires at least two 100-liter Dewars of liquid helium, which required very careful planning compared with experiments using either dry dilution systems or cryocoolers that can run continuously at substantially less expense.

An additional disadvantage is complexity. As described in Harvard University's "Hitchhiker's Guide to the Dilution Refrigerator,"[103] "A dilution refrigerator, at first blush, appears to be a horribly, intricately, awfully twisted labyrinth of tubes and valves and KF flanges designed with the sole purpose of hastening a physics student's descent into madness. This is, to a large extent, quite true. Nonetheless, much of the mystery of dil fridge operation may be dispelled by a bit of hands-on experience and a few helpful pointers."

More detailed discussions of our fridge - an Oxford Instruments Kelvinox MX400 [104] - may be found elsewhere [103, 105, 106, 107, 108]. Due to the complexity of the system, this section provides only a brief overview of the operation and function of a $^3$He-$^4$He refrigerator.

At the heart of a dilution refrigerator is the mixing chamber where milliKelvin temperatures are achieved and where our devices our mounted. Within this chamber at a temperature above 0.87 K, a mixture of $^3$He and $^4$He gas ("the Mix") condenses into a homogeneous solution. Below 0.86K, this mix separates into a "concentrated phase" that is rich in $^3$He, and a "dilute phase" that is more rich in $^4$He. The concentrated phase, being less dense than the dilute phase, floats over the latter, creating a "phase boundary" between them. The enthalpy of the $^3$He in the two phases is different, making the concentrated phase much like liquid $^3$He, while the dilute phase is much like a gas (surrounded by noninteracting $^4$He). Aided by a pump, $^3$He "evaporating" from the concentrated

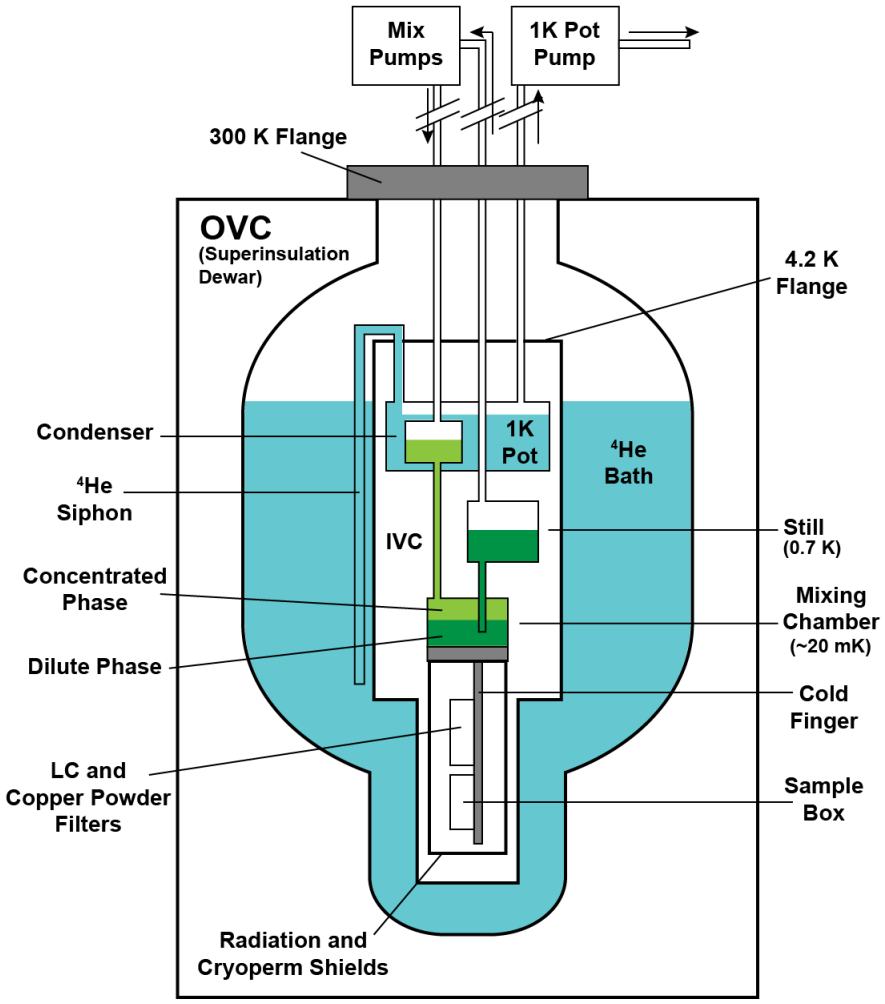


**Figure 2.1:** Schematic of our helium dilution refrigerator. The outer vacuum chamber (OVC) isolates the $^4$LHe in the main bath from the room environment. The inner vacuum chamber (IVC) is evacuated to allow its contents to reach temperatures below the 4.2 Kelvin of the main bath. Pumping on the $^4$LHe in the 1K pot reduces its temperature to $\sim$1.2 K. Pumping on the still, combined with the additional phase transition between the condensed phase and dilute phase of the $^3$He and $^4$He mix allow the cold finger, and attached components, to reach our base temperature of 23 milliKelvin. Our devices are placed in an aluminum sample box attached to the cold finger, surrounded by electric and magnetic shielding.

phase into the dilute phase provides the cooling required to reach mK temperatures. By circulating the gases, $^3$He in the concentrated phase is replenished, and continuous cooling is realized.

The mixing chamber is surrounded by other stages that cool it to its operational temperature. The "Outer Vacuum Chamber" (OVC), "Inner Vacuum Chamber" (IVC), and the dilution fridge probe are kept under vacuum. The "Outer Vacuum Chamber" (OVC) consists of many layers of aluminized mylar superinsulation, isolating the "main bath" from the ∼290 K environment. The main bath is a 70.7 L Dewar surrounding the fridge.

A separate, closed-cycle system contains a mixture of $^3$He and $^4$He ("the Mix"). After passing through nitrogen and helium traps that maintain the purity of the Mix, it is allowed to pass through the 1K Pot. As it does so, it condenses to liquid. This then flows down into the Still and settles in the mixing chamber. At the mixing chamber, an additional set of vacuum pumps reduces the pressure of the condensed Mix. This sets up the cooling cycle within the mixing chamber, described above.

Of course, there are many other essential aspects to properly conducting experiments with a dilution fridge. The necessary skills are often best acquired by experience: first observing others familiar with its operation, then assisting them, before finally taking charge (although many activities require two or more people).

## 2.2 Noise Suppression

While many ultra-low temperature experiments are situated in basements of buildings, with the entire cryostat inside a galvanized steel shielded room [109], our experiments were conducted in an open room near a major transportation hub in Philadelphia, in an active classroom building, during construction projects that took place just outside the window. As a result, we faced a number of unusual challenges in reducing electrical and magnetic noise. It took a combination of systematic troubleshooting and trial and error to reduce noise to acceptable levels. Even after we developed solutions, we had to be very careful: slight bumps, mis-plugged in equipment, etc. disturbed the configuration, leading to more hours of debugging. It is likely that we did not discover the optimal configuration; however, once we found something that worked, we were careful not to change it.

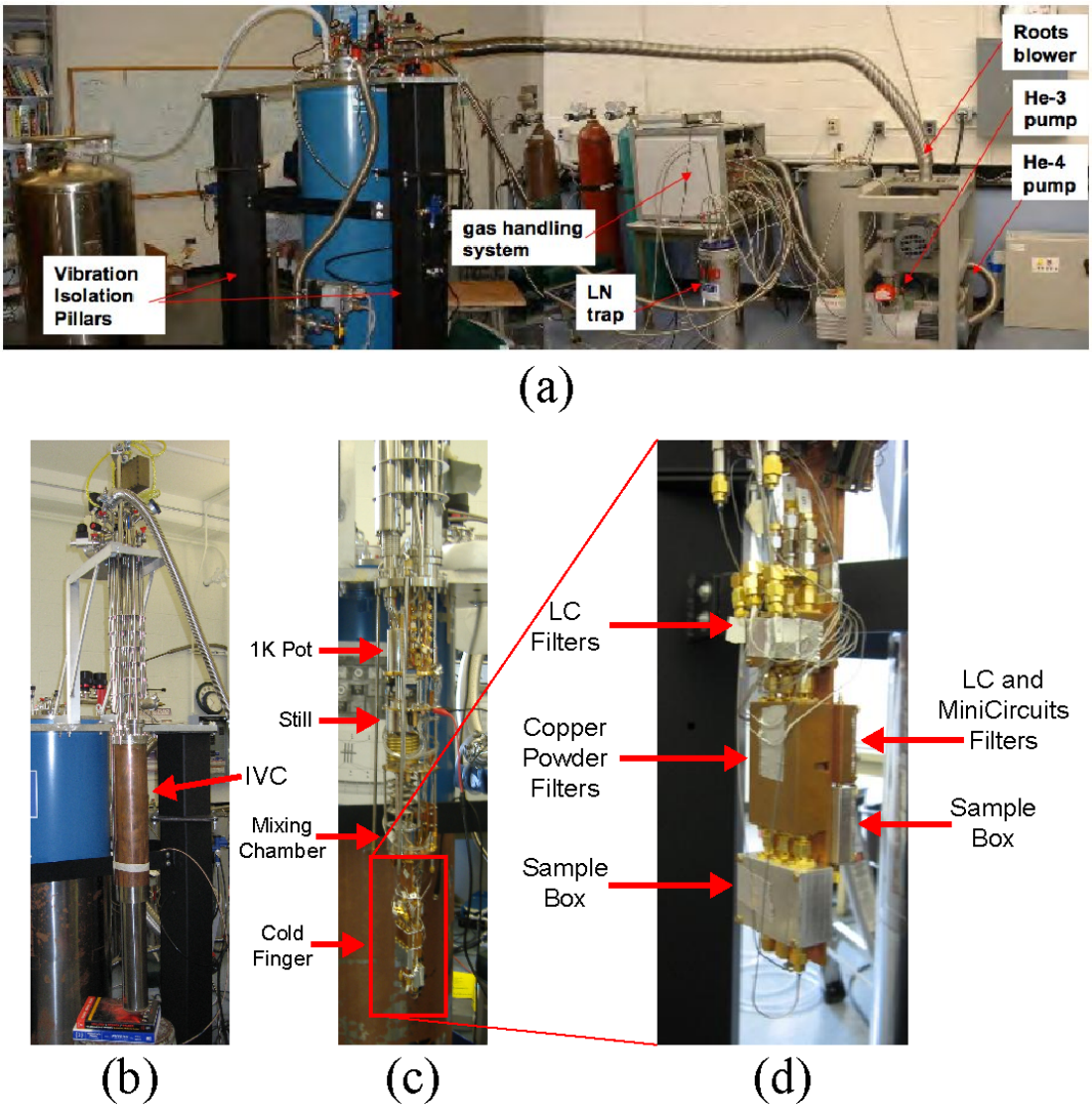


**Figure 2.2:** Our experimental system. (a) The Kelvinox MX400, which provides a cooling power of 400$\mu$W at 100mK. Vibration isolation pillars isolate the cryostat from floor vibrations. Note that this photograph was taken prior to placing the vacuum pumps in their acoustical enclosure. (b) The inner vacuum chamber (IVC), removed from the cryostat for leak detection, prior to conducting an experiment. (c) The contents of the IVC exposed, revealing the 1K pot, still, and mixing chamber, which allow us to reach 23mK, and the cold finger, on which our experiments are mounted. (d) A closer view of the copper cold finger, showing the two sample boxes, and filtering for each.

The following subsections outline some of the measures we took to reduce noise in the system.

### 2.2.1 Environmental Isolation

The cryostat itself must be kept isolated from the environment as much as possible. Three main issues were addressed:

**Vibration:** The vacuum pumps required for a Helium dilution refrigerator are often placed in a separate room from the cryostat. That was not possible due to limited space. In our lab, this resulted in vibrations to the floor, as well as generating a lot of sound.

Additionally, many of the experiments reported in this thesis were conducted during the construction of LeBow Hall, roughly 100 ft. away from our lab in Disque Hall - itself a busy classroom building. A trolley line passes beneath the busy Market St., roughly 200 ft. away.

Vibrations from these multiple sources can complicate our experiments in three ways. First, vibrations can couple directly to elements of the system we are trying to maintain at milli-Kelvin temperatures. Second, typical cables can generate up to tens of nanoAmps of current due to triboelectric effects: when the outer shield of a coaxial cable rubs against the cable's insulation, electrons may be stripped from the insulation and added to the current [110]. Third, movement of the wires through magnetic fields generates an induced voltage. For example, "In the earth's field, a centimeter of line vibrating at 1kHz with an amplitude of 0.1 mm will induce a signal of order a microvolt" [111].

We took several measures to minimize the negative effects of vibrations:

- The top flange of the cryostat is suspended by an aluminum plate supported by three vibration-isolation pillars from VERE. These pillars, which contain bladders of compressed air, isolate the cryostat quite well from vibrations in the floor: we were unable to notice any effect from people walking, stomping, or even jumping, in the vicinity of the cryostat.
- When the earliest data presented in this thesis was taken, the vacuum pumps were open to the room (as shown in Figure 2.2), leading to a very loud working environment. Later,

a wooden box lined with acoustical foam was built around the pumps and reduced the sound level in the room dramatically. A fan was required to prevent the enclosure from getting too hot.

- To damp vibrations, the still pumping line (with a 4" diameter) was clamped to the wall, and foam rubber was placed around it at the wall clamp and under it where it connects to the cryostat. Several smaller-diameter pumping and circulation lines in contact with the cryostat were also surrounded by foam rubber, which not only damped vibrations, but also prevented unwanted electrical contact.
- To minimize the movement of the coaxial signal lines, we employ several measures. We use short cables to avoid "dangling" portions that are prone to swinging or getting bumped. We stiffen the cables, both by twisting output and return cables together where possible, and by wrapping cables in aluminum foil. Such recipes also reduce the area for pickup loops, as discussed below. Finally, the stiffened cables rest, as much as possible, on foam rubber, as recommended in [110]. In principle, semirigid coax and/or triax cable would have been better options, but the methods we used were sufficient to reduce noise below the level of our desired signals.

**Magnetic Fields:** Magnetic fields are well-known to suppress superconductivity in most superconductors [112], and are used to modulate and control critical currents in Josephson junctions [113].

However, an external experimental magnetic field was not crucial for our experiments. More importantly, any changes in the external magnetic field could obscure all of the effects we seek to observe, or create features that would be impossible to disentangle from the features we use as the foundations for our conclusions. Our results are most clear and compelling if we keep the magnetic field constant, at zero.

In principle, this could be quite a challenge. As noted above, there is significant magnetic field noise from the road and rail traffic nearby. Indeed, direct magnetometer measurements inside

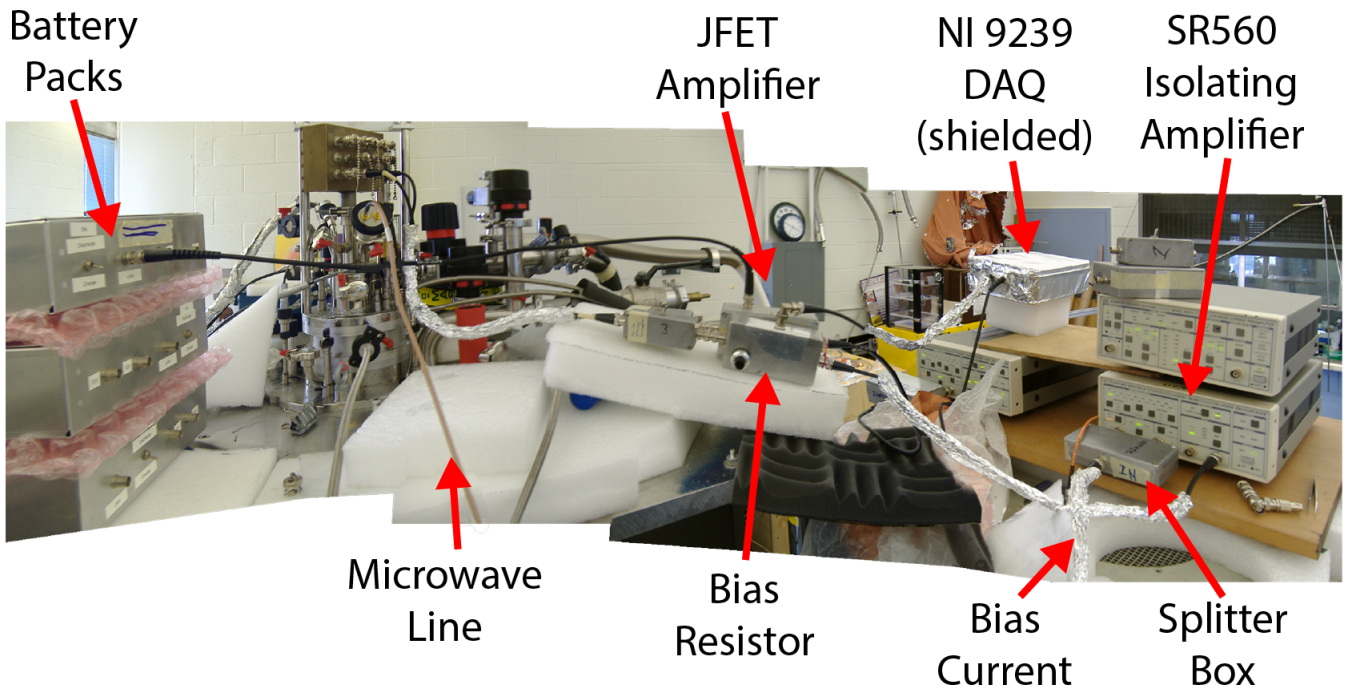


**Figure 2.3:** The top of our Helium dilution refrigerator, showing the wiring. Noise produced in the bias current cable is prevented from compromising the measurements by first splitting the signals from the inner and outer conductors, then passing the differential signal through a unity-gain SR 560 "isolating" amplifier operating in battery mode. The resulting current passes through a well-characterized bias resistor before reaching the junction. The voltage across the junction is amplified by a JFET amplifier powered by a battery-powered ultra-low noise power supply. As much as possible, all components are shielded from RF noise, are electrically isolated from each other, and are supported to minimize vibrations. Extensive use of foam and aluminum foil aided in all of these goals.
Even for experiments that did not require the junction to be excited by microwaves, we usually used the microwave line as the connection of the apparatus to ground. This provided a single, consistent method of providing a stable ground.

our cryostat by other members of our group reveal significant and periodic fluctuations of the magnetic field (Figure 2.4).

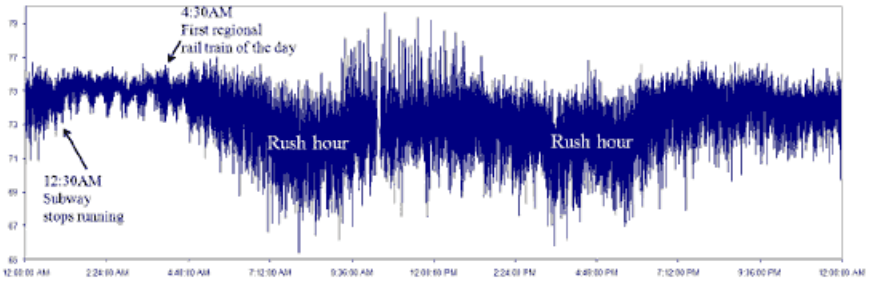


**Figure 2.4:** Magnetic field (in mG) on a typical weekday, measured by a magnetometer placed inside of the OVC of our cryostat. Fluctuations are substantially larger during active times (when the subways are running, and when people are likely to be using Disque hall) than in the early morning hours.

Despite this, we never observed difficulties due to this effect, due to measures taken prior to conducting any experiments.

First, the interior of the tail of the inner vacuum chamber (IVC) can (which provides thermal radiation and electromagnetic shielding to the cold finger) was lined with a 3-inch diameter Cryoperm 10 cylinder from Amuneal Manufacturing Corp. A large, external $\mu$-metal shield at room temperature was concluded to be less effective than a smaller Cryoperm shield with enhanced shielding at 4.2 K.

Second, the sample boxes containing the junctions were machined from aluminum. Due to the Meissner effect, magnetic fields are entirely expelled from superconducting materials below their critical temperature. $T_c$ for aluminum is 1.2 K. As a result, we are confident that most measurements made below $T_c$ were in zero magnetic field. However, we did not notice any dramatic change in the behavior of our junctions or the quality of our data (aside from that expected by an increase in temperature) by passing through 1.2K. Therefore, it appears that the shielding from the Cryoperm cylinder was sufficient.

**Inductive Coupling:** A wide variety of sources emit electromagnetic waves, largely at 60Hz. Any conducting loop will act as a one-turn transformer or antenna that produces a voltage in response to changing magnetic flux. Often referred to as "the dreaded ground-loop," it behaves

as a good constant voltage source, with an effective impedance $<< 1\ \mu\Omega$ [114, 115].

It is essential for the experiment to be grounded: otherwise, capacitive coupling between noise sources and the signal lines introduces noise that is difficult to correct for. Even in the absence of clear noise sources, the voltages will tend to "drift" due to capacitive coupling with a changing environment.*

If care is not taken, the ground connection may be made at two or more locations, forming large loops. Additional conductive loops, such as those caused by contact with the outer shielding of coaxial cables, must also be avoided. Due to the number of components connected in our experiments (as shown in the block diagrams of Sections 3.2 and 4.2), this issue prevented us from taking useful data in several of our earlier cooldowns. Ultimately, with great care, we were able to eliminate this source of noise.

Since we designated the cryostat itself as our experiment ground, everything in contact with the cryostat must be properly isolated. The stainless steel pumping lines that connect the cryostat to the vacuum pumps form large pickup loops susceptible to electromagnetic signals, and connect directly to the vacuum pumps which can provide significant electrical noise. To eliminate these sources of noise, we replaced the metal clamps and centering rings with plastic ones.

A massive aluminum top plate that suspended the cryostat rested on three vibration-isolation metal pillars from VERE. Both the plate itself and the support structure of the pillars form pickup loops. To prevent their signals from reaching the electronics in contact with cryostat, white foam blocks were inserted between the plate and the electronics, as shown in Figure 2.3. The cryostat itself was electrically insulated from this plate by rubber tubing, which also provided additional vibration damping.

Several of our electronic components were powered by rechargeable lead-acid batteries. While these eliminated connections to wall ground, the battery's bare aluminum case (connected to

*I often encountered the frustrating situation when the data would look very good while standing on a stool, looking over the apparatus; but the instant I stepped down, it was far worse. Or, there were times when I could record a set of data, and decipher how I had walked around the room during that data run based on shifts in the data. In retrospect, this occurred when the cryostat was isolated "too well," thereby having a floating ground.

the outer conductor of BNC connectors) served as its ground. To prevent unwanted electrical connections, we used rigid foam between the aluminum plate and the batteries, and bubble wrap between batteries.

Instrument ground was isolated from cryostat ground for all BNC cable connections by using Stanford Research model 560 voltage preamplifiers, operating on battery power. By using them in differential mode, any common-mode noise signals, appearing equally on the inner and outer conductors of the BNC cables, are cancelled out. The split between inner conductor and outer conductor is made as close to the amplifier as possible, to minimize the area of the loop created there.

In cases where loops were unavoidable, equal-length coaxial cables were twisted together to cancel out inductive coupling with the environment. This also stiffens the cables and reduced vibrations.

Our recipe for overcoming these issues: First, diagram every physical connection anywhere, even if it seems unlikely for it to cause a problem. Eliminate any loops found on this diagram, and develop connections that lead to only one ground connection to the cryostat.

Second, isolate the grounds of all instruments (using 3-2 adapters). Then, choose one instrument as "instrument ground," and tie that to ground strap. (In our case, we chose the bias function generator, as described below.) The grounds for all other instruments from a "star" configuration, leading directly from that instrument to the rest, without forming loops. Note that sometimes this ground comes via the output signal cable itself.

Third, using a battery-powered handheld multimeter, verify that the cryostat has no electrical connection with instrument ground without that one final ground connection. Then, using the diagram, ensure that the addition of that component has not produced a loop.

Resolving all of these issues, and ensuring they didn't reappear, required tremendous attention to detail, almost to the point of obsession.

These methods proved very effective. Before making these changes, 60 Hz noise was very obvious in current vs. voltage ($I - V$) data; afterwards, no periodic signal was discernable. Likewise, superconducting-to-normal switching data taken before these changes were prone to sudden shifts in switching current, accompanied by drastic changes in the width of the switching histogram - key features of the data I was seeking. But after resolving these issues, although there was some drift, it tended to be far smaller; using subsets of the full data sets allowed completely satisfactory use, in most cases.

### 2.2.2 High-Frequency Electronic Filtering

As with vibrations, high-frequency electromagnetic waves can result in heating. When coupled with signal lines, they can significantly affect junction behavior. Therefore, the presence of cell phones, wireless internet, and radio stations - all very strong in our lab - requires that signal lines to our samples be filtered.

The ramp frequency in our $I - V$ experiments is typically on the order of 1 Hz, and the ramp frequency in our superconducting-to-normal switching experiments is on the order of 1 kHz. However, a Josephson junction produces a highly nonlinear response to a source current. This results in fairly sharp discontinuities. As a result, we require low-pass filtering with a typical cut-off frequency of several MHz.

To achieve this, we used miniature coaxial cables which are lossy at high frequencies, typically followed by LC filters, and closest to the sample, by copper powder filters.

For a thin coaxial cable, attenuation increases as the square root of the frequency, due to the skin effect in its conductors. Originally designed as heater cables, Thermocoax® cables (manufactured by Philips) are widely used [116, 117] for filtering in cryogenic applications, providing about 100dB/meter at 5GHz. More precise characterizations of its filtering capabilities may be found in [116, 117]. The cables we use have a Nichrome inner conductor, and an outer conductor of stainless steel with an outer diameter of 0.5 mm. They are attractive for cryogenic applications because the thermal conductivities of these metals are closely related and very low.

Copper powder filters also use the skin effect to filter microwave frequencies. In these filters, a

thin wire is surrounded by fine-grained copper powder, embedded in Stycast epoxy which thermalizes the wire. The small size of the grains makes the effective surface area near the wires very large, which leads to strong skin-effect damping [116, 118]. These filters were enclosed in long boxes machined from copper, which were on a cold finger bolted to the mixing chamber of our dilution refrigerator.

These filtering stages were designed and installed before I joined this research group at Drexel. To allow for multiple experiments to be conducted during a single cooldown, I assisted in adding to the system a new sample box, with its own filtering. The experiments on three of the samples reported below (the "terraced" $MgB_2$/I/Sn junction and *c*-axis $MgB_2$/I/Pb junction, plus the Nb/AlOx/Nb reference junction), were conducted in the "old" sample box, with the copper powder filters in place. Those on the remaining sample (the "columnar" $MgB_2$/I/Pb junction) were conducted in the "new" sample box, with Mini Circuits miniature filters in place of bulky copper powder filters.

The "new" filter box contained a three node T-filter incorporating two 820 nH inductors and one 620 pF capacitor. These have a 3dB cutoff frequency of about 10 MHz and impedance of about 50 ohms. To achieve better attenuation at higher frequencies, we connect it in series with a set of three high frequency ceramic low pass filters from Mini Circuits [116]. Each has a cutoff frequency of about 8 Mhz and a flat attenuation of about 20-30 dB per device, for a total of about 80dB attenuation. All six components were designed for surface mounting, but I soldered them by hand, to fit in the space available. Each of the cells in Figure 2.5(b) were filled with Stycast epoxy to provide additional thermal anchoring of the bias and measurement lines. This epoxy was mixed with copper powder to provide additional skin-effect damping, although we do not rely on it, given the limited length of the wires.

## 2.3 Electronics

Block diagrams for current and conductance vs. voltage and superconducting-to-normal switching experiments are shown in sections 3.2.1 and 4.2.1, respectively. However, it is useful to describe major components common to both types of experiment here.

In each case, a current is ramped through the junction; the resulting voltage across the junction is then measured.

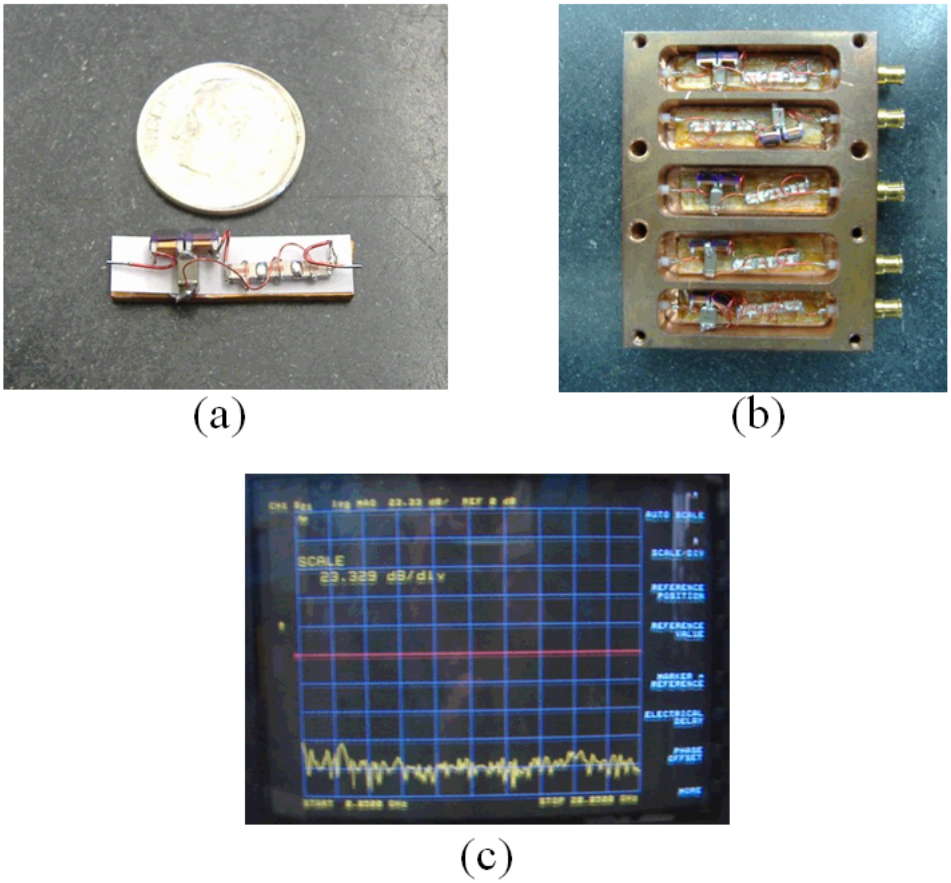


**Figure 2.5:** (a) A hand-soldered LC T-filter in series with three ceramic filters from Mini Circuits. A dime is shown for scale. (b) Five sets of filters, arranged in the filter box. (c) The output from the Thermocoax, LC, and ceramic filters, measured on a network analyzer. We reach the -80dB noise floor of the analyzer over the entire 0.05-20.05GHz range.

### 2.3.1 Current Bias

In all of our experiments, we used either one or two Agilent 33220A arbitrary waveform generator(s). It proved to be a very reliable and durable element of our experiments, with noise levels below that resolvable in our experiments.

For current-voltage experiments (Chapter 3), we used the built-in triangle ramp. This provided highly linear changes in voltage (<0.1% of peak output [119]) through the sweep in voltage. With a linear ramp, equal times were spent at any given voltage, which simplified our analysis programs.

For the superconducting-to-normal switching experiments (Chapter 4), we created a custom waveform, shown in Figure 4.13. With 14 bits of precision in the digital-to-analog conversions from the programmed waveform to the output voltage, the resolution of the function generator itself did not limit the precision of our results.

By biasing the current through a resistor whose resistance is large in comparison with the junction, the 33220A function generator, which is a voltage source, is effectively converted to a current source. In practice, we choose this bias resistor to be as large as possible, while still allowing the desired maximum current to be reached. By placing this bias resistor between all other components and the junction (while remaining at room temperature for ease in changing resistors), any noise voltages are attenuated as they pass through the resistor before reaching the junction. This attenuation was significant since the bias resistors were typically on the order of 1-100 kΩ.

One problem with the Agilent 33220A is that the outer conductors of its BNC output connectors are not well isolated from other grounds. To resolve this problem, we sent the output signals from the function generator directly to a battery-powered SR560 voltage preamplifier, operating in differential mode with an amplification of 1, prior to passing through any other components (as described above). The amplifier was tuned such that there was no voltage offset, so this did not reduce the quality of our data in any way. However, it did reduce the quantity: we could only run continuously for as long as the batteries provided consistent output. Since the signals continually ramped from zero through the maximum ±5V output of the amplifier, this was a heavy load. Even so, we could acquire data for several hours at a time, before needing to recharge the batteries.

### 2.3.2 JFET Amplifier

For our current vs. voltage experiments, voltages across the junction reached ∼10 mV; to find features within the signal, we needed resolutions better than 10 $\mu$V. Additionally, the current flowing down the voltage measurement lines must be as near zero as possible. Finally, no noise of any kind at any frequency may be allowed to pass down these lines to the extremely-sensitive Josephson junction. An extremely low-noise amplifier with well-isolated grounds makes these measurements possible.

For some early experiments, we used an SR560 voltage preamplifier, operating in differential mode. While the resulting data were reasonable, they were noisier than those provided by a home-built battery-powered JFET amplifier, a schematic of which is shown in Figure 2.6.

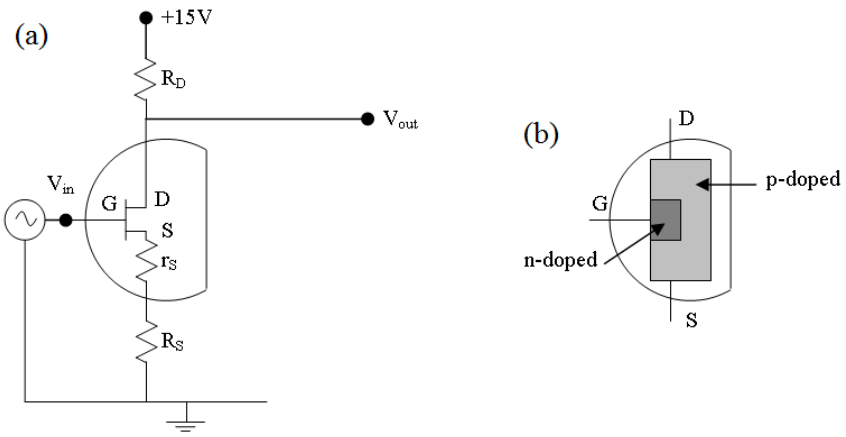


**Figure 2.6:** The JFET amplifier. (a) The full amplifier circuit. The 2SK117 JFET has its gate (G) source (S) and drain (D) labeled. The internal source-drain resistance, which varies for each JFET, is modeled as an internal resistance $r_S$. The drain and source resistances $R_D$ and ($r_S$+$R_S$) set the gain of the amplifier. For the 2SK117 JFET, $r_S \approx 67\ \Omega$ [6], so in each of our amplifiers, we use $R_S \approx 0$ (i.e. a simple wire). For our single-JFET amplifier, we used a single 1.4 k$\Omega$ resistor for $R_D$, giving a gain of ∼20. For our four-JFET amplifier, we used four matched 2SK117 JFETs in parallel, resulting in an effective $r_S \approx 67/4\ \Omega$. $R_D$ was constructed of six 67 $\Omega$ resistors in series, to reduce the heating by any one resistor, and resulting in a gain of ∼24. (b) A schematic of the JFET itself. As indicated in the figure, this model of transistor is symmetric, so that the performance is nearly equivalent whether the current flows D to S or S to D.

A JFET (junction gate field-effect transistor) is a simple three-terminal field-effect transistor, with pins denoted the "drain" D, the "source" S, and the "gate" G (Figure 2.6 (b)). A current flowing between the source and drain is modulated by variations in the voltage applied at the gate.

It can be visualized as a "pinched hose," with the degree of "pinching" controlled by the addition or removal of charge carriers at the gate. The internal resistance of the JFET itself is modeled by a resistance at the source pin $r_s$.

In our amplifier (Figure 2.6 (a)), we use a 2SK117 JFET from Toshiba, designed for low noise audio amplifiers [6]. (Note that this model of transistor is symmetric, so that the performance is nearly equivalent whether the current flows D to S or S to D.) A current runs continuously from the +15V supply, through the drain resistor $R_D$, through the transistor (D to S), and finally to ground. Therefore, $V_{out}$ is positive when $V_{in}$ is zero. Applying a positive voltage to the gate further removes charge carriers in its vicinity, expanding the depletion region around the gate, increasing the transistor's resistance; applying a negative voltage shrinks the depletion region, thereby decreasing its resistance. As a result, positive gate voltages decrease the current through the transistor, while negative voltages increase it. Therefore, $V_{out}$ varies inversely with $V_{in}$. The expected gain of such an amplifier is $\frac{R_D}{r_S+R_S}$. Some care must be taken: a sufficiently large positive input will cause the gate to be positively biased relative to the source, which may burn out the JFET. We never approached that level of signal in our experiments, though a positive input does give a slightly nonlinear amplification, while a negative input is almost perfectly linear.

This type of amplifier is attractive for several reasons. First, its simplicity makes debugging the system significantly easier. Second, JFETs in general have very high input impedances, with the 2SK117 having an input impedance of $3 \times 10^{10}$ $\Omega$ [6]. This ensures that, as long as the ground (attached to the source pin S) is properly isolated, any signals from the power supply or the devices connected to the amplifier output cannot return to the junction being measured. Third, by using a simple battery pack to provide the +15V connection, we eliminate a potential ground issue. Finally, these types of amplifiers have been used with great success in similar experiments [1, 120].

While the 2SK117 JFET is already designed for low noise applications, I was able to improve its performance even further by connecting several JFETs in parallel. The noise reduction should ideally go as $1/\sqrt{n}$, where $n$ is the number of JFETs in parallel. So, in principle, the more JFETs used, the better. In practice, it rarely works this well. First, transistors are never identical, so noise

tends to be dominated by the poorest-performing component. Second, heating rapidly becomes an issue. For multiple JFETs wired in parallel, all of the current passes through the same $R_D$. So, although the noise is reduced as $1/\sqrt{n}$, the power dissipated by $R_D$ goes as $n^2$. Since this resistor is housed in the same project box with all the other components, any significant heating can have adverse effects on the quality of the output signal. And from a practical perspective, this power drain would limit our time for experiments, with the battery life decreasing roughly as $n^2$.

It is important to note that, even in the absence of a signal to amplify, this amplifier design still draws current through $R_D$, $r_S$, and $R_S$. As a result, when no experiments are running, it is important to turn off the power to the amplifier: otherwise, the batteries may become drained by the time the experiment is ready.

Some of my early experiments were conducted with only the SR560 voltage preamplifier. In others, I used an amplifier with a single JFET (with or without additional amplification by the SR560). But my best results were achieved with an amplifier employing four JFETs in parallel. I constructed these amplifiers after measuring over 20 individual JFETs, looking for ones with appealing characteristics, and finding a reasonably matched set (for the four-JFET amplifier). A 16-JFET amplifier, which had been made before I joined the group, never produced acceptable results, largely due to excessive heating.

Although the JFET amplifiers did perform very well, the analysis was somewhat more complicated than for an ideal amplifier. These required different adjustments for each type of experiment, and are therefore discussed in Sections 3.2.3 and 4.2.1. Still, in each case, the resulting data was superior than that using only the SR560 amplifier to amplify the measured voltage across the junction.

### 2.3.3 Low-Noise Power Supply

As is apparent from the diagram for the JFET amplifier (Figure 2.6 (a)), any fluctuations in the +15 V power supply will appear directly on the measured output. So, although this source of noise does not feed back to the junction itself, it will pollute all measurements of the junction. And, since a variety of noise sources may be associated with the coaxial cable connecting the battery to the

project box containing the JFET amplifier, in addition to changes in the battery output as it is drained, additional circuitry is needed to ensure minimal noise from the power supply.

Therefore, I built an ultra-low-noise power supply, following the designs in [1, 120]. The circuit has two main components: A +15V voltage regulator to provide long-term stability and eliminate low-frequency changes to the supplied voltage, and a feedback circuit centered on an NPN transistor, to eliminate higher-frequency signals. Some critical features of this circuit are not described in [1, 120]; I outline these below.

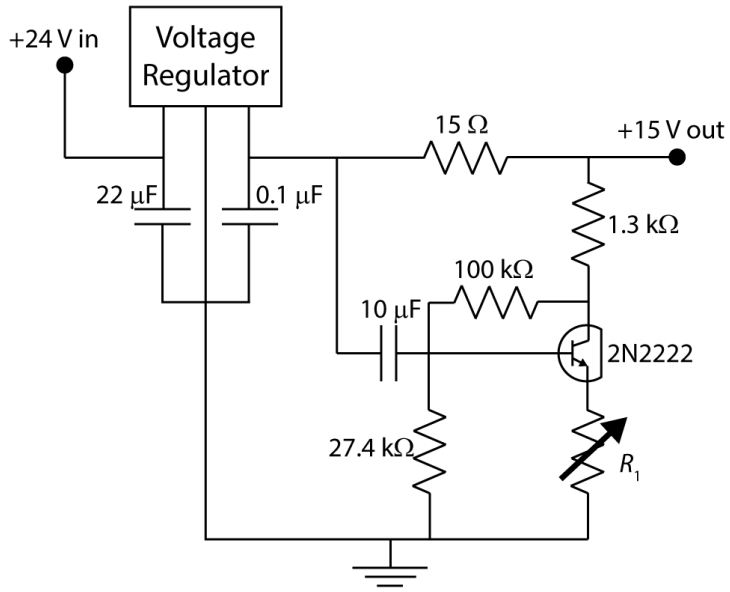


**Figure 2.7:** Ultra-low-noise power supply. The +15V voltage regulator provides long-term stability and eliminates low-frequency changes to the supplied voltage. Its coupling capacitors attenuate high-frequency signals from the input power cables. The remaining feedback circuit using the 2N2222 NPN transistor eliminates any remaining high-frequency signals. The variable resistor $R_1$ must be tuned for optimal performance of the feedback circuit; values from 5-20 Ω are typical.

The 7815 +15V voltage regulator, while seemingly a simple IC component, is a critical element which must be chosen carefully. The quality of the output varies from regulator to regulator, so they must be tested. My method for selection is as follows: First, I connect the input pin of the voltage regulator to the +24V lead-acid battery pack that we use in our experiments. Then, I connect the output of the voltage regulator to a Keithley model 2000 Multimeter, and observe the output voltage. The exact value of the voltage is not critical (so long as it is generally near +15V); stability in holding that voltage is far more important. This procedure allows me to see variations as low

as 1$\mu$V when scaled to observe 15V output, so any fluctuations are obvious. The voltage should experience minimal drift as the IC heats, with minimal rapid fluctuations. Poorly-performing voltage regulators vary in the 10mV range, while the most stable have fluctuations (both slow and fast) in only the $\mu$V digit. Roughly 5% of the 7815 chips we tested had this quality, so we needed to test a large number prior to using them in each of our circuits. After assembling the circuit, I screwed the heatsink of the 7815 IC to the aluminum project box for grounding and thermal anchoring. (Note that I also tested three voltage regulators in Texas Instruments' TL780 series. One was of sufficient quality for the JFET amplifier; the others were not.)

I also had the misfortune to discover, in the midst of a cooldown, that the performance of these voltage regulators may degrade with the heavy use we put them through - so it is important to test each power supply circuit before the $^4$LHe arrives (when the time available for experiments becomes limited).

The feedback circuit uses the 2N2222 NPN bipolar junction transistor. Any fluctuations in the output from the voltage regulator are coupled to the base electrode of the transistor. This causes the current through the transistor to change inversely to this change in voltage, leading to a change in the voltage drop across the 15 $\Omega$ resistor. If the variable resistor $R_1$ is tuned properly, the voltage change in the 15 $\Omega$ resistor will exactly cancel the initial change in the voltage regulator's output, and the output voltage from the entire circuit will be kept constant.

Because each transistor is unique, each assembled circuit must be tuned. This is not described in [1, 120], so I developed the following procedure. First, superpose a small-amplitude square wave on a +15V DC voltage. Then, send that signal through only the feedback portion of the power supply circuit, and observe both the input and output voltages on an oscilloscope. (In Figure 2.8, a 500mV square wave at 3kHz is shown.) No matter how $R_1$ is set, the amplitude of the fluctuation always reduced. But if this resistance is too high, the changes in current are not enough to cancel the fluctuation, causing the input and output waves to be in phase. If too low, the changes in current overcompensate, causing the signals to appear out of phase. But with the correct resistance, the fluctuations are eliminated: even after zooming in significantly on one step of the square wave,

minimal residual signal remains. A variable resistor from 0-100 Ω was used for $R_1$, with resistance of roughly 15 Ω typically used.


**Figure 2.8:** Tuning the feedback circuit. In yellow is the signal fed into the feedback circuit: a square wave superimposed on the +15V DC signal. In blue is the output from the feedback circuit. Curves have been offset for clarity. At left, the variable resistor $R_1$ is set to too high a value, leading insufficient current to flow through the feedback circuit to completely cancel the high-frequency signal. At right, $R_1$ is set properly. Further zooming in time and in voltage reveals a similarly flat response, even at the near-discontinuous step edges of the square wave input signal.

In Section 4.2.1, additional components are described, which require +5V, -5V, and -15V. These follow an identical circuit, except that voltage regulator ICs for the proper voltages are used, and the negative voltage circuits use a 2N4403 PNP transistor in place of the 2N2222 NPN transistor in the feedback circuit. Also, one must be careful, because the heat sinks in the negative voltage regulator ICs must not touch the enclosing project box; otherwise, they violently short out the battery packs.

## 2.4 Junction Fabrication

All of the hybrid $MgB_2$/insulator/counterelectrode Josephson junctions reported in this thesis were fabricated by our collaborators: Wenqing Dai at Penn State University (working under Dr. Qi Li), and Dan Cunnane at Temple University (working under Dr. Xiaoxing Xi). We are very grateful for all of their efforts, and their skill in producing such high-quality junctions. Because most of the details regarding fabrication are addressed well elsewhere [121, 122, 8], this section will summarize the process, paying special attention to those properties that affect our results.

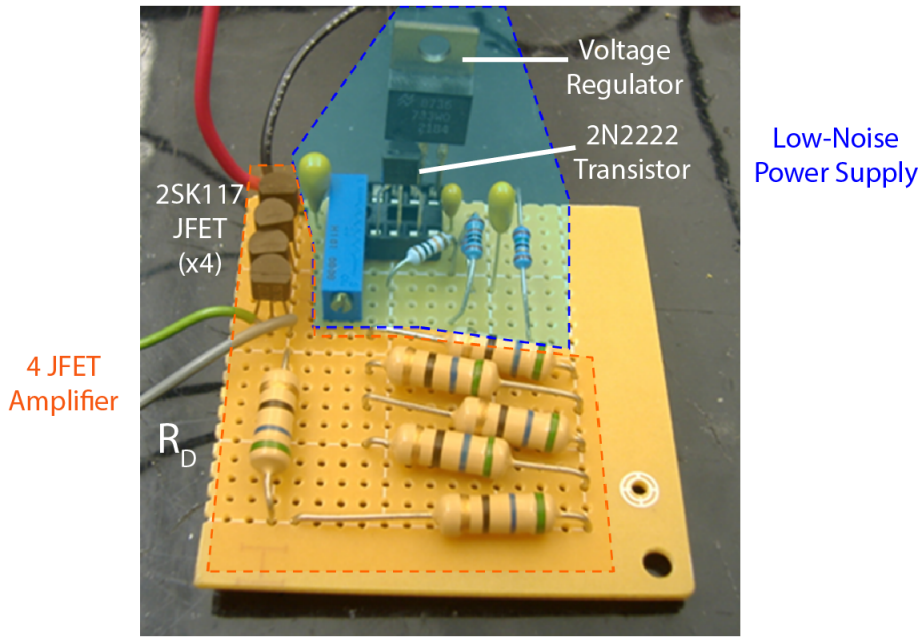


**Figure 2.9:** The fully assembled amplifier circuit, before inserting into the project box. Outlined in blue is the ultra-low-noise power supply. The voltage regulator and 2N2222 transistor were placed in a chip holder to allow them to be swapped easily. Outlined in orange is the JFET amplifier circuit, incorporating four 2SK117 JFETs in parallel. The resistor $R_D$ is made up of six resistors in series to distribute the heat load evenly. As described in Figure 2.6, no external resistor $R_S$ is required; the internal source resistance $r_S$ was sufficient.

### 2.4.1 Magnesium Diboride Thin Films

The $MgB_2$ electrodes of all the junctions used in this study consist of thin $MgB_2$ deposited via hybrid physical-chemical vapor deposition (HPCVD) on single-crystal silicon carbide (SiC) substrates. This method produced very high-quality films on the order of 100 nm thick, over the entire surface of each ~7-mm × 7-mm SiC chip. Although the same technique was used to grow $MgB_2$ films on the same substrate material, three substantially different film geometries were produced: *c*-axis, "terraced", and "columnar."

As found by Dai *et. al.* [7], on smooth 0° SiC, a largely-planar $MgB_2$ film forms, exposing primarily the *c*-axis for tunneling. On SiC whose polished surface is tilted 8° from the *c*-axis, the $MgB_2$ film takes on a "terraced" shape, exposing the *a*-*b* plane. On rough 0° SiC, the growth of the $MgB_2$ film forms columnar structures, exposing even more of the *a*-*b* plane, while still maintaining clean high-quality films. (See Figure 2.10.)

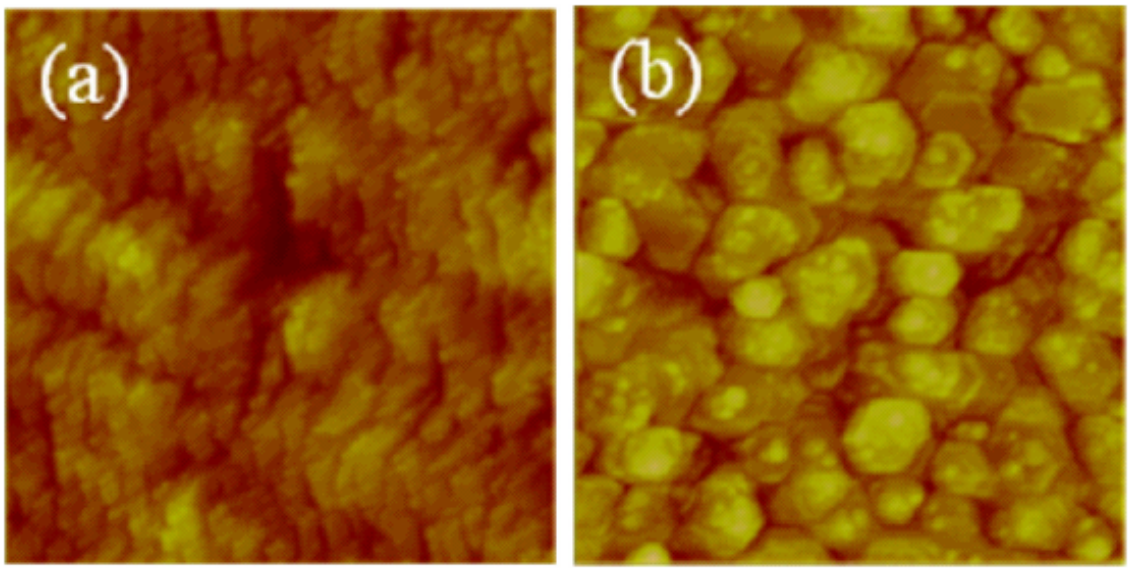


**Figure 2.10:** AFM images of representative $MgB_2$ films on SiC (Reprinted from J. Appl. Phys. 113, 083902. Copyright 2013, with the permission of AIP Publishing. [7]). Each image represents a 2-$\mu$m $\times$ 2-$\mu$m area. (a) A "terraced" film on 8° SiC, similar to that used for the $MgB_2$/I/Sn junction discussed below. (b) A "columnar" film on rough $c$-axis SiC, similar to that used for a $MgB_2$/I/Pb junction discussed below. Note that similar AFM images for a film that exposes only the $c$-axis are nearly featureless [8], and are not reproduced here.

These HPCVD $MgB_2$ films begin their growth as isolated hexagonal crystallite islands. As the film grows thicker, the islands coalesce [8]. Tensile strain associated with the coalescence is thought to be one reason that the critical temperature $T_c$ of HPCVD $MgB_2$ films is higher than that of than bulk samples ($\sim$39 K). An additional tensile strain is provided by the thermal contraction of the $MgB_2$ film relative to the substrate, as the sample cools. Similar experiments using similar samples find that both the $\pi$ and $\sigma$ gap energies of $MgB_2$ are significantly elevated when using SiC as the substrate for the $MgB_2$ film, when compared with MgO [7, 98]. This is logical, because MgO has a much smaller mismatch in thermal expansion coefficients with $MgB_2$ than with SiC.

### 2.4.2 Josephson Junction Fabrication

As described in Section 1.2, a Josephson tunnel junction requires two superconducting electrodes separated by an insulating barrier. In our junctions, the counterelectrode was Pb or Sn, while the barrier was formed by a native oxide - a thin oxide that forms naturally on the surface when exposed to air.

Reference [8] describes the barrier formation process ("Process B"). The $MgB_2$ film is initially grown on SiC at 710°C, then exposed to nitrogen gas which is used to repressurize the reaction chamber and cool the sample, and finally removed from the reactor and exposed to ambient air. Remarkably, this process produced the most reliable barriers with best junction properties, compared with the controlled deposition of a barrier layer [8, 123].

In order to control the area of contact between the top electrode and the $MgB_2$ film, and to allow the creation of a conventional cross-stripe geometry, a thin layer of Duco cement was applied to the film immediately after the barrier had formed, leaving only a narrow strip uncovered by cement. The Pb or Sn top electrode was thermally evaporated through a shadow mask. Depending on the mask used, four or five junctions were formed on the same $MgB_2$ film, each with an area of $\sim 0.3 \times 0.3$ mm. (See Figure 2.12.)

The relatively "gentle" thermal evaporation of the Pb or Sn counterelectrode preserved the ∼2-nm native oxide as a good barrier. We also tested some $MgB_2$/I/Nb and $MgB_2$/I/$MgB_2$ junctions, with less success, likely due to degradation of the barrier. The results of these tests are not presented in this thesis.

Success with Pb and Sn as electrode materials is not uncommon. These soft metals, widely used since the early pioneering experiments on superconductive tunneling, have been found to be very easy to handle and produce junctions whose experimental behavior generally allows "excellent and straightforward comparison with the theory" [124].

### 2.4.3 Junction Degradation

Soft metals like tin and lead are not typically recommended for applications where long life and thermal cyclability are important. Under thermal cycling between room and liquid helium temperatures (4 - 300K), they undergo mechanical stresses that lead to dislocation flow and grain boundary deformations. The resulting film imperfections, such as hillocks and whiskers, can protrude from the film and pierce the oxide layer [124].

Most of the junctions we tested performed very well for our purposes. They provided an excellent insulating barrier (see Section 3.3), and a moderately high quality factor (see Section 4.4).

The $MgB_2$ films themselves degraded over time since they are very sensitive to water and moisture [8]. Some other fabrication techniques produce $MgB_2$ samples that show no noticeable degradation with exposure to atmosphere for many months, and have large amounts of impurities. However, we encountered significant issues over a much shorter timescale. The $MgB_2$-based junctions we tested did not have an observable degradation after months of time in ultra-high vacuum. However, weeks in a desiccator or days exposed to room air led the $MgB_2$ films to degrade beyond the point of usability. Since these effects were cumulative, and we received our devices after they'd been tested several times at Temple or Penn State, we were limited to only 3-4 rounds of experiments with each device.

## 2.5 Mounting Samples for Measurement

I mounted each ~7-mm×7-mm SiC chip containing the $MgB_2$ junctions to the sample box using silver paint applied to the entire rear of the chip. This secure physical connection withstood thermal cycling and provided thermal anchoring to the sample box.

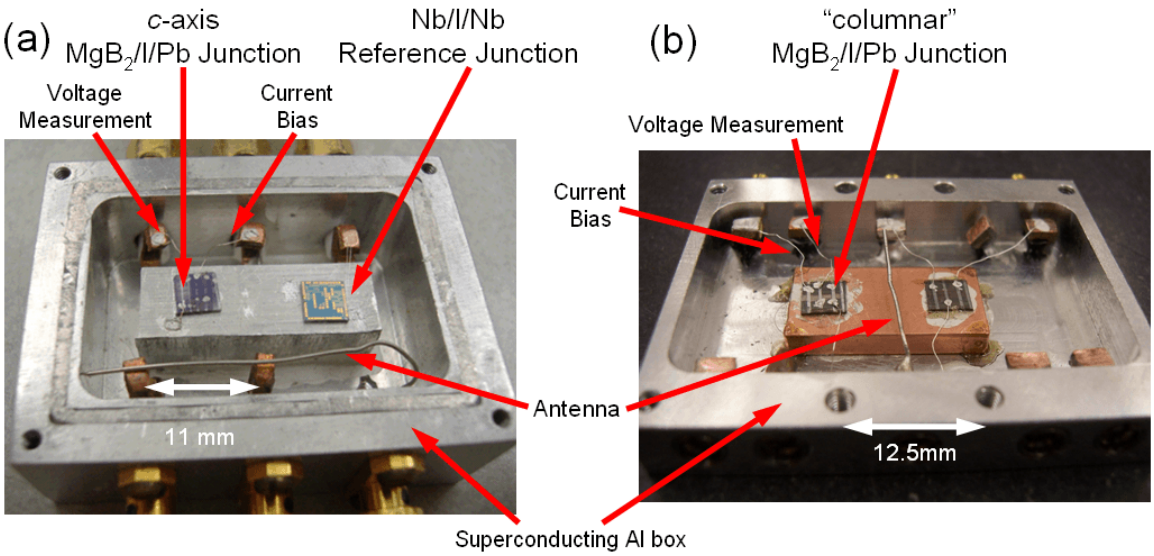


**Figure 2.11:** (a) "Old" sample box, containing the higher-resistance *c*-axis $MgB_2$/I/Pb junction and the reference Nb/I/Nb junction. Note that the microwave antenna has been moved aside for sample mounting and wiring; it hovers over both chips during an experiment. (b) "New" sample box, containing the "columnar" $MgB_2$/I/Pb junction (and another that did not provide any useful data).

For electronic contact to the top Pb/Sn electrodes, I used 0.1-mm diameter silver wires and silver

paint. In principle, it would have been better to have one wire contact the Pb/Sn top electrode, and another directly to the $MgB_2$ film. But as described above, the $MgB_2$ film had an oxide layer, and the samples had been exposed for an unknown time before we received them. So, the properties of the film, in areas unprotected by the junction top electrodes, were unknown. Therefore, silver paint was likely to encounter a thick insulator rather than conducting to the $MgB_2$ film. Even without such a barrier, it may have formed a superconductor/insulator/normal-metal (SIN) junction. With too thick an insulating barrier, we would have been unable to take any measurements whatsoever; having a SIN junction to the $MgB_2$ film would have complicated our results beyond our ability to disentangle the effects.

In practice, we did not encounter problems by using only the Pb/Sn top electrodes. As shown in Figure 2.12, the only area in common between the current bias and voltage measurement lines is the junction being measured, plus Ohmic contact resistances and the silver wire connecting the measured junction's top electrode to the sample box. This Ohmic resistance is easy to correct for, in our analysis. And, since the bias resistor has a resistance much larger than junction resistances, having an extra junction in series on the current measurement side does not affect measurement of current.

As shown in Figure 2.11, a microwave antenna allows microwaves to excite the junctions (see Section 4.4). These are capacitively coupled to the junction, since there is no direct physical contact. This design is simpler than those that couple the microwaves in with the current bias and was sufficient for our purposes [1, 120].

## 2.6 Nb/AlOx/Nb Comparison Junctions

In order to demonstrate that the effects were observed were due to the material properties of $MgB_2$, rather than junction geometry or artifacts of our experimental system, we qualified each type of data by taking equivalent measurements on Nb/AlOx/Nb junctions.

These junctions were manufactured by Hypres, Inc., and designed at the University of Maryland's Center for Superconductivity Research. This design includes an on-chip LC isolation circuit, to allow the operation of the junction as a phase qubit, well-decoupled from the environment. Similar devices

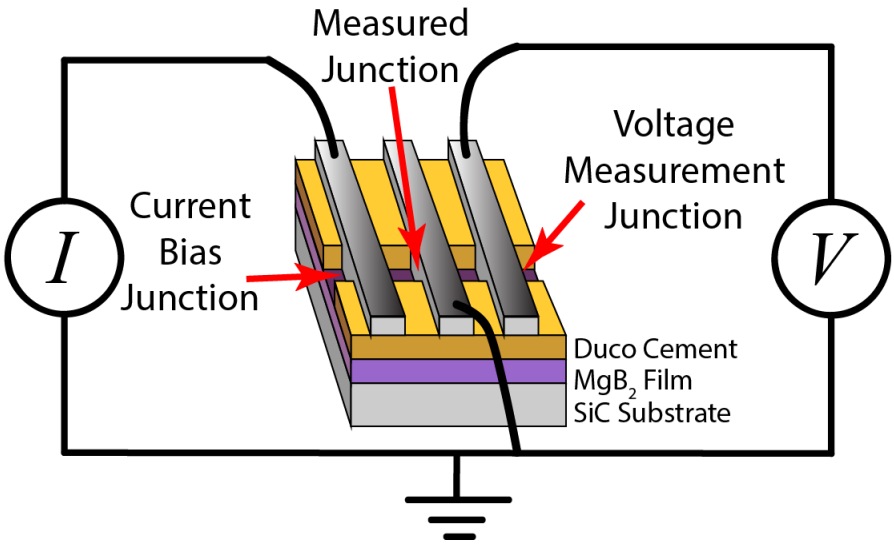


**Figure 2.12:** A schematic of the samples we measured, and how they were connected to the electronics. The bias current passes from the room-temperature and low-temperature cables, through the Current Bias junction, through the $MgB_2$ film, before passing through the measured junction to ground. The measured junction and wires to ground are the only current-carrying portions of the system that are measured on the detection side. Additional filtering and amplification stages are not shown here, for simplicity.

have demonstrated the ability to couple two phase qubits [125].

Nb/AlOx/Nb junctions have been widely studied, so their properties are well-understood. Also, this junction design is geometrically much smaller than the $MgB_2$ junctions used in this study: 10 $\mu$m $\times$ 10 $\mu$m. This is much more common for the study of superconducting-to-normal switching experiments (Chapter 4). Therefore, these junctions are well-suited for establishing the characteristics of our measurement system.

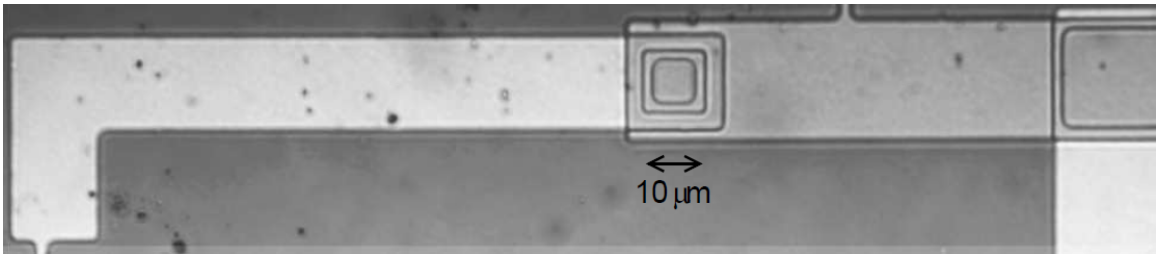


**Figure 2.13:** Close-up view of a Nb/AlOx/Nb junction, of the same design as that used in this thesis (reproduced from [1]). Two niobium electrodes are separated by a thick insulating layer, except in a 10 $\mu$m $\times$ 10 $\mu$m region with a thin aluminum oxide barrier. These electrodes pass to an on-chip LC isolation circuit on the order of 100 $\mu$m away. Contact pads for wirebonding then allow these circuits to be coupled to the rest of our electronic apparatus.

## 2.7 Conclusion

This chapter contains a broad view of our experiments, after many iterations of study and improvements. As is true for much experimental work, I spent far more hours understanding, building, and debugging the equipment than in acquiring or analyzing data.

With these systems and high-quality samples in place, I was able to make the highest-resolution conductance measurements yet made on $MgB_2$, and conducted the first superconductor-to-normal state switching experiments on a hybrid 2-gap/single gap Josephson junction.

# Chapter 3: Current and Conductance vs. Voltage

Measuring the current vs. voltage ($I-V$) and conductance vs. voltage ($dI/dV-V$) characteristics are widely-used techniques to study many important properties of Josephson junctions and the materials of which they're made. I have used these methods to explore the two superconducting energy gaps of magnesium diboride and structures within each gap.

In this chapter, I review the theory describing electrical conduction from one material to another and apply it to hysteretic superconducting tunnel junctions. I then expand the theory to include multiple energy gaps and a phenomenological broadening parameter to allow a discrete set of gaps to model a more complex distribution. Next, I describe the experiment design particular to this type of measurement and review how I processed the resulting data. Finally, I present high-resolution results on three separate devices with three very different film geometries.

My results demonstrate that, in order to fully characterize experimental tunneling results on high-quality magnesium diboride films, more than two discrete gaps are necessary.

Note that substantial portions of this chapter are reproduced from the publication: S. Carabello, J. G. Lambert, J. Mlack, W. Dai, Q. Li, K. Chen, D. Cunnane, C.G. Zhuang, X. X. Xi, and R. C. Ramos, "Energy gap substructures in conductance measurements of $MgB_2$-based Josephson junctions: beyond the two-gap model", Superconductor Science and Technology, 28(5):055015, 2015. [99]

## 3.1 Theory

### 3.1.1 Superconducting Tunnel Junctions

The current-voltage characteristics of a generalized junction between two materials may be expressed as

$$I(V) = G_n \int_{-\infty}^{\infty} N_1(E) N_2(E+eV)[f(E) - f(E+eV)]\, dE \tag{3.1}$$

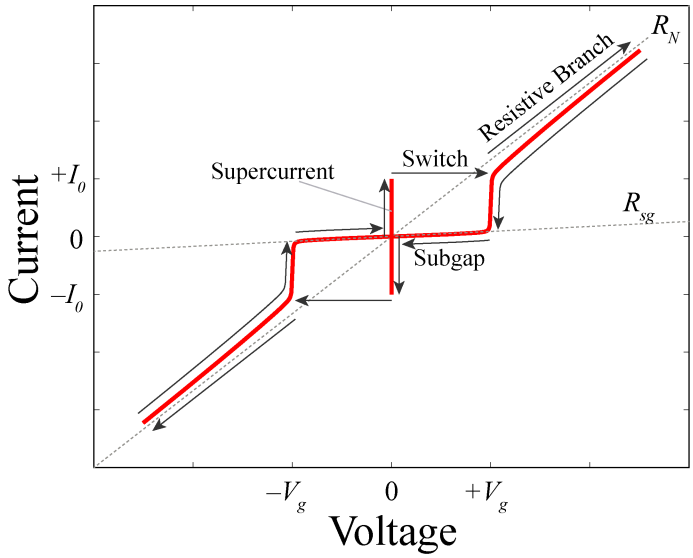


**Figure 3.1:** A theoretical current vs. voltage curve for a hysteric Josephson tunnel junction. As the current through the junction is increased from zero, the junction remains superconducting, with the $I - V$ curve tracing the supercurrent branch. When the junction current approaches the critical current $I_0$, the junction switches to the resistive state, at which time the voltage suddenly jumps from zero to near the gap voltage $V_g = \frac{\Delta_1 + \Delta_2}{e}$. The inverse of the slope of the resistive branch equals the normal-state resistance $R_N$. As the current is then reduced, the voltage remains near $V_g$ until the subgap region is reached, where the voltage rapidly falls toward zero. The inverse of the slope of the subgap region equals the subgap resistance $R_{sg}$. Each of these values is useful in characterizing the junction.

where $G_n$ is the normal-state conductance of the junction (assumed constant), $N_i(E)$ is the density of states for the $i$th electrode, and $f(E)$ is the Fermi distribution

$$f(E) = 1/\left(e^{(E-E_F)/k_BT} + 1\right) \tag{3.2}$$

where $E_F$ is the Fermi energy.

Note that the conductance $G$ may be computed from the derivative of the current with respect to the voltage $dI/dV$. The normal-state conductance $G_n$ may be visualized as the slope of the $I-V$ curve for $V \gg V_g$, or the inverse of the normal-state resistance $R_N$ (see Figure 3.1).

The density of states of a normal metal is usually approximated by a constant value up to the Fermi level, above which it equals zero. This leads to a perfectly linear increase in current with voltage, as expected for an Ohmic system. However, when one or both of the materials is superconducting, the situation becomes more interesting.

When considering a pure tunnel junction between two superconductors, the BCS density of states for a superconducting material is used,

$$N(E) = \Re\left\{\sqrt{\frac{E^2}{E^2-\Delta^2}}\right\} \tag{3.3}$$

where $E$ is the energy distance from the Fermi level, and $\Delta$ is the superconducting energy gap of the superconductor, and $\Re$ refers to the real part of the bracketed term. This function is plotted in Figure 3.3(a). Since we measure junctions made from two different electrode materials, each density of states will use a different energy gap $\Delta_1$ and $\Delta_2$, where $\Delta_1$ ($\Delta_2$) represents the lower (higher) of the two gaps.

The combination of these equations gives the current-voltage characteristics of a pure tunnel junction for $V \neq 0$. At $V = 0$, Cooper-pair tunneling gives rise to the Josephson supercurrent, as described in section 4.1. For a voltage above the gap voltage $|V| > V_g \equiv \frac{\Delta_1+\Delta_2}{e}$, sufficient energy is provided by the applied voltage to break Cooper pairs into their component electrons, and the electron current is nearly Ohmic. For $|V| < V_g$, known as the "subgap" region, the current is carried

by quasiparticles, some mechanisms of which are outlined below.

The effect of these expressions may be understood by applying the semiconductor model for a Josephson junction.

In Figure 3.2, the vertical scale is energy, while the horizontal distance from the center line corresponds to the density of states in each electrode. As indicated in Equation 3.3, the density of states is sharply peaked at $E = \Delta$, and has no states available for $|E| < \Delta$. At $T = 0$, all of the states below $E = 0$ are filled, while all states above $E = 0$ are empty.

The effect of the Fermi distributions in equation 3.1 is to promote some electrons from $E < \Delta$ to $E > \Delta$. This becomes especially prominent for $k_B T > eV_g$.

Considering Equation 3.1, the effect of an applied voltage $V$ may be thought of as sliding one of the density-of-states curves up or down relative to the other. No current may flow until filled states from one electrode reach available empty states in the other.

It is clear that, at $T = 0$, this will not happen until $|eV| \geq (\Delta_1 + \Delta_2)$, at which point there will be a discontinuous jump in the current, and an infinite conductance. For $|eV| \gg (\Delta_1 + \Delta_2)$, the access of filled states in one electrode to available states in the other grows in a nearly linear fashion, leading to a linear increase in current, as in an Ohmic resistor. The normal-state resistance $R_n$ is defined as the inverse of the slope of the $I - V$ curve for $|eV| \gg (\Delta_1 + \Delta_2)$, or the inverse of the normal-state conductance $G_n$.

At finite temperatures, some Cooper pairs are broken up, creating available electron states (above the energy gap) and hole states (below it). These thermally-excited quasiparticles carry some current throughout the range $|V| < V_g$. Its contribution is greatest at $|V| = \frac{\Delta_1 - \Delta_2}{e}$, where the peak in the (relatively small) population of thermally-excited electrons (holes) of one electrode meets the peak in available hole (electron) states of the other electrode. This gives a smaller conductance peak at $|eV| = |\Delta_1 - \Delta_2|$, which will grow in magnitude as the temperature increases. Additionally, the peak at $|eV| = (\Delta_1 + \Delta_2)$ becomes broadened, with the Fermi distribution effectively "smearing out" that peak. As $T \to \infty$, the electron populations are so thoroughly spread above and below the gap that Ohmic behavior is again observed.

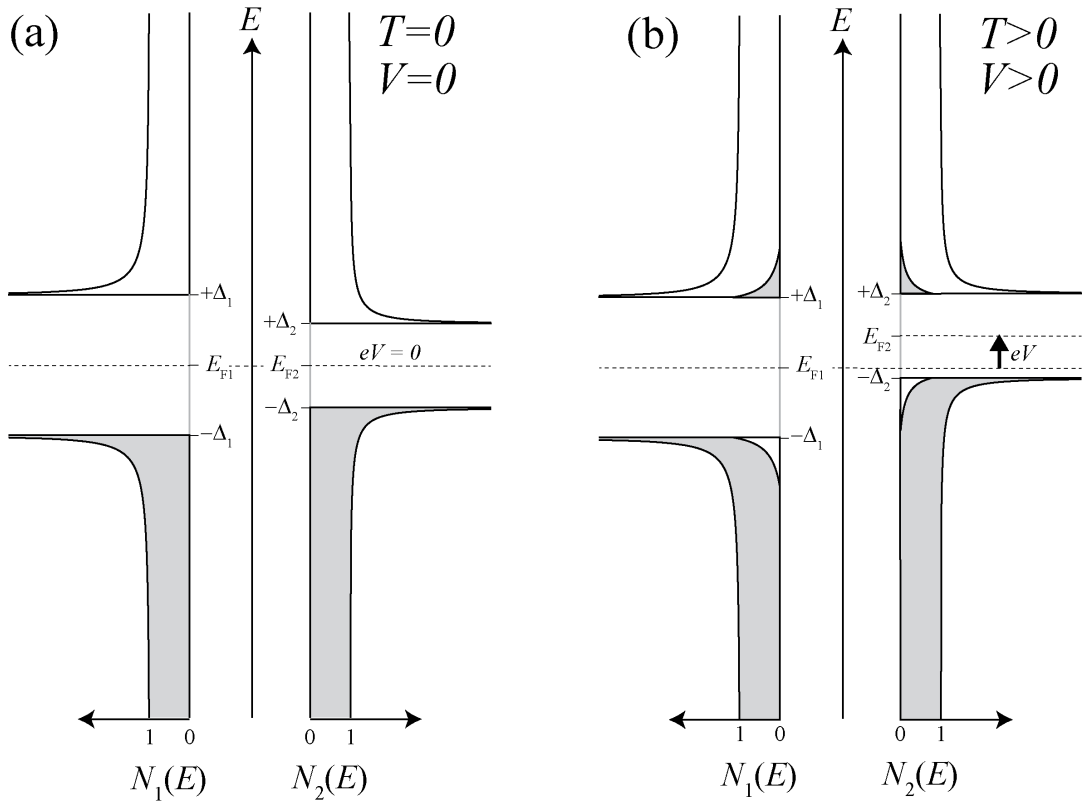


**Figure 3.2:** The semiconductor model for conduction in an idealized Josephson junction. For each figure, the BCS density of states $N(E)$ for superconductors of two different gap energies $\Delta_1$ and $\Delta_2$ is shown horizontally, with energy on the vertical axis. In this picture, applying a voltage across the junction corresponds to shifting the Fermi level of one of the electrodes relative to the other. At any temperature, for $|eV| \gg \Delta_1 + \Delta_2$, the overlap of electron states of one electrode with hole states in the other will change nearly linearly with voltage, leading to a nearly Ohmic response at large voltages. (a) At $T = 0$, all the available states below the Fermi level $E_F$ are filled; above it, they are empty. As a result, no current flows when $|eV| < (\Delta_1 + \Delta_2)$. At $|eV| = (\Delta_1 + \Delta_2)$, the sharp peak in filled states in electrode 1 (2) meets the sharp peak in empty available states in electrode 2 (1), leading to a discontinuous jump in current. (b) For $T > 0$, thermal energy breaks up some Cooper pairs, causing some electron states above the Fermi level to be occupied, leaving behind hole states below $E_F$. These thermally-excited quasiparticles carry some current throughout the range $|V| < V_g$ ($V_g \equiv \frac{\Delta_1+\Delta_2}{e}$). Its contribution is greatest at $|eV| = (\Delta_1 - \Delta_2)$, where the peak in the (relatively small) population of thermally-excited electrons (holes) of one electrode meets the large peak in available hole (electron) states of the other electrode. Even so, the jump in current at $|eV| = (\Delta_1 + \Delta_2)$ will be much greater, at most temperatures.

Each of these behaviors can be observed in Figure 3.3.

### 3.1.2 A Model for Multiple Energy Gaps

The material I study in this thesis is magnesium diboride, which is often considered to be a two-gap superconductor. However, as discussed in Section 1.4, several theoretical models suggest a distribution within each gap. Perhaps the simplest model for these distributions is four broadened gaps, with differing weights.

Therefore, in my analysis, I compare and contrast my data with two-gap and four-gap theoretical fits. The fits are not an attempt to create a complete physical model of the dynamics of the junctions. Instead, I chose the simplest possible models, with the fewest free parameters - models which were sufficient for much of the published data revealing two gaps (see, e.g. [22]). My data clearly resolve the difference between these simple models and the true nature of the energy gap distribution of $MgB_2$. As a result, these findings are one of only a few published data sets [98, 7, 126, 127, 128] able to help distinguish between competing theoretical models. (See Figure 3.18 for a comparison between these detailed theoretical models and our data.)

In the simplified model I used for a multi-gap superconductor (matching that described in [22]), two additional effects are incorporated:

**Broadening Factor Γ**: Dynes *et al.* [129] found a broadening in conductance peaks that could not be attributed to temperature. Instead, the quasiparticle lifetime provides a broadening that can be accounted for by replacing all instances of $E$ with $E + i\Gamma$ in the BCS density of states.

Γ has also been used to simulate the effect of a convolution of the theoretical conductance with a distribution of gap values [22]. In this thesis, I model the gap distribution as distinct gap energies, with a broadening that phenomenologically matches the experimental gap distribution from our experiments.

Including a constant Γ reveals a feature in the subgap region of the $I - V$ curve, which I have observed and used in my analysis. When Γ is included, the modified BCS density of states is nonzero even at $E = 0$, whether or not the transparency of the junction is zero. This allows the formation of peaks at $\Delta_1$ and $\Delta_2$ in the subgap region, down to $T = 0$, in the absence of Andreev reflections

(which require a finite transparency). Because of their strong sensitivity to thermal broadening, the peaks virtually disappear above 3 K in theoretical calculations using values similar to those of our junctions. But, the peak at $\Delta_1$ becomes quite sharp as $T \to 0$.

The effects of $\Gamma$ can be seen by comparing Figures 3.3 and 3.4.

**Weighting for multiple gaps**: An additional refinement must be made when considering a multi-gap superconductor. For a model including both the $\pi$ and $\sigma$ gaps of $MgB_2$, the density of states becomes:

$$N(E) = w_\pi N_\pi(E) + w_\sigma N_\sigma(E) \tag{3.4}$$

Because the sum of the weights must equal 1, a single weighting factor may be used (substituting $w_\sigma = 1 - w_\pi$). If additional peaks are observed, they can be modeled as additional gaps, each with its own gap energy $\Delta$, its own broadening factor $\Gamma$, and its own weight $w$, as long as the sum of the weights equals 1.

For $MgB_2$, two gaps are usually assumed. The weighting factors depend on junction geometry, with $w_\sigma = 1 - w_\pi$ ranging from less than 1% for pure *c*-axis tunneling, to $\sim 33\%$ for pure *a*-*b* plane tunneling [130, 22].

However, as indicated by the theories shown in Figure 3.18, two smoothly-broadened gaps (one each for $\pi$ and $\sigma$) are not sufficient to represent the density of states of $MgB_2$. As a result, *within the $\pi$ (or $\sigma$) gap, substructures are necessary, each with its own weighting factor.* For simplicity, I have chosen to model each structure as its own gap, with its own broadening. This will lead to a conductance peak for each of the chosen gap values.

From the Fermi surface of $MgB_2$ (Figure 1.8 (a)), it is evident that the observable contributions to each gap will be dependent on the tunneling direction. Therefore, the weights for each substructure should differ for different samples fabricated in different ways and on different substrates.

I have chosen to compare and contrast the data with a simple 2-gap model (one gap for $\pi$ and one for $\sigma$) vs. a model consisting of four gaps (two each for $\pi$ and $\sigma$). I have observed that a 4-gap model is superior below $T_c$ of the Pb or Sn single-gap counterelectrode. Above that temperature, the features are sufficiently broadened that only two peaks may be distinguished, whether a 2-gap

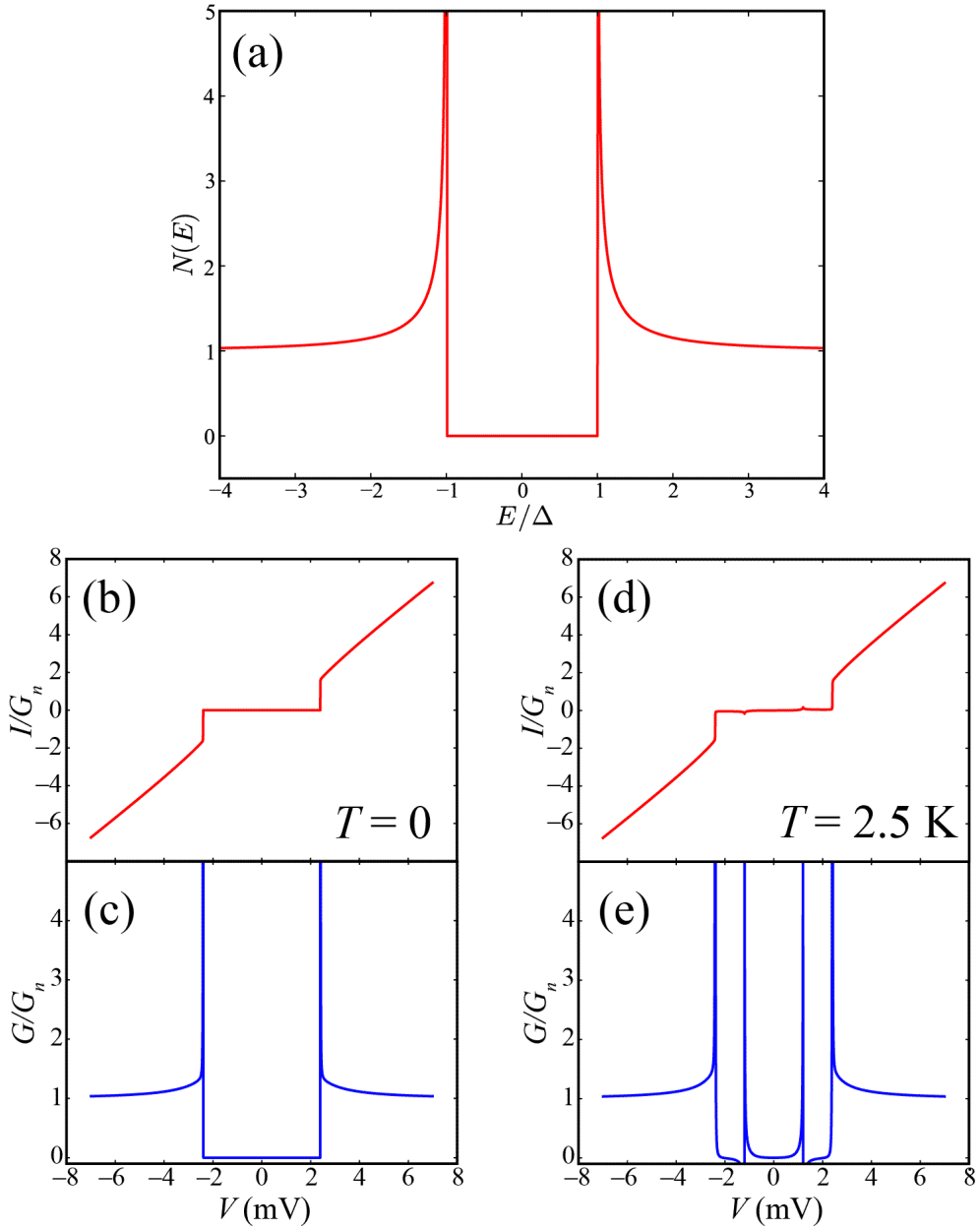


**Figure 3.3:** (a) The BCS density of states, as in Equation 3.3. (b) Theoretical normalized current vs. voltage and (c) conductance vs. voltage at $T = 0$, from Equation 3.1, for a junction where $\Delta_1 = 0.6$ meV and $\Delta_2 = 1.8$ meV. This assumes that the BCS density of states $N(E)$ applies for both superconductors. Note the sharp conductance peak at the gap voltage $V_g = \frac{\Delta_1+\Delta_2}{e}$. (d) and (e) are the corresponding curves at $T = 2.5$K. The conductance peak at $\frac{\Delta_2-\Delta_1}{e}$ is dramatic at this elevated temperature, when using the infinitely-sharp BCS density of states. In (a), (c) and (e), the plot area has been limited; the peaks are infinitely high.

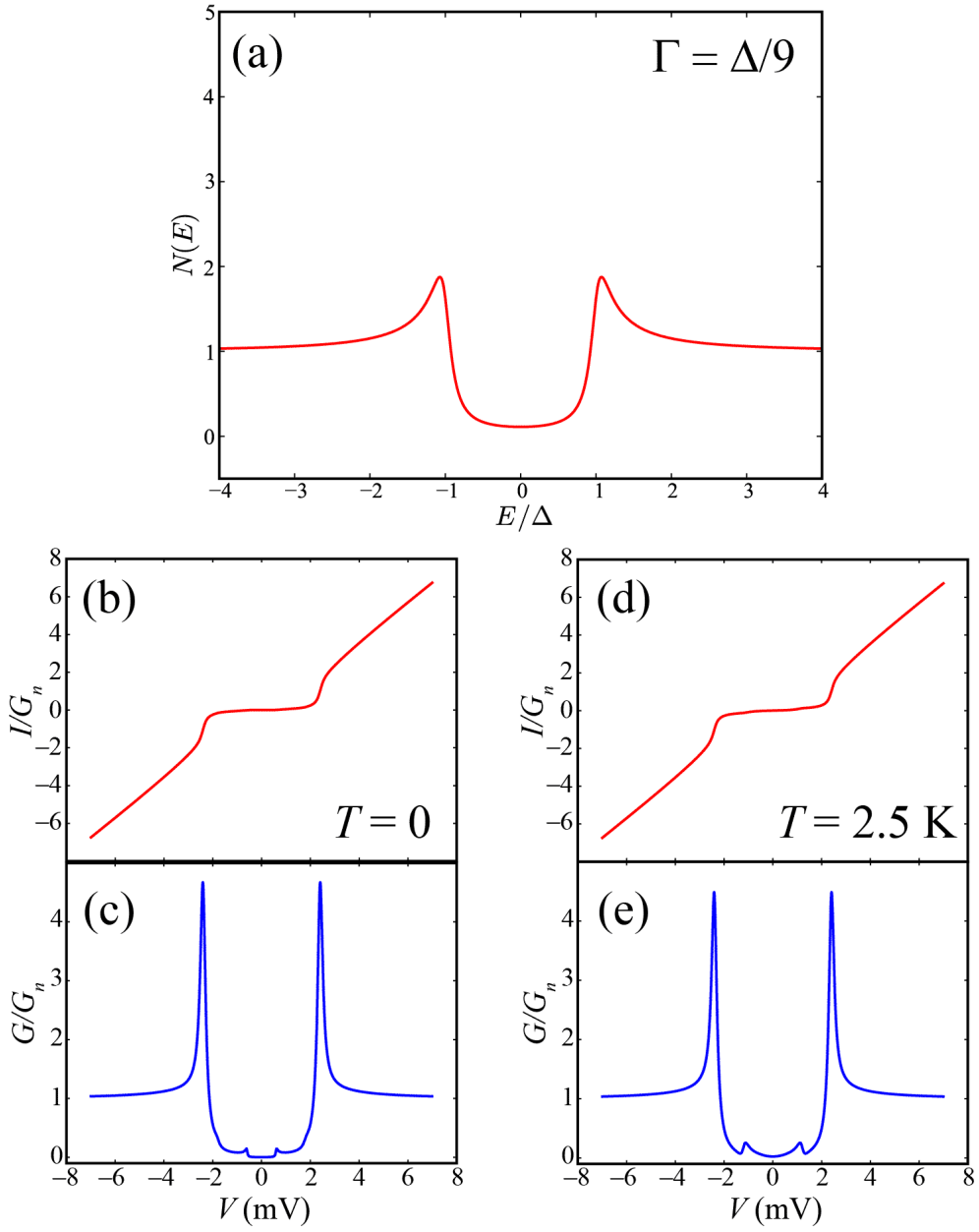


**Figure 3.4:** (a) The BCS density of states broadened by Γ, as described in the text. For this curve, $\Delta = 1.8$meV and $\Gamma = 0.2$meV. (b) Theoretical normalized current vs. voltage and (c) conductance vs. voltage at $T = 0$, for a junction where $\Delta_1 = 0.6$ meV and $\Delta_2 = 1.8$ meV (as in Figure 3.3), but $\Gamma_1 = 0.01$meV and $\Gamma_2 = 0.2$meV. (d) and (e): the corresponding curves at $T = 2.5$K. The conductance peak at the gap voltage $V_g = \frac{\Delta_1+\Delta_2}{e}$ remains the most prominent feature at both temperatures, though it is more rounded compared with Figure 3.3. Two new features appear in the subgap region at $T = 0$: at $\frac{\Delta_1}{e}$ and $\frac{\Delta_2}{e}$. The peak at $\frac{\Delta_2}{e}$ is barely distinguishable, due to its broadening and proximity to the broadened peak at $V_g$. At $T = 2.5$K, both are broadened beyond recognition, for these settings; they persist to somewhat higher temperatures when $(\Delta_1 + \Delta_2)$ is larger. The peak at $\frac{\Delta_2-\Delta_1}{e}$ again appears at 2.5K (and not at $T = 0$), although it is far less pronounced than in Figure 3.3.

or 4-gap model is used (see Figure 3.5).

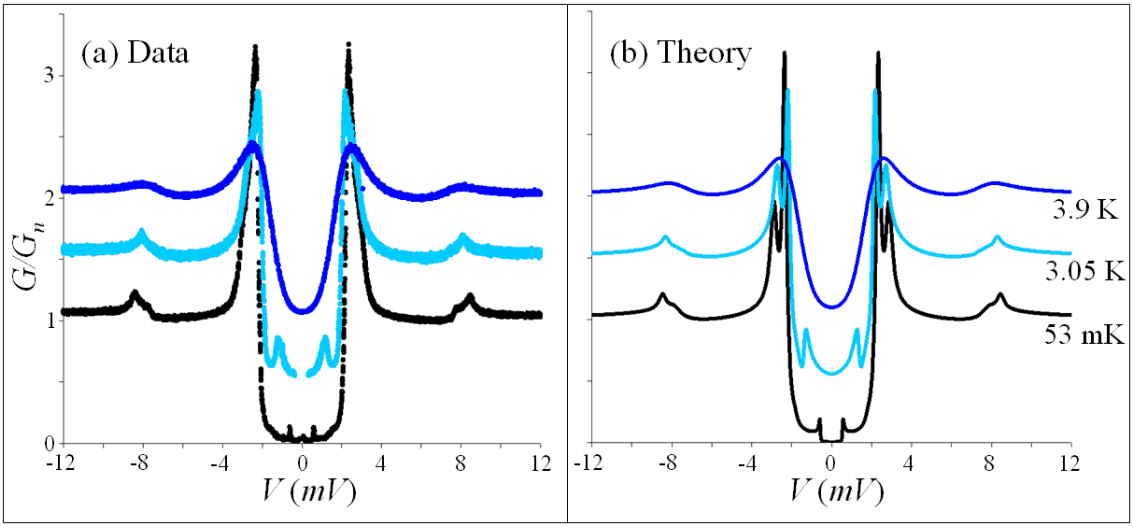


**Figure 3.5:** (a) Experimental and (b) theoretical normalized conductance vs. voltage curves at 53mK, 3.05K, and 3.9K of an $MgB_2$/I/Sn junction, using a 4-gap model. Curves have been offset for clarity. The ability to resolve features improves dramatically as the junction transitions from $T > T_{c\,Sn}$ (forming an $NS$ junction) to $T < T_{c\,Sn}$ ~3.7K (forming an $SIS'$ junction). Above $T_{c\,Sn}$, the features of the 4-gap model are sufficiently broadened that only two peaks are apparent.

Hereafter, I will refer to these gaps as $\pi_1$, $\pi_2$, $\sigma_1$, and $\sigma_2$, with subscripts 1 (2) referring to the lower- (higher-) energy sub-peaks of the $\pi$ and $\sigma$ gaps. I assume a single sample-dependent gap value $\Delta$, broadening parameter $\Gamma$, and weight $w$ for each gap. I emphasize that I am not suggesting a physical source for these gap values. Instead, they serve as a convenient phenomenological model for the true gap distribution.

## 3.2 Experiment Design

Chapter 2 provided an overview of the operation of our helium dilution refrigerator, and some components used in all of our experiments. In this section, I describe elements particular to this class of tunneling spectroscopy experiments.

### 3.2.1 Electronic Apparatus

A block diagram of a typical experiment is shown in Figure 3.6. As described in Section 2.3.1, an Agilent 33220A function generator provides a triangular wave output voltage, used to ramp the junction current. For quickly characterizing the junctions, the bias current was swept at 10 Hz. For

much of the data below, excellent results were achieved with a sweep frequency of 1 Hz. To resolve $dI/dV$ to finer detail, a frequency of 10-50 mHz was helpful.

As noted in Section 2.2.1, an SR560 voltage preamplifier operating in differential mode (with unity gain) isolated the ground of the function generator from that of the rest of the experiment. In order to operate in differential mode, we built a splitter box, which takes the inner and outer conductors of a single BNC cable and separates them into the inner conductors of two separate BNC connectors.

This isolated voltage is then placed across the remaining elements of the system: the bias resistor, filters, and sample. The circuit is completed through the ground connection of the measured junction to the sample box: the entire body of the cryostat then serves as the ground connection, in contact with the outer conductors of all room-temperature BNC cables. Note that experiments with the "columnar" junction used the newer, more compact LC and Mini Circuits filters, while experiments with the *c*-axis and "terraced" samples used the older LC and copper powder filters.

The bias resistor is chosen to have a resistance as high as possible while still allowing the desired currents to be reached. A high resistance serves two purposes: 1. By using a bias resistor very large in comparison with the (nonlinear) resistance of the junction itself, the voltage source is effectively converted to a current source. 2. Because the bias resistor is the closest component to the cryostat, any noise from sources further "upstream" is attenuated.

One channel of the data acquisition card (DAQ) is used to measure the voltage across the bias resistor. Simply dividing this voltage by the resistance of the bias resistor gives us the current. We always use 5-band (1%) resistors tested for temperature stability, and always measure its resistance prior to taking data (rather than using the label values).

To measure the voltage, the signal is first amplified. The *c*-axis and "terraced" junctions used the custom-built JFET amplifier, as shown in Figure 3.6; the "columnar" junction used the commercial SR560 voltage preamplifier in its place. In both cases, the amplified signal is sent to a second channel of the DAQ.

The user is able to select the sampling rate of the DAQ. When quickly characterizing the junction,

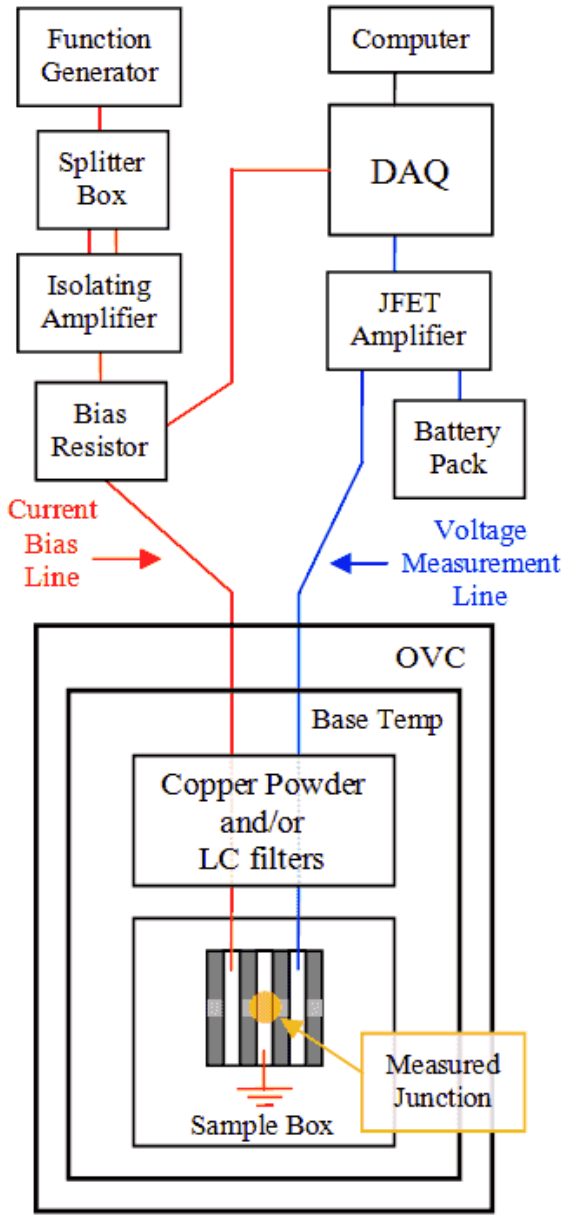


**Figure 3.6:** A typical block diagram used for current-voltage measurements. All red and blue lines outside of the OVC correspond to coaxial BNC cables. Within the OVC, lines outside of the sample box are the inner conductors of Thermocoax cables, and within the sample box, they are fine silver wires. The junction being measured is grounded to the sample box itself, allowing the entire cryostat to serve as the current return line. All other components are discussed in the text.

sample rates of 100-1000 samples/s worked well. Most of the publication-quality data were acquired at 10,000 samples/s, although some at 1000 samples/s up to 50,000 samples/s were used.

For the "columnar" junction, a 16-bit National Instruments (NI) 9215 DAQ was used. Although the results were reasonably good, the outer conductors of its separate channels are not isolated from each other. As can be seen in Figure 3.6, this allowed the outer conductors to form a large loop, resulting in significant 60 Hz noise. With sufficient averaging, good results were achieved, especially with data gathered at 10 mHz. I tried a number of different averaging schemes, and compared the results from multiple data runs acquired at 10 Hz, 1 Hz, and 10 mHz; in each case, all of the features shown in the figures below appeared at the same voltages. So, I am very confident that the results were not adversely affected by this noise and that they did not include artifacts of my data processing techniques.

For the *c*-axis and "terraced" junctions, I used an NI 9239 DAQ, purchased using a grant I received from Sigma Xi. The outer conductors of its separate channels are well-isolated, and it has 24 bits of precision. With it in place, no periodic noise was observed, leading to simpler analysis and superior results. This is the primary reason why data in the subgap region are presented for the *c*-axis and "terraced" junctions, but not for the "columnar" junction, in Section 3.3.2 (although the benefits of the JFET amplifier contributed as well).

Using this arrangement, we had to be extremely careful about the grounding of the cryostat, because all exposed metal is at the experiment ground. Additionally, we are unable to perform a true 4-wire measurement, which requires additional corrections to be made in analyzing the data (described in Section 3.2.3). But the method provided significant advantages. By requiring the use of only two lines from room temperature to the sample box (rather than four), we are able to measure twice as many devices per cooldown. Additionally, the heat load increases with an increasing number of lines, so keeping the lines to a minimum allows us to reach a lower stable base temperature.

Additionally, Figure 3.6 shows that the current passes through one top Pb or Sn electrode, through one Josephson junction to the $MgB_2$ film below, then up through a second junction to a separate Pb or Sn top electrode, before flowing to ground. Similarly, the voltage measurement line is

actually across two junctions rather than just the one being measured. As described in Section 2.5, we did this because it was a relatively simple matter to contact the top electrodes, while there was substantial risk that we would have been unable to obtain any useful data had we tried to contact the $MgB_2$ film directly. This did not require any additional corrections in my $I - V$ results. The current was found by measuring the voltage across the bias resistor; this is independent of any other portions of the circuit. As long as no other elements are in parallel with the measured junction, the current through it will be equal to the current through the bias resistor.

For the voltage measurement side, in principle, we are measuring the voltage across the measured junction plus the junction contacted by the voltage measurement line (together with the Ohmic connection to ground). However, the extremely high input impedance of the JFET amplifier guarantees that a negligible current will run through both the voltage measurement line and the junction it contacts directly. So, because we do not exceed the critical current of that junction, making the voltage across it is exactly zero. But even if that junction were to have a finite resistance, the tiny current will lead to a similarly tiny voltage - far below the level of our signals.

### 3.2.2 Data Acquisition

In the seminal experimental papers on Josephson junctions, results were often reported as photographs of traces on oscilloscopes or plotter paper. We were able to do significantly more sophisticated analysis, by acquiring data files to the computer using LabVIEW programs, and using Python programs to process them.

When we first started work with the NI 9215 DAQ, we used the SignalExpress software from National Instruments. While this was successful in recording the raw voltages across each channel, it did not allow us to view real-time voltage traces as we could on an oscilloscope. In addition, we needed a separate file containing essential information, such as which device was being measured, the device temperature, the value of the bias resistor, etc. Without these values, it is impossible to make sense of the data files.

As a result, I supervised and collaborated with Mariyan Stoyanov, an undergraduate student working in our group. This resulted in a program that was fast and easy to work with, capable of

adjusting many settings through the program rather than manually, and ensuring that proper values needed for future analysis were recorded. It also required both of us to learn how to program in LabVIEW, a skill I've already found helpful in other settings.

### 3.2.3 Data Analysis

The current vs. voltage curve allows us to directly establish several useful junction parameters: critical current, gap voltage $V_g$, normal state resistance $R_n$ and subgap resistance $R_{sg}$. However, when seeking more detailed features of the gaps and within the subgap region, the conductance $G = dI/dV$ is more helpful.

We determined the voltage across the junction by dividing the voltage measured by the DAQ by the total amplification factor. We found the current by dividing the measured voltage across the bias resistor by the resistance. This gives us a series of discrete current and voltage data points. One might expect to find the conductance by taking differences between the currents of consecutive data points, and dividing by the difference between the voltages at those points. However, we ramp the current at 10mHz to 10Hz, while acquiring data at 100Hz to 50kHz. As a result, even the slightest random noise would completely overwhelm any features within the conductance curve, using this method. Reasonable results could be achieved by sampling the data at a far slower rate, although this would dramatically reduce the maximum possible resolution, and would prevent the more advanced analysis possible with oversampling.

To improve the speed and ease in data analysis, I wrote Excel spreadsheets that took differences between data points some fixed number of data points apart, rather than immediately adjacent data points. And, rather than discarding the intervening data points, this process is repeated for each consecutive data point in the file.

In order to ensure that the raw $I - V$ data files would reveal the conductance peaks as desired, I often used these spreadsheets immediately after gathering the data. The results proved extremely valuable in optimizing settings and in illustrating when noise had re-emerged in the system (via e.g. a "touch" between cable outer conductors, leaving an SR560 amplifier plugged in, etc.). The spreadsheets also produced results suitable for presentation at conferences and for verifying that our

system is capable of observing fine details in conductance curves (as shown in Section 3.2.4).

However, the results presented below required a more sophisticated method, for several reasons. First, the amplification provided by our JFET amplifier is not perfectly linear, so a careful correction is needed. Second, the current-voltage curve itself is highly nonlinear. So, any time the difference is taken across the discontinuous superconducting-to-normal switch, extraneous points appear in the conductance curve. Additionally, because the current changed at a steady rate, the voltage must change at a varying rate for a nonlinear device. Since the amplitude of the voltage noise remained roughly constant, that noise has a disproportionately large effect when the voltage changes slowly, such as near the gap voltage $V_g$. So, no single step size can provide optimal results for all regions of the conductance curve, for nonlinear devices such as these Josephson tunnel junctions.

As a result, I wrote a program in Python capable of averaging data points in a way that produces useful results for the entire data set.

First, the program excludes data points near $V = 0$, and those immediately following them, so that points on the supercurrent branch are never averaged with points after the junction has switched to the resistive state. Then, at each point, it estimates how quickly the voltage is changing. If the voltage is changing quickly, fewer points are averaged together; if the voltage is changing slowly, more points are averaged together. The averaged currents and voltages are then stored, and all data points used in that average are set aside, never to be used in any other average (so that one aberrant point in the raw data file will affect no more than one point in the resulting output). Differences between adjacent currents and voltages averaged in this way are then used to determine the conductance $dI/dV$. This process was used to produce all of the plots shown in Section 3.3.

Before this process can be done, the raw data must be corrected. As noted above, the current is the voltage across the bias resistor (recorded in the raw data file) divided by its resistance. But the voltage recorded from the output of the JFET amplifier required three corrections prior to being used in averaging.

- As described in Section 2.3.2, the voltage out of the amplifier is positive when the input voltage is zero - i.e. there is a DC offset (in our case, roughly 3.2 Volts). This is a simple matter to

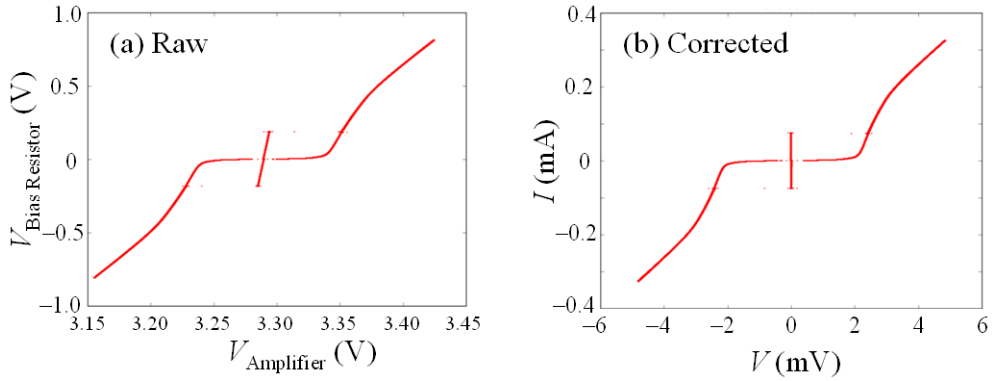


**Figure 3.7:** Data taken on the "terraced" $MgB_2$/I/Sn junction at $T$=23mK. (a) Raw voltage data recorded by the DAQ. (b) The resulting $I-V$ curve, after applying all corrections.

correct. In all of the results shown below, the junctions exhibited a supercurrent, which must appear at $V = 0$. So, I plotted each raw data file, and recorded the voltage of the supercurrent branch; this voltage was subtracted from the raw voltages for each point, prior to all other processing.

- Section 2.3.2 also shows that the amplification of the JFET amplifier is slightly nonlinear, for negative input to (positive output from) the amplifier. To resolve this, I took $I-V$ data with both the SR560 and JFET amplifiers for the "terraced" $MgB_2$/I/Sn junction, which exhibited features over the entire voltage range of interest. I then developed a simple function to correct the slight nonlinearity. The results compared quite favorably with data measured across a room-temperature resistor: as expected, the amplification was slightly nonlinear for positive input to the amplifier. Each voltage was divided by this nonlinear amplification factor before applying the final correction.

- Section 3.2.1 shows that our experiment has an Ohmic resistance in series with the junction; its effects must be removed. Once again, the observation of a supercurrent made this correction simple: as long as the current changes "slowly" (typically, less than MHz), the voltage across the junction will remain zero for any current below the critical current $I_0$. This leads to a perfectly vertical slope on the $I-V$ curve. The series resistance causes the supercurrent branch to have a constant slope instead. So, for each data set, I found the resistance such

that subtracting $IR$ resulted in a vertical supercurrent branch. Then, for each data point, its current $I$ times this same resistance $R$ is subtracted from each voltage.

### 3.2.4 System Qualification

In order to characterize the quality of our measurement system, after acquiring the 9239 DAQ and installing the plastic clamps and centering rings, I gathered data on a conventional Nb/I/Nb Josephson junction. As shown in Figure 3.8, even using the simple differencing analysis from my Excel spreadsheet (described above), I was able to observe a series of Andreev reflections, which compare quite favorably with published high-resolution results on a similar type of device [9].

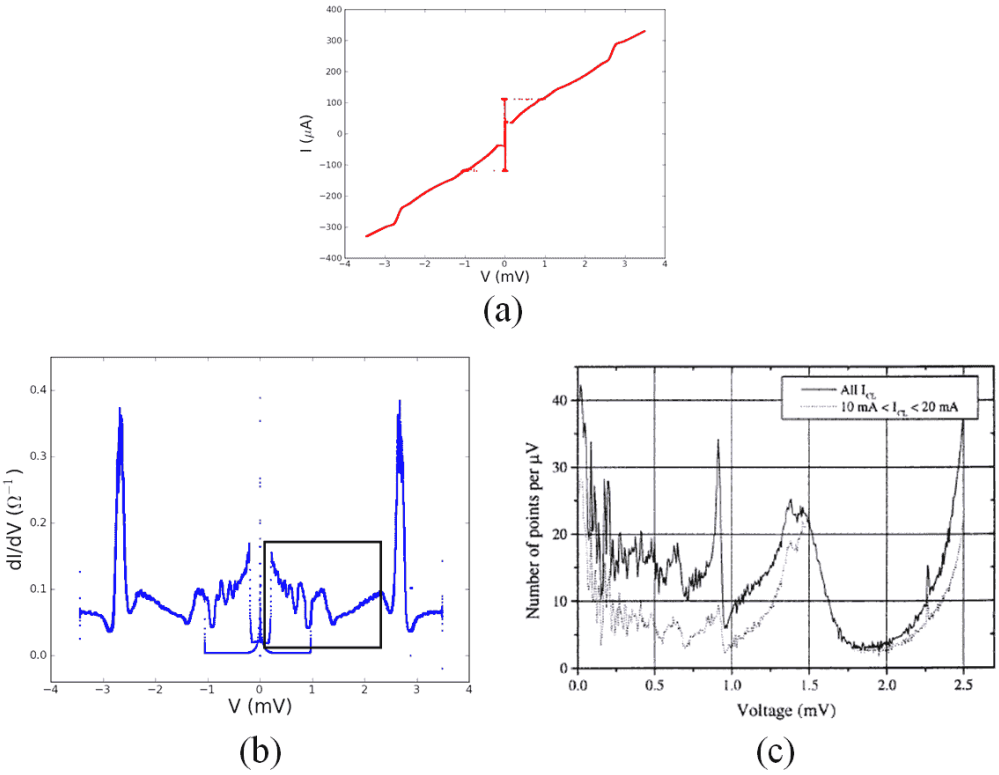


**Figure 3.8:** Results for a Nb/I/Nb junction. (a) $I$-$V$ data I acquired, after correcting for the DC offset and series resistance. (b) The resulting conductance $dI/dV$-$V$ curve, using the simple differencing method described in Section 3.2.3. As described there, stray points near $V = 0$ and $dI/dV = 0$ are artifacts, due to the supercurrent branch. (c) Results published by another group [9], revealing similar features. The region shown in (c) corresponds roughly with the black box indicated in (b). ((c) reproduced with permission from [9] ©IOP Publishing.)

Therefore, I am quite confident in the ability of our system to resolve fine features in the conductance curves of Josephson junctions.

## 3.3 Results

I seek to identify substructure within each of the energy gap peaks of conductance data of $MgB_2$-based junctions, by contrasting fits using only two peaks (i.e. in the absence of these structures) with fits using four peaks (a gross simplification of the theoretical gap distributions shown in Figure 3.18).

The distinguishing features will be far more prominent at the energy gap peaks $(\Delta_{Pb/Sn} + \Delta_{MgB_2 i})/e$ than at any other part of the conductance curves (as indicated in Figures 3.13, 3.14, 3.16, and 3.17, below). However, by making use of other portions of these curves, I gain confidence that these features within each energy gap are indeed properties of $MgB_2$ (and not the counterelectrode material), and significantly reduce the parameter space for fitting the data.

A 2-gap fit for these SIS' junctions has seven independent parameters. Two are associated with the counterelectrode material: its energy gap $\Delta$ and broadening factor $\Gamma$. Then, each of the two energy gaps of $MgB_2$ has a characteristic gap energy ($\Delta_{MgB_2\pi}$ and $\Delta_{MgB_2\sigma}$) and a broadening factor ($\Gamma_{MgB_2\pi}$ and $\Gamma_{MgB_2\sigma}$). Finally, there is one independent weighting factor $w_\sigma = 1 - w_\pi$.

Similarly, a 4-gap fit has 13 parameters: gap energies and broadening factors for the counterelectrode and each of the four energy gaps of $MgB_2$, together with three independent weighting factors (where $w_{\pi 1} + w_{\pi 2} + w_{\sigma 1} + w_{\sigma 2} = 1$).

I can derive three of these parameters from data, before using any feature of the energy gap peaks $(\Delta_{Pb/Sn} + \Delta_{MgB_2 i})/e$:

1. From the region between the $\pi$ and $\sigma$ peaks, I determine (to moderate precision) the relative weights of the $MgB_2$ $\pi$ and $\sigma$ gaps.

2. From peaks within the subgap region, I determine the energy gap $\Delta$ and the broadening factor $\Gamma$ of the counterelectrode material (Pb or Sn).

### 3.3.1 Calculating Gap Weights

When properly normalized, both theoretical and experimental conductance curves must approach 1 as $V$ approaches infinity. As indicated in Figure 3.9, the normalized conductance is very nearly

1 at $V \sim 14mV$ for the $MgB_2$/I/Pb junction shown in this model. I use the conductance at the maximum acquired voltage, well above the $\sigma$ peak at $\left(\Delta_{MgB_2\sigma} + \Delta_{Pb/Sn}\right)/e$, as the normalization factor $G_n$.

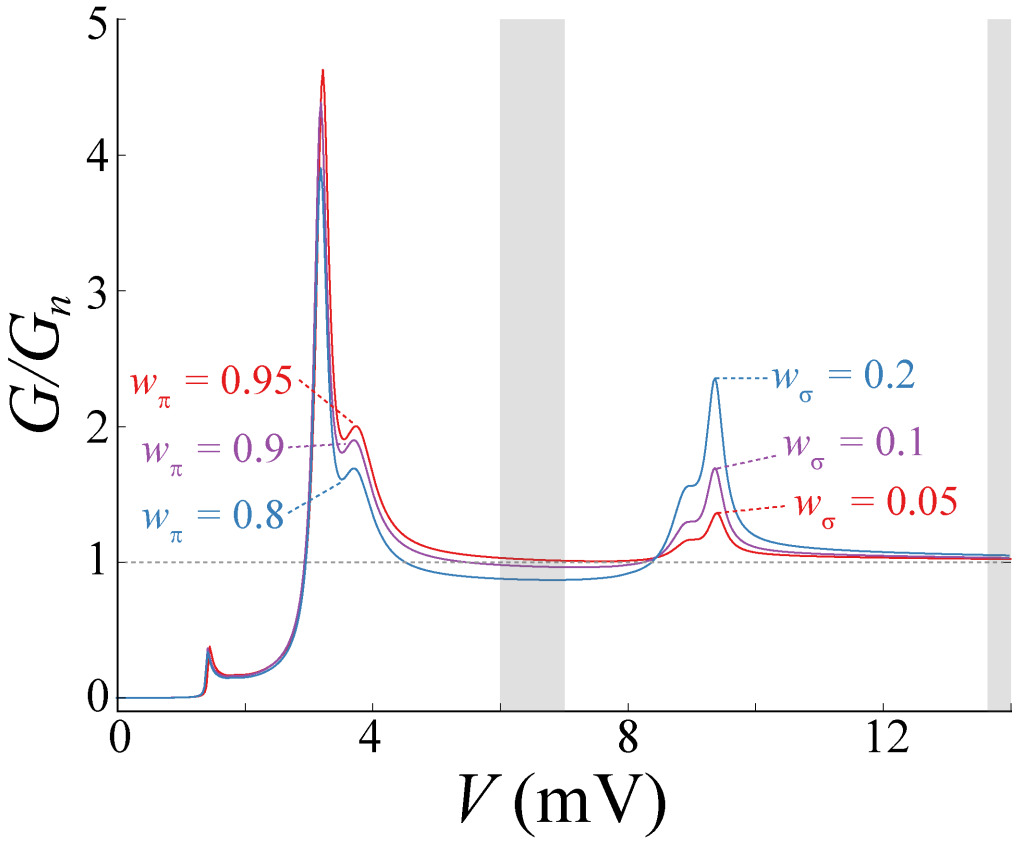


**Figure 3.9:** 4-gap models of normalized conductance, for an $MgB_2$/I/Pb junction with varying weights associated with the $\pi$ and $\sigma$ gaps. At high $V$, the normalized conductance approaches 1, regardless of the relative gap weights. (See the shaded region ~14 mV.) The conductance of data in this region is used to normalize the conductance data of all three junctions. Between the gap voltages, the conductance decreases as $w_\sigma$ increases. (See the shaded region ~6-7 mV.) This provides a measure of $w_\pi$ and $w_\sigma$, independent of features of the gap peaks themselves.

When two- or four-gap models are used, the conductance in between the gap voltages is lower than it otherwise would have been, if there had been only a single gap at the lower gap energy. (See the shaded region near 6-7 mV in Figure 3.9.) The greater the weight that is assigned to the higher gap, the greater this suppression in the conductance will be, in this region. This provides a moderately sensitive measure for the gap weights, regardless of the features attributed to the $\pi$ and $\sigma$ gap distributions themselves.

Applying this method to the "columnar" $MgB_2$/I/Pb junction, whose conductance is shown in

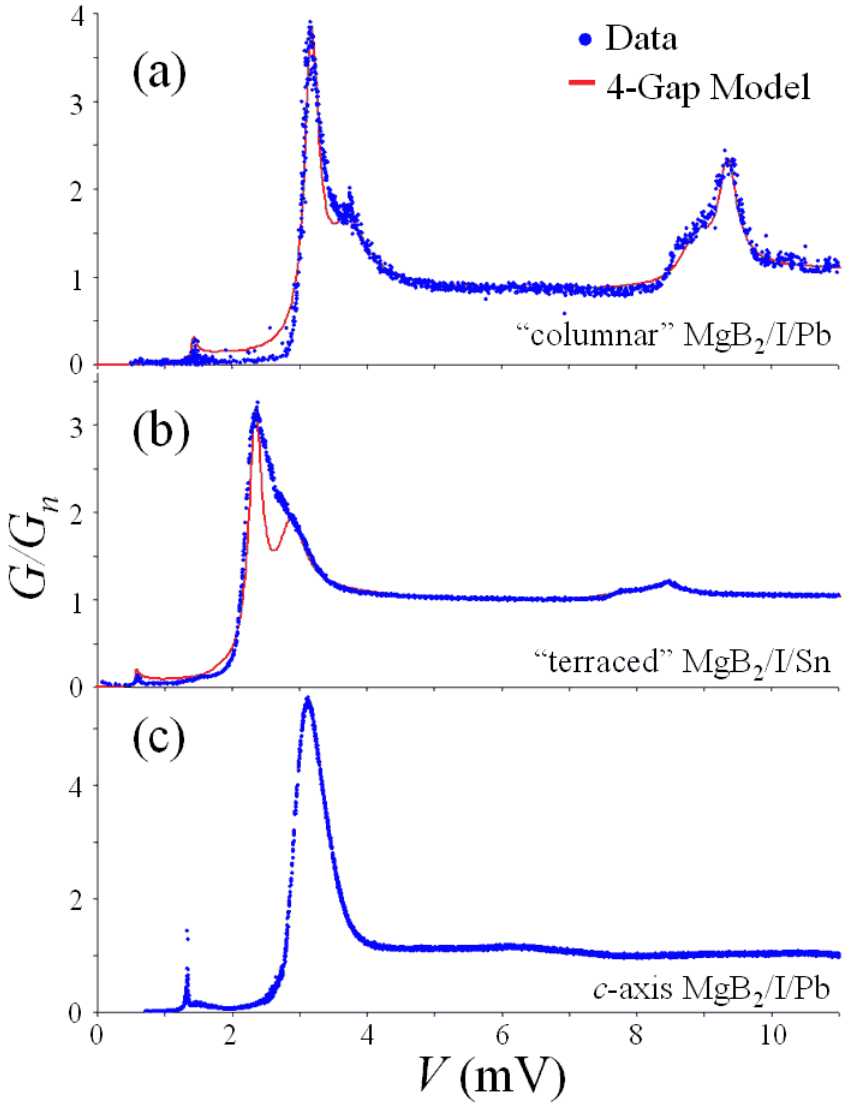


**Figure 3.10:** Conductance data for two different counterelectrode materials and three film geometries. These data were used to determine the gap weights. (a) $MgB_2$/I/Pb results with a "columnar" $MgB_2$ film. $w_\sigma$ ∼20%, indicating significant tunneling along the $a$-$b$ plane. (b) $MgB_2$/I/Sn results, with $w_\sigma$ ∼6%. (c) $MgB_2$/I/Pb results with a planar "$c$-axis" $MgB_2$ film, with negligible contribution from the $\sigma$ gap. Peaks in these three curves are shifted in voltage due to the difference between the energy gaps of lead ($\Delta_{Pb} \simeq$1.4meV) and tin ($\Delta_{Sn} \simeq$0.57meV).

Figure 3.10(a), I find $w_\sigma \simeq 20\%$. This value is remarkably high, considering that the $MgB_2$ film was deposited on 0° SiC, and the theoretical maximum for pure *a*-*b* plane tunneling is $\sim 33\%$. The "terraced" $MgB_2$/I/Sn junction I studied has $w_\sigma \sim 6\%$ (Figure 3.10(b)). And, as expected, for tunneling to a pure *c*-axis $MgB_2$ film, the $\sigma$ peak was indistinguishable ($w_\sigma < 1\%$) (Figure 3.10 (c)).

Although these weights are not exact, they are sufficient to narrow the parameter space when fitting for our desired values ($\Delta_{\pi 1}$, $\Delta_{\pi 2}$, $\Delta_{\sigma 1}$, $\Delta_{\sigma 2}$). With these weights thus approximated, uncertainty in the weights has negligible impact on the uncertainties in the energy gap values.

### 3.3.2 Obtaining $\Delta_{Pb}$ and $\Delta_{Sn}$ from Subgap Features

As discussed above, when a nonzero $\Gamma$ is used, conductance peaks are expected to appear at the gap voltages $\Delta/e$ of each superconductor (Pb or Sn in our case). It is unusual to observe this peak in a low-transparency/high-barrier junction. It is especially unusual for it to be sharp enough to use for establishing an energy gap value. My data in the subgap region of the conductance curves, shown in Figures 3.11 and 3.12 attest to the high purity of the samples, the low transparency of the contacts, and the low noise inherent in our measurement system.

These peaks are extremely useful for three reasons. First, they allow us to determine the gap energy of the Pb and Sn counterelectrode to high precision, particularly as $T \to 0$. Second, because these subgap peaks are sharp and narrow, I am confident that the features I observe in the $(\Delta_{MgB_2} + \Delta_{Pb/Sn})/e$ peaks (below) are due to $MgB_2$ rather than the counterelectrode material. Finally, they establish that $\Gamma$ for the counterelectrode material is small.

I also note that the peak at $\Delta_{MgB_2\pi}/e$ is quite broad, which is appropriate for the distribution in gap values expected in $MgB_2$.

At higher $T$, the peak at $(\Delta_{MgB_2\pi} - \Delta_{Pb/Sn})/e$ appears (above 1.69 K in Figure 3.11 and above 4.5 K in Figure 3.12). This peak is due to quasiparticles thermally excited across the energy gap [17], as discussed in Section 3.1.1. The well-defined peaks at both $(\Delta_2 + \Delta_1)/e$ and $(\Delta_2 - \Delta_1)/e$ are widely used to find unique numerical values for both gaps. In this case, however, the $(\Delta_2 - \Delta_1)/e$ peak takes on a rounded appearance due to the distribution in the $\pi$ gap energies of $MgB_2$, in addition to thermal broadening. Therefore, the sharp subgap peaks at $\Delta_{Pb/Sn}/e$ combined with the

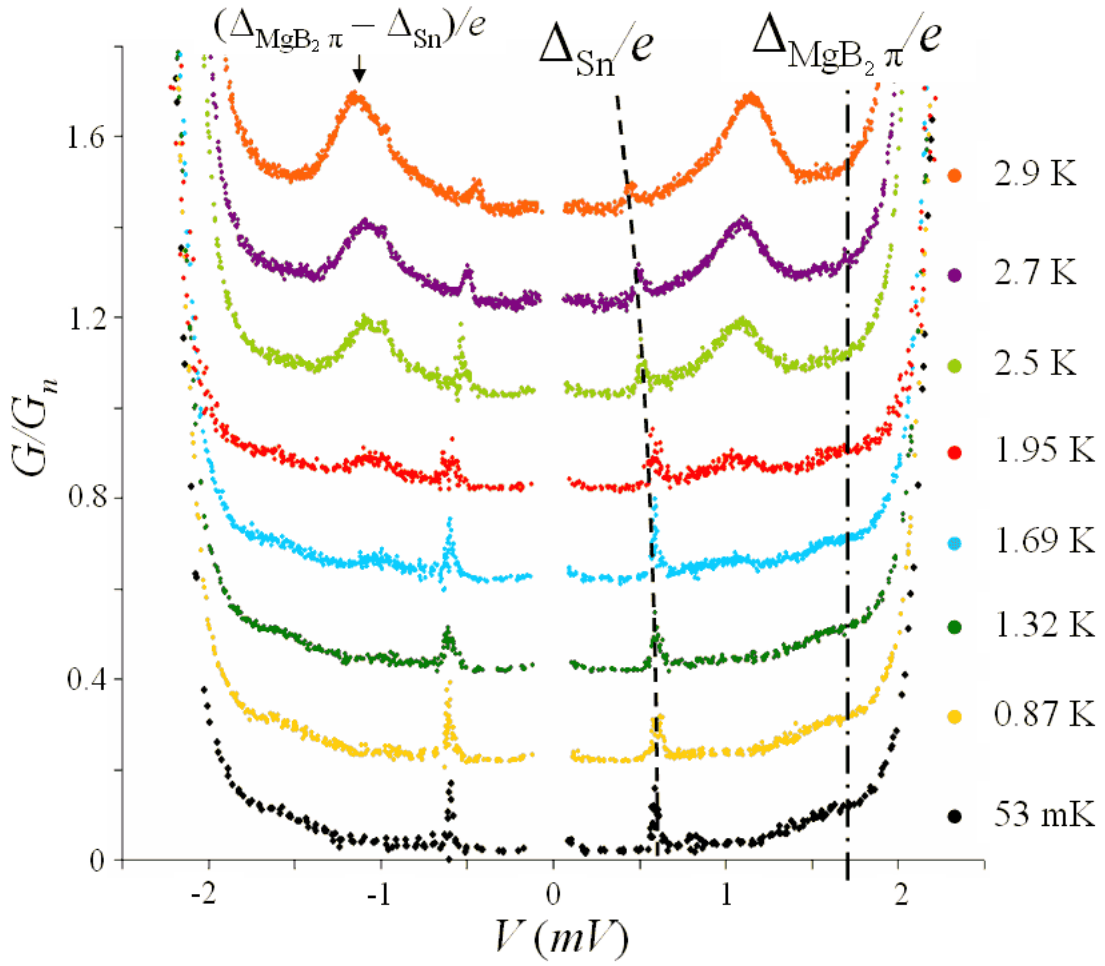


**Figure 3.11:** Conductance data in the subgap region, for a "terraced" $MgB_2$/I/Sn junction with $R_n = 15\ \Omega$ and $R_{sg} \gtrsim 600\ \Omega$, from 53 mK to 2.9 K. Curves have been offset for clarity. The sharp peak at $\Delta_{Sn}/e$ (full width $< 0.07$ mV) is used to establish $\Delta_{Sn}$ in my analysis. This is superior to using the thermally-broadened peak at $(\Delta_{MgB_2\pi} - \Delta_{Sn})/e$.

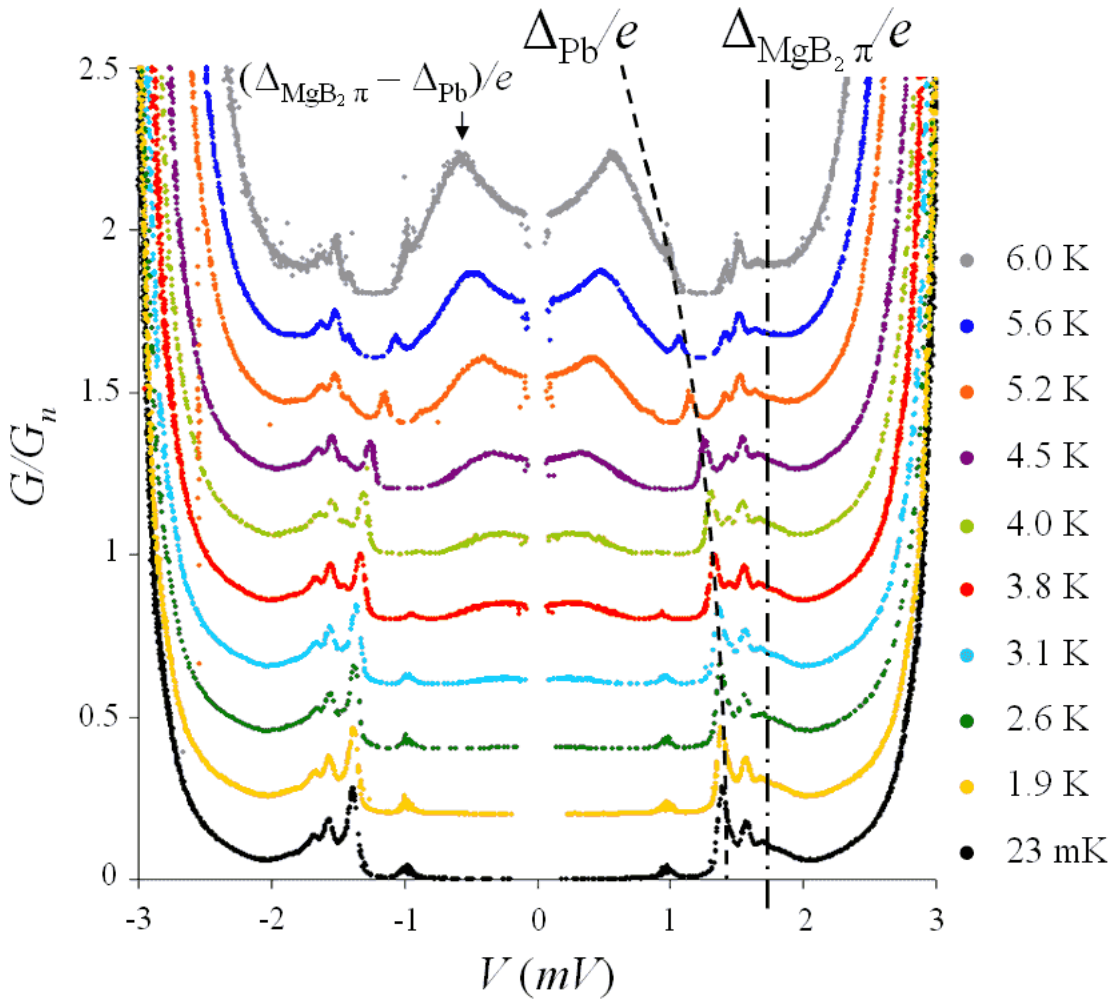


**Figure 3.12:** Conductance data in the subgap region, for a $c$-axis $MgB_2$/I/Pb junction with $R_n = 104\ \Omega$, from 23 mK to 6 K. The most prominent low-temperature peak appears at $\Delta_{Pb}/e$. The sharpness of this peak (full width $< 0.1$ mV), and the small conductance at voltages below this peak ($G/G_n < 0.002$), are indications of a small $\Gamma_{Pb}$. A broader peak at $\Delta_{MgB_2\,\pi}/e$ is also evident, exhibiting far less temperature dependence, which is expected for $MgB_2$ ($T_c = 39$ K).

peaks at $(\Delta_{Pb/Sn} + \Delta_{MgB_2})/e$ provide far better measures of the values for each gap.

Many of the observed features are reasonably consistent with the simple 2-gap (one for $\pi$ and one for $\sigma$) and 4-gap (two each for $\pi$ and $\sigma$) models described above, as can be seen in the subgap portions of Figures 3.13, 3.14, and 3.15. However, a more sophisticated model is required to completely reproduce all of the features in the subgap region. (For example, an Andreev reflection peak at $(\Delta_{Pb} + \Delta_{MgB_{2\,\pi}})/3e \simeq 1$ mV appears at low temperature in Figure 3.12.)

Having determined the gap energies and broadening factors of the counterelectrodes, I now discuss the gap structures themselves.

### 3.3.3 $\pi$ Gap Substructure

A majority of Cooper pairs tunneling into an $MgB_2$ surface are expected to tunnel to the $\pi$ gap. However, the precise details will be sample-dependent. Here, I consider the three significantly different film geometries described above.

"**Columnar**": On a rough 0° SiC substrate, an $MgB_2$ film was grown, which formed columnar structures (Figure 2.10 (b)). Pb was thermally evaporated to form the counterelectrode. Since the $MgB_2$ crystallites were far smaller than the area of Pb in contact with the film, tunneling could occur along the *c*-axis, along the *a*-*b* plane, and anywhere in between. This allows the entire Fermi surface to be explored simultaneously.

The gap distributions for Theories I and II in Figure 3.18 [5, 10] suggest that the $\pi$ gap has a double-peaked structure. As predicted, low-temperature data for this "columnar" sample, shown in Figure 3.13, display a double peak at the gap voltage $(\Delta_{MgB_2\pi} + \Delta_{Pb})/e$.

Complementary data on junctions with similar film geometry and quality may be found in [98] and [7]. Qualitatively, the features are quite similar. The precise details will be sample-dependent due to differences in the accessibility to the various portions of the Fermi surface and in the effects of electron scattering on smearing out fine structures. Additionally, the data presented in this thesis are at a somewhat higher resolution through a combination of measurement technique and lower temperatures.

Clearly, a model possessing a single $\pi$ gap cannot reproduce this structure. However, a simple

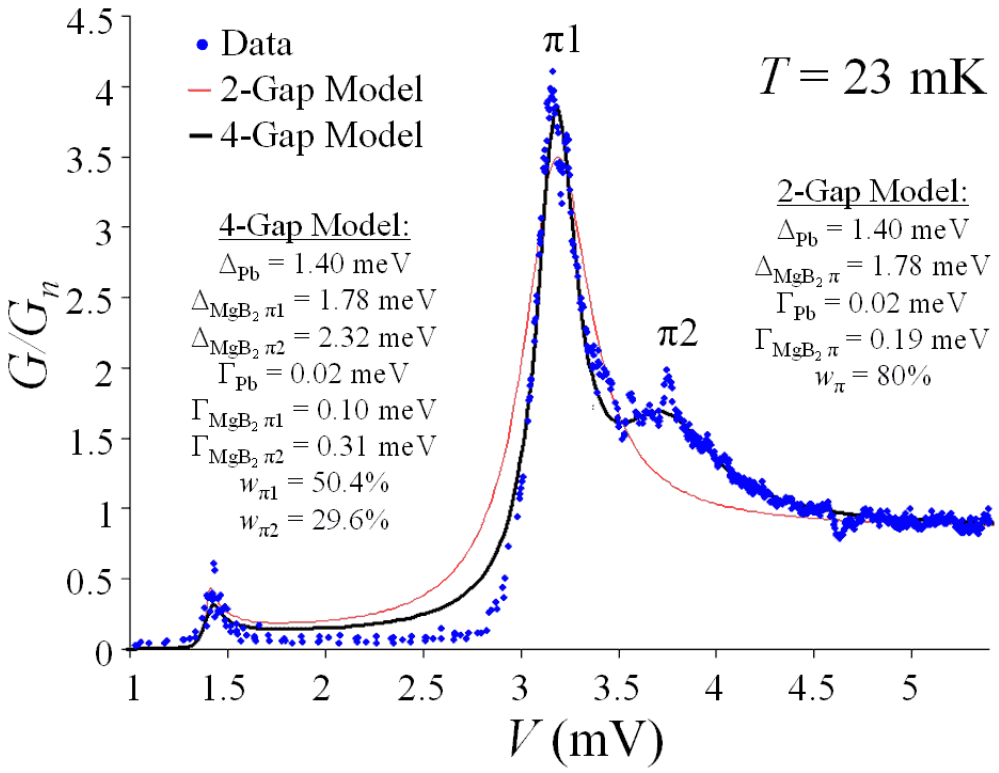


**Figure 3.13:** Normalized conductance, showing the $\pi$ gap for the $MgB_2$/I/Pb "columnar" junction. The data are well-modeled using two $\pi$ gaps at 1.78 and 2.32 meV (with additional gaps for sigma), while a single $\pi$ peak is unable to capture significant portions of the data.

model reflecting features for both $\pi_1$ and $\pi_2$ (in addition to multiple $\sigma$ gaps, described below) produces remarkable agreement.

Because different portions of the Fermi surface are associated with different portions of the gap distributions of the theories in Figure 3.18, it is likely that all portions of the Fermi surface are accessible for tunneling, in similar proportions; this conclusion is supported by the remarkably high $w_\sigma$ for this tunnel junction. It is also likely that a two-peaked character is the correct one for the $\pi$ peak.

The peak in the subgap region establishes $\Delta_{Pb}$, while the level of the normalized conductance between ∼5 mV and ∼8mV establishes $w_\pi$ in a 2-gap model, or $(w_{\pi 1} + w_{\pi 2})$ in a 4-gap model. Using the taller peak at $(\Delta_{MgB_2\pi 1} + \Delta_{Pb})/e$, $\Delta_{MgB_2\pi 1}$ was determined to a high precision: 1.78meV with an uncertainty of ±0.02meV. (All uncertainties are estimated by finding a range of parameters that produce reasonable fits, similar to the method outlined in [22].)

The remaining parameters in the 4-gap model are less certain. Given the asymmetry of the $\pi_2$ shoulder, reasonably good 4-gap fits yield $\Delta_{MgB_2\pi 2}$ of 2.32 meV with an uncertainty of $\sim \pm 0.10$ meV. The weights $w_i$ and the broadening parameters $\Gamma_i$ are more uncertain, because according to the model, any peak may have its height decreased by increasing $\Gamma_i$ or by decreasing $w_i$, and vice versa.

However, as seen in Figure 3.18, none of the theoretical results produce two simple sharp peaks for the $\pi$ gap; and the broadening parameter is here being used exclusively as a means of approximating a distribution in the gap energies. So, although $w$ and $\Gamma$ are necessary parameters in the fit, they do not affect my goal in establishing the need for more than a single broadened $\pi$ gap.

Therefore, I have demonstrated that a single gap energy for the $\pi$ gap is quite far from the real behavior of $MgB_2$, while a $\pi$ gap possessing two distinct sub-bands is a reasonable approximation.

"**Terraced**": The $MgB_2$/I/Sn "terraced" junction used an $MgB_2$ film formed of parallel tilted layers, each exposing a portion of the *a*-*b* plane as well as the *c*-axis.

Once again, a single $\pi$ gap model fits the data very poorly. As shown in Figure 3.14, my simple model including $\pi_1$ and $\pi_2$ is less successful than for the "columnar" sample, though capturing some

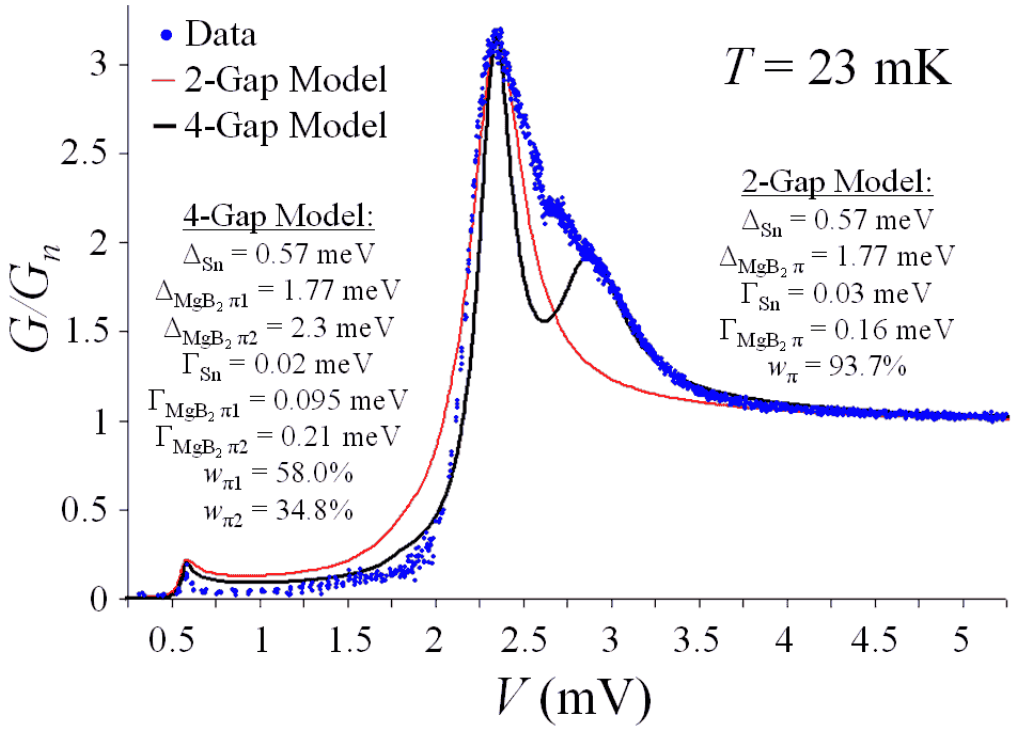


**Figure 3.14:** Normalized conductance, showing the $\pi$ gap for the $MgB_2$/I/Sn "terraced" junction. The prominent shoulder at $\sim$3 mV indicates that a single gap energy is not appropriate for the $\pi$ gap. A better fit is given by a four-gap model with $\pi$ gap values of $\pi_1 = 1.77$ meV and $\pi_2 = 2.3$ meV.

of the main features. Fitting to the tallest peak yields a $\pi_1$ gap energy of 1.77±0.04 meV. However, the broad shoulder can be fit by a wide range of $\pi_2$ gap energies, with an uncertainty of $\sim \pm 0.2$ meV.

Within the model, it was not possible to faithfully fit the data, as shown in Figure 3.14. This is not surprising: as indicated by the lower value of $w_\sigma$ for this junction, a higher proportion of the tunneling is along the *c*-axis. This indicates that less of the Fermi surface of $MgB_2$ is accessible for tunneling than in the "columnar" junction of Figure 3.13. So, some portions of the gap distribution within the $\pi$ peak will be relatively unexplored, while others that may seem low in the models of Figure 3.18 will be relatively overrepresented. Additionally, the shorter height of the crystallites will tend to increase electron scattering. Each of these effects can easily lead to a distribution that is not well-approximated by two rounded peaks. Similar results were found by Dai *et al.* [7] from 40 K to 1.8 K, with some further broadening due to temperature.

Even so, this prominent shoulder at $V \sim 2.7$ mV ($\Delta_{MgB_2\pi 2} \sim 2.3$mV) demonstrates that a single $\pi$ gap, no matter how it is broadened, is inconsistent with the data. Therefore, even with samples that do not fully explore the Fermi surface, I demonstrate that the $\pi$ gap must form a distribution rather than a single gap value, which may prove illuminating in refining theoretical models.

$c-$**axis**: In pure *c*-axis tunneling, almost all of the tunneling is to the $\pi$ gap, with minimal contribution from the $\sigma$ gap. Moreover, the distribution within the $\pi$ gap should be more limited than in cases where the *a*-*b* plane is exposed, since less of the Fermi surface is being explored.

Low-temperature data on a *c*-axis $MgB_2$/I/Pb junction are shown in Figure 3.15. It consists mainly of a single peak, centered at the lower-energy $\pi_1$ sub-gap. (That is, the peak appears at a voltage $(\Delta_{MgB_2\pi_1} + \Delta_{Pb})/e$.) However, using a single-gap theory with variable $\Gamma$, it was not possible to find a combination of $\Delta$ and $\Gamma$ which make the peak broad enough to match the data. A model including two $\pi$ gaps also fails to provide a good match.

From these data alone, it is not clear whether a distribution in gap energies is required, or if a different broadening (which cannot be modeled using $\Gamma$) is sufficient.

However, I gain increased confidence in the significance of features observed in the other film

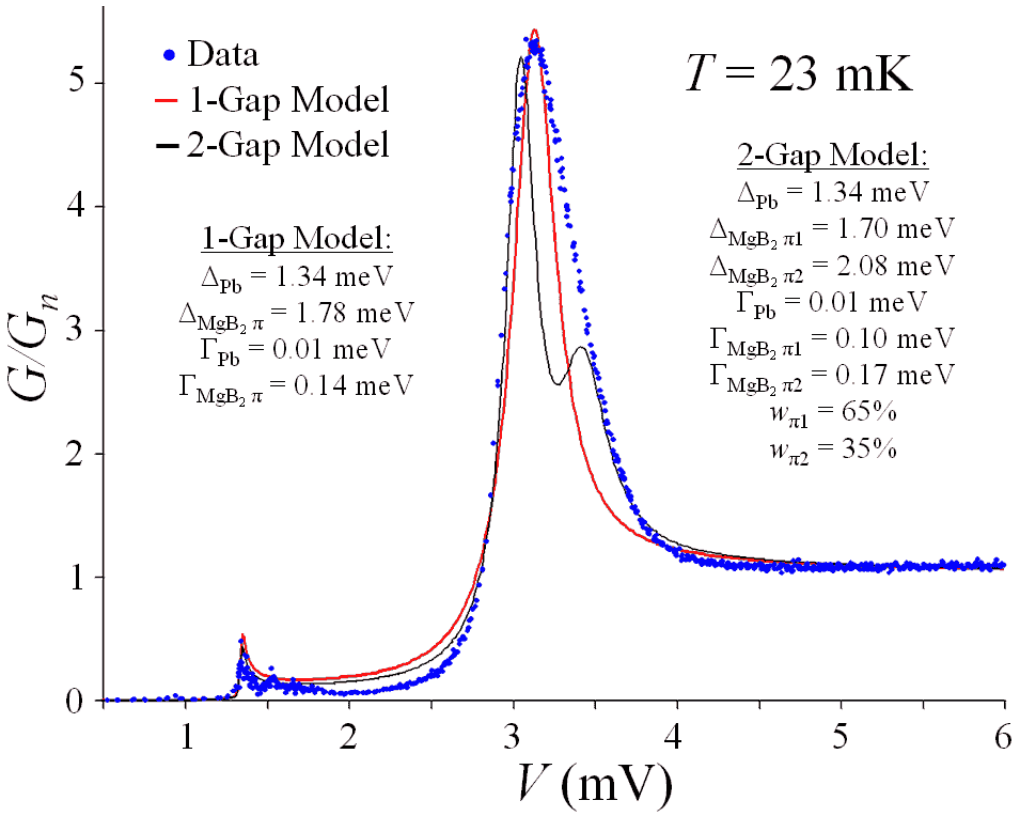


**Figure 3.15:** Normalized conductance, showing the $\pi$ gap for a $MgB_2$/I/Pb c-axis junction. By tunneling purely along the $c$-axis of $MgB_2$, far less of the Fermi surface is explored. As a result, the gap distribution is not apparent. Even so, a single $\pi$ gap (broadened via $\Gamma$) is unable to match the data. A sample model, using two $\pi$ gap energies, is shown for illustration only. Because there is neither a shoulder nor a second peak, a wide range of parameters fits the data similarly well, in a 2-gap model.

geometries because, as expected, this junction shows a more limited distribution. All three films were fabricated using similar methods, all were deposited on SiC, and all were measured using the same apparatus. So, if there were any spurious artifacts in the conductance curves, one would expect them to appear in these $c$-axis samples as well. Their absence supports our conclusion that the gap structures seen in the other samples are inherent properties of $MgB_2$.

### 3.3.4 $\sigma$ Gap Substructure

The high $T_c$ of $MgB_2$ is primarily due to the strongly-coupled Cooper pairs forming in the $\sigma$ band. Therefore, understanding structure of the $\sigma$ gap is of key importance in theories modeling superconductivity in $MgB_2$. As shown in Figure 3.18, the competing models predict different distributions within the $\sigma$ gap. Our high-resolution gap measurements have the potential to validate these theories.

As seen in Figure 3.10(c), tunneling to a $c$-axis $MgB_2$ surface naturally shows no features in the $\sigma$ gap. However, the other contact geometries do produce useful information.

The "columnar" $MgB_2$/I/Pb junction data exhibit features that are clearly incompatible with a simple 2-gap model, as shown in Figure 3.16. If there is only a single $\sigma$ gap, then the resulting curve must take on the shape of a broadened BCS density of states, with a steeper low-energy edge, and a gradual decay toward its limiting value of 1 at higher energies. My data reveal exactly the opposite: a relatively sharp peak at high energies, together with a prominent lower-energy shoulder. These features are reasonably well-modeled by two separate $\sigma$ gaps (which, together with the two $\pi$ gaps form a 4-gap model). However, there are some features that cannot be fit by two sub-gaps within $\sigma$. Indeed, as shown in Figure 3.18, the major competing theoretical models suggest that two peaks are insufficient to accurately portray the $\sigma$ gap.

The "terraced" $MgB_2$/I/Sn junction also exhibits a sharper peak at higher energies, and a prominent lower-energy shoulder. However, since $w_\sigma$ is $\sim 6\%$ (in contrast to the "columnar" junction's $\sim 20\%$), the peaks are less pronounced. As shown in Figure 3.17, a two-gap model (with a single $\sigma$ gap) is far from adequate for representing the data, while a four-gap model (with two $\sigma$ sub-peaks) models the data fairly well.

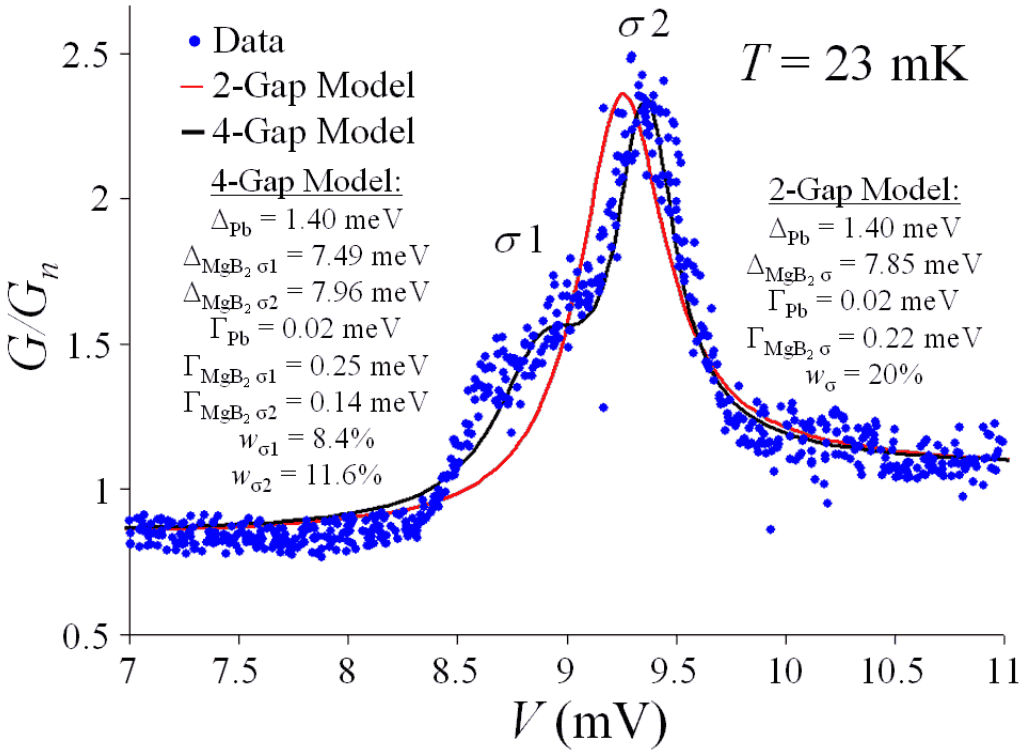


**Figure 3.16:** Normalized conductance, showing the $\sigma$ gap for the $MgB_2$/I/Pb "columnar" junction. A series of features, including a prominent shoulder at a lower voltage than the main peak, indicate that the $\sigma$ gap is more complex than a single broadened peak.

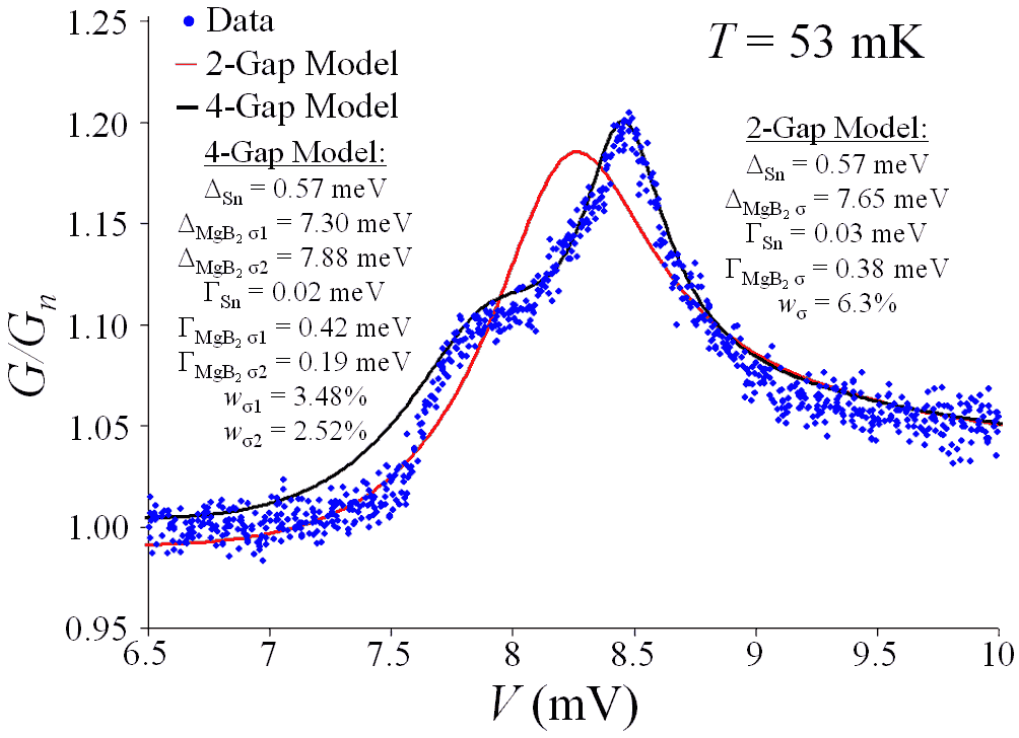


**Figure 3.17:** Normalized conductance, showing the $\sigma$ gap for the $MgB_2$/I/Sn "terraced" junction. As above, a prominent shoulder appears at a voltage below that of the main peak. Therefore, the $\sigma$ gap cannot consist of a single peak. Note that, due to junction self-heating near the $\sigma$ gap voltage, the lowest stable temperature for observing the $\sigma$ peak was 53 mK.

**Table 3.1:** Comparison of energy gap values of $MgB_2$ derived from fits to experimental data vs. peaks in theoretical density of states calculations. Experimental uncertainties are estimated by the range of gap values for which a 4-gap fit may produce reasonable agreement with the data. Theoretical values are based on the center of each peak (see Figure 3.18). Values for $\Delta_\sigma$ for Theory II are approximate, as it is not easily separated into two sub-peaks.

| Feature | "Columnar" Data | "Terraced" Data | Theory I [5] | Theory II [10] |
|---|---|---|---|---|
| $\Delta_{\pi\,1}$ (meV) | 1.78±0.02 | 1.77±0.04 | 1.51 | 1.3 |
| $\Delta_{\pi\,2}$ (meV) | 2.32±0.10 | 2.3±0.2 | 2.06 | 2.2 |
| $\Delta_{\sigma\,1}$ (meV) | 7.49±0.30 | 7.30±0.20 | 6.61 | ∼8.2 |
| $\Delta_{\sigma\,2}$ (meV) | 7.96±0.05 | 7.88±0.05 | 7.13 | ∼8.7 |

## 3.4 Discussion

I have summarized my results in Table 3.1 and Figure 3.18. These results show that our experiments can resolve features in the gap structures of $MgB_2$ less than 0.5 meV apart, with a precision as low as 0.02 meV.

As noted earlier, features in $NS$ conductance data are expected to be thermally smeared by $\sim 2k_BT$. This corresponds to 0.69 meV at 4 K, and 0.17 meV at 1 K. $SIS'$ conductance data should be even sharper. This suggests that energy gap differences of these orders are resolvable at the temperatures of this study, using $SIS'$ junctions. The fact that I have observed independent features associated with the counterelectrode materials in the subgap region, to similar precision, further support the conclusion that these features are inherent in $MgB_2$.

Scattering will also limit the ability to resolve features within the energy gaps. The scattering rate $\gamma^*$ may be calculated from $\gamma > \sqrt{\langle\Delta\rangle\,\delta\Delta}$ [94], where $\langle\Delta\rangle$ is the average order parameter, and $\delta\Delta$ is the variation of the order parameter over the Fermi surface. If I equate these with the average energy gap value and the resolution of our energy gap data, respectively, I find a scattering rate on the order of 1 meV. This implies a mean free path beyond 300 nm. Since this distance is on the same order as irregularities in the film surface [7], it is surprising to observe this energy gap substructure, even with extremely clean samples. Nevertheless, prior tunneling spectroscopy experiments at temperatures from 1.8 K to 7.0 K have exhibited such resolved features [98, 7], in

*Although the symbols conventionally used for each quantity are the same, this scattering rate $\gamma$ is not related to the phase difference across the two electrodes of a Josephson junction $\gamma = \theta_1 - \theta_2$.

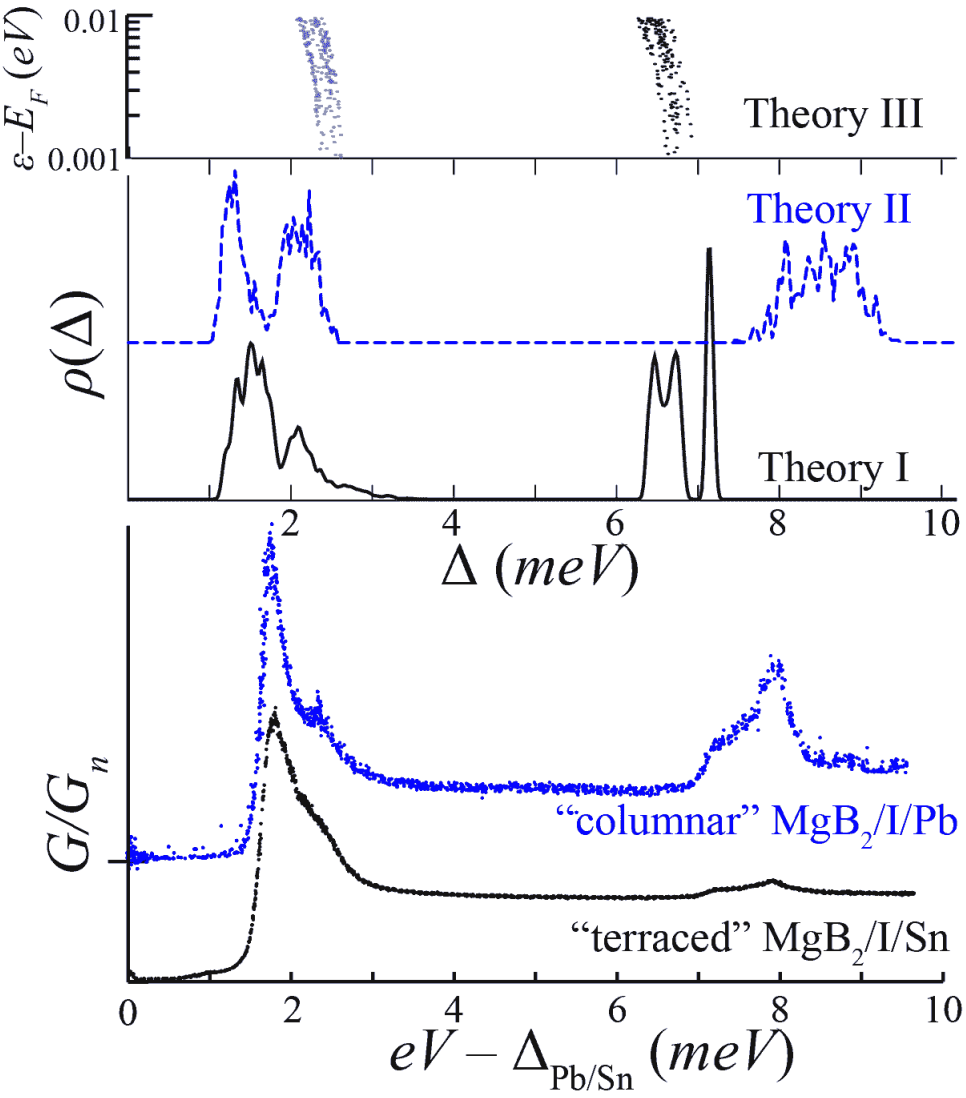


**Figure 3.18:** My normalized conductance data of $MgB_2$, obtained using $MgB_2$/I/Pb and $MgB_2$/I/Sn junctions, compared with theory. Curves are offset for clarity. For the data, the counterelectrode gap energy has been subtracted, leaving only the contribution from $MgB_2$. Theory I [5] and Theory II [10] show the local density of states vs. gap energy at low temperature. Theory III [11] shows the superconducting energy gap, for energies within 0.01 eV of the Fermi energy at $T$=0. A histogram of its points, at the Fermi energy, would produce distributions analogous to Theories I and II. The data resolve features that may be useful in refining theoretical models.

addition to our experimental results presented here.

Table 3.1 and Figure 3.18 also show that none of the three published theoretical models showing a distribution of gap energies [5, 10, 11] matches the data precisely. However, Theory I [5] bears the strongest qualitative similarity, most notably in the shape of the sigma gap structures (with the strongest feature at the highest energy). In fact, if the features from Theory I are scaled up in energy by a factor of 11%, there is very good agreement with our data (see Table 3.1). There are several reasonable explanations for this.

Similar experiments on similar samples find that both the $\pi$ and $\sigma$ gap energies of $MgB_2$ are significantly elevated when SiC is the substrate for the $MgB_2$ film, when compared with MgO [7, 98]. This is logical, considering the thermal contraction that occurs as the sample is cooled after growing the film - MgO and $MgB_2$ have a much smaller mismatch in expansion coefficients than do SiC and $MgB_2$. Therefore, $MgB_2$ films on SiC experience an increased tensile strain.

Pogrebnyakov et al.[131] have found that tensile strain increases $T_c$ in $MgB_2$ films deposited by HPCVD. They attribute this increase to the softening of the $E_{2g}$ phonon mode (associated with the $\sigma$ gap). For $MgB_2$ films on SiC, they find $T_c$ is approximately 41.5 K, rather than the bulk value of 39.4 K. Because each gap energy is proportional to $T_c$ (with $2\Delta_\sigma(0) = 4.18k_BT_c$ and $2\Delta_\pi(0) = 1.59k_BT_c$)[130], elevating $T_c$ from 39.4 K to 41.5 K provides a roughly 5.3% increase in the energy gap values for each gap.

The remaining discrepancy may be due to assumptions used to simplify the theoretical analyses. These experimental results may prove useful in refining models.

## 3.5 Conclusion

I have performed high-resolution tunneling measurements of low-transparency $MgB_2$ tunnel junctions using "terraced," "columnar," and *c*-axis geometries, at low (4 K) to very low (23 mK) temperatures. With these measurements, I have probed the substructures within the $\pi$ and $\sigma$ gaps of $MgB_2$ and generated data useful in validating and refining existing theoretical models.

Within the subgap, I observed very sharp peaks that identify, to high precision, the values of the energy gaps of the junction counterelectrodes (Pb and Sn). These lead us to conclude that the

substructures seen in the $\pi$ and $\sigma$ gaps are due to $MgB_2$, consistent with prior reported measurements [98, 7, 126, 127, 128].

Using a simplified two-band and four-band model with variable gap weights and broadening factors, I demonstrate how these sub-structures illustrate the need to go beyond a two gap model.

# Chapter 4: Superconducting-to-Normal Switching

The analysis described for current and conductance vs. voltage in Section 3.1 took the BCS density of states as a given, and disregarded the Josephson supercurrent. Considering the supercurrent in more detail highlights some interesting physics worth studying in its own right, and provides the foundation for several applications. The focus of those studied in this chapter involves the transition from the superconducting state to the normal state ("switching").

Experiments that analyze the switching from the superconducting to normal states can be very sensitive probes of the properties of Josephson junctions and the materials of which they are made. The washboard potential model of Josephson junctions allows the problem to be recast into the thoroughly-studied system of the escape of a particle from a potential well. Several experimental signatures have been found that distinguish classical from quantum mechanical behavior in these experimental devices. Some of these distinctive features are most apparent in the resonant behavior of a junction exposed to microwave irradiation.

Additionally, highly underdamped Josephson junctions (quality factor $Q \gg 1$) are useful for a variety of applications, whether or not new physics are involved. For example, they are used in high-frequency detectors, and single-photon detectors over a wide range of frequencies (e.g. [132, 133]). The ability to set and read quantum states using macroscopic electronics has also led Josephson junctions to be proposed as useful for quantum computing. In order to preserve the quantum state long enough for computations to be possible, the junctions used in superconducting qubits (e.g. [134, 135, 136]) require a high quality factor.

In this chapter, I describe the theory leading to the washboard potential model, and its implications for our switching measurements. I then discuss the features unique to this type of experiment, and how to extract properties of the junctions from the data.

Finally, I present our results, which form the first switching experiments on hybrid Josephson junctions (i.e. junctions incorporating both single-gap and multi-gap materials as their two super-

conducting electrodes). These results demonstrate it as a viable technique for exploring the physics of such a junction. For the most part, my results are consistent with theory developed for conventional junctions; however, there are some indications of new processes at work. Also, with quality factors $Q_0 \sim$100, I show that these devices may be useful for applications.

## 4.1 Theory

### 4.1.1 The Josephson Equations

As described in Section 1.1.3, superconductivity occurs as electrons with opposite spins form Cooper pairs. As Bosons, they can collapse into a single quantum state. Therefore, all Cooper pairs in a macroscopic superconductor are described by a single wave function, with a single (position- and time-dependent) phase.

As described in more detail in Section 1.2, imposing a phase difference across two coupled superconductors directs a current flow across the boundary. This is described by the Josephson equations:

$$I = I_0 sin\,(\gamma) \tag{4.1a}$$

$$V = \frac{\Phi_0}{2\pi}\frac{d\gamma}{dt} \tag{4.1b}$$

where $\gamma$ is the phase difference between the two superconductors, $I_0$ is the critical current through the junction, and $\Phi_0$ is the flux quantum $\frac{h}{2e} = 2.07 \times 10^{-15}$ Wb.

Often, Josephson junctions are assumed to be "small" (described as "lumped junctions"), so that the phase difference $\gamma$ and current density $J$ vary negligibly with position. This is satisfied whenever the longest dimension of the junction is significantly smaller than the Josephson penetration depth $\lambda_J = \sqrt{\frac{\hbar}{2\mu_0 edJ}}$ [137], where $J$ is the critical current density of the junction, and $d = (\lambda_1 + \lambda_2 + t)$ is the magnetic penetration; $\lambda_1$ and $\lambda_2$ are the London penetration depths of the two superconducting electrodes, and $t$ is the barrier thickness. Using the values applicable to our junctions, $\lambda_J \sim 1.4 - 2.8$ mm, while our longest lengths are $\sim$ 0.3 − 0.6 mm. So, although our junctions are physically much larger than many used for superconducting-to-normal switching experiments (e.g. [138] and

references therein), we are still reasonably in the "small junction" limit, with $L/\lambda_J \lesssim 0.1$. In contrast, the "large junction" limit applies when $L/\lambda_J > 1$. All of the following analysis assumes a single, uniform phase difference across the junction.

### 4.1.2 The Washboard Potential

The Josephson equations describe only the pure junction aspect of a physical system of coupled superconductors. Of course, a real junction, being constructed of physical superconductors with a physical barrier will have some resistance intrinsic to the barrier and capacitance across the electrodes as well. Also, it is coupled to an environment which contributes a noise current. For some experiments, the junction is capacitively coupled to a microwave source, providing an additional high-frequency current source. This leads us to the resistively and capacitively shunted junction (RCSJ) model of a Josephson junction (Figure 4.1) [139].*

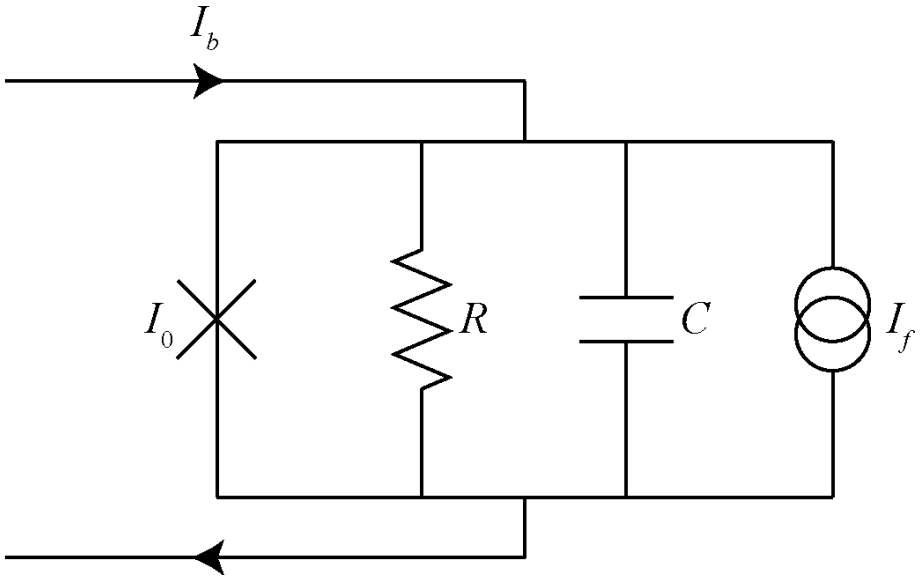


**Figure 4.1:** The RCSJ model of a Josephson junction. An external driving bias current $I_b$ is divided among all channels. The cross represents the "pure junction" channel, described by the Josephson relations. The resistive and capacitive channels are provided by the junction geometry, with some contributions from parallel circuitry. The current source $I_f$ denotes any current fluctuations, whether due to thermal noise, electronic noise, or intentional excitations, such as via microwaves.

Since these components are in parallel, $V_J = V_R = V_C = V$. Likewise, the bias current is

* By taking the derivative of the first Josephson relation, and combining it with the second, we see that the voltage across the "pure junction" component of the RCSJ model depends on the rate of change of current. As a result, a junction is sometimes modeled as a nonlinear inductor. Since the junction inductance usually dominates over the inductance of the "resistive" channel, we do not explicitly include an inductive shunt in the RCSJ model.

split among these components: $I_b = I_J + I_C + I_R + I_f$, where $I_f$ represents any source of current fluctuations (e.g. thermal noise, electronic noise, or microwave excitation). Since $I_R = \frac{V}{R}$ and $\frac{dQ_C}{dt} = I_C = C\frac{dV}{dt}$, combining these results with the Josephson relations (Equations 4.1a and 4.1b) leads to:

$$\begin{aligned} I_b &= I_J + \frac{V}{R} + C\frac{dV}{dt} + I_f \\ &= I_0 sin\gamma + \frac{\Phi_0}{2\pi R}\frac{d\gamma}{dt} + C\frac{\Phi_0}{2\pi}\frac{d^2\gamma}{dt^2} + I_f \end{aligned} \tag{4.2}$$

This differential equation may be more easily understood by considering an analogue mechanical system obeying an equation of motion that is identical to Equation 4.2. Therefore, we recast the equation as:

$$C\left(\frac{\Phi_0}{2\pi}\right)^2\frac{d^2\gamma}{dt^2} = -\frac{1}{R}\left(\frac{\Phi_0}{2\pi}\right)^2\frac{d\gamma}{dt} - \left(\frac{\Phi_0}{2\pi}\right)(I_0 sin\gamma - I_b + I_f) \tag{4.3}$$

By equating the phase difference $\gamma$ with a fictitious position coordinate, we see that this is equivalent to the motion of a fictitious "phase particle" with mass $m = C\left(\frac{\Phi_0}{2\pi}\right)^2$ subject to a damping force $\frac{1}{R}\left(\frac{\Phi_0}{2\pi}\right)^2$, in a "tilted washboard potential" $U(\gamma) = -\left(\frac{\Phi_0}{2\pi}\right)(I_0 cos\gamma + I_b\gamma - I_f\gamma)$ (plus a constant of integration, which we choose to be zero). (See Figure 4.2.) Note that, by arranging the constants in this way, the washboard potential has units of energy.

A convenient energy scale is the Josephson coupling energy $E_{J0} = \frac{\Phi_0 I_0}{2\pi}$, which is half the depth of each well at zero bias. Defining $I = I_b - I_f$, we find

$$U(\gamma) = -E_{J0}\left(cos\gamma + \frac{I}{I_0}\gamma\right) \tag{4.4}$$

In this model, the mass is proportional to the junction capacitance, the damping is inversely proportional to the junction resistance, the tilt of the washboard is provided by the bias current, and the speed at which the phase particle is rolling down the washboard is proportional to the voltage across the junction. The fluctuation currents $I_f$ may be thought of as providing small, rapid

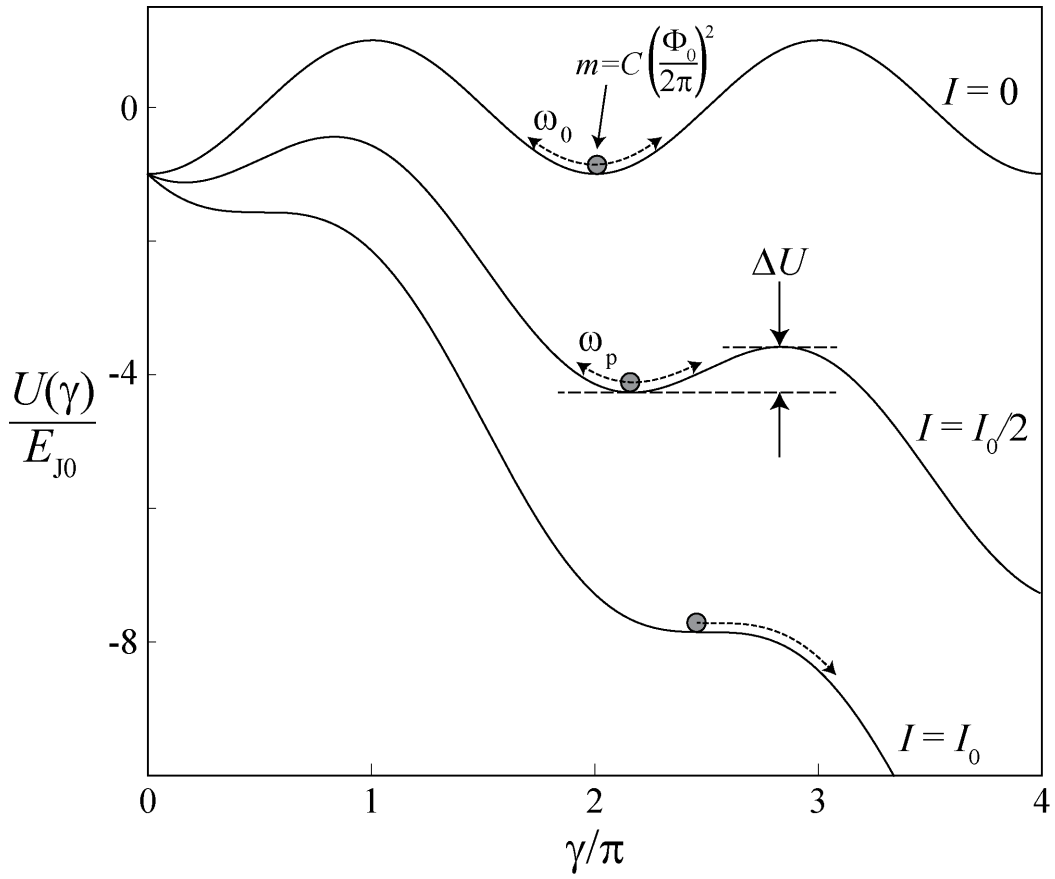


**Figure 4.2:** The washboard potential for an ideal tunnel junction. The behavior of a "phase particle" in this potential mimics that of a Josephson tunnel junction. The mass of the phase particle is proportional to the junction capacitance, a damping force is inversely proportional to the junction resistance, and the speed of the phase particle is proportional to the junction voltage. When $I < I_0$, local minima exist, allowing the phase particle to be "trapped", giving an average voltage of zero across the junction. However, for $0 < I < I_0$, these states are metastable, as there is always a lower potential beyond the barrier $\Delta U$. As the bias current increases, the barrier height $\Delta U$ and resonant frequency $\omega_p$ decrease. For $I > I_0$, there are no potential minima, meaning the phase particle must be "running" down the washboard potential, resulting in a finite voltage across the junction.

variations in the bias current/tilt of the washboard.

Alternative models exist, including a damped pendulum with an external torque proportional to the current $I$, and considering the junction as a nonlinear inductor. Each model has appealing aspects, and is able to enhance understanding for different physical situations. For the processes considered in this chapter, the tilted washboard model provides the clearest insights.

By setting the derivative of $U(\gamma) = 0$, we see that local minima exist which may "trap" the phase particle when $I < I_0$. Therefore, for a fixed nonzero current, the voltage across the junction may remain zero; this current is known as the Josephson supercurrent. Even for a changing current, the resulting voltage is usually negligible below $I_0$: since $V = \frac{\Phi_0}{2\pi}\frac{d\gamma}{dt}$ and the position $\gamma$ of each local minimum changes slowly with changes in current, the current would need to grow from zero to an appreciable percentage of $I_0$ on the order of a nanosecond in order to produce a voltage on the order of a microvolt. As a result, any portion of the $I - V$ curve associated with negligible voltages is usually described as the "supercurrent branch." (See Figure 3.1.)

When the phase particle is trapped at a local minimum, it will tend to oscillate at a frequency referred to as the plasma frequency, $\omega_p$,[†] which can be found from the curvature, $k \equiv \frac{\partial^2 E_{pot}}{\partial \gamma^2}$, at the local minima of the washboard potential, $\gamma = sin^{-1}\left(\frac{I}{I_0}\right) + 2\pi n$. Combining this with Equation 4.4 gives $k = E_{J0}\sqrt{1 - \left(\frac{I}{I_0}\right)^2}$.

Small oscillations about the local minimum will occur at $\omega_p = \sqrt{\frac{k}{m}}$, or

$$\omega_p = \omega_0 \left(1 - (I/I_0)^2\right)^{1/4} \tag{4.5}$$

where the plasma frequency at zero bias $\omega_0 = \sqrt{\frac{2eI_0}{\hbar C}}$.[‡]

It is worth noting that the resistance that appears in the RCSJ model is the resistance at the plasma frequency. If the quasiparticle resistance of the junction dominates, the subgap resistance $R_{sg}$ is used. However, this is rarely the case - in most systems, the shunt impedance provided by the

[†]By using $\omega$, it is to be understood that these equations are for *angular* frequency (in $\frac{rad}{s}$). In Section 4.4, we use frequency $f$ (in $Hz$) $= \frac{\omega}{2\pi}$. For convenience (and consistency with the literature), we use the term "frequency" to describe both; the symbols and units resolve any ambiguity.

[‡]This notation and terminology are not uniformly applied in the literature: a significant fraction applies it as described here, while a significant fraction calls $\sqrt{\frac{2eI_0}{\hbar C}}$ the "plasma frequency of the junction" and labels it as $\omega_p$ rather than $\omega_0$. Additional notations are also used; care must be taken when researching the literature.

leads connected to the junction is a stronger effect at high frequency, giving a resistance typically between 10 and a few 100 Ω [140, 141, 142, 143, 144]. This is why groups seeking to use Josephson junctions for quantum computing often use on-chip isolation circuits, or at least isolation in very close proximity to the junction itself [1, 120]. Our devices do not have such isolation, so we expect to use a resistance substantially lower than $R_{sg}$.

For $I \geq I_0$, there are no local minima. Therefore, the phase particle is guaranteed to be in the "running state," moving down the washboard. Since $\gamma$ must be changing, there must be a finite voltage.[§] At this point, the voltage suddenly jumps to near the gap voltage $V_g = \frac{\Delta_1+\Delta_2}{e}$. The time required, given by $\tau_{turn-on} = \sqrt{\frac{C\Phi_0}{2\pi I_c}}$ [145], is extremely small: on the order of a few picoseconds.

For $I < I_0$, local maxima also exist, at $\gamma = \pi - sin^{-1}\left(\frac{I}{I_0}\right) + 2\pi n$. The energy difference between adjacent maxima and minima, known as the barrier height, is given by

$$\Delta U = 2E_{J0}\left[\sqrt{1-\left(\frac{I}{I_0}\right)^2} - \frac{I}{I_0}cos^{-1}\left(\frac{I}{I_0}\right)\right] \tag{4.6}$$

Prior to considering the washboard model, one may expect that a Josephson junction would switch from the superconducting state to the normal (resistive) state only at the critical current $I_0$. Many references do refer to the current at which the switch happens as the critical current.

However, this model makes it clear that that is not the case. Because we have a particle confined to a well, the phase particle must escape at a current lower than the current at which there are no local minima at all. It may escape "over" the barrier, when either the thermal energy $k_BT$ or energy provided by fluctuation currents are at least on the order of $\Delta U$. Even in the absence of fluctuations and for $T \to 0$, the phase particle may quantum-mechanically tunnel "through" the barrier. The switching current $I_{sw}$, defined as the current at which the voltage suddenly jumps from zero to a finite value, must therefore be below $I_0$.

[§] All of this is consistent with the material discussed in Chapter 3. However, it reveals a new detail: In the analysis there, we considered the voltage to be a function of the current. Here, we see that, at a constant current, the phase particle will not progress down the washboard at a steady speed; instead, it will have a higher terminal velocity on steeper sections, and a lower one on shallower sections. This means the voltage will fluctuate, at a frequency that depends on the current (tilt of the washboard) and the resistance (damping force acting on the phase particle). Therefore, all of the $I-V$ curves do not truly plot current vs. the voltage, but instead the current vs. *average* voltage.
In our case, however, the junction capacitance acts as an effective shunt to the oscillating part of the junction voltage. So, the instantaneous voltage and mean voltage may be used interchangeably, as we did above.

Since escape over the barrier and tunneling through the barrier are stochastic processes, repeatedly ramping the current from 0 through $I_0$ will produce a distribution in values for $I_{sw}$. A great deal of interesting physics may be revealed by repeating the ramping process many times, and producing histograms of the results. This method was first developed by Fulton and Dunkleberger [146].

The RCSJ model also provides a convenient analogy for another useful measure: the quality factor $Q$. In a parallel RLC circuit, $Q = \omega_0 RC$. In our case, we must use the bias-current-dependent $\omega_p$, to get $Q = \omega_p RC$, with $\omega_p$ as defined in Equation 4.5. (Of course, at zero bias, $Q_0 = \omega_0 RC$.)

### 4.1.3 Histograms and Escape Rates

Because the escape of a particle from a potential well is such a widely-studied problem, there is a large body of theoretical results that may be applied. Often, these analyses are in terms of the escape rate – the rate at which a particle or group of particles is able to escape; or equivalently, the inverse of the lifetime of the particle in the well.

As described in Section 4.2, our apparatus records the time of a switching event; we are able to extract a switching current by knowing the rate at which the current is ramped. Since the escape rate has dimensions of $[\text{time}]^{-1}$, it is convenient to leave our data in terms of times, and only convert to currents after performing the histogram and escape rate calculations.

We record $\sim 10^3 - 10^6$ switching events, in order to produce reliable histograms. When creating histograms, we bin the data into a large number of bins, each with a width $\Delta t$, centered at the times $t_i$.[¶] We denote the number of counts in the bin at $t_i$ as $H(t_i)$. The number of counts in bin $t_i$ plus the counts in *all later bins* is denoted $N(i) = \sum_{t=t_i}^{\infty} H(t)$. With these definitions, the escape rate $\Gamma$ is given by[‖]

$$\Gamma(t_i) = \frac{1}{\Delta t} \ln\left(\frac{N(t_i)}{N(t_{i+1})}\right) \tag{4.7}$$

[¶]When choosing the bin width, there is no "best" method. That is, it must not be so wide as to obscure relevant features, nor to have a dramatically different escape rate from beginning to end of the bin. But it must not be so narrow that statistical fluctuations between adjacent bins become the most prominent features. Even with arbitrarily high statistics, results displayed using excessively narrow bins will be affected by noise at a level below that needed to observe relevant features; and ultimately, the resolution of the timer provides a limit. However, as long as one does not go too far to either extreme, the appearance of the histograms and escape rate plots will be quite similar, giving useful results.

[‖]Although the symbols conventionally used for each quantity are the same, the escape rate $\Gamma$ is not related to the broadening factor $\Gamma$ used in Chapter 3.

where $\Delta t$ is the time width of each histogram bin.

This can be understood by considering the number of particles that escape $-dN$ during the time $dt$, under an escape rate (or inverse lifetime) $\Gamma$ that is assumed constant over this infinitely-small time:

$$dN\left(t\right) = -\Gamma\left(t\right) N\left(t\right) dt \tag{4.8}$$

where $N(t)$ is the number of particles that have survived up to time $t$. The value is negative because the number of surviving particles decreases with time.

By integrating Eq. 4.8 from $t_i$ to $t_{i+1} = t_i + \Delta t$, we obtain Eq. 4.7. This result assumes that $\Gamma(t_i)$ is constant over $\Delta t$, which is reasonable for the relatively small time-width chosen.

Conceptually, we imagine an ensemble of states in the well, with some percentage of the total states escaping in each time interval. The greater the proportion of "available" states (i.e. those which have not yet escaped) which escape during the bin $t_i$, the greater the escape rate $\Gamma\left(t_i\right)$ must be.

We may also apply Eq. 4.8 to simulate an experimental histogram, based on a theoretical escape rate (e.g. using the equations presented in Section 4.1.4). Consider the events binned in current increments $\Delta I$ rather than time increments $\Delta t$. We compute the current $I$ at a particular time $t$ simply by multiplying by the known ramp rate $dI/dt$. Let us define $P(I)$ as the probability of finding an escape in a particular bin; i.e. $P(I) = H(I)/N(I = 0)$. Equating the number that escape $-dN$ with the histogram counts in that bin $H(I)$, we find:

$$P\left(I\right) = \Gamma\left(I\right)\left(\frac{dI}{dt}\right)^{-1}\Delta I\left(1 - \sum_{u=0}^{I-\Delta I} P\left(u\right)\right) \tag{4.9}$$

Note that an equivalent expression, in integral form, is presented as Eq. 6 in [146].

Theoretical histograms and escape rates, plotted according to Equations 4.9 and 4.12, are shown in Figure 4.4.

Of course, this escape rate calculation will not be perfect, since there is a finite amount of sampled

data. The errors will tend to be greatest when the number of counts in a bin $H(t_i)$ is smallest. Ignoring any systematic experimental errors, the statistical error in the escape rate will be [1]**

$$\delta\Gamma = \sqrt{\alpha^2 N(t_i) + \beta^2 H(t_i)} \tag{4.10}$$

where

$$\alpha = \frac{1}{\Delta t}\left(\frac{1}{N(t_i)} - \frac{1}{N(t_i) - H(t_i)}\right) \tag{4.11a}$$

$$\beta = \frac{1}{\Delta t}\left(\frac{1}{N(t_i) - H(t_i)}\right) \tag{4.11b}$$

These equations are the basis of the experimental plots below, such as Figure 4.3.

### 4.1.4 Classical vs. Quantum Escape

As the bias current approaches the critical current $I_0$, the barrier height goes to zero, and the escape probability increases exponentially. This is true whether the escape is dominated by quantum tunneling through the barrier, or classical promotion over the barrier.

Roughly speaking, classical behavior will dominate when $k_B T$ is on the order of $\Delta U$ and/or when there are many energy levels in the well, which occurs when $E_0 \ll \Delta U$. (These two conditions are effectively equivalent at high escape rates: if $k_B T \sim \Delta U$, then nearly all of the phase particles will have escaped by the time that $E_0 \sim \Delta U$.)

In the event that escapes are dominated by classical (thermal) effects, the escape rate in a system with low damping follows that found by Büttiker, Harris and Landauer [147].

$$\Gamma_{BHL} = a_t \frac{\omega_p}{2\pi} \exp\left(-\frac{\Delta U}{k_B T}\right) \tag{4.12}$$

where the prefactor $a_t$ is given by $a_t = \frac{4}{\left[\sqrt{1+5Qk_BT/(9\Delta U)}+1\right]^2}$.

** Because $\Gamma(t_i)$ uses $N(t_i)$, which depends on a series of bins, the bins are correlated with each other. As a result, this expression is not exactly correct. However, it is close enough to give a useful representation of the statistical uncertainty in the escape rate.

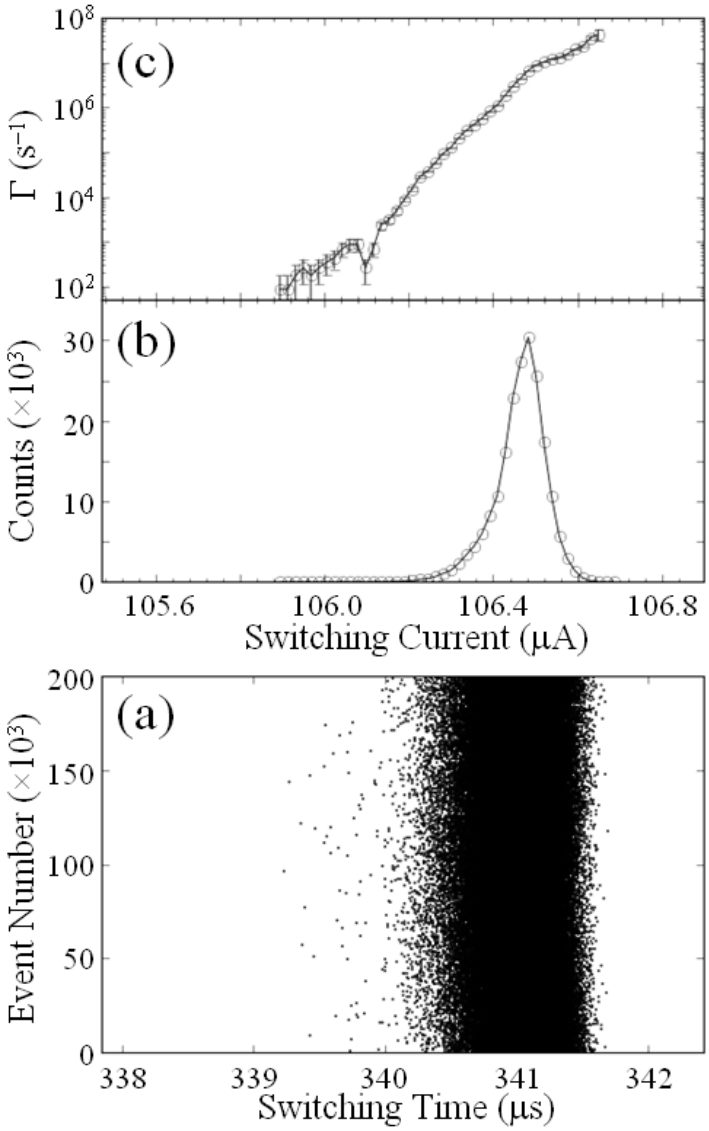


**Figure 4.3:** Switching data taken on the "terraced" $MgB_2$/I/Sn junction at 23 mK. (a) Raw switching times, recorded for 200000 events. (b) The resulting histogram, with the current calculated as (switching time - time offset)$\times dI/dt$. (c) The escape rate, calculated from Eq. 4.7, with statistical uncertainties computed from Eq. 4.10. The probability of escape increases roughly exponentially with current. By recording so many events, we are able to obtain reasonable results for the escape rate far from the densest portion of the histogram. When fewer events are captured, the escape rate is reasonably certain over a much smaller range.

The bulk of the expression follows from the results of Kramers [148], equating the plasma frequency $\omega_p$ with an attempt frequency for the phase particle escaping from one well to a lower, adjacent well. The additional prefactor $a_t$ is needed because there is a very high escape rate for particles with energies near or above $\Delta U$. Especially for high-Q systems, it takes a significant time to reach equilibrium once the particles with high energies have escaped, leading to a population depletion for high-energy particles, and a reduction in the escape rate.

Equation 4.12 is used to define an "escape temperature," $T_{esc}$, of the junction. In the analysis below, $T_{esc}$ was selected as the temperature that provided the best fit to the data.

Figure 4.4 shows simulated escape rates and histograms, computed from equations 4.12 and 4.9. As indicated there, the mean switching current decreases as the temperature increases. The above analysis provides a more accurate representation of this effect, although it is reasonably approximated by $\langle \delta i_{sw} \rangle \equiv \frac{I_0 - \langle I_{sw} \rangle}{I_0} = \left[ \left( \frac{k_B T}{2E_{J0}} \right) \ln \left( \frac{\omega_0 I_0}{2/pi \dot{I}_b} \right) \right]^{2/3}$ where $\dot{I}_b$ is the bias current ramp rate [142, 149]. This allows for a relatively fast and simple estimation of the effective temperature of the junction, based on the shift in the histogram peak. Of course, this is only valid when the system is dominated by thermal escapes from the well.

In the absence of quantum behavior, $T_{esc}$ should decrease, all the way to $T = 0$. Below a certain temperature, however, quantum tunneling through the barrier dominates. This crossover temperature is given by [150, 151]

$$T_{cr} = \left( \frac{\hbar \omega_p}{2\pi k_B} \right) \left[ \left( 1 + \frac{1}{4Q^2} \right)^{1/2} - \frac{1}{2Q} \right] \tag{4.13}$$

For high-$Q$ junctions, this expression is often simplified as $T_{cr} = \frac{\hbar \omega_0}{2\pi k_B} \left[ 1 - \left( \frac{I}{I_0} \right)^2 \right]^{1/4}$ [152].

Therefore, a leveling off of $T_{esc}$ as the temperature is further reduced is commonly seen as evidence of quantum behavior. As indicated in Figure 4.4, the histogram width also decreases with temperature. So, as with $T_{esc}$, this width should reach a minimum near $T_{cr}$ as quantum effects begin to dominate. Because of the general difficulty in fitting the escape rate (discussed in section 4.3.3), the standard deviation in the switching current distribution is commonly used to determine

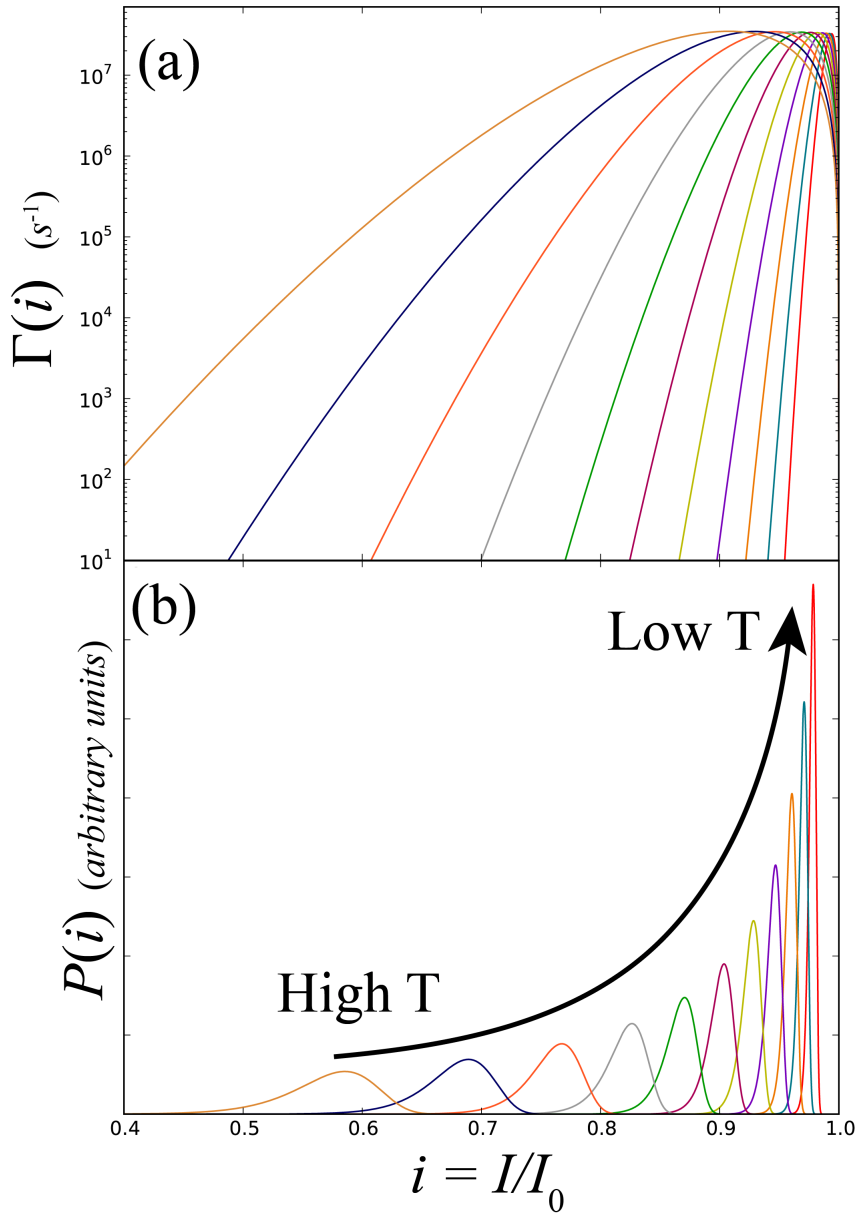


**Figure 4.4:** Theoretical escape rates (a) and probability distributions (b) vs. normalized current for classical (thermal) escape of the phase particle from the washboard potential, computed from Eq. 4.12 and 4.9, respectively. (b) is equivalent to experimental histograms of switching events. Each curve corresponds to a temperature 1/3 lower than the previous curve. As the temperature decreases, the mean switching current increases and the standard deviation decreases, in the probability distribution (b). The curvature in the escape rate (a) is due to running out of high-energy phase particles. Notice that above the most probable switching current, the probability distribution (b) decreases, even as the escape rate (a) continues to increase. This is because, with an ensemble of phase particles initially in the local minimum "well," most of the particles will have escaped prior to the escape rate reaching its maximum. With few particles available to escape, few counts will be observed, no matter how rapidly they would escape if present.
This figure assumes that the critical current $I_0$ is not itself a function of temperature. This is a reasonable approximation when the temperature remains below roughly 1/3 of the critical temperatures of both superconducting electrodes.

the crossover temperature.

However, observing that the escape temperature and/or standard deviation reaches a constant value below a certain temperature is not a guarantee of a crossover from classical to quantum-mechanical behavior. Instead, it may indicate that, rather than being quantum-limited, the system is becoming noise-limited. In this case, although the standard deviation and fit temperature remain constant as the temperature decreases below the effective "noise temperature," the mean switching current continues to approach the critical current [153].

If the system is dominated by quantum-mechanical tunneling through the barrier, the escape rate takes on a different form: [154]

$$\Gamma_q = a_q \frac{\omega_p}{2\pi} \exp\left[-\frac{7.2\Delta U}{\hbar\omega_p}\left(1+\frac{0.87}{Q}\right)\right] \tag{4.14}$$

where the prefactor $a_q \cong \left[120\pi\left(7.2\Delta U/\hbar\omega_p\right)\right]^{1/2}$.

As indicated in Figure 4.5, there are no true stationary states within the tilted washboard. However, only states corresponding to quasi-bound states have a high amplitude, so that it is reasonable to consider them as bound states for the duration of the ramp.

Each of the equations in this section have most often been applied to the analysis of physically-small junctions, incorporating the same material for both junction electrodes, neither of which includes multiple gaps. There has been little theoretical and no experimental considerations of junctions analogous to those in this thesis. What theoretical work has been done is addressed in Section 4.1.9.

### 4.1.5 Microwave Resonant Activation

Microwave excitation is commonly used to study the resonant modes of the washboard beyond what is possible with only changes in temperature. When microwaves are applied, they become the dominant source of fluctuation currents $I_f$, at controlled frequencies and powers. Their inclusion has several distinct effects on the phase escape from the washboard.

The most obvious effect occurs when the microwave driving frequency $\omega_{\mu w}$ coincides with the

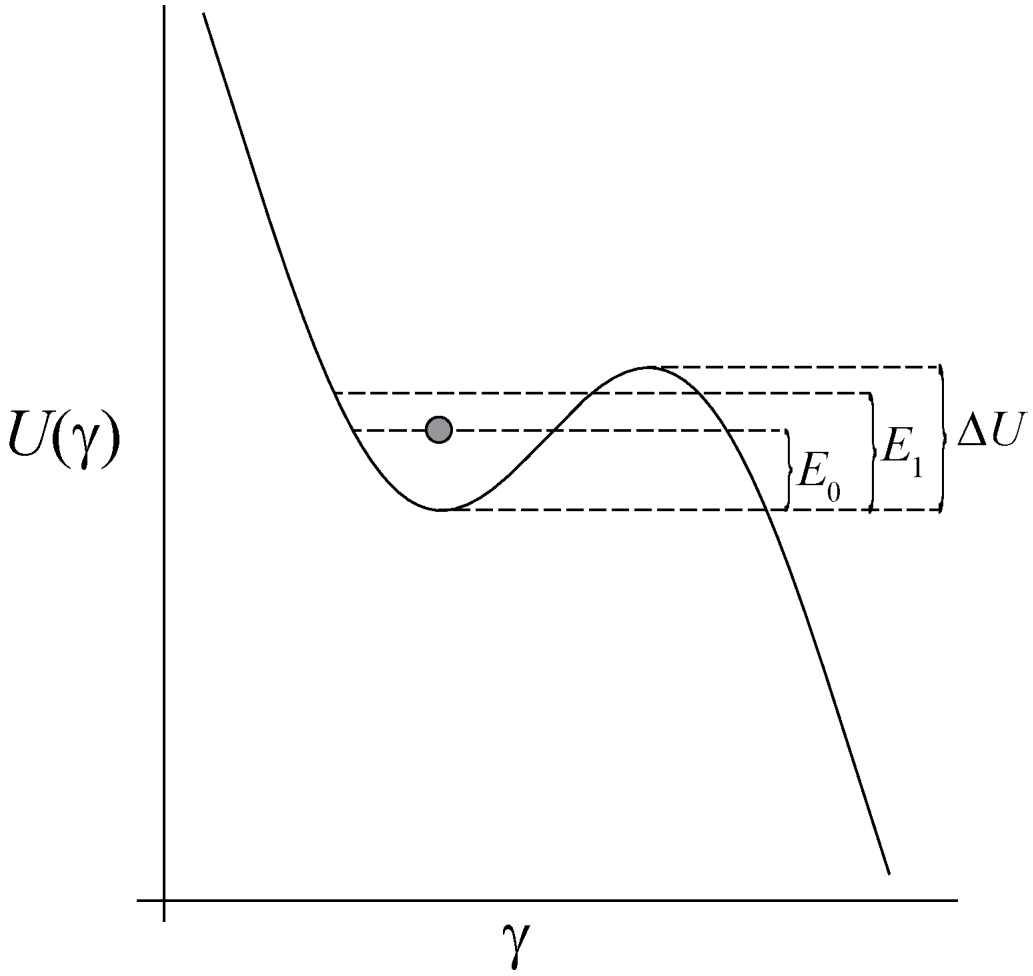


**Figure 4.5:** A schematic of the washboard potential, for a phase particle in the ground state when the bias current is sufficiently high that only two quantum states are available in the well. The states are not equally spaced in energy because the potential is anharmonic. When $E_0$ is an appreciable fraction of $\Delta U$, the barrier is sufficiently short and narrow that quantum tunneling provides a significant contribution to the escape rate. Note that the states shown are not true stationary states, since the potential continually decreases as $\gamma$ increases. Prior to escape, however, the phase particles are highly likely to be in one of these metastable states. Exciting the phase particle to a higher quantum energy level causes the phase particle to see a smaller barrier, greatly increasing the escape rate. This is discussed in Section 4.1.5. In contrast, when the local minimum is much deeper than the energy level spacing, there is effectively a continuum of states, and the system behaves classically.

plasma frequency $\omega_p$ of Equation 4.5. Classically, when there are enough states spaced closely together so as to behave as a continuum, the phase particle must acquire sufficient energy to escape "over" the barrier. This occurs at the plasma frequency, when, especially in the case of low damping, little energy is lost each cycle, so the contributed energy is accumulated. These classical escapes at the plasma frequency also happen when the well is sufficiently deep that it is reasonably approximated by a harmonic oscillator potential.

Because $\omega_p$ depends on the current, maintaining a constant microwave drive frequency $\Omega$ while ramping the current from 0 through $I_0$ will lead to a resonance at $\omega_p$ only at one particular current. If the fluctuation currents are of the proper strength, a "resonant peak" in the histogram of escape events will appear at the bias current $I_r$ corresponding to $\omega_p = \omega_{\mu w}$, together with the "primary peak" at a current $I_p$ - associated with those particles that did not resonantly escape.

At very low microwave power, so few phase particles resonantly escape that only a single primary peak is observed at $I_p$. At very high powers, they all resonantly escape, leading to only a single resonant peak (which under some circumstances could be mistaken for a shift in the primary peak, as discussed in Section 4.1.7). A clear resonant signal, with both primary and resonant peaks, occurs in a relatively limited range of powers. One example is shown in Figure 4.6.

Recalling Equation 4.5, we see that $\omega_p$ is a function of the current $I$. As $I$ increases, each local minimum in the washboard potential gets flatter, resonating at a lower frequency. That trend is observable, as indicated in Figure 4.7.

In the quantum regime, the phase particle may be promoted from a lower quantum energy level within the well to a higher energy level where the height and thickness of the barrier are reduced, thereby significantly increasing the probability of tunneling. This leads to a resonant enhancement of escapes at microwave frequencies that correspond to the energy level spacings.

For temperatures well below $T_{cr}$, when nearly all of the phase particles are in the ground state, the transition to the first excited state is the most likely one to be observed. Applying a cubic approximation to the washboard potential, the corresponding frequency is $\omega_{01} \simeq \omega_p \left(1 - 5\hbar\omega_p/36\Delta U\right)$ [155]. This leads to the observation of a resonant peak, shifted slightly from the classical $\omega_p$.

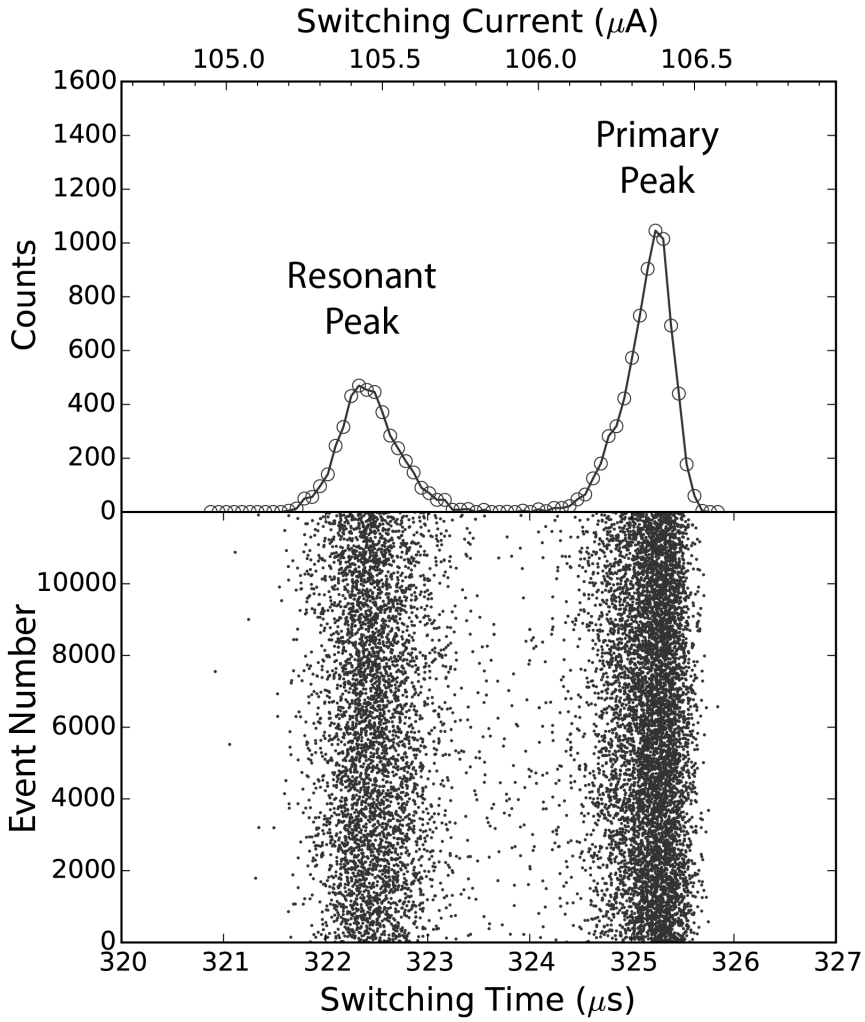


**Figure 4.6:** Raw switching times, and the resulting histogram, for the $MgB_2$/I/Sn junction at $T = 24$ mK, when driven by microwaves at frequency 0.90 GHz and power 42.5 dBm. The double-peaked structure, with both primary and resonant peaks, is apparent.

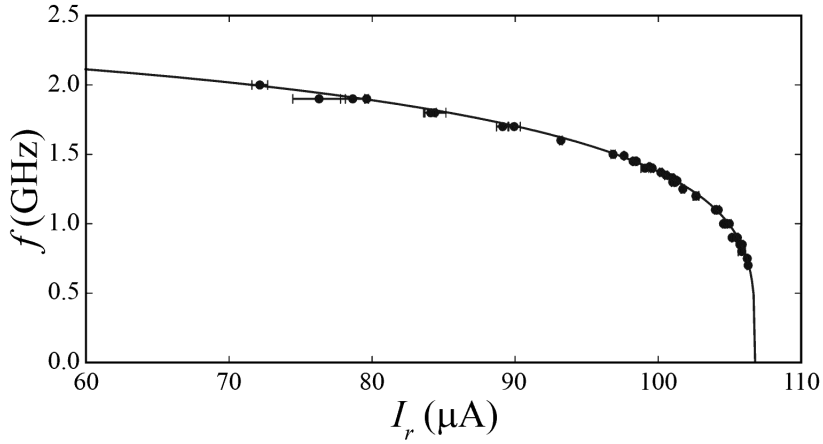


**Figure 4.7:** Microwave driving frequency $f$ vs. resonant current $I_r$ for the $MgB_2$/I/Sn junction, fit according to Equation 4.5. Only two parameters, $I_0$ and $C$, are needed to generate the fit. In this case, $I_0 = 106.78 \pm 0.05\,\mu$A and $C = 1523 \pm 14$ pF.

At higher temperatures (but still below $T_{cr}$), a sufficient population of phase particles occupies both ground and first excited states, so that both the $0 \rightarrow 1$ and $1 \rightarrow 2$ transitions are observed. In the cubic approximation, the latter corresponds to a frequency $\omega_{12} \simeq \omega_p\,(1 - 5\hbar\omega_p/18\Delta U)$. Such multiple resonant peaks have been observed (e.g. Figure 4.8 and [143]), and are seen as a signature of quantum mechanical behavior.

This ability to set, and read, the presence of a phase particle in the 0 or 1 state has led to the proposed use of current-biased Josephson junctions as a quantum bit – the "Josephson phase qubit" [51].

Experimentally, these resonances are observed by constructing histograms as described in section 4.1.3. In this case, microwaves are applied for the duration of the current ramp. At low microwave power, few enough phase particles resonantly escape that the histogram is nearly unchanged, and only one peak is observed at a current slightly below $I_0$ – the "primary peak" at $I_p$. At a certain threshold power, enough phase particles resonantly escape that they form an appreciable portion of the histogram/escape rate plots. In this case, two peaks are observed: the "primary peak" at $I_p$ and the "resonant peak" at $I_r$. At even higher powers, essentially all of the phase particles experience resonant escape, and a single peak is again observed. This progression is illustrated for our $MgB_2$-based junctions in Figure 4.18.

The resonant peak moves to lower currents as the microwave power is increased. Classically, this may be understood as additional microwave energy allowing the phase particle to escape a deeper well than at resonance. Quantum mechanically, this is consistent with a microwave-induced suppression in the barrier height, as described in section 4.1.7 below.

Therefore, in order to create plots such as Figure 4.7, a strict definition for $I_r$ must be chosen. Three different methods are used in the literature, all leading to nearly equivalent values for $I_r$, but each best suited for different circumstances. These are discussed in Section 4.3.2. One of them uses the concept of an enhancement in the escape rate, discussed in the following section.

### 4.1.6 Escape Rate Enhancement

Some resonances occur at currents very close to the mean switching current in the absence of microwaves. The resulting histograms and escape rate plots reveal a shoulder rather than a distinct peak. This makes it difficult to extract a value for the resonant current from the histograms or escape rates alone.

However, these resonances are often of primary interest: because the wells of the washboard potential get shallower as the current increases, fewer quantum states are available at high currents. So, quantum mechanical signatures tend to be most clear for these resonances. (It must be noted that the crossover temperature (Eq. 4.13) is lower at high currents, due to the decrease in $\omega_p$ with current. So, although these resonances at high currents are more likely to reveal quantum behavior due to the few available energy levels, the required temperatures are significantly reduced.)

In order to extract information about the resonance, we use data taken both with and without microwaves.

We define the enhancement $\gamma$

$$\gamma = \frac{\Delta\Gamma}{\Gamma} = \frac{\Gamma_{\text{RF On}} - \Gamma_{\text{RF Off}}}{\Gamma_{\text{RF Off}}} \tag{4.15}$$

With this, the effects of the microwave fluctuation current $I_f$ are clearly distinguished. This technique was first used by Martinis, Devoret and Clarke [50] to demonstrate the existence of quantum-

mechanical energy levels in a current-biased Josephson junction.

If the system is dominated by quantum-mechanical processes, the enhancement forms a Lorentzian peak [120, 143]. If only the ground state $|0>$ and first excited state $|1>$ energy levels are occupied, then, in the absence of noise and at zero temperature, the full width at half maximum (FWHM) of the Lorentzian fit is equal to the relaxation rate from the $|1>$ to the $|0>$ state.

Increasing temperatures thermally populate the $|1>$ state sufficiently so that the $|1>$ to $|2>$ resonance becomes more observable, as shown in Figure 4.8(a). At even higher temperatures, more transitions become likely, with each being thermally broadened. Eventually, this approximates a continuum of states. At this point, the escape rate takes on the shape of a plateau of roughly constant enhancement at currents below the resonant current [50, 143, 156]. As indicated in Figure 4.8(b), the resonant current is found at the intersection between the horizontal plateau and the sloped shoulder.

This plateau is taken to be an indication of classical behavior, and appears at a current corresponding to $\omega_p$ rather than $\omega_{01}$.

Whether the system is behaving classically or quantum mechanically, most research work (e.g. [50, 143, 156]) is in the linear enhancement regime, where $\ln \Gamma$ increases linearly with microwave power. In most cases, this occurs when the enhancement $\gamma \lesssim 10$.

### 4.1.7 Strong Microwave Driving

The discussions above assume that the microwaves leave the washboard potential itself effectively unperturbed. However, when the microwave source provides a strong signal to the junction, additional effects may appear. We must consider these effects for a proper understanding of the movement of both the primary and resonant peaks to lower currents as the microwave power is increased, an effect which is prominent in our processed data.

According to [142], "strong" microwave driving leads to an effective suppression of the potential barrier – a suppression which is especially strong at resonance (i.e. when the microwave frequency $\omega_{\mu w}$ equals the plasma frequency $\omega_p$).

This can become a strong effect when $\left(\omega_{\mu w}/\omega_0\right)^5 \gg \left(\hbar\omega_0\right)/E_{J0}$. For the junctions in this study,

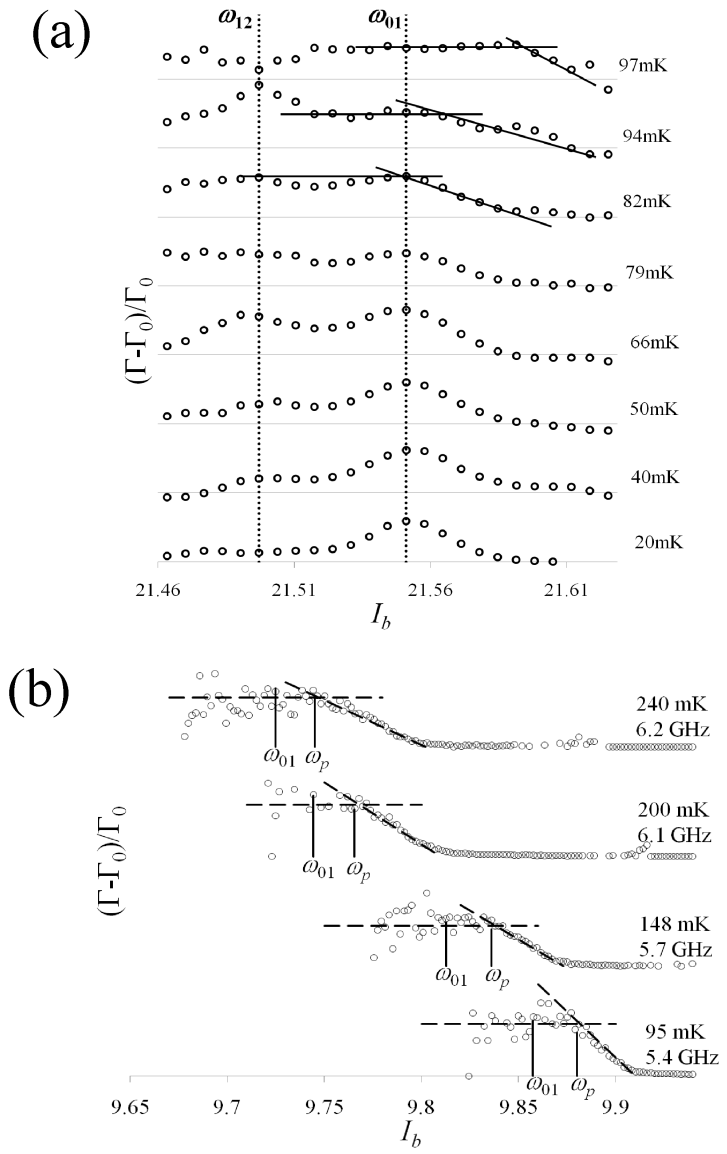


**Figure 4.8:** Quantum-mechanical and classical enhancement plots, using data from two Nb/AlOx/Nb junctions taken by our research group (excerpted from [12]). (a) Well below $T_{cr}$, a single Lorentzian peak appears at the current corresponding to $\omega_{01}$. As the temperature is increased, we observe an additional peak at $\omega_{12}$. At sufficiently high temperatures, the classical plateau appears. (b) Data taken on a second Nb/AlOx/Nb junction above its crossover temperature reveals the classical plateau at each of the temperatures shown. The intersection between this plateau and the sloped shoulder occurs at the current corresponding to the classical $\omega_p$. As the temperature increases, the histogram shifts to lower current (as discussed in Section 4.1.4), increasing the plasma frequency $\omega_p$ (Eq. 4.5) required to excite a resonance on the RF Off histogram.

this effect should be significant when $f_{\mu w}$ is much greater than hundreds of Hz. Because all of our measurements were at 0.5 GHz and above, we can anticipate this process to influence our results, especially as the amplitude of the microwave driving is increased.

The resulting modified washboard potential can be obtained by writing the phase difference coordinate $\gamma$ as a sum of two terms: a term $\gamma_0$ which varies slowly in time (due to the ramp in the bias current), and a quickly oscillating resonant term (associated with the microwave signal). Then, considering only the two energy levels $n$ and $m$ that resonantly interact, the potential becomes [142]

$U_{eff}\left(\gamma_0\right) = -E_{J0}\left[\frac{I_b}{I_0}\gamma_0 + cos\gamma_0\left(1 - P_{eff}\sum_{nm}\frac{f_{nm}^4}{(\hbar^{-1}E_{nm}(I)-\omega_{\mu w})^2+\alpha^2}\right)\right]$

where $P_{eff}$ is the effective microwave power reaching the junction, $f_{nm}$ are the matrix elements $\langle n|\hat{\gamma}|m\rangle$, and $\alpha$ is the damping parameter $\frac{\hbar\omega_0}{2eRI_0}$.

This is nothing more than the original washboard potential with an additional term suppressing the $cos\gamma_0$ term. This means that $U_{eff}$ will have no local minima at a current lower than the critical current. So, the effective critical current will be a function of microwave power. Therefore, there is a shift in the effective critical current

$$\delta I_{eff} \equiv \frac{I_0 - I_{eff}}{I_0} = P_{eff}\sum_{nm}\frac{f_{nm}^4}{\left(\hbar^{-1}E_{nm}\left(I\right)-\omega_{\mu w}\right)^2+\alpha^2} \tag{4.16}$$

To arrive at a solvable equation, they assume the $0 \rightarrow 1$ transition is the most important, and use the harmonic oscillator energy difference $E_{01} = \hbar\omega_0\left(2\delta I_{eff}\right)^{1/4}$. This leads to a transcendental equation which is multi-valued for some values of $\alpha$ and $P_{eff}$.

For the matrix elements $f_{nm}$, I used those for the cubic approximation [157]. Although this choice does not produce perfectly accurate results, it allows Equation 4.16 to be inverted, permitting an analytical solution. And although the results are not correct in detail, their qualitative features are largely correct.

Figure 4.9 shows the results. As expected, at too low a microwave power, the resonance cannot be excited. As the power is increased, two effects are observed: first, the primary peak gradually shifts to a lower current - in this model, as a result of the effective suppression in the barrier height. Then, over a certain range of microwave powers, both the primary and resonant peaks appear. This

reflects a microwave-induced bistability of the junction predicted by Equation 4.16. (The black portion of the curve in Figure 4.9 is unstable and not observed in experiments.) Eventually, only the resonant peak remains, which moves to progressively lower currents.

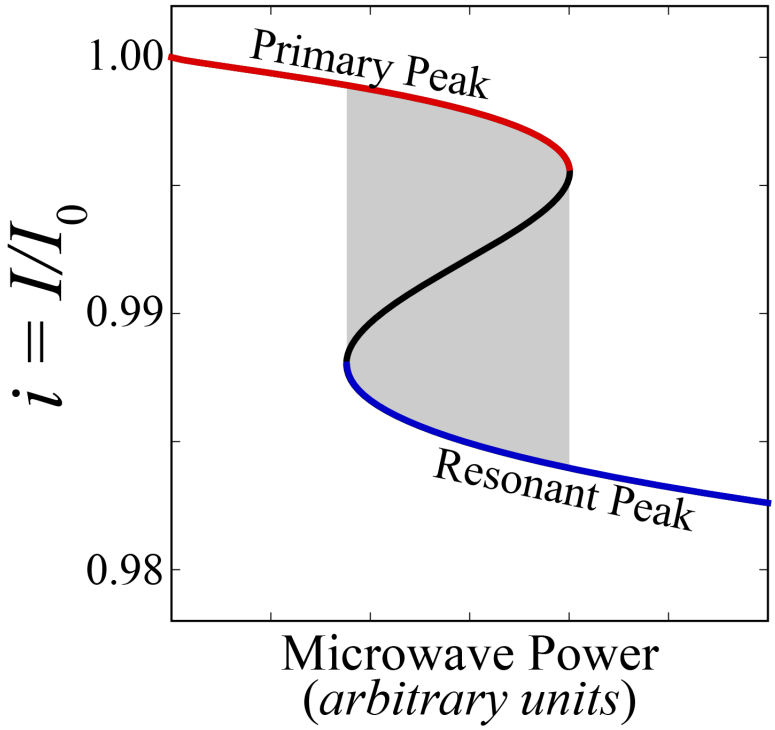


**Figure 4.9:** Dependence of the switching current on microwave power, according to Equation 4.16, assuming harmonic oscillator energy levels, and matrix elements in the cubic approximation. For the particular curve shown here, $\omega_{\mu w}/\omega_0 = 0.4$ and $\alpha/\omega_0 = 0.03$. At low power, only the primary peak (red) is observed; at high power, only the resonant peak (blue) appears. In a certain range of microwave powers (gray), we expect to observe both the primary and resonant histogram peaks in a switching current distribution.

Additional features of this model may be explored, including the effects of damping $\alpha$ and temperature, as discussed in [142]. However, the above analysis is sufficient for interpreting the results of our experiments.

For example, if I consider the series of histograms plotted in Figure 4.18, but include more powers, I produce the perspective plot shown in Figure 4.10. The progression of peak currents as the power is increased bears a strong similarity to the theoretical results of Figure 4.9.

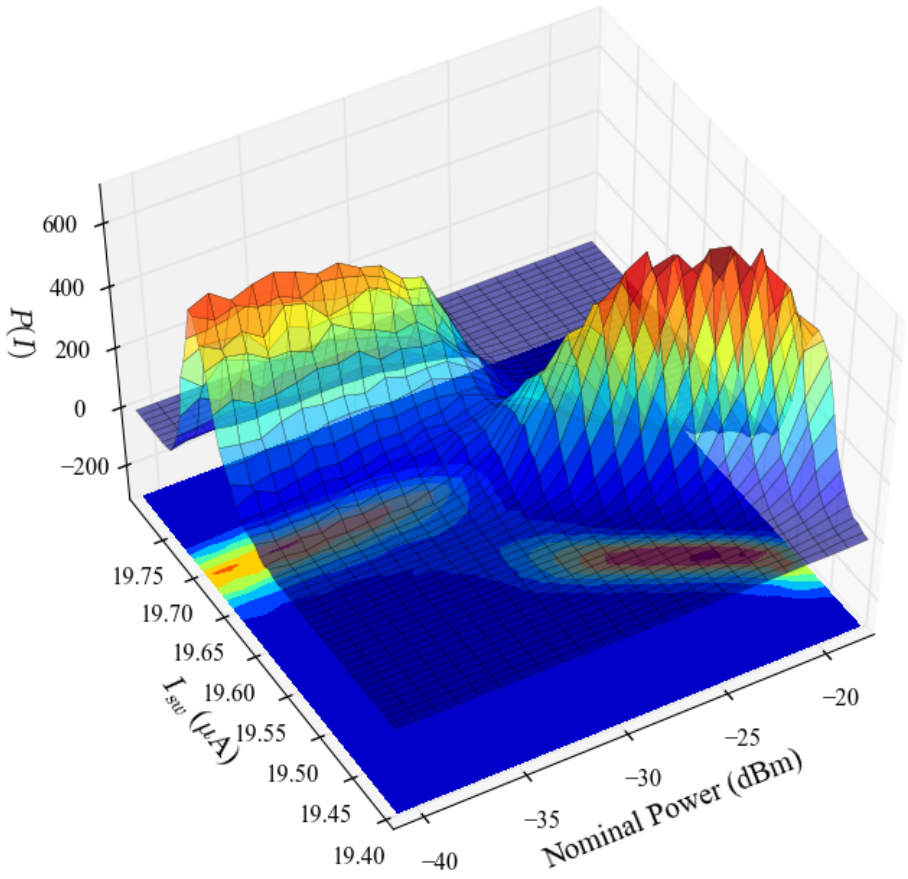


**Figure 4.10:** A progression of histograms with increasing microwave power. These data were taken on the $c$-axis $MgB_2$/I/Pb junction at $T = 23$ mK, when driven by microwaves at 1.35 GHz. Each probability $P(I)$ vs. switching current $I_{sw}$ histogram is acquired at a single power, forming a slice of the main perspective plot. Along the floor of this plot, the same data are plotted in analogy to Figure 4.9. Each histogram in this plot is computed from 5000 switching events. By applying a range of microwave powers, the transition from the primary to the resonant peak becomes apparent. The overlap in histograms, with both primary and resonant peaks, occurs over a relatively narrow range of powers – roughly -31 to -27 dBm. The Nominal Power is that at the microwave source; it is attenuated somewhat prior to reaching the junction.

### 4.1.8 "Multiphoton" Transitions

Several researchers [158, 159, 144, 160, 161, 162, 163, 155, 13, 164] have detected resonances in the switching behavior of Josephson junctions not only at $\omega_{\mu w} = \omega_p$, but also at $\frac{\omega_p}{n}$ $(n = 1, 2, 3...)$. These subharmonic resonances, commonly referred to as multiphoton transitions, have been explained using either classical or quantum mechanical arguments.

Considering only classical dynamics, a system with a non-parabolic (anharmonic) potential will undergo large-amplitude oscillations at both subharmonics and higher harmonics of its resonant frequency [156, 159, 162, 155, 164]. This is especially apparent when driving the system more strongly than required to observe the primary $n = 1$ resonance (Figure 4.12). Some classical subharmonics were observed in Josephson junctions in relatively early explorations of the Josephson plasma frequency [165, 166].

Quantum-mechanical transitions between energy levels by the simultaneous absorption of multiple photons is quantum mechanically allowed. These will also appear as resonances at fractions of the primary resonant frequency (Figure 4.11) when a system is under high-intensity coherent radiation [167]. This was first predicted in 1931 [168], but not observed in atomic systems until the advent of the laser in 1961 [169]. Their explanation requires the presence of a virtual state. There is no electron population within these virtual states, as each electron must receive $n$ photons effectively simultaneously to reach the higher energy level. They may be thought of as a superposition of stationary states with an extremely short lifetime (giving an energy between energy levels), or as a manifestation of Heisenberg's uncertainty principle (normally disallowed energies are allowed, for extremely short times).

The multiphoton fluorescence microscope [170] has made effective use of this technique, allowing, for example, specific transitions to be excited in organic systems that would suffer damage from the higher frequencies required to excite the transition directly. The widely-applied Raman scattering process also relies on the excitation of such virtual states, though these do not lead to multiphoton transitions.

Controversy remains as to whether any of the subharmonic resonances observed thus far in the

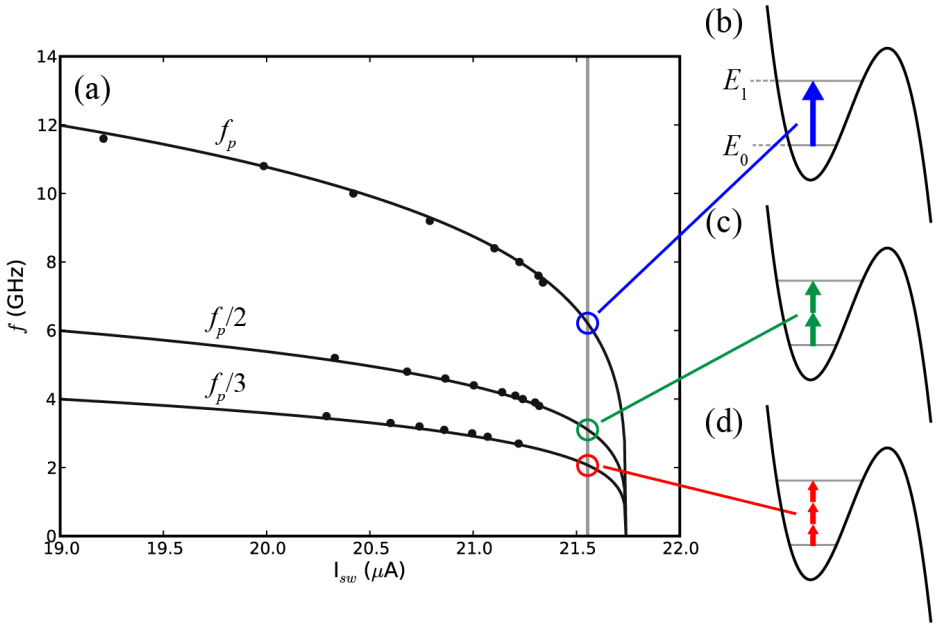


**Figure 4.11:** (a) Microwave driving frequency vs. resonant current for an Nb/AlOx/Nb reference junction. The dots represent resonances observed in our experiment; the curves are fits to these data according to Equation 4.5 and its subharmonics, with $I_0 = 21.74\,\mu$A and $C = 5.65$ pF. At a current somewhat higher than the maximum observed resonant current, only a single quantum state is available in the local minimum of the washboard potential. (b) A resonant escape may be observed when a single photon at the plasma frequency $f_p$ drives the phase particle from the ground state to the first excited state, thereby dramatically increasing the probability of tunneling. At sufficiently high powers, two photons each at $f_p/2$ (c), or three photons each at $f_p/3$ (d), may also excite the phase particle to this same level, similarly producing resonant escapes.

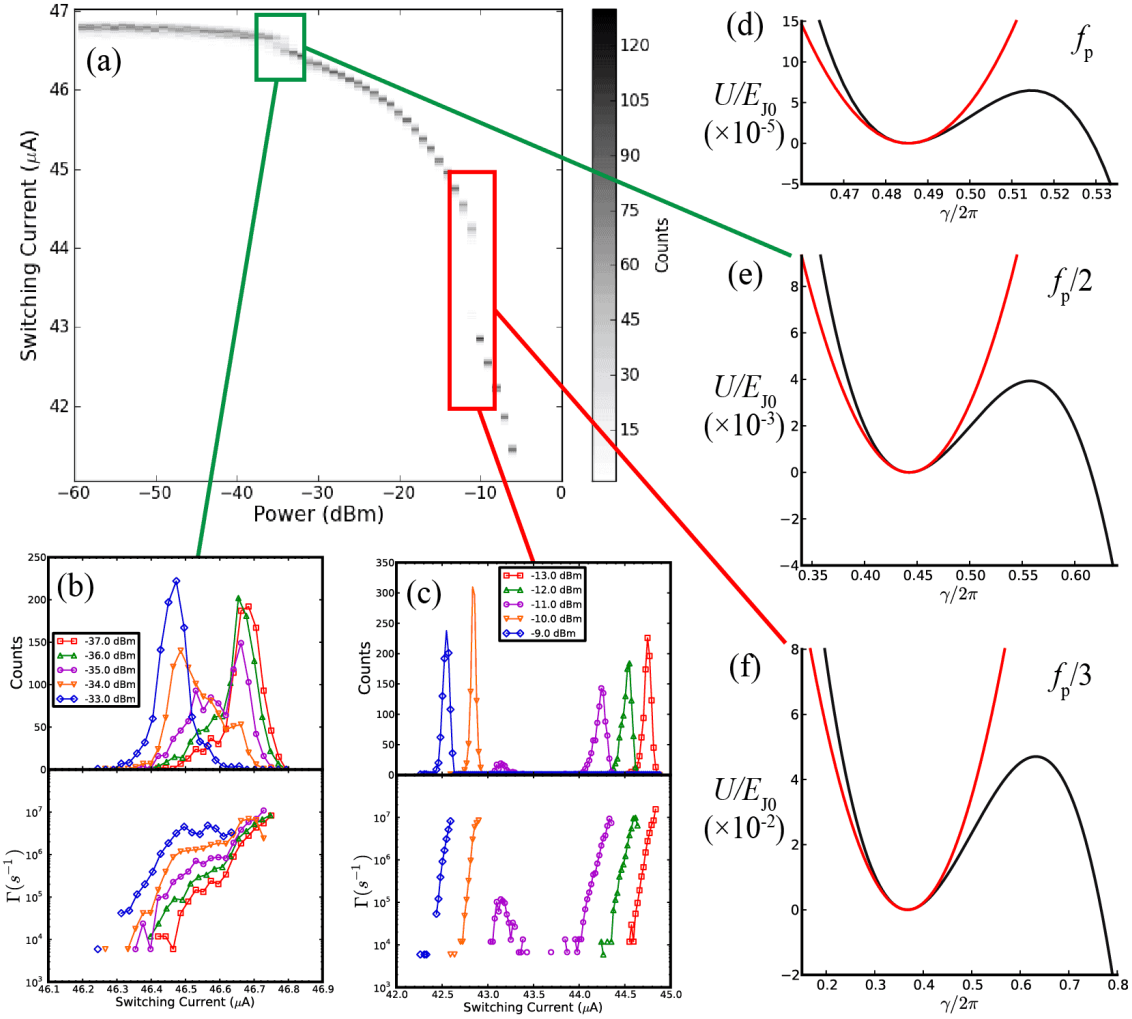


**Figure 4.12:** Resonances at subharmonics of the plasma frequency $f_p$ may also be explained classically. (a) Switching current vs. microwave power analogous to Figure 4.10 for an Nb/AlOx/Nb junction at 26 mK with $C = 5.8$ pF and $I_0 = 47.2\,\mu$A driven by microwaves at 5.30 GHz. (b, c) Histograms and escape rates near the threshold power for resonance at one-half (b) and one-third (c) the plasma frequency $f_p$. (d) The washboard potential (black) and equivalent harmonic potential (red), when the plasma frequency of the washboard is equal to the driving frequency. This resonance is not observed experimentally because the photon energy at the plasma frequency $\hbar\omega_p$ is greater than the barrier height $\Delta U$. (e, f) The washboard potential when the plasma frequency is one half or one third of the driving frequency, respectively (black), and harmonic potentials for one half or one third of the plasma frequency (red). These resonances at both $f_p/2$ and $f_p/3$ are observed in (a), at progressively higher powers. Note that (d - f) are plotted to dramatically different energy scales.

Josephson plasma frequency have been conclusively proven to be quantum-mechanical in nature [156]. Even so, they remain most commonly described as "multiphoton" processes in the literature.

Both quantum and classical theory suggest that these resonances should be observed at relatively high microwave powers. Therefore, many of the items discussed in Section 4.1.7 apply to any multiphoton results.

Observation of these subharmonic resonances is useful, whatever their nature. The equation defining these resonances is simply that for the plasma frequency (Eq. 4.5), divided by $n$: $\omega_{pn} = (\omega_0/n)\left[1-(I/I_0)^2\right]^{1/4}$. Therefore, several families of curves may be fitted by a single equation with only two parameters. Observing resonances along multiple curve families provides much more certainty in these parameters - the junction capacitance $C$ and the critical current $I_0$ - each of which is very useful in characterizing the junction.

### 4.1.9 Effect of Hybrid Junctions

There are no prior published results for switching experiments in hybrid single-gap/multi-gap junctions. There has also been little theoretical exploration.

Ota *et al.* [171] and Asai *et al.* [172, 173, 174] have explored quantum tunneling for such a hybrid junction, but without explicit attention to microwave signals, and considering only two potential processes. Each of these processes involves the coupling of the washboard potential with the Josephson-Leggett (JL) mode – an interband fluctuation which occurs in multi-gap superconductors.

The JL mode does not couple directly to electric fields, but does couple to the washboard [172]. It has been observed in Raman spectroscopy [83], with some suggestions coming from conductance measurements [175, 176].

The two effects explored by Ota *et al.*[171] and Asai *et al.*[172] have some tendency to cancel each other. The first leads to an effective suppression of the potential barrier $\Delta U$ (Figure 4.2), similar to a slight reduction in the critical current. The second allows the phase particle to dissipate energy to the JL mode, allowing the phase particle to remain trapped at higher currents, thereby increasing the critical current. According to their analysis, for most of the parameter space they explored, the suppression of the potential barrier is expected to be the stronger of these two effects.

However, as they note, the effects they explored are not the only ones of interest in such a system "because a system with two degrees of freedom generally has many tunneling routes"[171]. Their analyses also explore a parameter space for the JL mode, rather than the behavior of a single physical system. Therefore, it is useful to determine experimentally which routes are of importance in physical systems, and to better understand the JL mode.

## 4.2 Experiment Design

Superconducting-to-normal switching experiments follow a sequence outlined in Figure 4.13. First, begin with a Josephson junction in the zero-voltage state - i.e. with the phase particle "trapped" in a local minimum of the washboard potential. Then, steadily increase the current to somewhat above the critical current $I_0$, to guarantee an escape of the phase particle: a switch to the voltage state. Next, detect the current at which it actually switched $I_{sw}$. Finally, return the junction to the zero-voltage state, by reducing the current to zero. Repeat this cycle sufficiently often (typically $10^3 - 10^6$ times) to gather a statistically significant distribution of switching currents $I_{sw}$.

These distributions, and the relevant features within them, are often narrower than the uncertainties of many current measurement techniques (such as those used in Chapter 3). $\sim$10 nA resolution is often necessary. Switching measurements are also far more sensitive to noise, because the features of interest necessarily depend on the state of the junction at the instant of the switch: noise cannot be averaged out, as we were able to do with some of our current and conductance vs. voltage results. Therefore, the measurement and analysis techniques, and the equipment, are somewhat different from those in Chapter 3.

### 4.2.1 Apparatus

Figure 4.14 shows a block diagram for our superconducting-to-normal switching experiments.

The source of all of our recorded data is the Stanford Research SR620 Universal Time Interval Counter (the "timer"). With 25 ps time resolution [177], it is able to provide far more precise measurements than would be possible with the DAQ we used for current vs. voltage experiments. The time for each switching event is sent to the computer via an IEEE-488 (GPIB) connection.

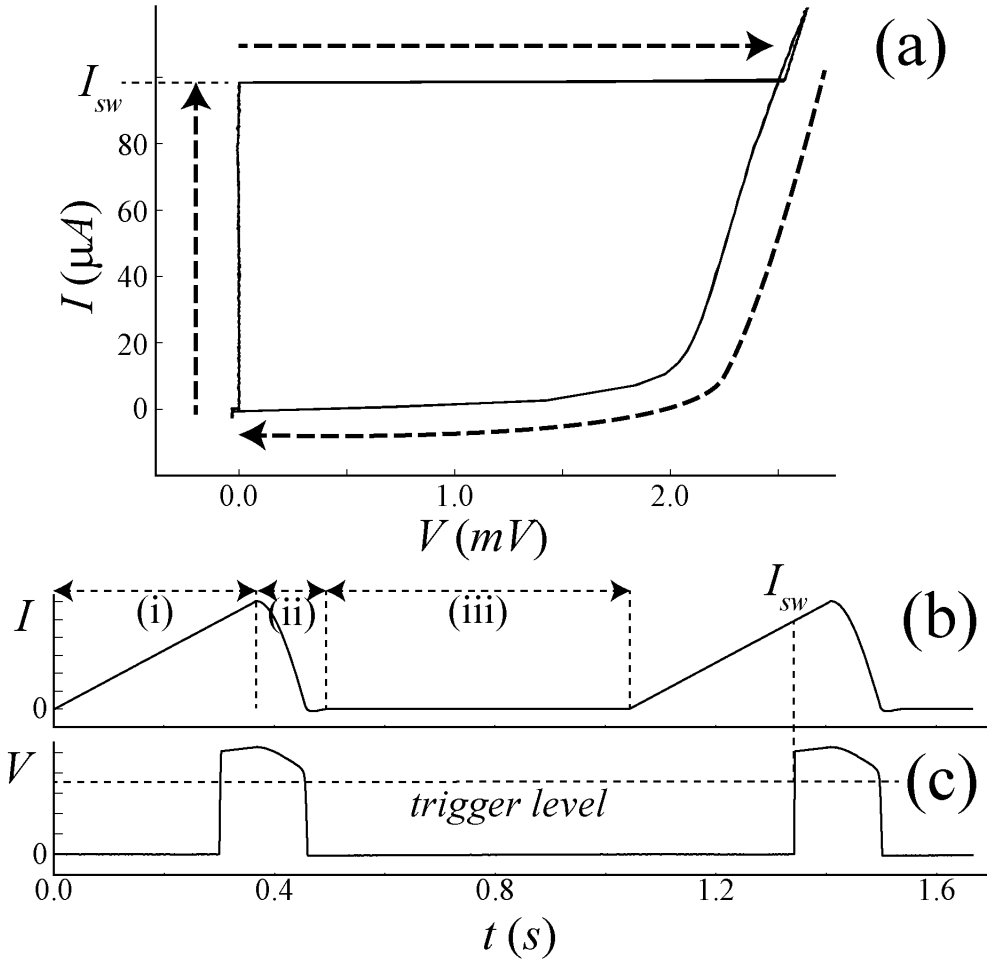


**Figure 4.13:** Measured current vs. voltage, current vs. time, and voltage vs. time for the $MgB_2$/I/Sn junction. (a) From the $I$-$V$ curve, the strongly hysteretic nature of the junction is clear. (b) The current ramp proceeds in three stages: (i) a linear increase from 0 through the critical current (ii) a smooth reduction to slightly negative values, to ensure retrapping of the phase particle (iii) the current remains zero, to allow the system to equilibrate. (c) The voltage across the junction suddenly jumps to a finite value at the switching current. This signals the timer to stop, allowing us to compute the switching current to high precision.

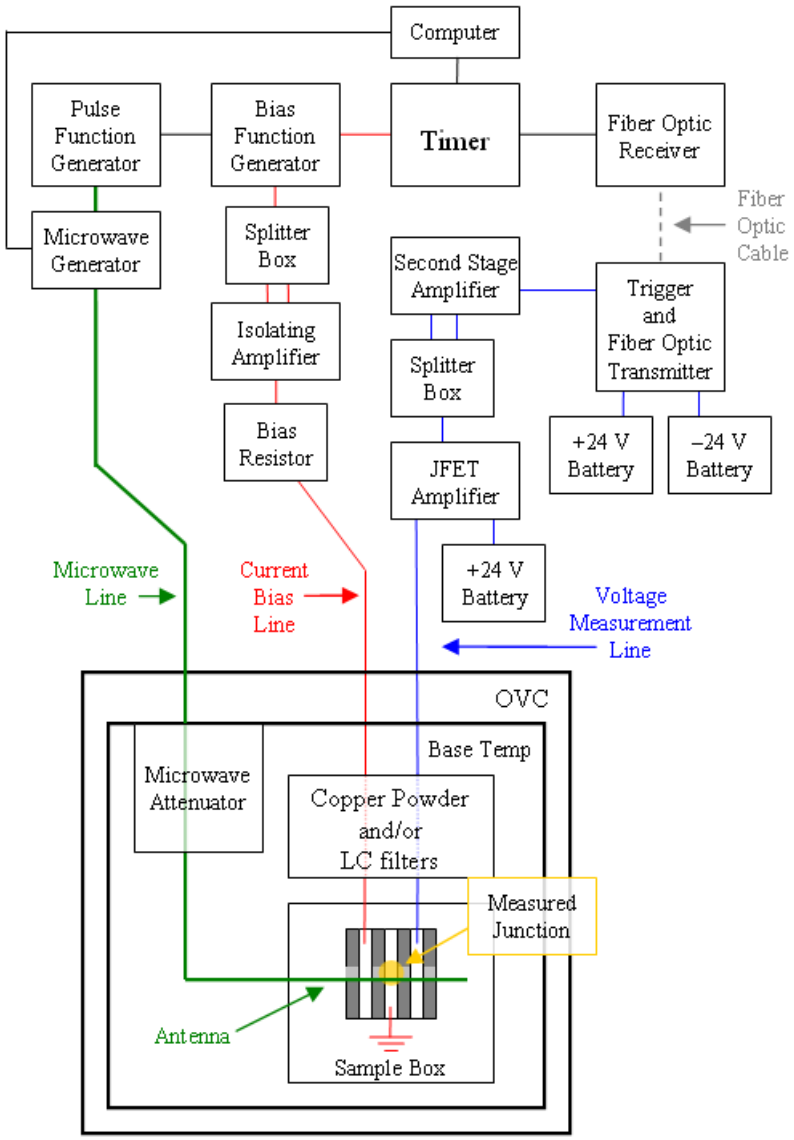


**Figure 4.14:** Block diagram for our superconducting-to-normal state switching measurements. The bias and pulse function generators are each Agilent 33220A function generators, just as used for the current and conductance vs. voltage experiments of Chapter 3. The voltage ramp (Fig. 4.13) is sent from the bias function generator through the same electronics as in Chapter 3, effectively acting as a current source. At the start of each ramp, a sync pulse is sent to the SR620 timer, initializing each time measurement. For those experiments requiring a microwave signal at the junction, a sync pulse is sent simultaneously to the "pulse function generator," which ensures that microwaves are transmitted only during the ramp, thereby reducing any unnecessary heat load. Each switching event is detected when the voltage across the junction passes a threshold. For additional stability and sensitivity, we use two stages of amplification: the four-JFET amplifier used in Chapter 3, and a battery-powered SR 560 voltage preamplifier (typically set $\times 50$). Its output is sent to a Schmitt trigger circuit, which sends a digital signal to a fiber optic transmitter/receiver. The fiber optic line eliminates the conducting path between current bias and voltage measurement sides of the experiment. The digital signal from the fiber optic receiver stops each timer measurement. This total time, times the known ramp rate $dI/dt$, is equal to the current at which the junction switched from the superconducting to the normal (resistive) state $I_{sw}$.

In order to record a time, it must receive a digital start and end pulse. At the start of each ramp, the bias function generator sends the start pulse to the timer. This voltage ramp, shown in Figure 4.13, is sent to the junction through the same equipment as the current vs. voltage experiments described in Section 3.2.1. Each full cycle of ramp/decrease/zero repeats at a frequency of 900 Hz.

The function remains at zero for roughly 2/3 of its cycle for two reasons. First, by remaining in the superconducting state most of the time, junction self-heating is minimized. Second, it provides the phase particle time to dissipate energy, allowing the junction to retrap to the superconducting state.

Our custom ramp function (Figure 4.13) gradually decreases to zero, rather than forming a step function to zero. We do this because a sharp endpoint can induce "ringing" from the filters on the current bias line, which will create a brief increase in the current going to the junction. This can cause the junction to switch even when the ramp itself never reaches the switching current. This can produce switching events that seem real, but do not reflect any true features of the junction behavior.

The ramp function also contains a small negative bias at the end of the ramp. This is because dissipation was very low for some of our $MgB_2$-based junctions. So, when using a ramp without a negative bias, the phase particle failed to retrap to the superconducting state several percent of the time. This made those events useless for our analysis. In the phase particle analogy, after reaching the voltage state, the phase particle gains significant momentum in the tilted washboard. After the current is reduced to zero, bringing the washboard back to horizontal, the phase particle has sufficient momentum to continue rolling for a time. Dissipation will bring it to rest ("retrap") in a local minimum, but this may take longer than the time before the next ramp. By forcing the phase particle to roll "uphill" briefly, even minimal damping allows the phase particle to retrap.

We end each timer cycle when the voltage across the junction switches from zero to near $V_g$. By recording the amplitude and frequency of the voltage ramp and the resistance of the circuit, we are able to compute the rate at which the current through the junction is changing $dI/dt$. Multiplying this rate by the time recorded by the timer allows us to translate the raw time data into the current

at which the junction switched to the voltage state.

The need to achieve a resolution on the order of 10 nA requires that we use more advanced detection electronics on the voltage measurement side.

The first stage of amplification is provided by the same JFET amplifier (powered by the same low-noise power supply) described in Section 2.3.2. Its slight nonlinearity in amplification is completely irrelevant in this case, as we only desire the time the junction switched to the voltage state. But, the DC offset in its output cannot simply be subtracted in the analysis (as we did in the current vs. voltage measurements). This voltage offset is incompatible with the following electronics. Therefore, we incorporated a passive high-pass RC filter within the project box with the JFET amplifier. This filter, made from a 10 $\mu$F capacitor and 2.4 M$\Omega$ resistor, has a cutoff frequency of roughly 0.007 Hz. Once the capacitor is charged, the average voltage output by the amplifier box remains zero, while the 900Hz ramp (and harmonics associated with the near-discontinuous switch) are essentially unaffected.

Its output is sent to a second stage amplifier. In our case, we used another battery-powered SR 560 voltage preamplifier, operating in differential mode. This is the same configuration of splitter box and amplifier as used in the current bias portion of our experiment, except that rather than being used simply for isolation (with an amplification $\times 1$), it also provides amplification (with an amplification typically $\times 50$). This additional isolation and amplification makes the trigger even less sensitive to stray noise signals injected by the cables leading from the three battery packs.

Because we only desire to know when the junction has switched from zero volts (superconducting) to a finite voltage (the normal state), it is logical to use a trigger circuit, which outputs an unambiguous digital pulse when its threshold has been reached. We constructed a Schmitt trigger circuit, following the same design as that in [120, 1]. Its output is fed to a fiber optic transmitter circuit within the same project box, again following the same designs as [120, 1]. These circuits require $\pm 15$ V and $\pm 5$ V inputs, which are provided by the low-noise power supplies described in Section 2.3.3. These are powered by two 24 V lead-acid battery packs (one for each polarity).

By using a fiber optic cable between the voltage amplification and the timer, we break the

**Table 4.1:** Properties of the microwave coaxial cable, reproduced from [1]. Values at 293 K came from the Lake Shore Cryogenics catalog; values at 4.2K were measured by A. J. Berkley [1]. As a result of this attenuation, the microwave source must provide higher power at higher frequencies, all other things being equal.

| Frequency (GHz) | Attenuation (dB/m at 293 K) | Attenuation (dB/m at 4.2 K) |
|---|---|---|
| 0.5 | 4.2 | - |
| 1.0 | 6.0 | 2 |
| 5.0 | 13.4 | 10 |
| 10.0 | 19.11 | 12.5 |
| 20.0 | 27.1 | 15 |

conductive path to the timer. This requires us to use an additional receiver circuit (again, described in [120, 1]). Since this is well-isolated from the junction and delivers large digital signals, it is powered by power supplies plugged directly to the wall.

For those experiments in which we want to observe microwave resonant activation, we must use several additional elements.

The microwaves themselves are supplied by an Agilent E8257D Signal Generator (the "microwave generator"), which is able to output signals from 10 MHz through 20 GHz, with a frequency resolution to 0.001Hz. Its output is sent via a coaxial cable to a connector at the top of the cryostat.

Within the cryostat, thin (∼0.5mm) coaxial cable connects the room-temperature connector to the sample box. Of course, we cannot use Thermocoax (as we use for the current bias and voltage measurement lines), because it has such strong attenuation at the frequencies of our desired signals. Instead, we use a semi-rigid cryogenic microwave coaxial cable with a stainless steel shield from Lake Shore Cryoelectronics Inc. While it does exhibit some attenuation at the frequencies we observe in our junctions, it is small enough to allow us to observe most of the resonances as long as we drive the signal at a higher power. The properties of this cable at 4.2 Kelvin have been explored in [1], and are reproduced in Table 4.1.

To prevent excessive heat from reaching the sample box, the inner conductor of the microwave cable must be thermalized. In Thermocoax, the insulating material between the inner conductor and shield conducts heat well enough that this does not require any additional measures. However, the microwave cable uses Teflon PTFE, which has a much lower thermal conductivity. We provide

thermal anchoring of the inner conductor using a microwave attenuator attached to the base plate below the mixing chamber, as shown in Figure 4.14. Its primary purpose is not to further attenuate the signal, but to provide a good thermal bridge in a simple commercially-available component. We gain an additional benefit by using attenuating lines and attenuator circuits: reflections due to impedance mismatches at any connector are reduced to a reasonable level [1] and do not affect our results.

Finally, the microwaves are capacitively coupled to the junction by an antenna. This is formed by a bare wire placed over the junction. A photograph of the sample box, with antenna, is shown in Figure 2.11.

The computer, via an ethernet connection, sets the frequency and power of the transmitted microwaves, and controls when the microwaves are turned on and off. The LabVIEW program performing this (and other data acquisition tasks) was written by Thilanka Galwaduge, an undergraduate student working in our group. Prior to this program, the microwave generator had to be controlled manually; without it, much of the data presented below would have taken impossibly long to gather.

Even with an ideal microwave source, using microwaves in an ultra-low temperature experiment can pose problems. Microwaves at sufficient power will heat the junction directly, and indirectly by heating the cold finger via dissipation in the attenuator. So, it is desirable to transmit microwaves for as short a duration as possible.

Heating effects are mitigated in part by acquiring data with RF on and RF off alternately. So, data sets used for the Results below are typically acquired by recording 1000 events with RF on, followed by 1000 events with RF off. Each on/off cycle lasts just over 2 seconds when ramping at 900Hz; this is repeated until the desired total number of switching events is acquired at that frequency and power.

We improve the ability of the system to equilibrate by leaving the microwaves on only during the linear ramp in current - i.e. the first third of our custom function (Figure 4.13). The computer is not connected to the bias function generator (doing so would introduce noise), so this is done

instead using a synchronization pulse from the bias function generator. At the start of each ramp, this pulse is sent to a second Agilent 33220A function generator (the "pulse function generator" in Figure 4.14), which sends a signal (using a second custom function) to the microwave generator, such that it transmits microwaves only during the first third of each cycle.

### 4.2.2 Keys for successful data

In $I - V$ data, fluctuations on the order of 10 $\mu$A are negligible; even significantly larger noise can be effectively wiped out by proper averaging. But here, the full histogram width is often on the order of 10 nA, and resonance peaks are even narrower. Therefore, a great deal of care is required in order for switching data to be useful.

**Grounding**

With far more connections, there are far more opportunities to create conflicting grounds or pickup loops. So, as shown in Figures 2.3 and 4.14, it was essential to use separate battery packs, and that the battery packs were well isolated; otherwise, they would form a large pickup loop that destroyed the ability to measure times to the desired resolution.

However, it was essential that the entire cryostat (and associated electronics) was not a floating ground. Otherwise, its capacitive coupling to the room (and those in it) produced unacceptable fluctuations. If this fact is not kept in mind, this source of noise can seem quite mysterious: for some time, I found that I had developed a very sensitive detector for people walking around the lab room. To resolve this issue, the cryostat must be grounded through one and only one wire.

Due to its expense and sensitivity, we chose to leave the microwave generator's ground pin directly connected to wall ground; all other grounds were established from there. So, we isolated the ground pins of the bias and pulse function generators, and the timer. The microwave generator also provided the ground connection for the cryostat. So, we left the microwave line connected, even when no microwaves were needed in the experiment.

**Voltage Drift**

After all grounding issues were resolved, there were two main sources of drift in the voltage observed by the Schmitt trigger, and therefore in the time at which the switch was recorded.

The first was due to the JFET amplifier discussed in Section 2.3.2. As indicated in Figures 2.6 and 2.9, the drain resistor $R_D$ used 4-band 5% resistors. These were chosen because they are capable of handling high power, for long durations. However, with even slight heating, their resistance changed by a few percent. This stabilized within roughly one minute of applying battery power to the amplifier, so with patience, this did not affect our results.

The second was due to the RC filter used to eliminate the voltage offset provided by the JFET amplifier's output. Its 24 second time constant ensured that the desired signals (at 900 Hz and above) remained stable. However, for the first experiment of the day, the capacitor needed to be charged. For sufficient stability, we waited several minutes between starting to charge the filter capacitor, and beginning to acquire data. Between subsequent runs, we used a switch to disconnect the filter capacitor, so that it would remain charged. So once again, with patience and care, this did not adversely affect our results.

## 4.3 Data Analysis

Acquiring usable data is a challenge of its own. But our interest is not in the switching times themselves, but for what they can tell us about the dynamics of the phase particle. As with the experiments of Chapter 3, some corrections must be made to the raw data. Then, we must know how to extract parameters accurately from the fits to the theory. The following sections outline this process.

### 4.3.1 Correcting Raw Switching Times

The actual switch of the junction to the voltage state is nearly discontinuous (on the order of picoseconds) [145]. However, this cannot be detected instantaneously in our experiments.

The difference in cable lengths between the start pulse to the timer, and the detection by the timer, is on the order of meters. Due to the speed of light, this produces a delay on the order of 10

ns. Other effects dominate - largely the rise time in the assorted filters and electronics. Rather than attempt to list and quantify all causes, I measured this lag using several methods.

First, I created a custom function for the bias function generator, with an output in the form of a square wave that simulates a switching event. This was sent through the entire block diagram of Figure 4.14, except that, in place of the junction, the bias and measurement lines were directly connected. When the amplitude of this signal was just barely sufficient to reach the Schmitt trigger threshold consistently, a total time lag of roughly 17 $\mu$s was observed. This rapidly decreased to $\sim 9\,\mu$s as the signal amplitude was increased. In fact, for most of the voltage range, the time delay between when the switch should have been detected, and when it actually was detected, was between 9 and 11 $\mu$s.

During one of the experiments using an $MgB_2$-based junction, I replaced the smooth ramp function of Figure 4.13 with one that immediately dropped to zero. Then, I reduced the amplitude to the point where the end of the ramp was in the middle of the switching current distribution. This sudden drop was very clear in the observed histogram. With the system thus configured, there was a roughly 17 $\mu$s delay between the end of the current ramp and the time this appeared on the timer. Since this matched the maximum time for the test described above, I concluded that this delay could be no more than 17 $\mu$s, with 9 to 11 $\mu$s being far more likely. So, all of the following analysis assumes a 10 $\mu$s delay between the actual switching event and its detection.

An error in estimating this delay would not produce any scatter or broadening in the histograms displayed below. Instead, the current axis would be offset by less than 2%. This is unlikely to affect any of the conclusions discussed below.

There was one effect of this somewhat uncertain offset that I observed during the analysis. Due to the rise time in the assorted filters and electronics, the trigger circuit experienced a gradual rise in voltage, rather than a discontinuous jump. Anything that would cause the entire output voltage curve to rise to a higher voltage would put the fixed trigger threshold voltage earlier on the rise; shifting the voltage down would cause the trigger threshold to be reached later. The RC filter on the output of the JFET amplifier can produce exactly this effect.

The filter capacitor will charge to the point where the voltage across the capacitor will be equal to the mean voltage over several time constants. This mean voltage does not correspond to zero volts across the junction. The voltage across the junction must remain zero during the roughly 2/3 of the cycle that the bias current is zero, and for the entire portion of the current ramp before it switches to the voltage state. After switching, the voltage remains near the gap voltage $V_g$ until the junction retraps. Since this is typically around 10% of the cycle, the "zero" of the filter is typically around 0.1 $V_g$.

Anything that causes the junction to switch at a lower current will cause the mean voltage across the junction over a full cycle to be higher. This causes the filter to pull the entire voltage vs. time curve to a lower center than it otherwise would have been. This in turn causes the switch to be detected later, which makes the current appear higher.

Each of the effects we seek to study - microwave resonant activation, and the effects of temperature as temperature increases - causes the junction to switch at lower currents. As a result, we expect the detected currents for microwave resonant activation experiments to be increasingly higher than they should be, for increasingly early switches; and we expect the current distributions in thermal activation experiments to be increasingly high, for increasing temperatures. Rather than attempt to estimate a different time lag for each experiment, I assumed a 10 $\mu$s delay in all the analysis.

As noted above, this effect should offset the current axis by less than 2% – much less, when the switch is only a little earlier. This is negligible on the scale of the frequency vs. switching current graphs that form the key results from the microwave resonant activation experiments.

However, fits to the escape rate using Equation 4.12 are sensitive to shifts in the critical current of this order. In fact, when fitting the escape rate for the $c$-axis $MgB_2$/I/Pb junction (in Section 4.4.4, the critical current at $\sim 0.5 - 1$ K was roughly 0.6% higher than that at low temperature ($\sim 0.02 - 0.2$ K), even though the critical current was expected to remain effectively constant.

Even so, this did not compromise our results. Such a small shift in critical current would not change the escape temperature $T_{esc}$ significantly. Instead, it meant that I could not constrain the

critical current $I_0$ as tightly as would have been possible otherwise, when fitting the escape rate. This led to a larger uncertainty in the junction resistance and in the escape temperature than may have otherwise been possible.

The extreme simplicity of this RC circuit, and the certainty in its behavior over a wide range of experiments, more than makes up for the relatively slight increase in the uncertainties of these parameters.

### 4.3.2 Determining the Resonant Current

Among the most useful results in a microwave resonant activation experiment is a plot of microwave frequency vs. resonant current, as it allows for comparison with Equation 4.5 (and its subharmonics). This requires the resonance to be associated with a single value of the current, for each frequency.

When observing switching events, the resonant histogram peak is sensitive to the microwave power; so, care must be taken when determining the current associated with it. In general, a single pair of histograms (one with and one without microwaves) is insufficient to determine this current with any confidence: at too low a microwave power, the resonant peak may not include enough events to produce a reliable histogram. At too high a power, the resonant peak will have shifted to a lower current, as discussed in Section 4.1.7.

As mentioned in Section 4.1.5, there are several alternative methods for determining the resonant current $I_r$.

- **Dual Histograms**

  Several sources [158, 162] define $I_r$ as the most probable current within the resonant peak, when the resonant peak is the same height as the primary peak. This method works well when the resonant peak is well-separated from the primary peak, when data are taken at fine power increments so that the proper power is known, and when the primary and resonant peaks are shifting relatively slowly with microwave power (see Section 4.1.7).

  For a system with multiple resonant modes, as in our hybrid junctions, we expect to observe multiple peaks at any given frequency. In many cases, the primary peak is greatly dimin-

ished or even entirely absent at powers below that at which one or more of these resonances appear. Additionally, in some cases the resolution in power was not fine enough to capture the power at which the two peaks were the same height: there is simply not enough time to maximize the resolution in all dimensions. In this case, we can achieve very reasonable results by interpolating between powers, though the following method was usually superior.

- **Escape Rate Peak**

  As indicated in Figures 4.18 and 4.10, the histogram peak moves to lower currents as the power increases. Therefore, the prior method fails if there is uncertainty in the power at which histogram heights are equal, or if that precise power was skipped while sweeping through powers during the experiment.

  Therefore, some sources [155] define $I_r$ as the current of a local maximum in the escape rate. This local maximum is much less sensitive to the applied microwave power, as shown in Figure 4.18. Within uncertainties, this gives the same result as the method described above.

  This method works best when the resonant peak is at least somewhat separated from the primary peak. I chose this method for a majority of resonant currents $I_r$ used in Section 4.4 because it is less sensitive to the microwave power chosen for a particular double-peaked histogram.

- **Enhancement**

  When resonances occur at currents very close to the mean switching current in the absence of microwaves, neither of the prior methods give satisfactory results.

  Therefore, we use the escape rate enhancement, as described in Section 4.1.6. When the system is in the quantum limit, the enhancement exhibits a Lorentzian shape; its center may be chosen as $I_r$. This resonance is expected to appear at a current corresponding to $\omega_{01}$. In the classical limit, $I_r$ is chosen at the intersection between the plateau at lower currents, and the shoulder near the resonant current. (See Figure 4.8.)

  Because this method is only possible when the resonant peak is at a current overlapping a

statistically significant number of events in the RF Off histogram, relatively few of my data sets required the use of the enhancement. They proved useful, however, in confirming the results of other fitted curves, and narrowing the parameter space for other fits.

Whether the switching behavior is classical or quantum-mechanical, these resonant peaks are commonly tracked on a plot of frequency vs. current. That is, a series of histograms is assembled from data when microwaves of a single frequency are applied (Figures 4.18 and 4.10). Once the primary and resonant currents are determined for that frequency, the microwave generator is set to a new frequency, and the experiment is repeated. Observing these points for a large number of frequencies provides compelling evidence that the resonances are due to the behavior of the phase particle in the washboard potential, rather than some spurious resonance related to the dimensions of the sample box, resonances with the electrical filtering, etc.

### 4.3.3 Extracting Junction Parameters

In order to determine whether or not a Josephson junction is useful for many applications, including as a quantum bit, it is essential to establish its critical current $I_0$, resistance $R$, and capacitance $C$, which allow us to determine $Q_0$ and $Q(I)$. We must know these values more precisely than is possible with measurements of current vs. voltage ($I-V$ curves). Additionally, because these applications often require the use of microwave excitations, the key figures of merit must be known at these $\sim$ GHz frequencies, rather than near DC (as would be found from $I-V$ curves). This section describes how I arrived at these values, from switching measurements.

**Fitting the Escape Rate**

Equation 4.12, for the thermal escape of a particle from our potential well, contains within its terms references to all of the values we seek to establish: $I_0$, $R$, and $C$. In addition, it also contains the escape temperature, which is useful in establishing whether the phase particle is behaving classically or quantum-mechanically. Therefore, one might expect to extract all of these values from a single measurement. However, the reality is much different.

Figure 4.15 shows the effect of changing each of these parameters, while holding the others

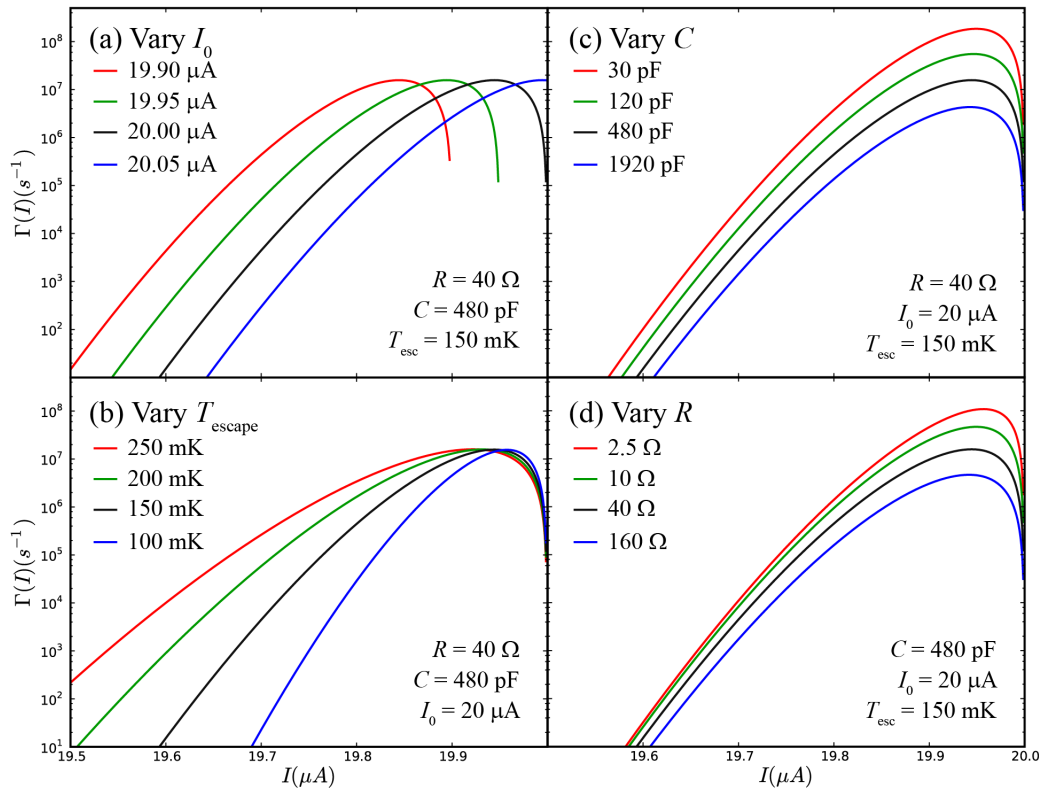


**Figure 4.15:** The effect of adjusting independently each of the four parameters of Equation 4.12: the critical current $I_0$, escape temperature $T_{esc}$, capacitance $C$, and resistance $R$. Note that in an experiment, only a limited range of escape rates is experimentally accessible; for these parameters, $\sim 10^4$ through $\sim 10^6$ is typical. (a) Varying $I_0$ (while keeping $T_{esc}$, $C$, and $R$ constant) mainly shifts the entire curve left or right, to higher or lower currents. There is also a very slight change in slope, barely detectable at this scale. (b) Varying only $T_{esc}$ produces a substantial change in slope of the escape rate vs. current, while also shifting the center of the experimentally-accessible portion of the curve to higher or lower currents. (c) Varying only $C$ mainly serves to raise or lower the entire escape rate curve, though there is also some change in slope. (d) Varying only $R$ has an effect similar to changing $C$, although the effects become somewhat less at very low $R$. The black curve in each of (a) through (d) uses the same parameters.

constant. From (c) and (d), it is clear that changes in $C$ and $R$ are largely interchangeable. Therefore, without a fairly well-constrained value of $C$, it is impossible to arrive at an independent value of $R$ (or vice versa).

When considering the others, it is important to recognize that, during any experiment, only a portion of the escape rate curve is effectively sampled. Depending on the junction parameters, the current ramp rate, and the number of events recorded, only the portion from $\Gamma \sim 10^4$ through $\sim 10^6$ may give statistically significant results. With few switching events recorded, this range will be smaller; for very high statistics, this range may be larger.

This portion will often be nearly linear, though at least some curvature is usually apparent.

If one arrives at a good fit to the escape rate, an equally good fit can usually be achieved by substantially increasing the critical current, substantially decreasing $R$ and/or $C$, and fine-tuning $T_{esc}$ as necessary. Other combinations are also possible. Figure 4.16 shows one such set of theoretical curves that would be extremely difficult to distinguish experimentally. For this figure, I held the capacitance constant in each case. It is remarkable that experimentally-indistinguishable simulated data can produce high-quality fits for $T_{esc}$ from 0.62 to 1.20 K, $I_0$ from 19.61 to 20.2 $\mu$A (a range nearly three times the FWHM of the histogram itself), and $R$ from 0.39 to 440 $\Omega$ (a range of over 3 orders of magnitude).

Fortunately, microwave resonant activation provides us with a method for constraining $I_0$ and $C$. And, we do not gather switching histograms and escape rates in the absence of microwaves (as shown for Figures 4.15 and 4.16) at only a single temperature.

With reasonably well-constrained values for $I_0$ and $C$, $R$ may be constrained as follows. At very low temperature, I determine the maximum resistance by increasing the fit resistance until the peak in the escape rate is below the maximum found in the data. I determine the minimum resistance using escape rate plots at higher temperatures. Using too low a resistance causes the fit to be appreciably flatter than the experimental curve. By checking the fits for consistency over the entire temperature range over which data was gathered, I gain confidence in these limits.

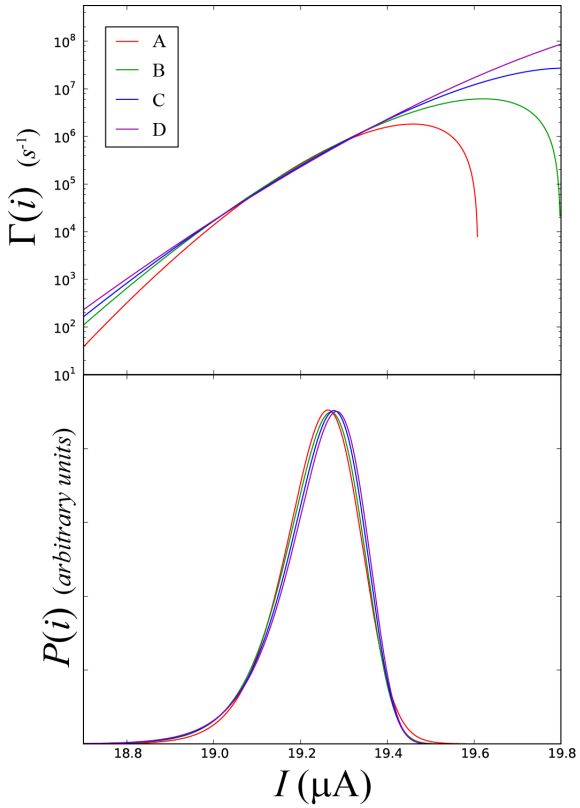


**Figure 4.16:** Theoretical histograms (bottom) and escape rates (top), for four very different sets of parameters, using Equations 4.12 and 4.9. At a particular ramp rate (0.053 A/s in this case), only a portion of the escape rate curve is sampled by the statistically-significant portion of the histogram. As a result, widely varying parameters can match an experimental histogram and escape rate curve extremely well. For all curves above, the capacitance $C = 480$ pF. For curve A, the remaining fit parameters are $R = 440\Omega$, $I_0 = 19.61\mu$ A, and $T_{escape} = 0.62$ K. For curve B, $R = 120\Omega$, $I_0 = 19.8\mu$ A, and $T_{escape} = 0.82$ K. For curve C, $R = 22\Omega$, $I_0 = 20.0\mu$ A, and $T_{escape} = 1.00$ K. For curve D, $R = 0.39\Omega$, $I_0 = 20.2\mu$ A, and $T_{escape} = 1.20$ K.

**Fitting Frequency vs. Current**

As noted in section 4.1.8, Equation 4.5 (and its subharmonics) contains only two parameters: $I_0$ and $C$.

Figure 4.17 shows the effect of varying $I_0$ and $C$ on the theoretical current-dependent plasma frequency $f_p(I)$, and its subharmonics. With a series of data points on such a family of curves, even a moderate sample of points is able to constrain $I_0$ and $C$ very well.

With $I_0$ and $C$ constrained, the fits to the escape rate shown above may provide reasonable estimates of $R$ and $T_{esc}$.

**Fitting the Enhancement**

Due to the difficulties in fitting the escape rate, it is useful to have an independent method of determining $R$. As discussed in Section 4.1.6, the enhancement of the escape rate under microwave excitation provides just such a technique.

A lower bound, or conservative estimate for $Q$ may be found using

$$Q(I) = \left\{ 2 \left[ 1 - (I/I_0)^2 \right] / (I/I_0) \right\} (I_0/\Delta I_{\rm res}) \tag{4.17}$$

where $\Delta I_{\rm res}$ is half of the FWHM of the enhancement peak [143].

From this, it is easy to extract a lower limit on $Q(0)$ and $RC$. With $C$ well-established from the frequency vs. current fit, this provides a lower limit on the resistance $R$. This can then be checked for consistency with the lower bound to the resistance from the thermal fits to the escape rate.

## 4.4 Results

Using switching experiments, I was able to characterize both the $c$-axis $MgB_2$/I/Pb and "terraced" $MgB_2$/I/Sn junctions discussed in the previous chapters. I established their parameters to a reasonable precision at these high (GHz) frequencies. Our results show that these junctions have a high quality factor $Q_0$, thereby making them potentially suitable for quantum device applications. Several independent measurements gave consistent results. Table 4.2 summarizes these results.

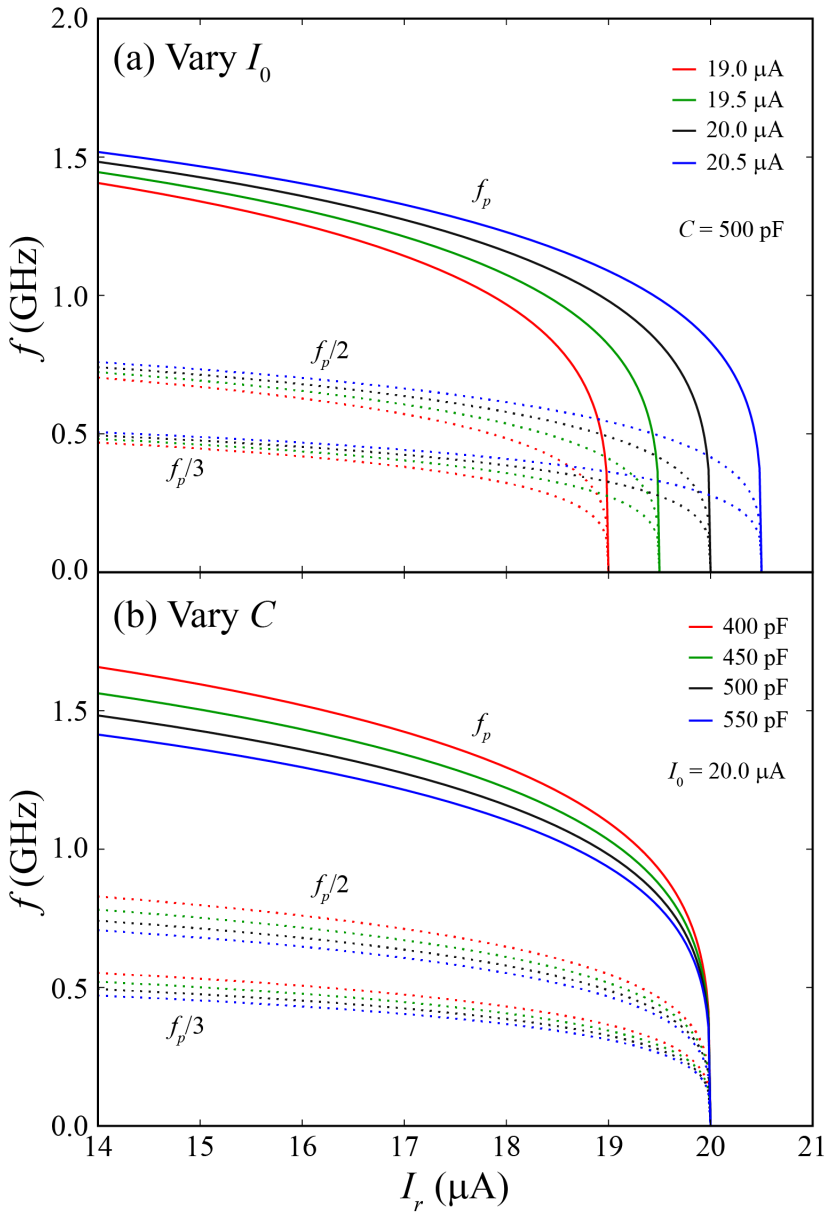


**Figure 4.17:** Theoretical 1-, 2-, and 3-photon curves for applied microwave frequency vs. resonant current, for parameters similar to those for the $c$-axis $MgB_2$/I/Pb junction. (a) Varying $I_0$ (while keeping $C$ constant) mainly shifts the entire curve left or right, to higher or lower currents. (b) Varying $C$ (while keeping $I_0$ constant) produces a change in the slope of each curve. Because there are only two parameters, each producing different effects on the curve, they may both be determined with high accuracy from experimental results. The black curves in each figure use the same parameters.

**Table 4.2:** Characteristics of the Josephson junctions analyzed below. $I_0$ and $C$ were determined from fits to the $f$ vs. $I$ curves (Figures 4.20 and 4.21). From these, $f_0 = \omega_0/2\pi$ was calculated according to Equation 4.5. $R$ was determined from fits to the escape rate at several temperatures, using Equation 4.12 (Figure 4.27). $Q_0$ is found via $\omega_0 RC$. A junction with $Q_0 \gtrsim 10$ is generally considered a "high Q" junction and potentially suitable for quantum device applications.

| Junction | $I_0$ ($\mu$A) | $R$ ($\Omega$) | $C$ (pF) | $f_0$ (GHz) | $Q_0$ |
|---|---|---|---|---|---|
| $c$-axis $MgB_2$/I/Pb | 19.93±0.04 | 46±24 | 478.6±18.6 | 1.790±0.038 | 250±140 |
| "terraced" $MgB_2$/I/Sn | 106.78±0.05 | 9±4 | 1523±14 | 2.323±0.011 | 200±90 |

### 4.4.1 Microwave Resonant Activation

To determine the characteristics of these junctions, I first turn to microwave resonant activation.

Figure 4.18 shows typical histograms and escape rates vs. current, for resonances observed at high fractions of the critical current.

All curves in Figure 4.18 were acquired near base temperature: 22.1 mK for (a), (b), and 22.7mK for (c), (d).

At low power, only the primary peak is visible. As the microwave power increases, the resonant peak grows until it dominates the histogram. The resonant current $I_r$ is chosen as the current of the resonant peak when both the primary and resonant peaks are the same height. The current of the resonant histogram peak decreases rapidly as microwave power increases; the local maximum in the escape rate is far less sensitive to changes in microwave power. Therefore, for all double-peaked histograms, we chose the local maximum in escape rate as the resonant current.

Uncertainties in this resonant current had three main sources: 1. the slight difference between the positions of the equal-height histogram peak and the escape rate peak; 2. difficulty in determining the local maximum in escape rate when using data sets with relatively low statistics (1000 - 3000 events); and 3. difficulty in defining the resonant current when the transition occurred over a smaller power increment than was acquired in the data sets (so that two peaks were never observed together at a single power).

At some frequencies, only a single resonance is observed at a current close to $I_0$, as in Figures 4.18

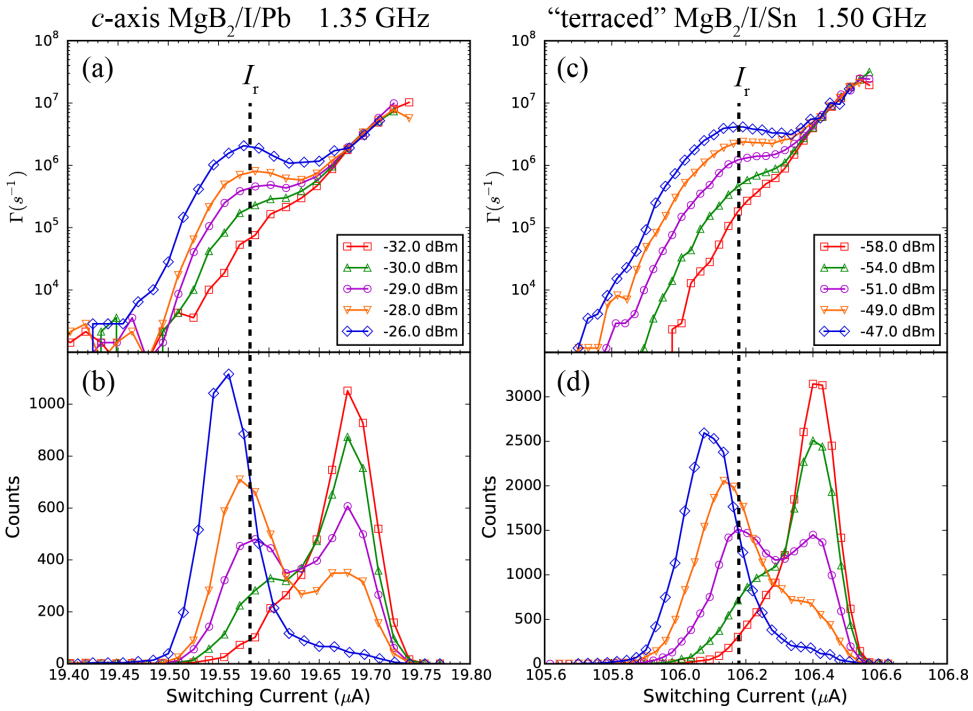


**Figure 4.18:** Escape rates and histograms of counts vs. current at powers near the critical power for resonance, for the $c$-axis $MgB_2$/I/Pb (a), (b) and "terraced" $MgB_2$/I/Sn (c), (d) junctions, respectively. At low power, only the primary peak is visible. As the microwave power increases, the resonant peak grows, until it dominates the histogram. The resonant current $I_r$ is chosen as the current of the resonant peak, when both the primary and resonant peaks are the same height. The current of the resonant histogram peak decreases rapidly as microwave power increases; the local maximum in the escape rate is far less sensitive to changes in microwave power. Therefore, for all double-peaked histograms, we used the local maximum in escape rate as the resonant current.

and 4.10. At other frequencies, more resonances were observed. One of those that is particularly feature-rich is shown in Figure 4.19. It shows the switching current vs. nominal power, as in Figures 4.10 and 4.12. It is derived from plots similar to Figure 4.18; this format allows useful features to be seen over a wider range of currents and powers. In addition to the primary peak (at $\sim$106 $\mu$A), four "families" of resonant peaks are visible.

Curve (1) indicates a single-photon resonance much farther from the primary peak than Figures 4.18 and 4.10. It falls very nicely along the predicted curve for a single-photon resonance, as indicated in Figures 4.7, 4.20 and 4.21. $I_r$ may be established both by considering the peak current when the resonant peak is the same height as the primary peak, and by finding a local maximum in the escape rate.

Curve (2) has a similar curvature, and occurs closer to the primary peak. In fact, if the plot were restricted to the region close to the primary peak, this would appear very similar to $n$-photon resonances. However, when considering resonances at $f_p/n$, higher-$n$ resonances always appear at higher powers and lower currents than lower-$n$ resonances. Because multiple different peaks appear at this power, I found $I_r$ from the local maximum in the escape rate.

Curves (3) also do not correspond to a resonance predicted by Equation 4.5 or its harmonics. They have several additional distinguishing features from these predicted resonances. First, they vary with power in a different way: the higher-current resonance (3a) is very insensitive to changes in power; (3b) decreases linearly with increases in power, in contrast with the curvature of $n$-photon resonances of type (1) and the predictions discussed in Section 4.1.7. Second, the histograms associated with these resonances have far narrower current widths. Finally, they are usually observed together, appearing at the same frequency, with similar threshold powers. I again found $I_r$ from the local maximum in the escape rate; however, given their properties, I could have used the histogram peaks at the powers they first appeared.

Curves (4) are difficult to associate with a particular resonant current. Resonances at $f_p/n$ are relatively insensitive to power at the powers at which they are first excited. And, they produce a histogram peak only at the resonant current. The resonances associated with curves (4) are extremely

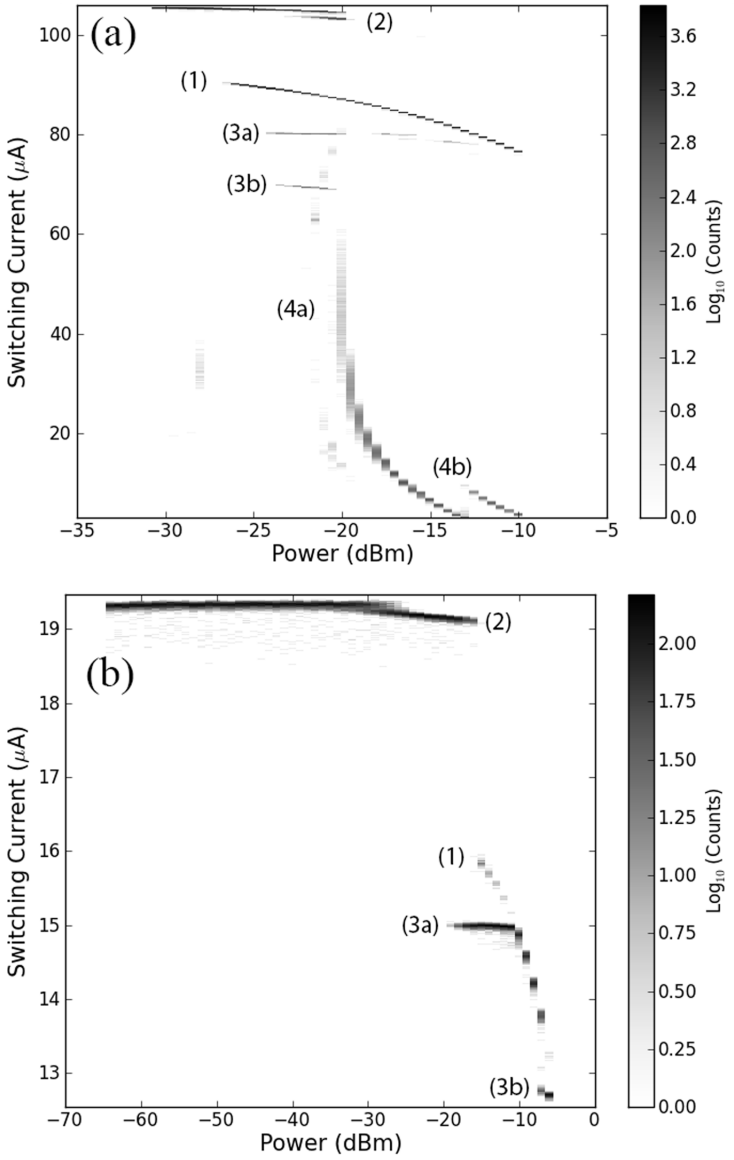


**Figure 4.19:** Switching current vs. power (a) for the "terraced" $MgB_2$/I/Sn junction at 23 mK, when excited by microwaves at 1.70 GHz and (b) for the $c$-axis $MgB_2$/I/Pb junction at 22 mK, when excited by microwaves at 1.35 GHz. The counts are on a log scale to make features with relatively small statistics more apparent. The highest-current feature (at $\sim$106 $\mu$A in (a) and $\sim$19.3 $\mu$A in (b)) is the primary peak. Four "families" of resonant peaks are visible. (1) A typical single-photon resonance. Multi-photon resonances are similarly curved on this type of plot. (2) A resonance for which the resonant current does not match Equation 4.5 or its harmonics. It is distinguished by appearing at a lower current than the lower $n$-resonance (for equal $f$) or higher power than the lower $n$-resonance (for equal $I$). (3) Two further resonances not predicted by Equation 4.5 or its harmonics. (4) Additional resonant peaks, where the resonant current $I_r$ is difficult to determine. These do not appear in (b) at this frequency, though similar features appear at other frequencies for the $c$-axis $MgB_2$/I/Pb junction.

sensitive to power, and produce a peak in the escape rate at every power. They are reminiscent of the predictions of Figure 4.9, highly detuned from the resonance, and at a substantially higher damping parameter $\alpha$. When they appear on Figures 4.20 and 4.21, they are typically at very low currents.

An additional aspect of these curves may be noted on this figure. The resonances at $f_p/n$ (such as curve (1)) are largely unaffected by the presence of the other curve families. However, the emergence of curves (4) changes the populations in curves (2) and (3) substantially. Similar correlations were observed for both the $c$-axis $MgB_2$/I/Pb and "terraced" $MgB_2$/I/Sn junctions over a range of frequencies and temperatures.

Resonances of types (1) and (2) appear as large circles in Figures 4.20 and 4.21. Resonances of types (3) and (4), and any others that are uncertain for some reason, are plotted as small circles.

In the following section, I use type (1) to establish the junction critical current and capacitance. I discuss types (2), (3) and (4) in Section 4.5.1.

### 4.4.2 "Multiphoton" Transitions

Figures 4.20 and 4.21 show the switching current and nominal power of each resonance observed for our measurements at different frequencies.

For each junction, the most prominent curve is that at the plasma frequency $f_p$. Fitting these points alone provides an excellent measure of the junction capacitance $C$ and critical current $I_0$. Our observation of additional curves, at both higher harmonics and subharmonics of the plasma frequency, strengthens confidence in these fits considerably.

From these fits, I find $I_0 = 106.78 \pm 0.05$ $\mu$A and $C = 1523 \pm 14$ pF for the "terraced" $MgB_2$/I/Sn junction. For the $c$-axis $MgB_2$/I/Pb junction, $I_0 = 19.93 \pm 0.04$ $\mu$A and $C = 478.6 \pm 18.6$ pF.

The data points falling on the plasma frequency and its harmonics bear substantial similarities to those reported in the literature. However, they also have some important differences, due in part to the unusually high capacitance of the junctions we tested.

Putting the barrier height of the washboard potential in terms of the harmonic oscillator energy

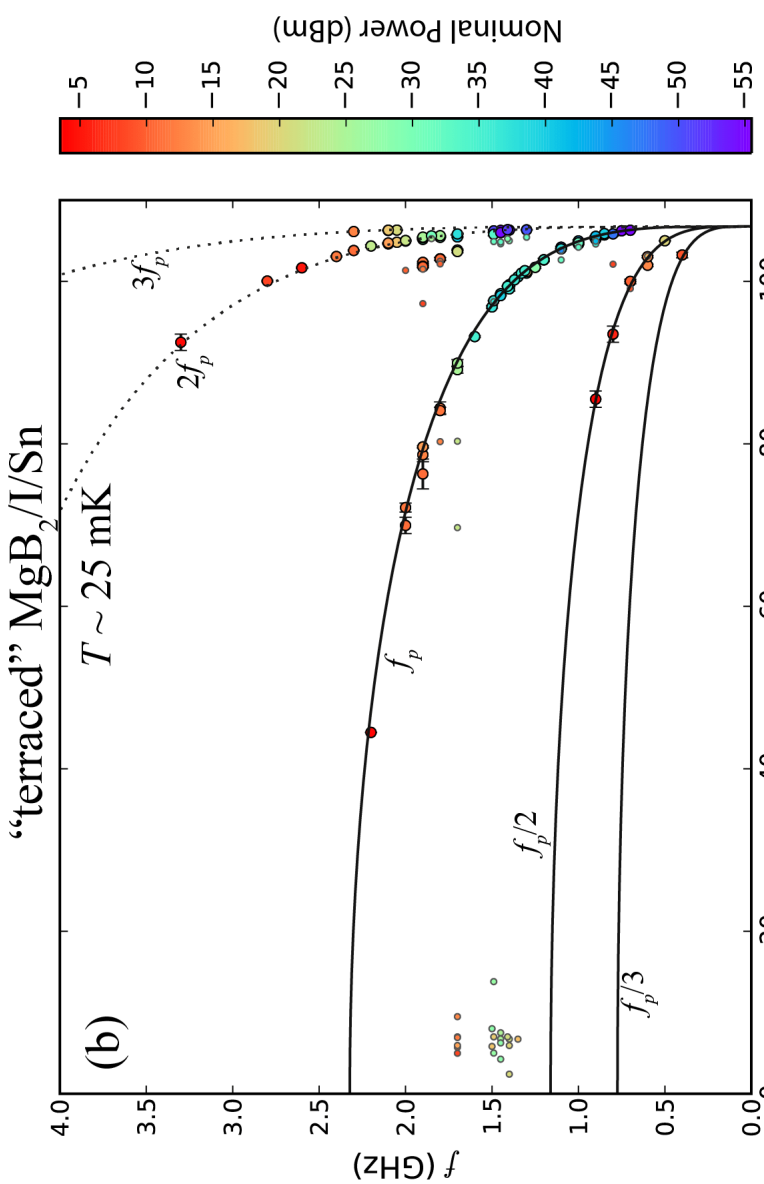


**Figure 4.20:** Applied microwave frequency vs. switching current, for the "terraced" $MgB_2$/I/Sn junction. Resonances at the plasma frequency $f_p = \omega_p/2\pi$ and integer subharmonics (solid lines) appear, and may be explained either as classical responses to driving a particle in an anharmonic potential, or as quantum-mechanical multiphoton processes. Resonances at higher harmonics (dashed lines) are explained only classically. As expected, resonances at lower currents, corresponding to a deeper washboard potential well $\Delta U$, require higher powers. Some of the differences in nominal power (i.e. power as indicated by the microwave generator) may also be explained by increasing attenuation with frequency of the microwave lines (see Table 4.1). All curves are produced from the two parameters $I_0 = 106.78 \pm 0.05$ $\mu$A and $C = 1523 \pm 14$ pF.

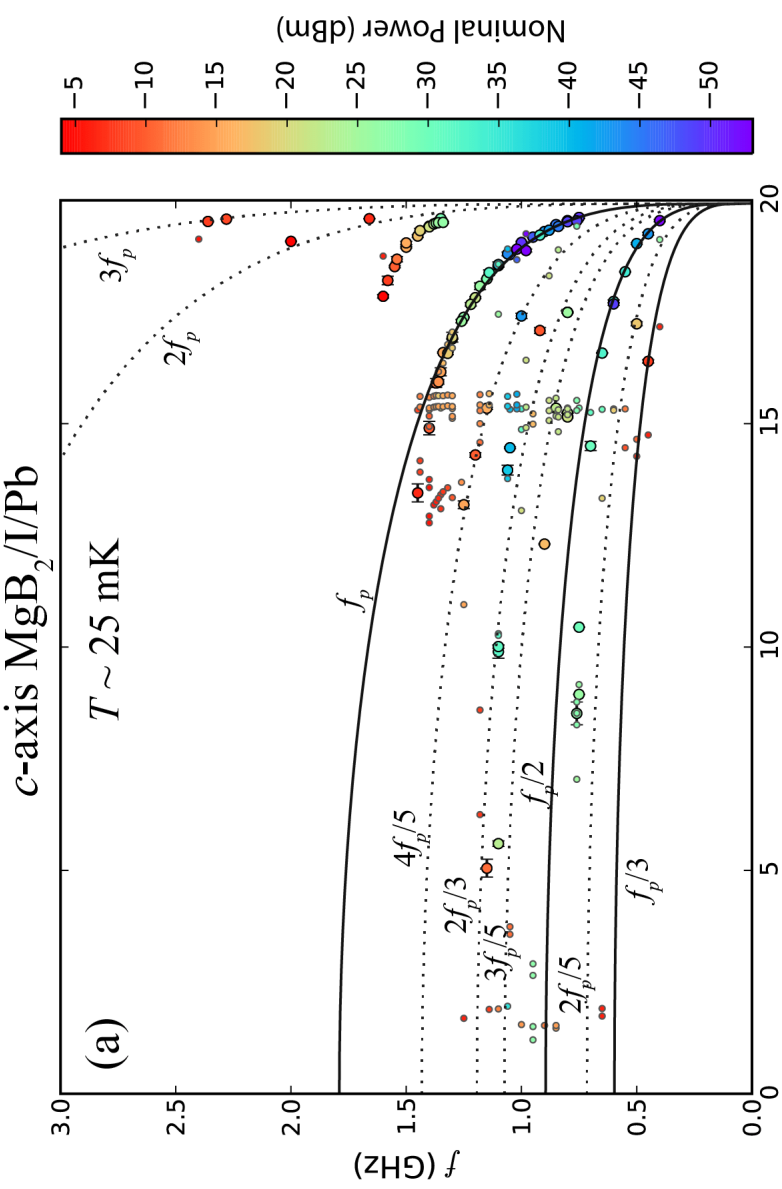


**Figure 4.21:** Applied microwave frequency vs. switching current, for the $c$-axis $MgB_2$/I/Pb junction, fit according to Equation 4.5 (and harmonics), with $I_0 = 19.93 \pm 0.04$ $\mu$A and $C = 478.6 \pm 18.6$ pF. The plasma frequency and integer subharmonics are shown as solid lines; higher harmonics and non-integer subharmonics are indicated as dashed lines. For a given current, resonances at higher harmonics and subharmonics require more microwave power to excite than those at $f_p$, as expected. A number of the resonant peaks are not predicted by classical or quantum-mechanical processes, and are discussed in Section 4.5.1.

level spacing provides a quick estimate of the number of levels in the well $N_s$ (Equation 4.18).

$$N_s \equiv \frac{\Delta U}{\hbar\omega_p} = \sqrt{\frac{\Phi_0 I_0 C}{2\pi e^2}}\left[\left(1-\left(\frac{I}{I_0}\right)^2\right)^{1/4} - \frac{I}{I_0}\left(1-\left(\frac{I}{I_0}\right)^2\right)^{-1/4} cos^{-1}\left(\frac{I}{I_0}\right)\right] \tag{4.18}$$

As $I$ approaches $I_0$, $N_s$ approaches 0. When increasing the current from zero, as in our experiments, all of the phase particles must have escaped by the time $N_s \gtrsim 1$. For each of our junctions, and for each of the results reported in the literature (Section 4.1.8), the maximum observed resonant current corresponds to a few states in the well.

$N_s$ at zero bias $N_s(0) = \sqrt{\frac{\Phi_0 I_0 C}{2\pi e^2}}$ approximates the maximum number of states in the well at any bias current. The remainder of Equation 4.18 depends only on the reduced current $\left(\frac{I}{I_0}\right)$, making it independent of junction properties.

$N_s(0)$ increases with both $I_0$ and $C$, each of which grows with area. As noted above, the junctions we studied were substantially larger than others for which "multiphoton" switching events have been observed.

For the "terraced" $MgB_2$/I/Sn junction, $N_s(0) \sim 46000$. For the $c$-axis $MgB_2$/I/Pb junction $N_s(0) \sim 11000$. In contrast, for the junctions reported in [158], $I_0 \sim 278\mu$A and $C \sim 1.6$ pF, giving $N_s(0) \sim 2400$ - roughly an order of magnitude smaller.

Not only were more states available, we observed resonances at much deeper levels than reported elsewhere. As indicated in Figures 4.20 and 4.21, we observed resonances at $f_p$ down to $\left(\frac{I}{I_0}\right) \sim 42\%$ for the "terraced" $MgB_2$/I/Sn junction, and $\sim 67\%$ for the $c$-axis $MgB_2$/I/Pb junction. These correspond to $N_s \sim 22000$ and $N_s \sim 2700$, respectively. In [158], the minimum $\left(\frac{I}{I_0}\right)$ observed for $f_p$ is $\sim 99.4\%$; the minimum $\left(\frac{I}{I_0}\right)$ observed for any subharmonic branch is $\sim 96.3\%$. These correspond to $N_s \sim 9.6$ and $N_s \sim 59.6$, respectively.

Observing these resonances over such a wide range in $N_s$ is unusual, and calls into question the attribution of these resonances to quantum-mechanical processes. However, the Lorentzian enhancements shown in the following section (Section 4.4.3) are commonly taken to be definitive evidence of quantum-mechanical behavior. Additionally, we observe these resonant currents down to

small numbers of states in the well - which should not be possible in the presence of excess thermal noise.

Furthermore, higher harmonics have only been reported to have a classical explanation - a system with an anharmonic potential (such as our washboard potential) will undergo large-amplitude oscillations at both subharmonics and higher harmonics of its resonant frequency, as described above (Section 4.1.8). A similar mechanism has been used to explain non-integer subharmonics [159].

The relatively strong microwave power required to excite each of the higher-harmonic resonances, and those at high $N_s$, may have been strong enough to drive the junction to classical behavior, even if they are behaving quantum-mechanically for the low-power resonances at $f_p$. This may occur either by directly heating the junction (even though the bulk of the cold finger and the attached thermometer remained at $\sim$25 mK) or by perturbing the washboard so strongly as to blend any metastable states into an effective continuum.

There is little evidence for non-integer subharmonics in our results, except possibly at $4f_p/5$ for the $c$-axis $MgB_2$/I/Pb junction. I include the non-integer theory curves on Figure 4.21 to demonstrate that some of the observed resonances cannot be explained as harmonics of the plasma frequency.

A discussion of these additional resonances (described as types (2), (3) and (4) in Section 4.4.1, and not corresponding to $f_p$ or its harmonics) appears in Section 4.5.1.

**Verifying $I_0$ and $C$**

I compared the values extracted from these fits with results suggested by other measurements. These alternative methods give values that are consistent with those from the frequency vs. current fits of Figures 4.20 and 4.21, although they are far less precise.

The critical current $I_0$ may be observed directly using the current vs. voltage characteristics discussed in Chapter 3. Although those measurements allowed very little noise to reach the junction, fluctuations in the measured current were $\lesssim 0.5\%$ of the critical current. Uncertainties in the bias resistance increased the overall uncertainty by $< 1\%$. The values observed directly on the $I-V$ curves were consistent, within these ranges, of those found here.

For the capacitance, I considered the junction geometry. For a parallel-plate capacitor, $C = \frac{\kappa\epsilon_0 A}{d}$ where $\kappa$ is the dielectric constant of the barrier material of thickness $d$, $A$ is the area of the junction, and $\epsilon_0$ is the permittivity of free space.

I estimated $A$ from photographs of the junctions. For $d$, the technique used in the fabrication of these junctions consistently produces a barrier thickness ∼2 nm [8]. A dielectric constant $\kappa$ cannot be less than 1. For comparison, $\kappa \sim$ 9-10 for pure MgO at room temperature [178]; for boron nitride at room temperature, $\kappa \sim 3 - 7$ [179].

For the "terraced" $MgB_2$/I/Sn junction, $A \approx 0.085$ mm$^2$. Taking $C = 1523$ pF and $d = 2$ nm gives $\kappa \approx 4$. For the $c$-axis $MgB_2$/I/Pb junction, $A \approx 0.059$ mm$^2$. Taking $C = 478.6$ pF and $d = 2$ nm gives $\kappa \approx 1.8$. Given the unknown nature of the barrier, and the substantial uncertainties in the area and thickness, these results are within a reasonable factor of the expected values.

When considering Figures 4.20 and 4.21, the data points near each arc could be attributed to different resonances. For example, the arc at $2f_p$ is well-populated for the "terraced" $MgB_2$/I/Sn junction could instead be interpreted as $f_p$. Without considering additional evidence, it would be difficult to establish the junction capacitance.

Changing the attribution produces several problems, as shown in Figure 4.22(a). First, each of the theoretically-predicted odd subharmonics would be absent from the data, although even subharmonics are seen. There does not appear to be a theoretical explanation for this. Second, the single-photon resonance should require the lowest power for a given well depth/bias current. Considering the observations around 100 $\mu$A, this change in attribution would indicate that the two-photon peak (at $\sim$ -40 dBm) would require far lower power than the single-photon peak (at $\sim$ -5 dBm). Finally, this would require a capacitance four times as large, which would indicate an unrealistic dielectric constant: the implied $\kappa$ would be $\sim$ 16. Similar problems occur when attributing the arc at $2f_p$ in Figure 4.20 as $f_p$, as shown in Figure 4.22(c).

Given the weight of the evidence, I am confident that these measurements have resulted in accurate results for the critical current $I_0$ and capacitance $C$.

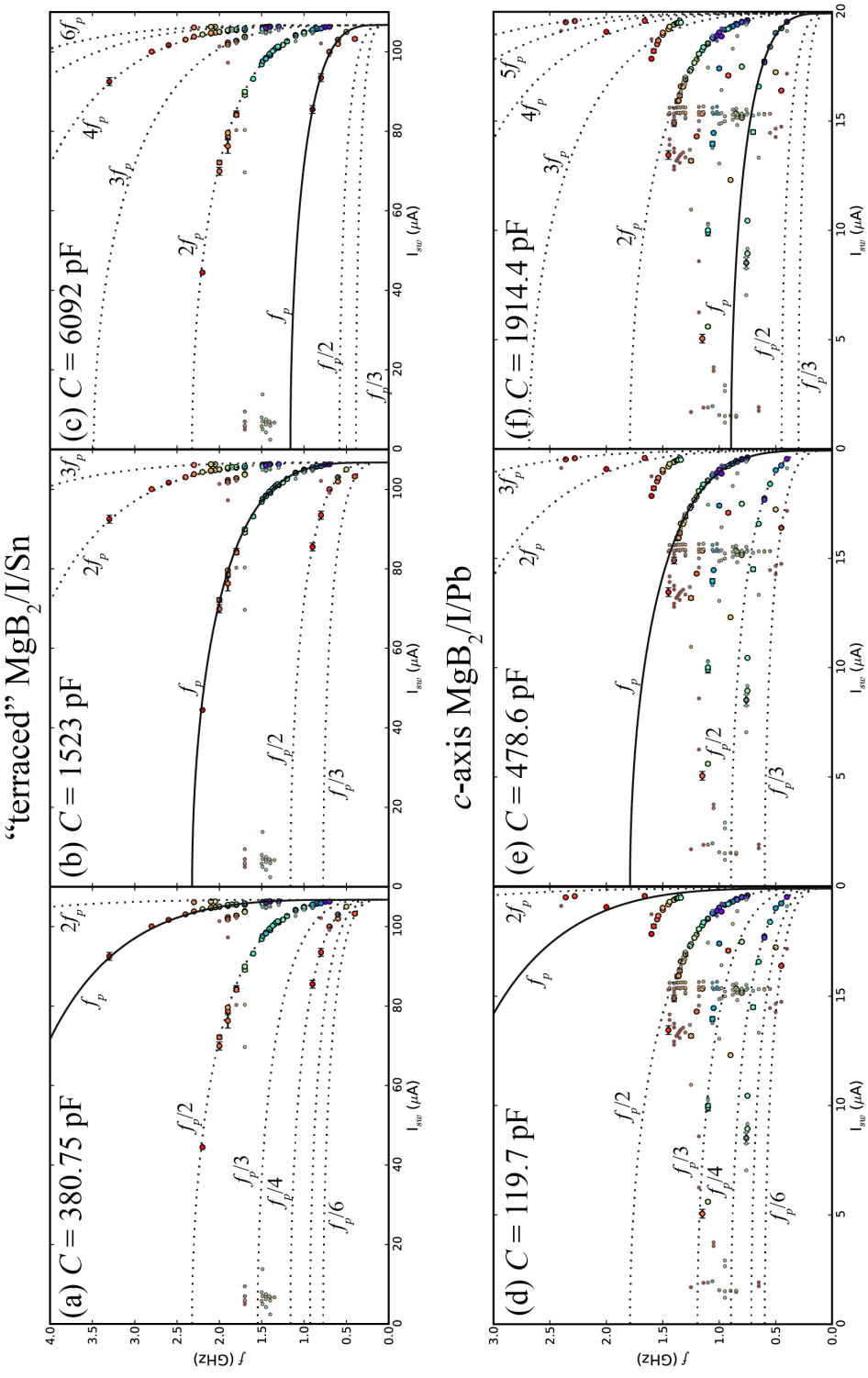


**Figure 4.22:** Checking alternative fits to the applied microwave frequency vs. switching current graphs, for the "terraced" $MgB_2$/I/Sn (a-c) and $c$-axis $MgB_2$/I/Pb junctions (d-f). If only the resonant frequencies were plotted, some of the alternative capacitances (a,c) and (d,f) would appear attractive in fitting these curves, rather than the parameters I used (b,e). However, each of these other choices are problematic. For example, some resonances that should have been observed would be absent (e.g. $f_p/3$ and $f_p/5$ in (a)). Also, the relative powers required to excite each resonance would be unreasonable. Finally, the capacitance would seem unrealistic, given the junction geometry. For (a-c), the critical current is kept fixed at 106.78 $\mu$A; for (d-f), $I_0 = 19.93$ $\mu$A.

### 4.4.3 Escape Rate Enhancement

A few of the points on $f$ vs. $I$ (Figures 4.20 and 4.21) were found using the enhancement to the escape rate, as discussed in Section 4.3.2. These also allowed me to estimate lower limits on $Q$ and $R$ for each junction, using Equation 4.17.

As discussed in Section 4.1.6, when switching in a Josephson junction is dominated by quantum-mechanical processes, the enhancement forms a Lorentzian peak. As shown in Figure 4.23, enhancements for both junctions are reasonably approximated by a Lorentzian.

A Lorentzian fit for the "terraced" $MgB_2$/I/Sn junction, as shown in Figure 4.23 (d), is centered at $I \sim 106.33$ $\mu$A and have a full-width at half-maximum (FWHM) of $\sim 0.12\mu$A. Using Equation 4.17, I find $Q(I{=}106.33\mu\text{A}) \sim 30$, or $Q_0 \sim 100$ . Using $Q = \omega_p RC$, together with $I_0 = 106.78$ $\mu$A and $C = 1523$ pF (as extracted from $f$ vs. $I$ above), this gives $R \gtrsim 15$ $\Omega$.

For the $c$-axis $MgB_2$/I/Pb junction, the fit is centered at $\sim$19.49 $\mu$A with a FWHM $\sim$0.01 $\mu$A. The resulting $Q(I{=}19.49\ \mu\text{A}) \gtrsim 45$, or $Q_0 \gtrsim 90$, leading to a resistance $R \gtrsim 70$ $\Omega$.

Although the subgap resistances are much higher for these junctions ($\gtrsim 1$ k$\Omega$), the resistance at these high frequencies is typically dominated by the leads connected to the junction. As discussed in Section 4.1.2, typical resistances are between ten and a few hundred Ohms. As such, these results appear reasonable, especially when considered as a lower limit.

Section 4.4.4 below shows a completely independent method for determining the resistance. The resulting zero-bias quality factors ($Q_0 = 200{\pm}90$ for the "terraced" $MgB_2$/I/Sn junction and $Q_0 = 250{\pm}140$ for the $c$-axis $MgB_2$/I/Pb junction) compare very favorably with the results discussed here.

### 4.4.4 Switching: Effects of Temperature

Many of the characteristics of the junctions could be found through the microwave resonant activation results described above. Tracking the superconducting-to-normal switching behavior through increasing temperatures provides a new family of results. These give a better insight into the junction resistance $R$, allow us to perform consistency checks on our prior results, and provide the opportunity to seek new physics in the behavior of the junctions.

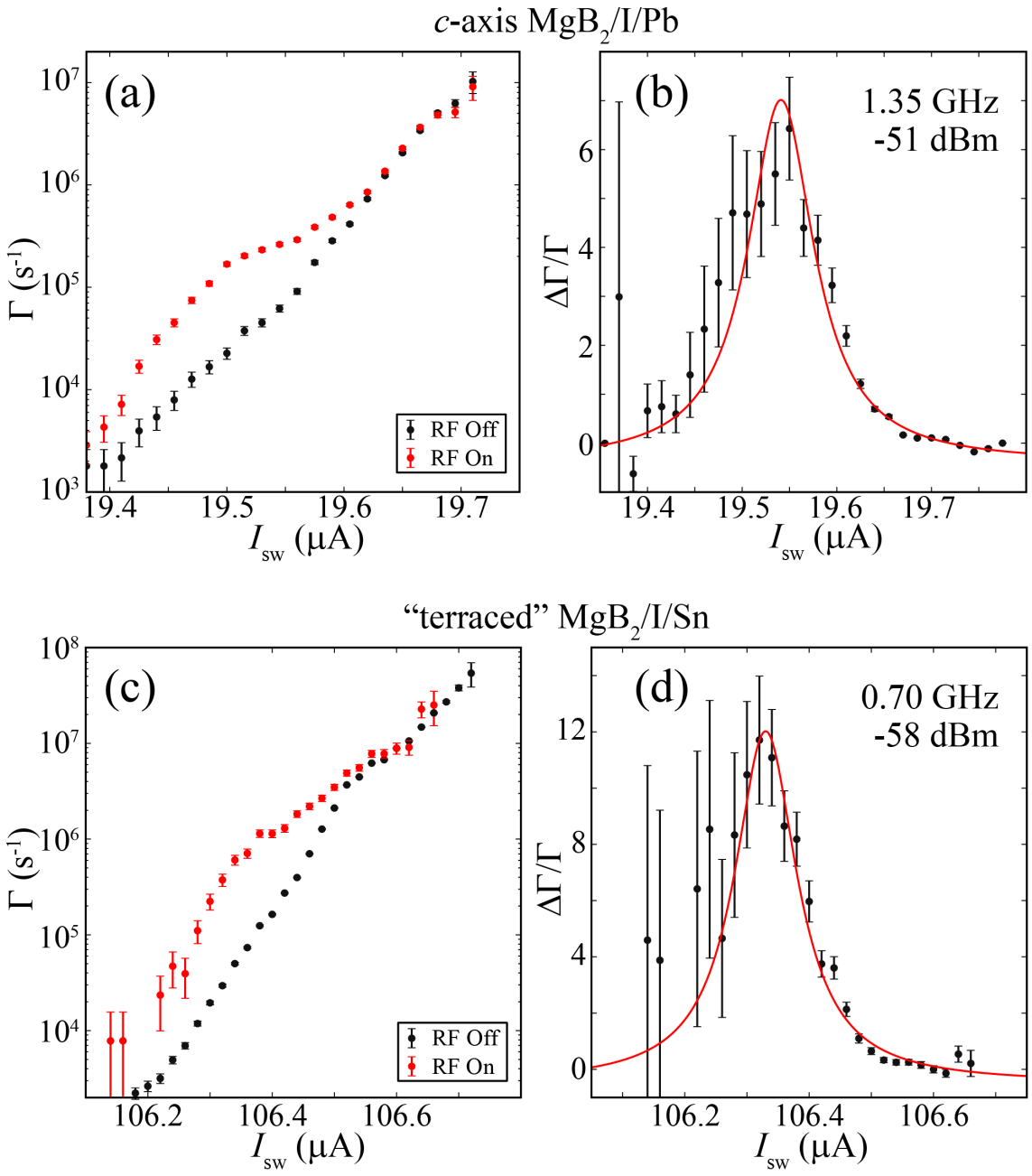


**Figure 4.23:** Escape rates (a, c) in the presence and absence of microwaves, and escape rate enhancements (b, d), for the *c*-axis $MgB_2$/I/Pb junction at 21 mK, and the "terraced" $MgB_2$/I/Sn junction at 22 mK, respectively. For (a) and (b), the microwaves were applied at 0.80 GHz at a nominal power of -51 dBm. For (c) and (d), the microwaves were applied at 0.70 GHz at a nominal power of -58 dBm. The Lorentzian fits to the enhancement give $Q(I{=}19.49\ \mu\text{A}) \sim 45$, or $Q_0 \sim 90$ for the *c*-axis $MgB_2$/I/Pb junction, and $Q(I{=}106.33\mu\text{A}) \sim 30$, or $Q_0 \sim 100$ for the "terraced" $MgB_2$/I/Sn junction.

**Histograms and Escape Rates vs. Temperature**

My exploration of the effects of temperature on the escape of the phase particle from the potential well begins with the histograms of the raw switching data, and the escape rates computed from them.

As expected, Figure 4.24 shows that the distribution of switching currents is concentrated in a narrow peak near the critical current $I_0$ at low temperature, while at high temperature, the peaks are substantially broader.

The $c$-axis $MgB_2$/I/Pb junction results compare quite favorably with the theoretical distributions of Figure 4.4. Because the critical temperature $T_c$ of Pb is 7.2 K, the gap voltage $V_g$ and the critical current $I_0$ are expected to be reduced by only $\sim 0.0002\%$ at 1 K, and $\sim 0.8\%$ at 2.5 K, by applying the BCS relationship for gap energy $\Delta$ vs. temperature (Figure 1.5).

In contrast, $T_c$ of Sn is 3.7 K. As a result, the gap voltage $V_g$ and the critical current $I_0$ are expected to be reduced by $\sim 1.4\%$ at 1 K, and $\sim 15\%$ at 2.5 K. The resulting shift in the histograms is quite apparent for the "terraced" $MgB_2$/I/Sn junction in Figure 4.4 (b).

The trend toward a narrowing of the distribution of switching currents, at currents increasingly near $I_0$, continues as the temperature is decreased. As indicated in Figure 4.35, this effect appears to saturate at very low temperatures - below $\sim$ 100 mK. This may be an indication of a crossover from classical to quantum mechanical behavior. In order to interpret the results, it is useful to turn to calculations of the mean switching current and the standard deviation, over the entire temperature range.

**Mean and Standard Deviation of Switching Current Distribution vs. Temperature**

As described in section 4.1.4, in the absence of quantum-mechanical tunneling, the standard deviation should continue to decrease roughly linearly as the temperature decreases, over the entire temperature range of the experiment. The observation of a minimum standard deviation is commonly taken as a sign of crossover from classical to quantum-mechanical behavior; the temperature at which the transition occurs is then assumed to be the crossover temperature $T_{cr}$.

Figure 4.25 shows the results from both junctions. In each case, the results are most clear if

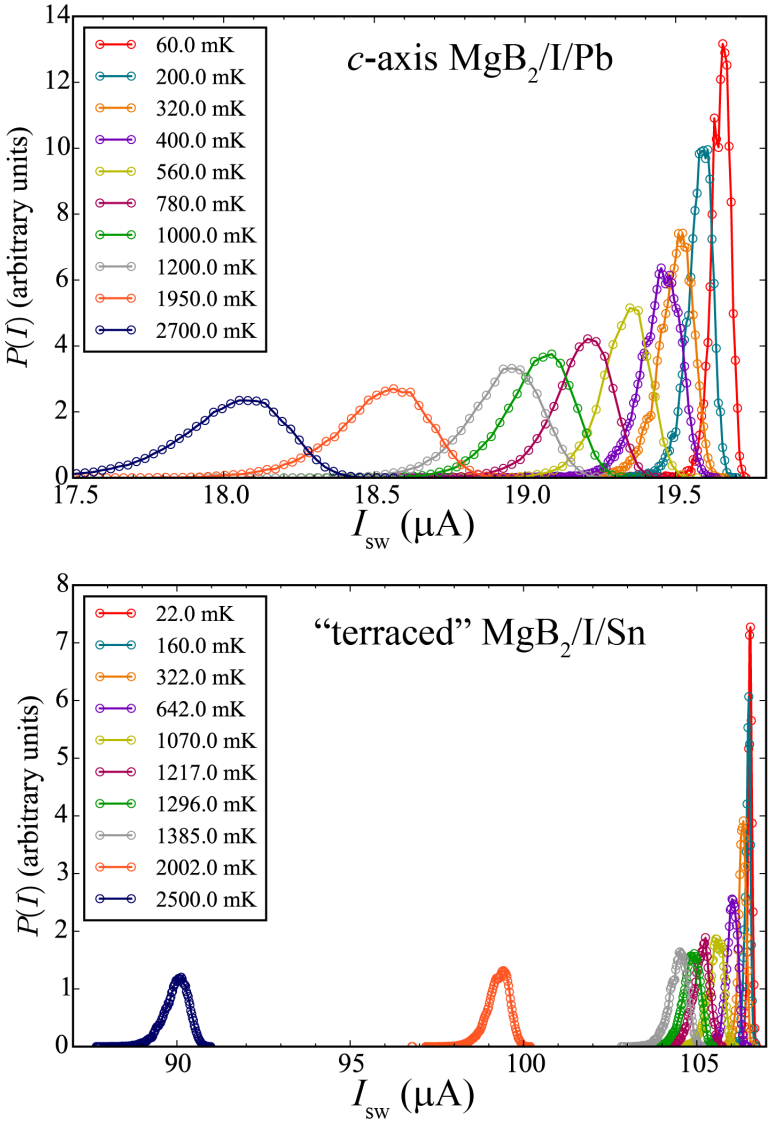


**Figure 4.24:** Escape probability (switching histogram) vs. current, for the $c$-axis $MgB_2$/I/Pb junction (a) and "terraced" $MgB_2$/I/Sn junction (b), respectively. In (b), as the temperature increases, the mean switching current $\langle I_{sw} \rangle$ decreases beyond that derived from thermal activation theory assuming a fixed critical current $I_0$. This reduction in critical current is expected for a junction incorporating Sn ($T_{c\,Sn} = 3.7$ K). This same effect also influences the data in (a), although to a far lesser extent ($T_{c\,Pb} = 7.2$ K).

$\langle I_{sw} \rangle$ vs. $T$ is shown on a linear-linear scale, while $\sigma$ vs. $T$ is shown on a log-log scale.

For the "terraced" $MgB_2$/I/Sn junction, the significant decrease in critical current above ∼1 K is clearly reflected in the mean of the switching current (c). The standard deviation (d) shows a nearly linear decrease, until a crossover to a roughly constant value, at ∼0.1 K.

For the *c*-axis $MgB_2$/I/Pb junction, the standard deviation (b) likewise shows a nearly linear decrease as the temperature decreases, until a crossover to a roughly constant value, again at ∼0.1 K. The mean switching current also appears to reach a stable value at ∼0.1 K. These results combined are entirely consistent with a crossover from classical to quantum-mechanical behavior at this temperature.

Although it may seem surprising that these apparent crossover temperatures would be so similar for two different junctions of such dramatically different critical currents and capacitances, the crossover temperature (equation 4.13) is proportional to $\omega_0$, which is a function of the critical current density. Since these junctions were fabricated using similar methods, with a barrier formed by a native oxide, their critical current densities are similar. So, while the similarities in crossover temperatures could be seen as evidence of a $\sim$ 100 mK noise floor, they are also reasonably consistent with the physics of the junctions.

Unfortunately, both curves for the *c*-axis $MgB_2$/I/Pb junction (Figure 4.25 (a,c)) are somewhat more limited than would otherwise have been possible. Although we also gathered data at additional temperatures as low as 22 mK, they do not appear in these plots, due to an accidental change to the electronic configuration below 60 mK.

The same device was also measured on two additional occasions prior to the measurements shown here and in Section 4.4.1. I did not present results from those experiments above because we were still determining the optimal configuration for microwave resonant activation experiments at that time, and were unable to achieve results nearly as reliable as those shown in Section 4.4.1.

However, we did gather useful measurements in the absence of microwaves, for the second of those experiments, as shown in Figure 4.36. Each of the results is largely consistent with those in Figure 4.25; both may be found in Figure 4.26. There are a few differences.

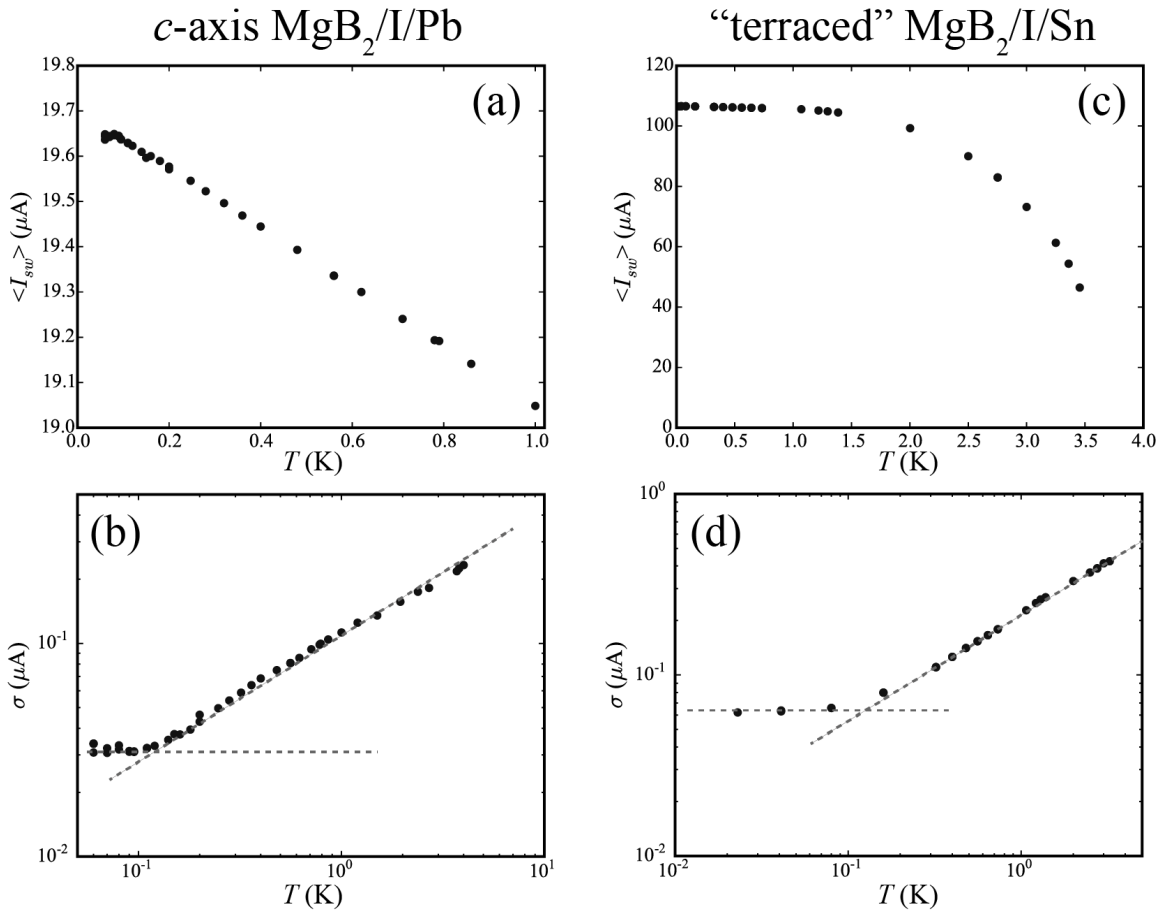


**Figure 4.25:** Mean switching current (a, c) and standard deviation in the switching current (b, d), for the $c$-axis $MgB_2$/I/Pb and "terraced" $MgB_2$/I/Sn junctions, respectively. (Linear scales are used for (a, c); log-log for (b, d).) Below ∼100 mK, the standard deviation remains a stable value, for both junctions. This may be suggestive of a transition from classical to quantum mechanical behavior, with a crossover temperature of roughly 100 mK for both junctions. (The dashed lines are guides for the eye.) The mean switching current for the $c$-axis junction (a) increases linearly as $T$ is decreased until $\sim$ 100 mK. This is consistent with a crossover from escape dominated by classical processes to quantum tunneling at $\sim$ 100mK. The trend in the mean switching current of the "terraced" junction (c) is dominated by the variation in the energy gap of tin with temperature (comapre with Figure 1.5). $T_c$ of the Sn electrode of ∼3.7 K.

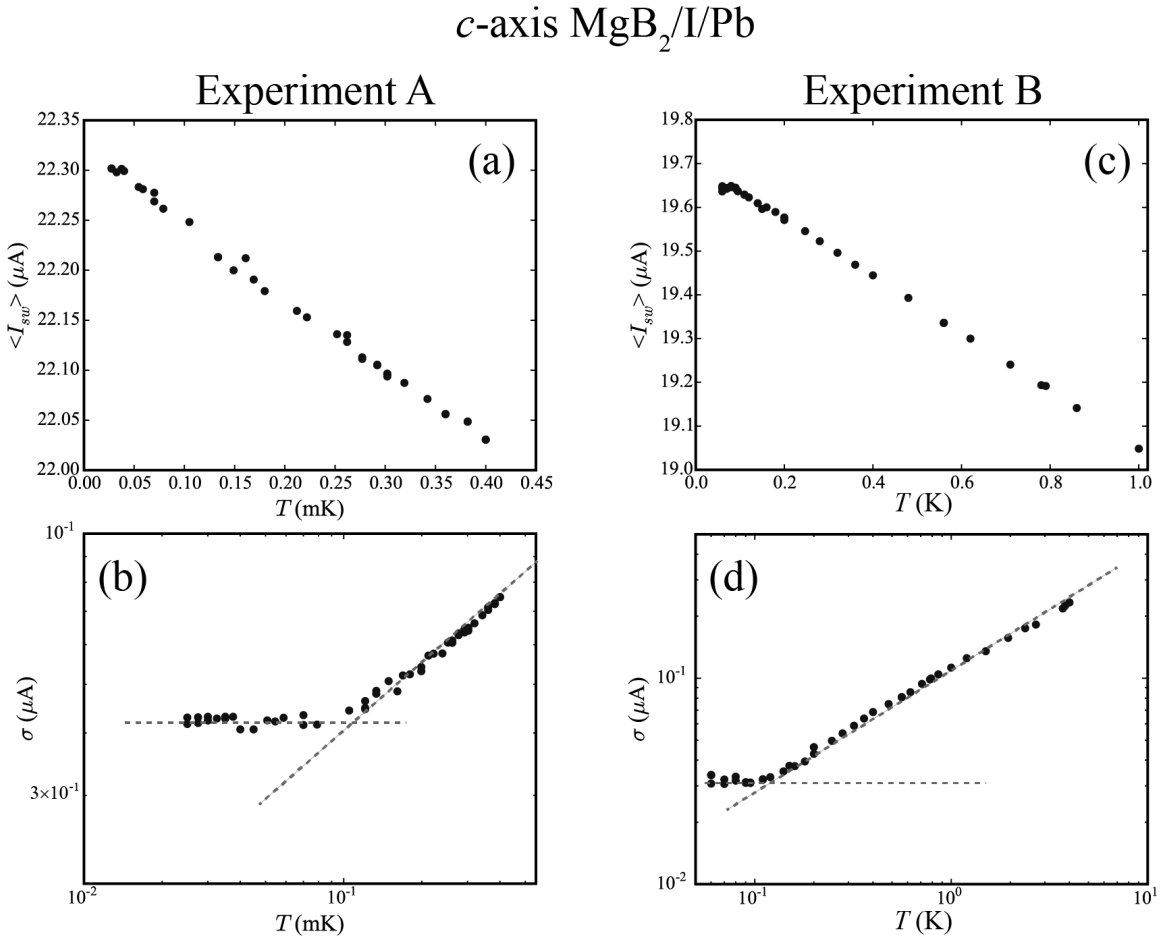


**Figure 4.26:** Mean switching current (a, c) and standard deviation in the switching current (b, d), for the $c$-axis $MgB_2$/I/Pb junction, for two different experiments. (As in Figure 4.25, linear scales are used for (a, c); log-log for (b, d).) In Experiment A, I sought to establish the quantum-to-classical crossover temperature; in Experiment B, I explored a wider temperature range. In both experiments, the standard deviation (b, d) reached a floor below ∼100 mK. In Experiment B, the mean switching current (c) increased as $T$ is decreased until ∼100 mK. However, in Experiment A, the mean switching current (d) did not stabilize until ∼40 mK.

First, the critical current was highest for our first series of experiments, and gradually decreased with each succeeding experiment. (Compare Figures 4.26 (a) and (c).) We attribute this to degradation in the junction; the most likely explanation is degradation of the $MgB_2$ film itself, since the sample was stored in a (non-vacuum) desiccator for $> 2$ weeks between experiments. It is also possible that the Pb electrode increased its separation from the $MgB_2$ film due to thermal cycling.

Second, in the earlier round of experiments, although the standard deviation appears to level off at ∼0.1 K, the mean switching current does not, until ∼40 mK (Figure 4.26 (a)). We are unsure of the reason for this discrepancy.

**Fitting the Escape Rate**

At worst, the above results suggest that our experimental system has a noise floor of $\sim$ 100 mK. But they may instead suggest a crossover to quantum-mechanical behavior - a distinction that is useful, when considering how relevant our results are for quantum device applications. Fitting the escape rate using Equation 4.12 provides additional insights.

Figure 4.27 shows typical results for fitting the escape rate. In this case, results for the "terraced" $MgB_2$/I/Sn junction are shown, for theoretical and experimental escape rates at 160 mK and 1.217 K. The curve fits were found using OriginPro software. As described above, $C$ was established from Figures 4.20 and 4.21. The minimum, maximum, and central values of $R$ were found as described in Section 4.3.3 by checking the escape rates at several temperatures. For these fits, $R$ and $C$ were held fixed, and OriginPro found the optimal $I_0$ and $T_{esc}$. I then checked $I_0$ for consistency with the result found from Figures 4.20 and 4.21, although with some flexibility due to a potential offset from the $RC$ filter (Section 4.3.1) and allowing for thermal suppression of the critical current.

Using these methods, I found $R = 9\pm4\ \Omega$ for the "terraced" $MgB_2$/I/Sn junction, and $R = 46\pm24\ \Omega$ for the $c$-axis $MgB_2$/I/Pb junction. Combining these with the junction capacitance established above gives $Q_0 = 200 \pm 90$ for the "terraced" $MgB_2$/I/Sn junction, and $Q_0 = 250 \pm 140$ for the $c$-axis $MgB_2$/I/Pb junction. These quality factors are sufficiently high that these junctions may be attractive for applications. And their consistency with those found from fitting the escape rate enhancement (Section 4.4.3) increases our confidence in their accuracy.

Uncertainties in $I_0$ and $T_{esc}$ were found by repeating the fit for the minimum and maximum $R$. $C$ remained fixed, both because its uncertainty was far smaller than that of $R$, and because the range chosen for $R$ was very likely an overestimate.

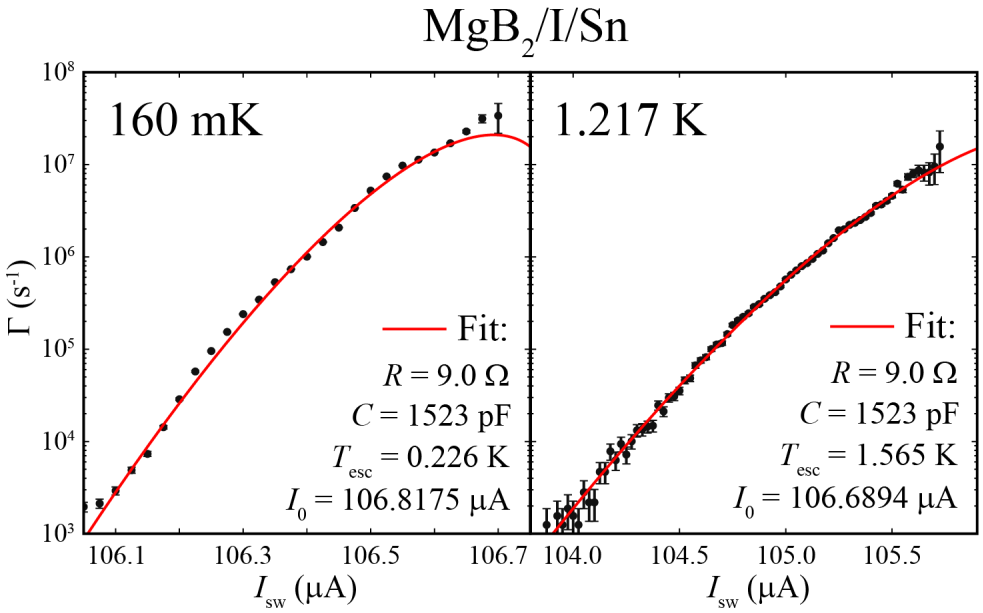


**Figure 4.27:** Fit of the escape rate in the absence of microwaves for the "terraced" $MgB_2$/I/Sn junction, at 160 mK and 1.217 K. Data for this junction were taken from 23 mK through 3.45 K; the resulting escape rates were fit according to Equation 4.12 over the entire temperature range. From these, we conclude that $R = 9 \pm 4\ \Omega$ for this junction.

Figures 4.28, 4.29 and 4.30 show the fit escape temperature $T_{esc}$ vs. the temperature measured by the mixing chamber thermometer $T_{MC}$.

As with Figure 4.25 for standard deviation vs. temperature (as measured by the mixing chamber thermometer), the escape temperature also follows a roughly linear decrease with $T_{MC}$, down to $\sim$ 100 mK. Specifically, the "terraced" $MgB_2$/I/Sn junction exhibits a crossover to a constant $T_{esc}$ at $T_{MC} = 130$ mK; the $c$-axis $MgB_2$/I/Pb junction crosses over at $T_{MC} = 89.9$ mK for Experiment A, and 117 mK for Experiment B.

Each of these results is fairly consistent from junction to junction and experiment to experiment, as shown in Figure 4.30.

Fitting the escape rate has, however, revealed two new features not apparent when plotting the standard deviation vs. temperature. First, for all three experiments (one for the "terraced"

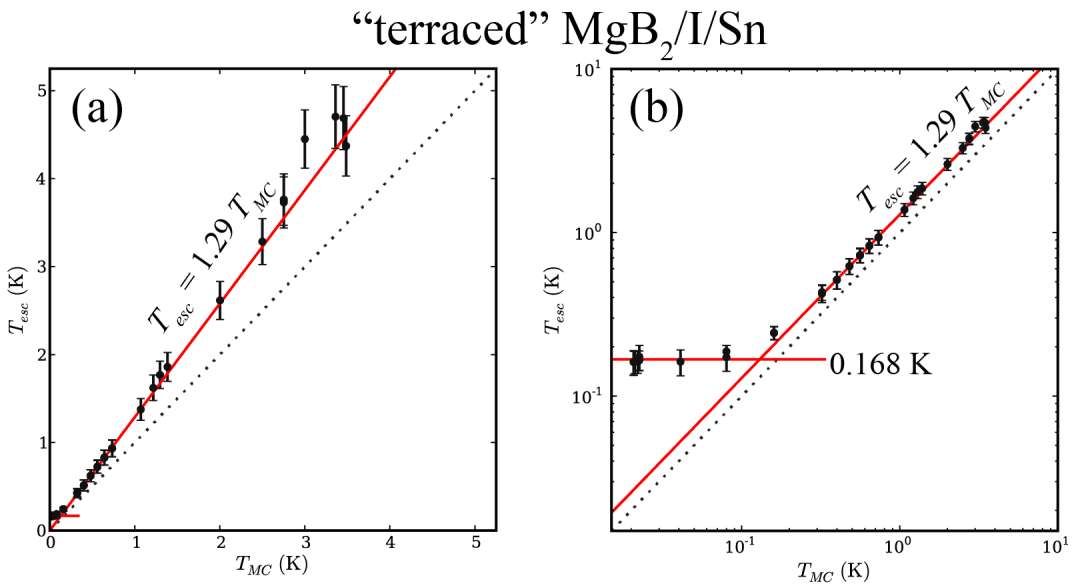


**Figure 4.28:** Escape temperature $T_{esc}$ as found from fits to the escape rate, vs. the temperature measured at the mixing chamber of our dilution refrigerator $T_{MC}$, for the "terraced" $MgB_2$/I/Sn junction. The red lines are fits to relevant subsets of the data points; their intersection, at $T_{MC} = 130$ mK, indicates the crossover temperature. The dashed line is $T_{esc} = T_{MC}$. (a) When plotted on a linear/linear scale, the linear trend with temperature is clear, as is the departure of the measured temperature from that extracted from escape rate fits. (b) The same data points, plotted on a log-log scale, shows the crossover far more clearly.

$MgB_2$/I/Sn junction, two for the $c$-axis $MgB_2$/I/Pb junction), the escape temperature is nearly 1.3 times the measured temperature for most of the temperature range above the crossover. Second, for both experiments on the $c$-axis $MgB_2$/I/Pb junction, the fit temperature $T_{esc}$ becomes a near-match with the measured temperature $T_{MC}$, above $\sim$ 2.5 K, rather than remaining $\sim$1.3 times larger. I discuss these further in Section 4.5.2

### 4.4.5 Evidence for Quantum Mechanical Behavior

Superconductivity and the Josephson effect are necessarily quantum-mechanical in nature. But, the phase particle may escape from a local minimum of the washboard potential classically or quantum-mechanically. Several applications and theoretical analyses require quantum-mechanical escape. Therefore, I summarize the evidence found from our experiments, in this subsection.

As noted in Section 4.4.4, we observed a floor in both the standard deviation of the switching current distributions, and in the escape temperature derived from fits to the escape rate. In each

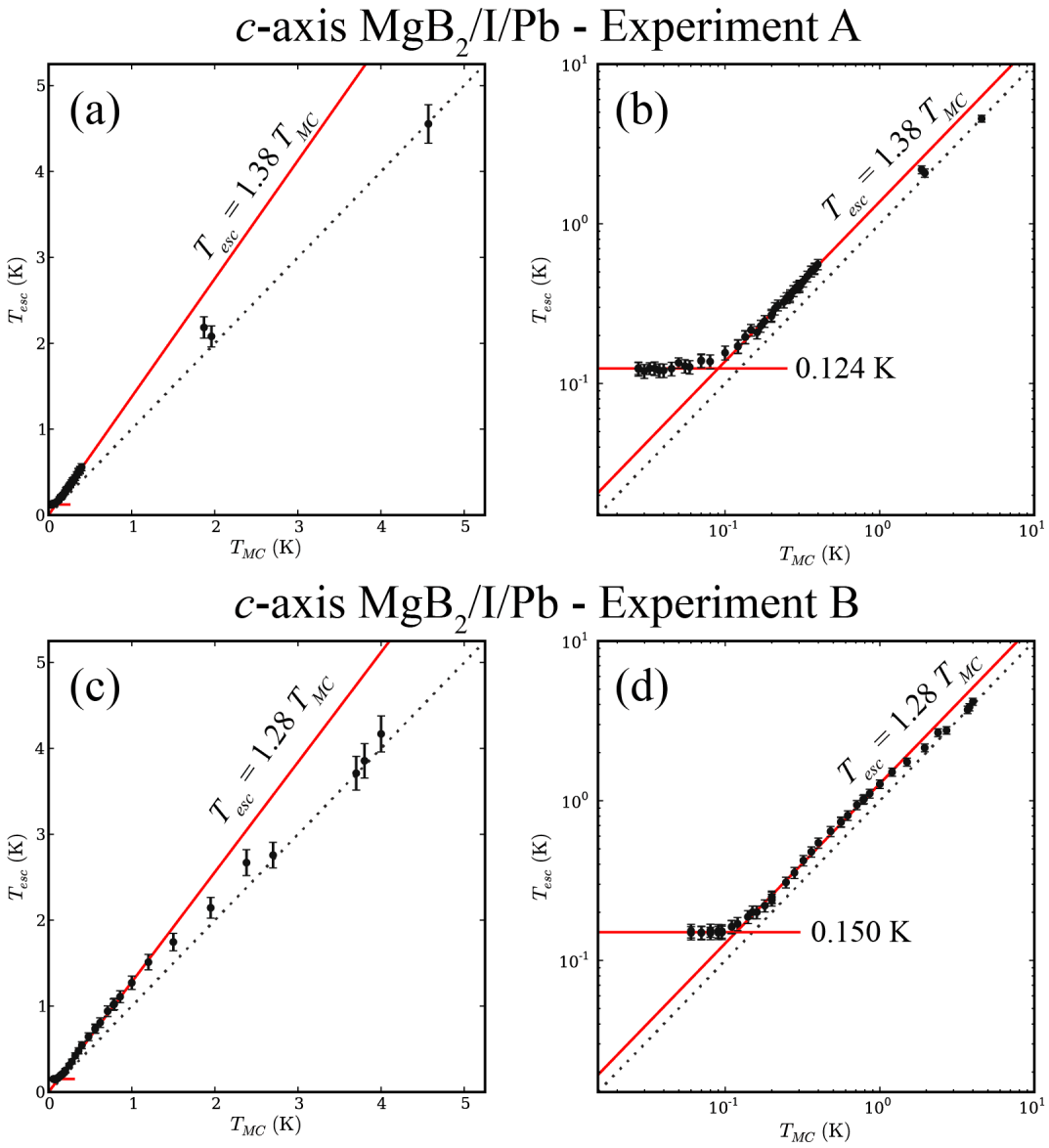


**Figure 4.29:** As above, escape temperature vs. measured temperature, for the *c*-axis $MgB_2$/I/Pb junction for both experiments for which I acquired useful results. The intersections of the fitted (red) lines for Experiment A indicate a crossover at $T_{MC} = 89.9$ mK; for Experiment B, at 117 mK. Plots on a linear-linear scale (a, c) and a log-log scale (b, d) emphasize different features of the same results.

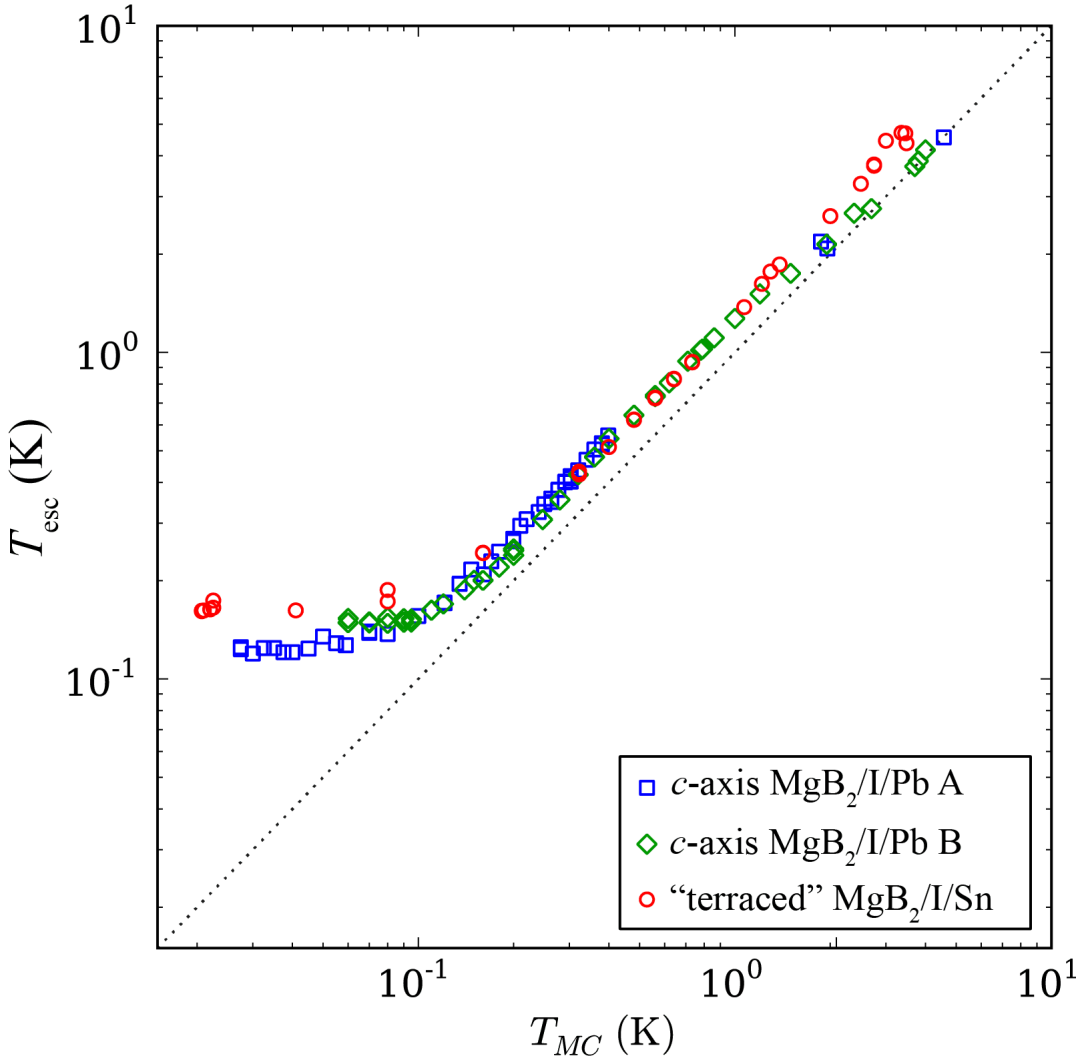


**Figure 4.30:** Escape temperature vs. measured temperature for all three experiments shown above, plotted together on the same log-log scale. Red circles: results for the "terraced" $MgB_2$/I/Sn junction. Blue squares: the *c*-axis $MgB_2$/I/Pb junction, Experiment A. Green diamonds: the *c*-axis $MgB_2$/I/Pb junction, Experiment B. The dashed line is $T_{esc} = T_{MC}$. The offset of the experimental results from this dashed line reflects the departure of $T_{esc}$ from $T_{MC}$ ($T_{esc} \sim 1.3T_{MC}$) below $\sim 2$ Kelvin.

case, for both junctions, this floor is ∼100 mK.

Although this is among the most common methods used in the literature to indicate a crossover from thermal to quantum-mechanical behavior, it may also indicate a noise floor. As such, it is only suggestive.

Far more compelling are the results that produce a peak in the escape rate enhancement. A criterion for classical activation is given [156] from comparing the slope of the escape rate in the presence of microwaves with that in the absence of microwaves. If $\frac{d\Gamma_{\mathrm{RF\ On}}}{dI} \lesssim \frac{d\Gamma_{\mathrm{RF\ Off}}}{dI}$ (leading to a "shelf" in the enhancement below $I_r$), it is deemed classical. However, if $\frac{d\Gamma_{\mathrm{RF\ On}}}{dI} > \frac{d\Gamma_{\mathrm{RF\ Off}}}{dI}$ (leading to a "peak" in the enhancement below $I_r$), this is taken as conclusive evidence that the switching is dominated by quantum-mechanical tunneling.

My results for $\Gamma$ vs. $I$, shown in Figure 4.23 (a,c), clearly have a steeper slope below $I_r$ in the presence of microwaves than in their absence. This leads to the peaks in the enhancement (b,d) that are in clear contrast to the "shelf" expected for classical behavior (Figure 4.8).

Additional evidence is provided by my microwave resonant activation results to support the conclusion that the standard deviation and escape temperature are not noise limited.

Figure 4.31 shows that the resonant peak is taller and narrower than the primary peak. If the system had reached a point where the distributions in switching currents were dominated by electrical noise rather than thermal fluctuations, at a higher temperature than the true crossover temperature, this "noise temperature" would affect both the primary and resonant peaks.

However, the resonant excitation of transitions between two quantum-mechanical energy levels should occur over a narrower range of currents than the distribution in the absence of microwaves. If the system were dominated by electrical noise, this narrowing would not be apparent. The fact that we observe it suggests that the resonances we observe at base temperature are due to quantum mechanical tunneling through the barrier. Reference [158] used this method to demonstrate that their measured distributions in the absence of microwaves were not limited by noise in their experimental setup, thereby indicating that escape was due to quantum tunneling through the barrier.

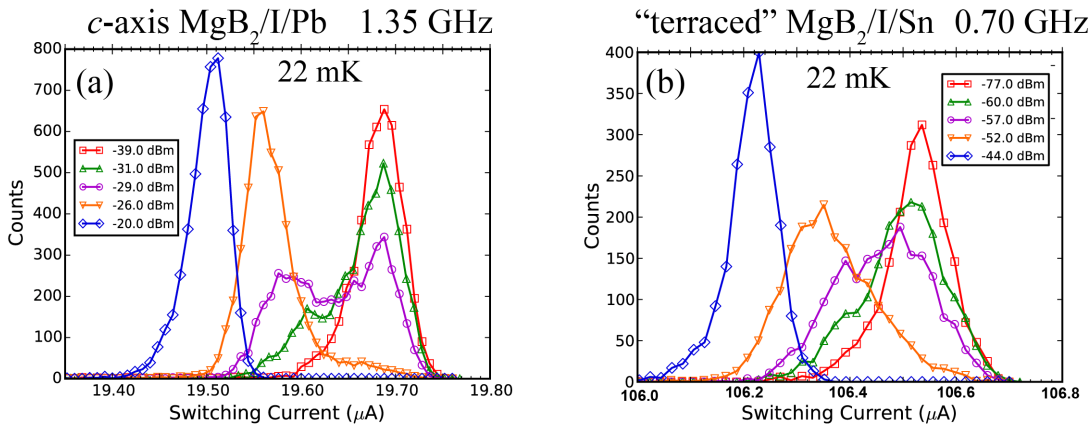


**Figure 4.31:** Histogram counts vs. current at powers near the critical power for resonance, for the $c$-axis $MgB_2$/I/Pb (a) and "terraced" $MgB_2$/I/Sn (b) junctions, respectively. Each set of curves was acquired near 22mK. At sufficiently high power, only the resonant peak appears. The fact that the resonant peak is taller and narrower than the primary peak suggests that the primary peak distribution is not dominated by thermal noise. This is strongly suggestive of quantum-mechanical behavior.

For the $c$-axis $MgB_2$/I/Pb junction, the standard deviation $\sigma$ for the resonant peak (at -20 dBm) is 0.032 $\mu$A, vs. 0.043 $\mu$A for the low-temperature data shown in Figure 4.25. For the "terraced" $MgB_2$/I/Sn junction, the standard deviation $\sigma$ for the resonant peak (at -44 dBm) is 0.054 $\mu$A, vs. 0.063 $\mu$A for the low-temperature data shown in Figure 4.25.

These substantial differences support the conclusion that we have observed quantum-mechanical tunneling of the phase particle through the washboard potential barrier.

## 4.5 Additional Features

Although most of the features I observed can be explained by conventional junction theory, the explanations for several others remain unresolved.

### 4.5.1 Microwave Resonant Activation

I observed several "families" of additional resonances, not explained by Equation 4.5, as shown in Figures 4.19, 4.20 and 4.21.

If the additional resonances had been scattered randomly across the $f$ vs. $I$ plots, then they might be dismissed as artifacts. However, especially for the $c$-axis $MgB_2$/I/Pb junction, several families of curves appear consistent across frequency ranges.

### Type (2)

One family is found between the curves for $f_p$ and $2f_p$ on Figure 4.21 (roughly 18 to 19.5 $\mu$A and 1.3 to 1.6 GHz). These are described as type (2) on Figure 4.19.

It exhibits some similarities to theoretical curves for a Josephson junction coupled to an $LC$ oscillator [13]. As they describe, the presence of two parallel circuits results in two parameters being relevant: $\varphi_J$ and $\varphi_s$. The resulting potential is a two-dimensional analogue to our washboard potential, with two resonant frequencies, shown in Figure 4.32.

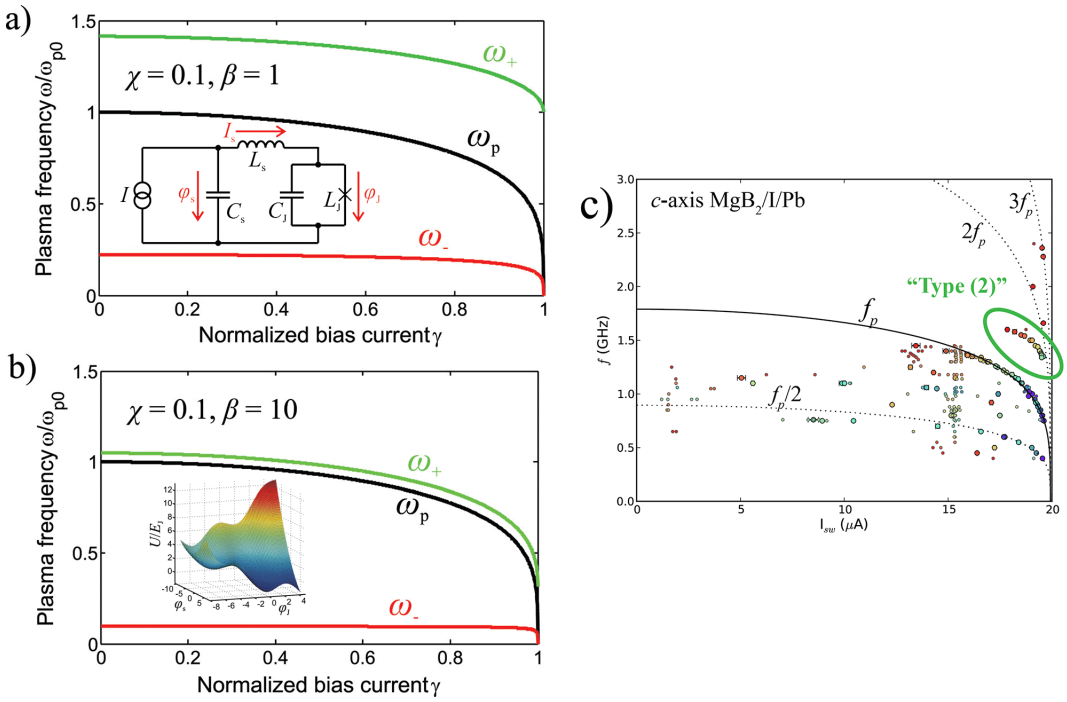


**Figure 4.32:** (a) Theoretical plasma frequency, from [13]. Inset: the circuit used in the model. Here, $\beta = L_S/L_{J0}$ gives the ratio between the inductance on the "shell circuit" and the zero-bias Josephson inductance $L_{J0} = \Phi_0/(2\pi I_0)$, and $\chi = C_J/C_S$ is the ratio of the capacitance of the junction itself, and the capacitance placed in the shell circuit. (b) Results of the same model, with a shell inductance 10 times greater than the Josephson inductance. Inset: the two-dimensional washboard potential arising from their model. (c) Measurements of our $c$-axis $MgB_2$/I/Pb junction. The arc labeled "Type (2)" bears some similarity to $\omega_+$, and is difficult to account for otherwise. ((a) and (b) reprinted from Kaiser et al., Journal of Applied Physics, 109(9), 2011, with the permission of AIP Publishing [13].)

Here, $\beta = L_S/L_{J0}$ gives the ratio between the inductance on the "shell circuit" and the zero-bias Josephson inductance $L_{J0} = \Phi_0/(2\pi I_0)$, and $\chi = C_J/C_S$ is the ratio of the capacitance of the junction itself and the capacitance placed in the shell circuit.

They fabricated an LC circuit in parallel with a Nb/$AlO_x$/Nb junction, and observed resonances at $f_p$ and its harmonics, together with these new normal modes and their harmonics.

In contrast, we did not have a separate LC circuit coupled to our junction. It is possible that the geometry of our devices themselves could contribute a similar effect, but this does not appear likely. It is also possible that this could be evidence of the elusive Leggett mode: it is modeled as a harmonic oscillator, coupled with the washboard potential [171].

For the $MgB_2$/I/Sn junction, I did not observe such a clear feature: those points between $f_p$ and $2f_p$ appear to better match $3f_p/2$. This may be due to its far larger critical current and capacitance, which could collapse the $\omega_+$ resonance onto $\omega_p$.

However, any such attribution for the source of this feature in our results remains speculative.

**Type (3)**

A second family, seen from ∼13 to ∼15 $\mu$A on Figure 4.21, seems much like $f_p$ (and its harmonics) for a lower $I_0$ and $C$. This is highlighted in Figure 4.33; here, the fit uses $I_0 = 15.4$ $\mu$A and $C = 320$ pF. (These parameters, especially the capacitance, are far more tentative than those above, due to the relative lack of data points, and the inability to use the threshold power to distinguish between arcs.)

Similar features also appear on Figure 4.20 near ∼70 and ∼80 $\mu$A, but only at 1.7 and 1.8 GHz. These are indicated as type (3) on Figure 4.19.

It is well-established that, if two junctions are coupled, then the switching of one junction from the superconducting-to-normal state can induce the other to switch at the same time [52]. Our experimental system does include separate junctions in close proximity to each other, connected by a superconducting plane of magnesium diboride. So, it is possible that multiple junctions could be coupled (though highly detuned from each other) which could, in principle, produce similar features.

However, there are actually three junctions participating in the measurement: the "current bias junction," the "measured junction," and the "voltage measurement junction," as shown in Figure 2.12. These resonances (and each of the others shown in Figures 4.20 and 4.21) remained consistent when the bias and measurement junctions were exchanged.

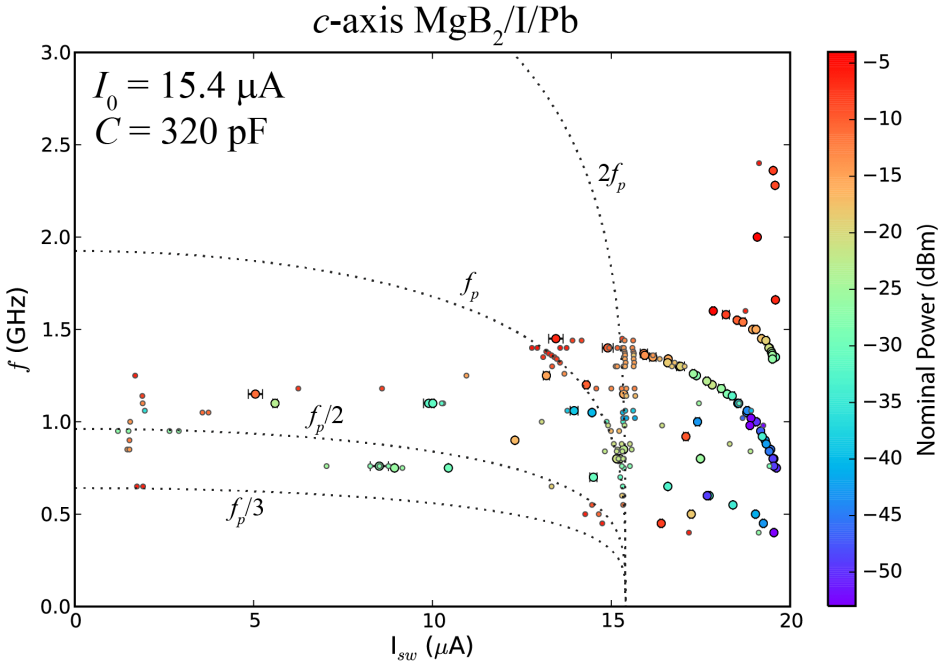


**Figure 4.33:** Applied microwave frequency vs. switching current, for the $c$-axis $MgB_2$/I/Pb junction, as in Figure 4.21. The resonances of "Type (3)" appear similar to those for a junction with $I_0 = 15.4$ $\mu$A and $C = 320$ pF, for which the fit according to Equation 4.5 and its harmonics are shown.

If the current bias junction had a lower critical current than the measured junction, then the measured junction should have been very likely to switch at that current, before its own critical current was reached, whether or not microwaves were applied. Instead, I never observed switches at this lower current in the absence of microwaves (even at higher temperatures), and they were only present at certain frequencies and powers when microwaves were applied.

Additionally, each of the junctions on a single chip must have different critical currents and capacitances from each other due to the fabrication methods. Exchanging the current bias and voltage measurement junctions was a simple matter of exchanging BNC cables at the breakout box at the top of the cryostat. Doing so should have ensured that these features would shift or be absent altogether. However, they remained the same. So, this cannot have been an artifact of the presence of the current bias junction.

So, although I have been able to exclude some possibilities, I have not been able to explain the source of this feature.

**Type (4)**

A further variety of resonance that occurred in both samples is indicated as type (4) on Figure 4.19. Unlike each of the other types of resonance, these have a number of distinct features.

First, they tend to span a wide range of currents for observations at a single frequency (e.g. Figure 4.19), rather than being concentrated within a range of currents. Second, for each of the other resonances, the resonant current is very nearly equal to the current at the lowest power for which it is observed, and remains near this current over a reasonable range of powers. These, in contrast, have their most rapid changes in current at low power, and evolve toward a more stable value at higher powers. Third, at certain powers, they tend to approach very low currents. Finally, they usually exhibited an escape rate peak at all powers, rather than only near the critical power to excite the resonance.

For Figure 4.21, I most often chose the "resonant current" as the local maximum in the escape rate for the lowest power at which this type of resonance appeared. In retrospect, this may have been inappropriate, and it is difficult to establish a single value, based on this type of measurement. This produced many of the small points on this figure to have a "scattered" appearance (aside from those associated with Type (3)).

For Figure 4.21, I was more selective, and generally chose to attribute these to lower resonant currents.

Resonances of Type (4) may explain a curious fact of our experiments. In each of the junctions we tested, our collaborators at Temple and Penn State had previously measured them, and had not observed any supercurrent. However, we did observe a supercurrent in each of these cases.

Their measurement systems were not filtered for high frequencies as ours were. If sufficient power at appropriate frequencies reached the junction (e.g. from wireless internet or cell phones), that may have prevented any supercurrent from being observed. This possibility remains speculative in the absence of further measurements.

As noted in Section 4.4.1, the resonances at $f_p/n$ (such as curve (1)) are largely unaffected by the presence of the other curve families. However, the emergence of curves (4) changes the populations

in curves (2) and (3) substantially. So it appears that each of the unresolved feature types (2-4) are correlated, and may share a single physical explanation.

### 4.5.2 Escape Temperature

In Section 4.4.4, I explored the switching of these junctions from the superconducting to the normal states, in the absence of microwaves, across temperatures. Fitting the escape rate to acquire an escape temperature revealed two surprising features.

**Departure of $T_{esc}$ from $T_{MC}$**

For all three experiments (one for the "terraced" $MgB_2$/I/Sn junction, two for the $c$-axis $MgB_2$/I/Pb junction), the escape temperature is nearly 1.3 times the measured temperature for most of the temperature range above the crossover. On a linear scale, this difference in slope is very clear; on a log-log scale (Figures 4.28(b) and 4.29(b,d)), this causes the curve to lie parallel to, but offset from, the curve for $T_{esc} = T_{MC}$.

This difference in slope is remarkably consistent for these three experiments. Figure 4.30 shows the results of all three superimposed on the same plot.

Second, for both experiments on the $c$-axis $MgB_2$/I/Pb junction, the fit temperature $T_{esc}$ becomes a near-match with the measured temperature $T_{MC}$, above $\sim 2.5$ K, rather than remaining $\sim$1.3 times larger. This result would be rather tentative if only the earlier experiment's results were considered: measurements were only made at three temperatures above 1 K (at 1.87, 1.96, and 4.57 K). Our goal at the time was only to observe the crossover temperature. Its results, however, are entirely consistent with those from the later experiment (with a slightly reduced critical current), increasing our confidence that this is a physical effect, rather than an artifact of some experimental error.

Neither of these differences has been accounted for in theoretical analyses of more traditional single-gap/single-gap junctions. However, a similar feature has been observed by Claeson et al. [14] for switching experiments on grain boundary Josephson junctions made from the high-$T_c$ superconductor $YBa_2Cu_3O_{7-\delta}$. There, they use thermal activation theory to extract a theoretical standard deviation, rather than an escape temperature, as shown in Figure 4.34(b).

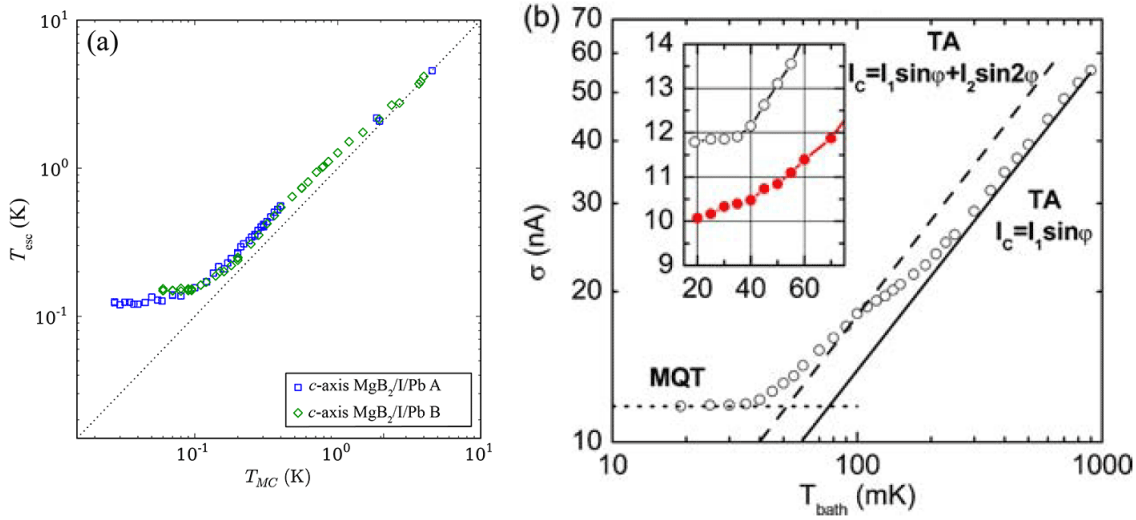


**Figure 4.34:** (a) $T_{esc}$ extracted from fits to the escape rate vs. the temperature measured at the mixing chamber thermometer $T_{MC}$ for the $c$-axis $MgB_2$/I/Pb junction, as reported in Section 4.4.4. (b) Standard deviation vs. temperature, for a $YBa_2Cu_3O_{7-\delta}$ grain boundary Josephson junction [14]. In both cases, the measured results match thermal activation (TA) theory above a certain temperature (∼2.5 K in (a) and ∼200 mK in (b)). Then, there is a transition to a different, parallel slope on this log-log scale. Finally, there is a transition to macroscopic quantum tunneling (MQT), below ∼100mK in (a), and ∼50 mK in (b). ((b) Reproduced from T. Claeson et al., "Macroscopic quantum phenomena in high critical temperature superconducting Josephson junctions", Journal of Superconductivity and Novel Magnetism, 19(3):341-347, 2006, with permission of Springer. [14])

Claeson et al. found that the standard deviation matched that predicted by thermal activation (TA) theory from ∼1 Kelvin down to ∼200 mK; between ∼200 mK and ∼50 mK, there was a shift to a different, parallel slope on their log-log plot of standard deviation vs. temperature. Finally, below ∼50 mK, the system transitioned to macroscopic quantum tunneling (MQT).

They attribute this shift to the d-wave order parameter symmetry of the Cooper pairs in the high-temperature superconductor, combined with the construction of their junction across grain boundaries. This led, in their analysis, to first and second harmonics in the current-phase relation: rather than $I = I_0 sin(\gamma)$ of the first Josephson relation (Equation 4.1a), it becomes $I = I_1 sin(\gamma) - I_2 sin(2\gamma)$ where $I_1$ and $I_2$ are the first and second harmonics, respectively. This second harmonic has an onset at low temperatures, which leads to an enhancement in the escape rate and an elevated standard deviation.

In contrast, the order parameter symmetry for $MgB_2$ is well-established to be s-wave [4]. So, this explanation would not appear to apply. It is possible that a theoretical model could be developed to explain this observation, but it does not yet appear in the literature.

**Anomalous Crossover Temperature**

For each of these devices, we would expect the crossover temperature to be significantly lower than our observed crossover. Using equation 4.13, we find, for the "terraced" $MgB_2$/I/Sn junction, $T_{cr} \simeq 17.7$ mK. For the *c*-axis $MgB_2$/I/Pb junction, $T_{cr} \simeq 13.7$ mK for the experiments that yielded the most fruitful results (described as Experiment B in Section 4.4.4). Assuming the capacitance did not change, $T_{cr} \simeq 19.5$ mK for the first series of experiments for this junction (Experiment A).

This is in contrast to the ∼100 mK crossover observed in Figures 4.25, 4.28, 4.29 and 4.30.

If I had only obtained these plots of $\sigma$ and $T_{esc}$ vs. $T_{MC}$, the most likely explanation would be that we have a noise floor near 100 mK (itself a difficult achievement). However, as described in Section 4.4.5, our microwave resonant activation results include features that are commonly taken as definitive evidence of quantum-mechanical escape of the phase from the potential well.

This suggests that either Equation 4.13 may not apply to hybrid junctions, or that the resonant activation results may not guarantee quantum behavior for hybrid junctions. In either case, this

suggests new avenues to pursue theoretically.

### 4.5.3 Escape Rate Features

The switching results reported in Section 4.4.4, also exhibited surprising features visible on individual histograms and escape rate plots. They remained consistent across temperature.

First, as is clear from Figure 4.35, additional features (visible as peaks in the histograms, or as kinks in the escape rate) are evident in both samples. These may be evidence of additional "noise" resonances [146] or the presence of additional resonant modes due to the combination of the single-gap and dual-gap $MgB_2$ electrodes [173]. It is unclear which interpretation is more likely at the moment.

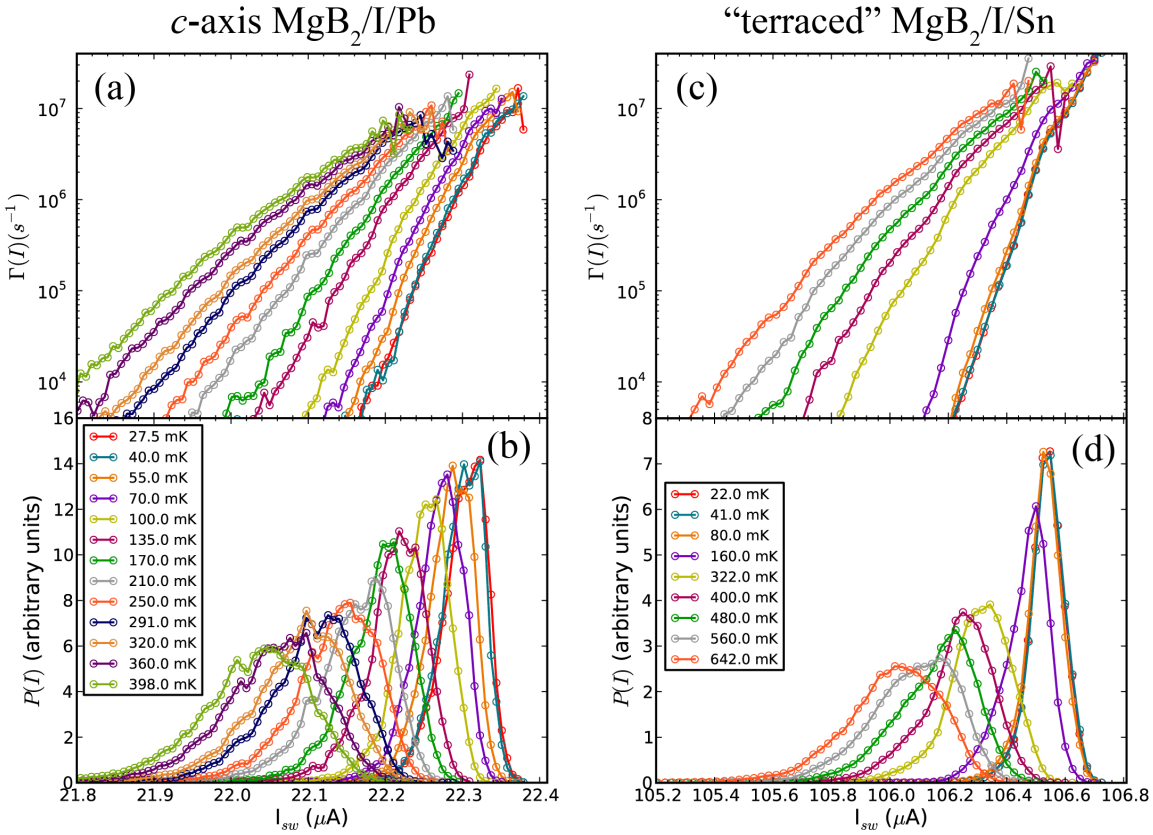


**Figure 4.35:** Escape rate (a, c) and switching current histogram (b, d) vs. current for the *c*-axis $MgB_2$/I/Pb and "terraced" $MgB_2$/I/Sn junctions, respectively. As expected, the mean switching current decreases and the distribution gets broader as the temperature increases. The primary structure of both the histograms and escape rates may be fitted rather well according to theory (compare Figures 4.4 and 4.24). Additional features (visible as peaks in the histograms, or kinks in the escape rate) are evident in both samples.

Second, we observed a feature at low escape rates that is especially prominent in the results for

the $c$-axis $MgB_2$/I/Pb junction below ~300 mK. Its consistency across a broad temperature range suggests that a physical process is at work, rather than resulting from random fluctuations that pollute a single data set. Its absence in the escape rate for the "terraced" $MgB_2$/I/Sn junctions could result from a variety of differences between these junctions. However, at the moment an interpretation remains unclear, as there are no published results, either theoretical or experimental, that show similar features.

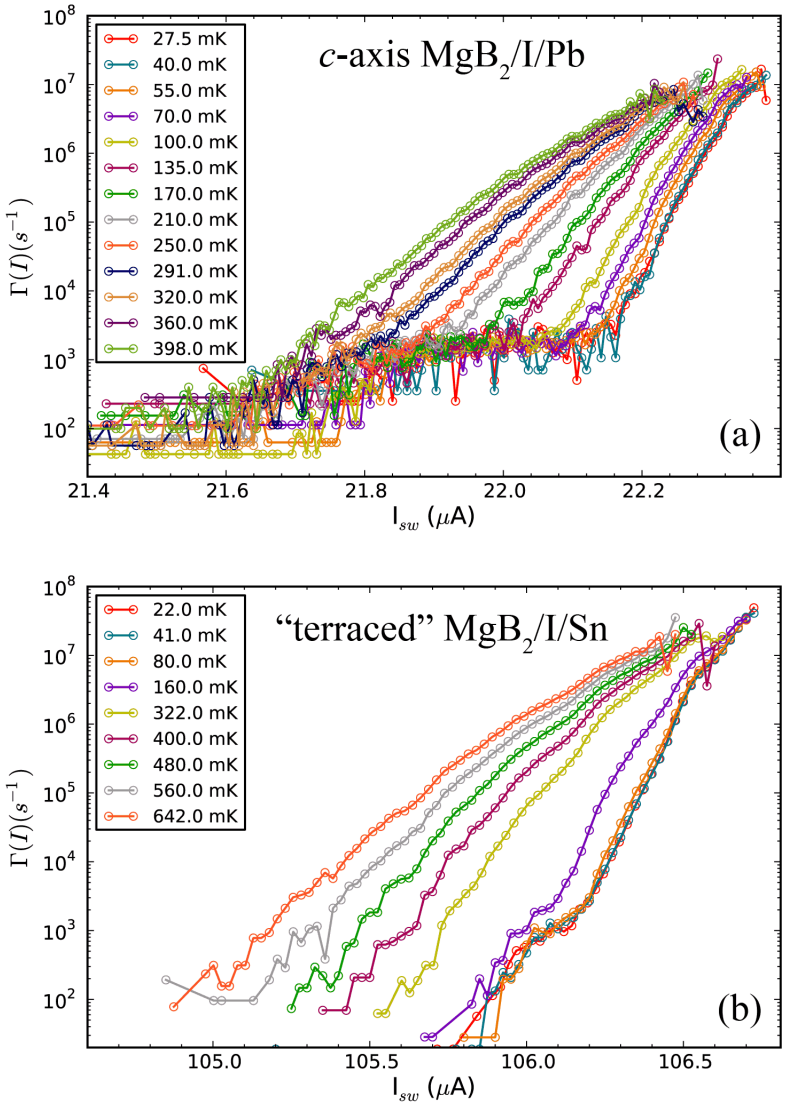


**Figure 4.36:** Escape rate vs. current, for the $c$-axis $MgB_2$/I/Pb (a) and "terraced" $MgB_2$/I/Sn (b) junctions, respectively. When considering low escape rates, an additional feature appears in the results for the $c$-axis junction. While it is true that this feature results from data with few switching events, its consistency across a broad range of temperatures suggests that a physical process is at work, rather than resulting from a random fluctuation. Its absence in the escape rate for the "terraced" $MgB_2$/I/Sn junction could result from a variety of differences between these junctions.

## 4.6 Conclusions

In this chapter, I have described the theory for superconducting-to-normal switching for conventional Josephson junctions, where both superconducting electrodes are single-gap materials.

My experimental results, the first for switching experiments on hybrid single-gap two-gap junctions, demonstrate that analysis methods developed for traditional junctions are successful when determining the resistance, capacitance, critical current, and quality factor of hybrid junctions.

Using these methods, I determined these junction parameters for two junctions with very different values and film geometries. In both cases, the conventional analysis provides consistent results, suggesting that superconducting-to-normal switching in these junctions is dominated by a single tunneling mode.

Some features, while consistent with the theory for conventional junctions, are novel due to the relatively large capacitance of these devices. In addition, I observed several features not currently explained by theory.

Both junctions proved to be highly underdamped Josephson junctions (quality factor $Q \gg 1$), which are useful for a variety of applications whether or not new physics are involved. Because my results also exhibit several signatures of quantum-mechanical behavior, these junctions may be suitable for certain quantum device applications.

# Chapter 5: Conclusions and Future Work

## 5.1 Conclusions

In this thesis, I have reported the results of my research characterizing the behavior of Josephson junctions incorporating magnesium diboride. To make these results possible, I improved, in cooperation with others, the functioning of our helium dilution refrigerator for low-noise, high-resolution measurements.

I used this system to characterize the superconducting energy gap structure of magnesium diboride, as discussed in Chapter 3. These are the highest-resolution results obtained thus far. Two gaps, while sufficient for many experimental results (including those on N/I/S junctions) are proven insufficient for these high-resolution results.

I also produced the first switching measurements in hybrid Josephson junctions, as discussed in Chapter 4. Most of the features can be explained using the theory developed for conventional junctions. It is useful to have such a body of theory to help explain our results. However, there are some as-yet unexplained features.

Several additional avenues for research are suggested by my results. I outline these in the following section.

## 5.2 Future Work

### 5.2.1 Magnetic Fields

Magnetic fields are often used in conjunction with experiments on Josephson junctions. From the earliest experiments, the response of a junction to applied magnetic fields has given conclusive proof of the Josephson effects. More recently, variations in the critical current vs. field relationship have been used to establish some novel behavior, such as in junctions incorporating high-$T_c$ superconductors. But because $MgB_2$ has been demonstrated to be a phonon-mediated $s$-wave superconductor, we do not expect any of these types of departures from conventional junction theory.

However, the main objectives for a magnetic field are different, when considering the results presented in this thesis.

For superconducting-to-normal switching experiments, the crossover temperature from classical to quantum-mechanical behavior $T_{cr}$ is a function of the critical current. The critical current is itself a function of the applied magnetic field. So, $T_{cr}$ should be controllable by a fixed applied field. Other researchers [180, 14] have used this property to prove that a leveling in plots of $\sigma$ vs. $T$ or $T_{esc}$ vs. $T$ is not due to a noise floor: no other experimental parameters were changed. This would put our results for quantum-mechanical tunneling on a more firm footing, or may reveal even more surprises.

Magnetic fields have also been used to selectively suppress the $\pi$ gap relative to the $\sigma$ gap, both in polycrystalline samples [181] and single crystals [182] of $MgB_2$. Doing so may help reveal the $\sigma$ gap in more detail, and reveal which effects depend on the presence (or weight) of the $\sigma$ and $\pi$ gaps. This would enhance the results of both Chapters 3 and 4.

On the theoretical front, it has been predicted [183] that a small feature caused by the Leggett mode should appear in the $I - V$ characteristics of a Josephson tunnel junction incorporating a two-gap superconductor. While this may be hard to distinguish among the many other features evident in such curves, it should, unlike the others, shift to different voltages in response to a weak magnetic field. This would provide compelling evidence of the Leggett mode in Josephson tunneling experiments.

### 5.2.2 Four-Wire Measurement

As indicated in Figures 2.12, 3.6 and 4.14, the bias current passed through one Pb or Sn electrode, through one junction to the $MgB_2$ plane, through another junction to a second Pb or Sn electrode, to ground. Voltage was measured from a third Pb or Sn electrode, through a third junction to the $MgB_2$ plane, through the measured junction, to the second Pb or Sn electrode, to ground.

A true four-wire measurement would have used two ends of a single Pb or Sn electrode, and two ends of the $MgB_2$ plane, as indicated in Figure 1.6. Our configuration introduced several potential complications.

The first is caused by the resistive portion shared in common between the current bias and voltage measurement sides of the experiment. The voltage measurement included cryostat as ground, through a non-superconducting silver wire, to a silver-paint contact, to the superconducting Pb or Sn electrode. The common resistance was corrected in Section 3.2.3 and was irrelevant (with the proper threshold) for the switching experiments, as discussed in Section 4.2. However, the contact between the silver wire and the Pb or Sn electrode could have formed an $NS$ junction (normal metal/superconductor junction) in series with the junction we intended to measure. This could have produced the strong peaks in the subgap region at $\Delta_{Pb}$ and $\Delta_{Sn}$ shown in Figures 3.11 and 3.12.

Whatever their source, these peaks established firm values for $\Delta_{Pb}$ and $\Delta_{Sn}$, which was useful for our fits. However, whether or not they exist in measurements of a single $MgB_2$/I/Pb or $MgB_2$/I/Sn junction (without the possibility for having an $NS$ junction in series with it) would clarify the nature of all of the subgap features, and may reveal interesting aspects of the energy gap structure of $MgB_2$ itself.

I note that although the voltage measurement also included an unnecessary junction, it should not have affected any of the measurements. By having nearly zero current pass through it, it should have remained superconducting, and been effectively equivalent to a continuation of the $MgB_2$ plane.

The current bias also passed through an additional junction, prior to reaching the measured junction. Because the voltage measurement did not include it, one might reasonably expect that it would have no effect on the results.

However, this did produce a second junction coupled with the junction we intended to study. By exchanging the junctions on the current bias and voltage measurement sides, I was able to conclude that it did not directly produce the as-yet unexplained features in the switching results (as discussed in Section 4.5.1). However, full theoretical analyses of the switching behavior of Josephson junctions coupled to external systems tends to be rather complex. It would be best to exclude them entirely.

We used our three-wire measurement technique for several reasons. First, we were only able to ensure reliable contact with the Pb or Sn electrodes; direct contact with the $MgB_2$ film can be problematic. With only limited samples and experiments available, the risk of a useless device was

very great. Second, using the cryostat as system ground allowed us to test substantially more devices during each cooldown. Third, all of the lines and filters were designed to use the cryostat as the ground of each junction; if we had made a four-wire measurement with our existing electronics, the filtering would have been ineffective.

Our system was designed for switching measurements on the Nb/I/Nb junctions described in Section 2.6. Each of the above issues would have been irrelevant or nonexistent for such devices. We are reasonably confident that our using it for a different type of experimental device did not compromise our results, but it would be useful to make additional measurements to ensure that that is the case.

### 5.2.3 On-Chip Isolation

As discussed in Chapter 4, many applications for Josephson junctions desire a high quality factor $Q$, at high frequency. However, at these frequencies, the impedance is dominated by the wires leading to the junction, rather than the junction itself. Several researchers have mitigated this problem by using isolation circuits.

Although we did use extensive filtering, there were still several centimeters of wires between the last filter stage and the junction itself. Using isolation within millimeters of the junction should allow $Q$ to be increased, expanding the potential of similar devices to be used for applications.

### 5.2.4 Additional Barrier Geometries

As is clear from Chapter 3, tunneling along the $c$-axis presents different behavior from tunneling along the $a$-$b$ plane. Some of the characteristics of the switching behavior may also be geometry-dependent. But it is difficult to tell from my results for two reasons. First, the only two samples for which we were able to produce these results had little ($\sim 7\%$) to no ($< 1\%$) direct tunneling with the $\sigma$ gap. Second, other junction properties (notably the critical current) were vastly different.

So, it would be useful to explore similar results varying the tunneling direction (and therefore the proportion of direct tunneling with the $\sigma$ gap), while keeping all other properties fixed. Although it may be possible to achieve a similar effect using magnetic fields (as discussed in Section 5.2.1), it

would be useful to exclude the possibility that magnetic fields are producing some other undesired effect.

### 5.2.5 All-$MgB_2$ Junctions

The theory of hybrid Josephson junctions is still being explored, with relatively little experimental verification of the results predicted thus far. Moving to a two-gap/two-gap junction should reveal even more interesting physics, although it may be a step ahead of the theory.

However, one of the primary appeals of magnesium diboride is its high critical temperature. If durable, high-quality Josephson junctions with consistent parameters are produced, capable of operation at a temperature an order of magnitude higher than conventional junctions, a wide array of applications becomes far more viable. These include the extreme sensitivity to magnetic fields of SQUIDs (superconducting quantum interference devices), electronics taking advantage of the extreme nonlinearity of Josephson junctions, single-photon detectors, etc.

But before any of these can be considered, the behavior of such junctions must be well-characterized. Measurements such as those presented in this thesis provide a step in that direction.

# Bibliography


[1] Andrew J. Berkley. *A Josephson Junction Qubit.* PhD thesis, University of Maryland at College Park, 2003.

[2] Peter Schmüser. Superconductivity, 2002. Institut für Experimentalphysik der Universität Hamburg.

[3] Antonio Barone and Gianfranco Paternò. *Physics and Applications of the Josephson Effect*, page 4. Wiley-VCH Verlag GmbH & Co. KGaA, 2005.

[4] X X Xi. Two-band superconductor magnesium diboride. *Rep. Prog. Phys.*, 71(11):116501, 2008.

[5] H. J. Choi, D. Roundy, H. Sun, M. L. Cohen, and S. G. Louie. The origin of the anomalous superconducting properties of $MgB_2$. *Nature*, 418(6899):758 – 760, AUG 15 2002.

[6] Toshiba. *2SK117 Data Sheet*, 2003. TOSHIBA Field Effect Transistor - Silicon N Channel Junction Type.

[7] Wenqing Dai, Ke Chen, X. X. Xi, and Qi Li. Tunneling investigation of the electron scattering effect on the momentum-dependent energy gap distribution in $MgB_2$. *J. Appl. Phys.*, 113(8), FEB 28 2013.

[8] Yi Cui. *Magnesium Diboride Thin Films and Devices.* PhD thesis, Penn State University, 2007.

[9] M A Nordahn, M H Manscher, J Mygind, and L V Filippenko. Experimental observation of subharmonic gap structures in long Josephson junctions. *Superconductor Science and Technology*, 12(11):963, 1999.

[10] E. R. Margine and F. Giustino. Anisotropic Migdal-Eliashberg theory using Wannier functions. *Phys. Rev. B*, 87:024505, Jan 2013.

[11] A. Floris, G. Profeta, N. N. Lathiotakis, M. Lüders, M. A. L. Marques, C. Franchini, E. K. U. Gross, A. Continenza, and S. Massidda. Superconducting properties of $MgB_2$ from first principles. *Phys. Rev. Lett.*, 94:037004, Jan 2005.

[12] Z. E. Thrailkill, J. G. Lambert, S. A. Carabello, and R. C. Ramos. Resonant activation of a current-biased Josephson junction near the classical-quantum crossover. arXiv:0910.2901 [cond-mat.supr-con].

[13] Ch. Kaiser, T. Bauch, F. Lombardi, and M. Siegel. Quantum phase dynamics in an LC shunted Josephson junction. *Journal of Applied Physics*, 109(9), 2011.

[14] Tord Claeson, Floriana Lombardi, Thilo Bauch, Tobias Lindström, Per Delsing, Antonio Barone, Francesco Tafuri, and Giacomo Rotoli. Macroscopic quantum phenomena in high critical temperature superconducting Josephson junctions. *Journal of Superconductivity and Novel Magnetism*, 19(3):341–347, 2006.

[15] W.E. Pickett. The next breakthrough in phonon-mediated superconductivity. *Physica C*, 468(2):126 – 135, 2008.

[16] Philip Ball. Material witness: Higher $T_c$. *Nat. Mater.*, 5:346, 2006.

[17] Michael Tinkham. *Introduction to Superconductivity: Second Edition*. Dover Publications, 1996.

[18] Antonio Barone and Gianfranco Paternò. *Physics and Applications of the Josephson Effect*. Wiley-VCH Verlag GmbH & Co. KGaA, 2005.

[19] Terry P. Orlando and Kevin A. Delin. *Foundations of Applied Superconductivity*. Addison-Wesley, 1991.

[20] T. Van Duzer and C. W. Turner. *Principles of Superconductive Devices and Circuits*. Elsevier, 1981.

[21] Paul Seidel. Josephson effects in iron based superconductors. *Superconductor Science and Technology*, 24(4):043001, 2011.

[22] D Daghero and R S Gonnelli. Probing multiband superconductivity by point-contact spectroscopy. *Supercon. Sci. Technol.*, 23(4):043001, 2010.

[23] I.I. Mazin and V.P. Antropov. Electronic structure, electron-phonon coupling, and multiband effects in $MgB_2$. *Physica C*, 385(1–2):49 – 65, 2003.

[24] M. Zehetmayer. A review of two-band superconductivity: materials and effects on the thermodynamic and reversible mixed-state properties. *Superconductor Science and Technology*, 26(4):043001, 2013.

[25] H. Kamerlingh-Onnes. Further experiments with liquid helium. C. on the change of electric resistance of pure metals at very low temperatures, etc. IV. The resistance of pure mercury at liquid helium temperatures. *Comm. Phys. Leb. Univ. Leiden*, 120b:13 – 18, 1911.

[26] M. Debessai, T. Matsuoka, J.J. Hamlin, W. Bi, Y. Mengy, K. Shimizu, and J.S. Schilling. Periodic table of superconductivity. *J. Phys.: Conf. Series*, 215:012034, 2010.

[27] Michael Tinkham. *Introduction to Superconductivity: Second Edition*, page 2. Dover Publications, 1996.

[28] W. Meissner and R. Ochsenfeld. Ein neuer effekt bei eintritt der supraleitfähigkeit. *Naturwissenschaften*, 21(44):787–788, Nov 1933.

[29] F. London and H. London. The electromagnetic equations of the supraconductor. *Proceedings of the Royal Society of London A: Mathematical, Physical and Engineering Sciences*, 149(866):71 – 88, 1935.

[30] Fritz London. *Superfluids, Vol. 1: Macroscopic theory of superconductivity*, volume 1. 1950.

[31] Terry P. Orlando and Kevin A. Delin. *Foundations of Applied Superconductivity*, page 7. Addison-Wesley, 1991.

[32] Lev Davidovich Landau and VL Ginzburg. On the theory of superconductivity. *Zh. Eksp. Teor. Fiz.*, 20:1064, 1950.

[33] J. Bardeen, L. N. Cooper, and J. R. Schrieffer. Microscopic theory of superconductivity. *Phys. Rev.*, 106:162–164, Apr 1957.

[34] M.L. Cohen and P.W. Anderson. Comments on the maximum superconducting transition temperature. In D.H. Douglass, editor, *Superconductivity in d- and f-Band Metals*, pages 17–27. American Inst. Physics, 1972.

[35] J. G. Bednorz and K. A. Müller. Possible high $T_c$ superconductivity in the Ba-La-Cu-O system. *Zeitschrift für Physik B Condensed Matter*, 64(2):189–193.

[36] Jun Nagamatsu, Norimasa Nakagawa, Takahiro Muranaka, Yuji Zenitani, and Jun Akimitsu. Superconductivity at 39 K in magnesium diboride. *Nature*, 410(6824):63, 2001.

[37] Yoichi Kamihara, Takumi Watanabe, Masahiro Hirano, and Hideo Hosono. Iron-based layered superconductor La[O1-xFx]FeAs (x = 0.05-0.12) with Tc = 26 K. *Journal of the American Chemical Society*, 130(11):3296–3297, 2008. PMID: 18293989.

[38] Evgeni S. Penev, Alex Kutana, and Boris I. Yakobson. Can two-dimensional boron superconduct? *Nano Letters*, 2016.

[39] Yinchang Zhao, Shuming Zeng, and Jun Ni. Superconductivity in two-dimensional boron allotropes. *Phys. Rev. B*, 93:014502, Jan 2016.

[40] Leon N. Cooper. Bound electron pairs in a degenerate Fermi gas. *Phys. Rev.*, 104:1189–1190, Nov 1956.

[41] Terry P. Orlando and Kevin A. Delin. *Foundations of Applied Superconductivity*, page 575. Addison-Wesley, 1991.

[42] B.D. Josephson. Possible new effects in superconductive tunnelling. *Physics Letters*, 1(7):251 – 253, 1962.

[43] Brian Josephson. University of Cambridge lectures on superconductivity: Electronics: Josephson junctions. Video, 2011. Applied Superconductivity and Cryoscience Group. http://www.msm.cam.ac.uk/ascg/lectures/electronics/tunnelling.php.

[44] Antonio Barone and Gianfranco Paternò. *Physics and Applications of the Josephson Effect*, page 23. Wiley-VCH Verlag GmbH & Co. KGaA, 2005.

[45] P. W. Anderson and J. M. Rowell. Probable observation of the Josephson superconducting tunneling effect. *Phys. Rev. Lett.*, 10:230–232, Mar 1963.

[46] Sidney Shapiro. Josephson currents in superconducting tunneling: The effect of microwaves and other observations. *Phys. Rev. Lett.*, 11:80–82, Jul 1963.

[47] T. Van Duzer and C. W. Turner. *Principles of Superconductive Devices and Circuits*, pages 186–187. Elsevier, 1981.

[48] E.L. Wolf. *Principles of Electron Tunneling Spectroscopy: Second Edition*. International Series of Monographs on Physics. OUP Oxford, 2011.

[49] A.O. Caldeira and A.J. Leggett. Quantum tunnelling in a dissipative system. *Annals of Physics*, 149(2):374 – 456, 1983.

[50] John M. Martinis, Michel H. Devoret, and John Clarke. Energy-level quantization in the zero-voltage state of a current-biased Josephson junction. *Phys. Rev. Lett.*, 55:1543–1546, Oct 1985.

[51] R.C. Ramos, M.A. Gubrud, A.J. Berkley, J.R. Anderson, C.J. Lobb, and F.C. Wellstood. Design for effective thermalization of junctions for quantum coherence. *IEEE Transactions on Applied Superconductivity*, 11(1):998–1001, Mar 2001.

[52] Philip R. Johnson, Frederick W. Strauch, Alex J. Dragt, Roberto C. Ramos, C. J. Lobb, J. R. Anderson, and F. C. Wellstood. Spectroscopy of capacitively coupled Josephson-junction qubits. *Phys. Rev. B*, 67:020509, Jan 2003.

[53] H. Suhl, B. T. Matthias, and L. R. Walker. Bardeen-Cooper-Schrieffer theory of superconductivity in the case of overlapping bands. *Phys. Rev. Lett.*, 3(12):552–554, Dec 1959.

[54] V. A. Moskalenko. Superconductivity in metals with overlapping energy bands. *Fiz. Met. Metallov*, 8:503–513, 1959.

[55] V. A. Moskalenko. The theory of superconductors with overlapping energy bands. *Soviet Physics Uspekhi*, 17(3):450, 1974.

[56] A. B. Migdal. Interaction between electrons and lattice vibrations in a normal metal. *Sov. Phys. JETP*, 7(6):993, 1958.

[57] G. M. Eliashberg. Interactions between electrons and lattice vibrations in a superconductor. *Sov. Phys. JETP*, 11(3):966, 1960.

[58] Antonio Barone and Gianfranco Paternò. *Physics and Applications of the Josephson Effect*, pages 56–58. Wiley-VCH Verlag GmbH & Co. KGaA, 2005.

[59] D. M. Ginsberg, P. L. Richards, and M. Tinkham. Apparent structure on the far infrared energy gap in superconducting lead and mercury. *Phys. Rev. Lett.*, 3:337–338, Oct 1959.

[60] P. L. Richards. Anisotropy of the superconducting energy gap in pure and impure tin. *Phys. Rev. Lett.*, 7:412–413, Dec 1961.

[61] G. I. Rochlin. Determination of the anisotropy of the energy gap in superconducting Pb by superconductive tunneling. *Phys. Rev.*, 153:513–532, Jan 1967.

[62] J.W. Hafstrom, R.M. Rose, and M.L.A. Macvicar. Evidence for a second energy gap in superconducting niobium. *Physics Letters A*, 30(7):379 – 380, 1969.

[63] B.L. Blackford. Energy gap anisotropy in bulk Pb via tunneling. *Physica*, 55:475 – 483, 1971.

[64] B. L. Blackford. Evidence for splitting of phonon structures in single-crystal Pb tunneling. *Phys. Rev. B*, 5:1171–1174, Feb 1972.

[65] L. J. Vieland and A. W. Wicklund. Specific heat of niobium-tin. *Phys. Rev.*, 166:424–431, Feb 1968.

[66] P.W. Anderson. Theory of dirty superconductors. *Journal of Physics and Chemistry of Solids*, 11(1):26 – 30, 1959.

[67] James W. Garland. Mechanisms for superconductivity in the transition metals. *Phys. Rev. Lett.*, 11:111–114, Aug 1963.

[68] K.R. Milkove, J. Bostock, and M.L.A. MacVicar. A new perspective on anisotropy and multiple energy gaps in superconductors. *Solid State Communications*, 19(11):1095 – 1097, 1976.

[69] J. Bostock, Kovi Agyeman, M. H. Frommer, and M. L. A. MacVicar. Determining accurate superconducting tunneling energy gaps: Anisotropy in single-crystal Nb. *Journal of Applied Physics*, 44(12):5567–5569, 1973.

[70] G. Binnig, A. Baratoff, H. E. Hoenig, and J. G. Bednorz. Two-band superconductivity in Nb-doped $SrTiO_3$. *Phys. Rev. Lett.*, 45:1352–1355, Oct 1980.

[71] B. L. Blackford and K. Hill. A tunneling investigation of energy-gap anisotropy in superconducting bulk tin crystals. *Journal of Low Temperature Physics*, 43(1):25–36, 1981.

[72] D.H. Lee and J. Ihm. Two-band model for high $T_c$ superconductivity in $La_{2-x}(Ba,Sr)_xCuO_4$. *Solid State Commun.*, 62(12):811 – 815, 1987.

[73] V.Z. Kresin and S.A. Wolf. Multigap structure in the cuprates. *Physica C*, 169(5–6):476 – 484, 1990.

[74] P. Seidel and M. Turtenwald. Multi-gap model for tunneling in high-$T_c$ superconductors. *Physica Status Solidi (a)*, 115(1):273–278, 1989.

[75] V. A. Moskalenko, M. E. Palistrant, and V. M. Vakalyuk. High-temperature superconductivity and the characteristics of the electronic energy spectrum. *Soviet Physics Uspekhi*, 34(8):717, 1991.

[76] A. Hahn, S. Hofmann, A. Krause, and P. Seidel. Tunneling results on gap anisotropy in niobium. *Physica C*, 296(1–2):103 – 118, 1998.

[77] D. Daghero, M. Tortello, G. A. Ummarino, and R. S. Gonnelli. Directional point-contact Andreev-reflection spectroscopy of Fe-based superconductors: Fermi surface topology, gap symmetry, and electron-boson interaction. *Reports on Progress in Physics*, 74(12):124509, 2011.

[78] A. Floris, A. Sanna, S. Massidda, and E. K. U. Gross. Two-band superconductivity in Pb from *ab initio* calculations. *Phys. Rev. B*, 75:054508, Feb 2007.

[79] J.G. Rodrigo and S. Vieira. STM study of multiband superconductivity in $NbSe_2$ using a superconducting tip. *Physica C*, 404(1–4):306 – 310, 2004. Proceedings of the Third European Conference on Vortex Matter in Superconductors at Extreme Scales and Conditions.

[80] Y. Noat, J. A. Silva-Guillén, T. Cren, V. Cherkez, C. Brun, S. Pons, F. Debontridder, D. Roditchev, W. Sacks, L. Cario, P. Ordejón, A. Carcía, and E. Canadell. Quasiparticle spectra of 2H-$NbSe_2$: Two-band superconductivity and the role of tunneling selectivity. *Phys. Rev. B*, 92:134510, Oct 2015.

[81] A. J. Leggett. Number-phase fluctuations in two-band superconductors. *Prog. Theor. Phys.*, 36(5):901–930, Nov 1966.

[82] Diana Dulić, A. Pimenov, D. van der Marel, D. M. Broun, Saeid kamal, W. N. Hardy, A. A. Tsevetkov, I. M. Sutjaha, Ruixing Liang, A. A. Menovsky, A. Loidl, and S. S. Saxena. Observation of the transverse optical plasmon in $SmLa_{0.8}Sr_{0.2}CuO_{4-\delta}$. *Phys. Rev. Lett.*, 86:4144–4147, Apr 2001.

[83] G. Blumberg, A. Mialitsin, B. S. Dennis, M. V. Klein, N. D. Zhigadlo, and J. Karpinski. Observation of Leggett's collective mode in a multiband $MgB_2$ superconductor. *Phys. Rev. Lett.*, 99:227002, Nov 2007.

[84] Daixiang Mou, Rui Jiang, Valentin Taufour, Rebecca Flint, S. L. Bud'ko, P. C. Canfield, J. S. Wen, Z. J. Xu, Genda Gu, and Adam Kaminski. Strong interaction between electrons and collective excitations in multiband superconductor $MgB_2$. *Phys. Rev. B*, 91:140502.

[85] Saroj Kumar Das, Amita Bedar, Aadithya Kannan, and Kabeer Jasuja. Aqueous dispersions of few-layer-thick chemically modified magnesium diboride nanosheets by ultrasonication assisted exfoliation. *Scientific Reports*, 5:10522, 2015.

[86] Robinson M. Swift and David White. Low temperature heat capacities of magnesium diboride ($MgB_2$) and magnesium tetraboride ($MgB_4$). *Journal of the American Chemical Society*, 79(14):3641–3644, 1957.

[87] Antonella Del Rosso. World-record current in a superconductor, Apr 2014. http://home.cern/about/updates/2014/04/world-record-current-superconductor.

[88] Dipak Patel, Md Shahriar Al Hossain, Khay Wai See, Wenbin Qiu, Hiroki Kobayashi, Zongqing Ma, Seong Jun Kim, Jonggi Hong, Jin Yong Park, Seyong Choi, Minoru Maeda, Mohammed Shahabuddin, Matt Rindfleisch, Mike Tomsic, Shi Xue Dou, and Jung Ho Kim. Evaluation of persistent-mode operation in a superconducting $MgB_2$ coil in solid nitrogen. *Superconductor Science and Technology*, 29(4):04LT02, 2016.

[89] R. Musenich, V. Calvelli, S. Farinon, R. Battiston, W. J. Burger, and P. Spillantini. A magnesium diboride superconducting toroid for astroparticle shielding. *IEEE Transactions on Applied Superconductivity*, 24(3):1–4, June 2014.

[90] K. Vinod, Neson Varghese, and U. Syamarasad. Superconductivity of $MgB_2$ in the BCS framework with emphasis on extrinsic effects on critical temperature. *Superconductor Science and Technology*, 20(10):R31, 2007.

[91] D. G. Hinks, H. Claus, and J. D. Jorgensen. The complex nature of superconductivity in $MgB_2$ as revealed by the reduced total isotope effect. *Nature*, 411(6836):457–460, Apr 2001.

[92] S. L. Budko, G. Lapertot, C. Petrovic, C. E. Cunningham, N. Anderson, and P. C. Canfield. Boron isotope effect in superconducting $MgB_2$. *Phys. Rev. Lett.*, 86:1877–1880, Feb 2001.

[93] Hyoung Joon Choi, David Roundy, Hong Sun, Marvin L. Cohen, and Steven G. Louie. First-principles calculation of the superconducting transition in $MgB_2$ within the anisotropic Eliashberg formalism. *Phys. Rev. B*, 66(2):020513, Jul 2002.

[94] I. I. Mazin, O. K. Andersen, O. Jepsen, A. A. Golubov, O. V. Dolgov, and J. Kortus. Comment on "First-principles calculation of the superconducting transition in $MgB_2$ within the anisotropic Eliashberg formalism". *Phys. Rev. B*, 69(5):056501, Feb 2004.

[95] Hyoung Joon Choi, David Roundy, Hong Sun, Marvin L. Cohen, and Steven G. Louie. Reply to "Comment on 'First-principles calculation of the superconducting transition in $MgB_2$ within the anisotropic Eliashberg formalism' ". *Phys. Rev. B*, 69(5):056502, Feb 2004.

[96] F. Bouquet, R. A. Fisher, N. E. Phillips, D. G. Hinks, and J. D. Jorgensen. Specific heat of $MgB_2$: Evidence for a second energy gap. *Phys. Rev. Lett.*, 87:047001, Jul 2001.

[97] M. Iavarone, G. Karapetrov, A. E. Koshelev, W. K. Kwok, G. W. Crabtree, D. G. Hinks, W. N. Kang, Eun-Mi Choi, Hyun Jung Kim, Hyeong-Jin Kim, and S. I. Lee. Two-band superconductivity in $MgB_2$. *Phys. Rev. Lett.*, 89:187002, Oct 2002.

[98] Ke Chen, Wenqing Dai, C.G. Zhuang, Qi Li, Steve Carabello, Joseph G. Lambert, Jerome T. Mlack, Roberto C. Ramos, and X. X. Xi. Momentum-dependent multiple gaps in magnesium diboride probed by electron tunnelling spectroscopy. *Nat. Commun.*, 3:619, Jan 2012.

[99] Steven Carabello, Joseph G. Lambert, Jerome Mlack, Wenqing Dai, Qi Li, Ke Chen, Daniel Cunnane, C.G. Zhuang, X. X. Xi, and Roberto C. Ramos. Energy gap substructures in conductance measurements of $MgB_2$-based Josephson junctions: beyond the two-gap model. *Superconductor Science and Technology*, 28(5):055015, 2015.

[100] F. Pobell. *Matter and Methods at Low Temperatures*, page 149. Springer-Verlag Berlin Heidelberg, 3 edition, 2007.

[101] H.E. Hall, P.J. Ford, and K. Thompson. A helium-3 dilution refrigerator. *Cryogenics*, 6(2):80 – 88, 1966.

[102] B. Neganov, N. Borisov, and M. Liburg. A method of producing very low temperatures by dissolving He3 in He4. *Soviet Physics JETP*, 23(6):959 – 1151, 1966.

[103] N. Craig and T Lester. *Hitchhikers Guide to the Dilution Refrigerator Version 2.00*. Marcus Lab, Harvard University, 2004.

[104] Oxford Instruments Superconductivity Limited. *KelvinoxMX400 Dilution Refrigerator System Operator's Handbook*, 2005.

[105] G. Frossati. Experimental techniques: Methods for cooling below 300 mK. *Journal of Low Temperature Physics*, 87(3-4):593–633, 1992.

[106] N.H. Balshaw. *Practical Cryogenics*. Oxford Instruments Superconductivity Limited, 2001.

[107] G. Jr. Nunes and K.A. Earle. Dilution refrigerators. In R.C. Richardson and R.N. Smith, editors, *Experimental Techniques in Condensed Matter Physics at Low Temperatures*, page 45. Advanced Book Classics, 1988.

[108] F. Pobell. *Matter and Methods at Low Temperatures*. Springer-Verlag Berlin Heidelberg, 3 edition, 2007.

[109] R.S. Germain. Electric and magnetic isolation. In R.C. Richardson and R.N. Smith, editors, *Experimental Techniques in Condensed Matter Physics at Low Temperatures*, pages 149–150. Advanced Book Classics, 1988.

[110] Jonathan L. Tucker. *Optimizing Low-Current Measurements and Instruments*. Keithley Instruments, Inc., 2011. No. 3110.

[111] R.S. Germain. Electric and magnetic isolation. In R.C. Richardson and R.N. Smith, editors, *Experimental Techniques in Condensed Matter Physics at Low Temperatures*, page 146. Advanced Book Classics, 1988.

[112] Michael Tinkham. *Introduction to Superconductivity: Second Edition*, pages 19–31. Dover Publications, 1996.

[113] Michael Tinkham. *Introduction to Superconductivity: Second Edition*, pages 213–234. Dover Publications, 1996.

[114] J.S. Denker. Electromagnetic compatibility. In R.C. Richardson and R.N. Smith, editors, *Experimental Techniques in Condensed Matter Physics at Low Temperatures*, page 280. Advanced Book Classics, 1988.

[115] J.S. Denker. Electromagnetic compatibility. In R.C. Richardson and R.N. Smith, editors, *Experimental Techniques in Condensed Matter Physics at Low Temperatures*, page 283. Advanced Book Classics, 1988.

[116] A. B. Zorin. The thermocoax cable as the microwave frequency filter for single electron circuits. *Review of Scientific Instruments*, 66(8), 1995.

[117] K. Bladh, D. Gunnarsson, E. Hürfeld, S. Devi, C. Kristofferson, B. Smålander, S. Pehrson, T. Claeson, P. Delsing, and M. Taslakov. Comparison of cryogenic filters for use in single electronics experiments. *Review of Scientific Instruments*, 74(3), 2003.

[118] J.M Martinis. *Macroscopic Quantum Tunneling and Energy-Level Quantization in the Zero Voltage State of the Current-Biased Josephson Junction*. PhD thesis, University of California, Berkeley, 1987.

[119] Agilent Technologies. *Agilent 33220A 20 MHz Waveform Generator User's Guide*, 4th edition, 2007. Publication Number 33220-9002.

[120] Huizhong Xu. *Quantum Computing with Josephson Junction Circuits*. PhD thesis, University of Maryland at College Park, 2004.

[121] X X Xi. $MgB_2$ thin films. *Superconductor Science and Technology*, 22(4):043001, 2009.

[122] Daniel Cunnane. *Magnesium Diboride Josephson Junctions for Superconducting Devices and Circuits*. PhD thesis, Temple University, 2013.

[123] Y. Cui, Ke Chen, Qi Li, X. X. Xi, and J. M. Rowell. Degradation-free interfaces in $MgB_2$/insulator/Pb josephson tunnel junctions. *Applied Physics Letters*, 89(20), 2006.

[124] Antonio Barone and Gianfranco Paternò. *Physics and Applications of the Josephson Effect*, page 199. Wiley-VCH Verlag GmbH & Co. KGaA, 2005.

[125] A. J. Beerkley, H. Xu, R. C. Ramos, M. A. Gubrud, F. W. Strauch, P. R. Johnson, J. R. Anderson, A. J. Dragt, C. J. Lobb, and F. C. Wellstood. Entangled macroscopic quantum states in two superconducting qubits. *Science*, 300(5625):1548–1550, 2003.

[126] Ke Chen, Y. Cui, Qi Li, C. G. Zhuang, Zi-Kui Liu, and X. X. Xi. Study of $MgB_2$/I/Pb tunnel junctions on MgO (211) substrates. *Appl. Phys. Lett.*, 93(1):012502, 2008.

[127] Ya.G. Ponomarev, S.A. Kuzmichev, N.M. Kadomtseva, M.G. Mikheev, M.V. Sudakova, S.N. Chesnokov, E.G. Maksimov, S.I. Krasnosvobodtsev, L.G. Sevastyanova, K.P. Burdina, and B.M. Bulychev. Investigation of a superconducting $Mg_{1-x}Al_xB_2$ system by tunneling and microjunction (Andreev) spectroscopies. *JETP Lett.*, 79(10):484–488, 2004.

[128] S. Carabello, J. Lambert, J. Mlack, and R. Ramos. Differential conductance measurements of $MgB_2$ -based Josephson junctions below 1 Kelvin. *IEEE Trans. Appl. Supercond.,*, 21(3):3083–3085, 2011.

[129] R. C. Dynes, V. Narayanamurti, and J. P. Garno. Direct measurement of quasiparticle-lifetime broadening in a strong-coupled superconductor. *Phys. Rev. Lett.*, 41:1509–1512, Nov 1978.

[130] A. Brinkman, A. A. Golubov, H. Rogalla, O. V. Dolgov, J. Kortus, Y. Kong, O. Jepsen, and O. K. Andersen. Multiband model for tunneling in $MgB_2$ junctions. *Phys. Rev. B*, 65:180517, May 2002.

[131] A. V. Pogrebnyakov, J. M. Redwing, S. Raghavan, V. Vaithyanathan, D. G. Schlom, S. Y. Xu, Qi Li, D. A. Tenne, A. Soukiassian, X. X. Xi, M. D. Johannes, D. Kasinathan, W. E. Pickett, J. S. Wu, and J. C. H. Spence. Enhancement of the superconducting transition temperature of $MgB_2$ by a strain-induced bond-stretching mode softening. *Phys. Rev. Lett.*, 93(14):147006, Sep 2004.

[132] J. Zmuidzinas and P. L. Richards. Superconducting detectors and mixers for millimeter and submillimeter astrophysics. *Proceedings of the IEEE*, 92(10):1597–1616, Oct 2004.

[133] A. Peacock, P. Verhoeve, N. Rando, A. van Dordrecht, B. G. Taylor, C. Erd, M. A. C. Perryman, R. Venn, J. Howlett, D. J. Goldie, J. Lumley, and M. Wallis. Single optical photon detection with a superconducting tunnel junction. *Nature*, 381(6578):135–137, May 1996.

[134] S. E. Shafranjuk and J. B. Ketterson. *Superconductivity: Conventional and Unconventional Superconductors*, chapter Principles of Josephson-Junction-Based Quantum Computation, pages 315–368. Springer Berlin Heidelberg, Berlin, Heidelberg, 2008.

[135] J. Q. You and Franco Nori. Atomic physics and quantum optics using superconducting circuits. *Nature*, 474(7353):589–597, June 2011.

[136] A.J. Berkley, H. Xu, M.A. Gubrud, R.C. Ramos, J.R. Anderson, C.J. Lobb, and F.C. Wellstood. Characterization of an LC-isolated Josephson junction qubit. *Applied Superconductivity, IEEE Transactions on*, 13(2):952–955, June 2003.

[137] Antonio Barone and Gianfranco Paternò. *Physics and Applications of the Josephson Effect*, page 474. Wiley-VCH Verlag GmbH & Co. KGaA, 2005.

[138] A. Wallraff, A. Lukashenko, C. Coqui, T. Duty, and A. V. Ustinov. High resolution measurements of the switching current in a Josephson tunnel junction: Thermal activation and macroscopic quantum tunneling. arXiv:cond-mat/0204527 [cond-mat.supr-con].

[139] Michael Tinkham. *Introduction to Superconductivity: Second Edition*, pages 202–205. Dover Publications, 1996.

[140] Gert-Ludwig Ingold and Yu.V. Nazarov. Charge tunneling rates in ultrasmall junctions. In Hermann Grabert and MichelH. Devoret, editors, *Single Charge Tunneling*, volume 294 of *NATO ASI Series*, pages 21–107. Springer US, 1992.

[141] Michael Tinkham. *Introduction to Superconductivity: Second Edition*, pages 249–250. Dover Publications, 1996.

[142] M. V. Fistul, A. Wallraff, and A. V. Ustinov. Quantum escape of the phase in a strongly driven Josephson junction. *Phys. Rev. B*, 68:060504, Aug 2003.

[143] John M. Martinis, Michel H. Devoret, and John Clarke. Experimental tests for the quantum behavior of a macroscopic degree of freedom: The phase difference across a Josephson junction. *Phys. Rev. B*, 35:4682–4698, Apr 1987.

[144] Thilo Bauch, Tobias Lindström, Francesco Tafuri, Giacomo Rotoli, Per Delsing, Tord Claeson, and Floriana Lombardi. Quantum dynamics of a d-wave Josephson junction. *Science*, 311(5757):57–60, 2006.

[145] Terry P. Orlando and Kevin A. Delin. *Foundations of Applied Superconductivity*, page 476. Addison-Wesley, 1991.

[146] T. A. Fulton and L. N. Dunkleberger. Lifetime of the zero-voltage state in Josephson tunnel junctions. *Phys. Rev. B*, 9:4760–4768, Jun 1974.

[147] M. Büttiker, E. P. Harris, and R. Landauer. Thermal activation in extremely underdamped Josephson-junction circuits. *Phys. Rev. B*, 28:1268–1275, Aug 1983.

[148] H. A. Kramers. Brownian motion in a field of force and the diffusion model of chemical reactions. *Physica*, 7(4):284 – 304, 1940.

[149] Michael Tinkham. *Introduction to Superconductivity: Second Edition*, page 208. Dover Publications, 1996.

[150] Peter Hänggi, Peter Talkner, and Michal Borkovec. Reaction-rate theory: fifty years after Kramers. *Rev. Mod. Phys.*, 62:251–341, Apr 1990.

[151] Hermann Grabert and Ulrich Weiss. Crossover from thermal hopping to quantum tunneling. *Phys. Rev. Lett.*, 53:1787–1790, Nov 1984.

[152] Michael Tinkham. *Introduction to Superconductivity: Second Edition*, page 261. Dover Publications, 1996.

[153] James A. Blackburn, Matteo Cirillo, and Niels Grønbech-Jensen. Classical statistical model for distributions of escape events in swept-bias Josephson junctions. *Phys. Rev. B*, 85:104501, Mar 2012.

[154] A. O. Caldeira and A. J. Leggett. Influence of dissipation on quantum tunneling in macroscopic systems. *Phys. Rev. Lett.*, 46:211–214, Jan 1981.

[155] H. F. Yu, X. B. Zhu, Z. H. Peng, W. H. Cao, D. J. Cui, Ye Tian, G. H. Chen, D. N. Zheng, X. N. Jing, Li Lu, S. P. Zhao, and Siyuan Han. Quantum and classical resonant escapes of a strongly driven Josephson junction. *Phys. Rev. B*, 81:144518, Apr 2010.

[156] G. Rotoli, T. Bauch, T. Lindstrom, D. Stornaiuolo, F. Tafuri, and F. Lombardi. Classical resonant activation of a Josephson junction embedded in an LC circuit. *Phys. Rev. B*, 75:144501, Apr 2007.

[157] Sudeep K. Dutta. *Characterization of Josephson Devices for use in Quantum Computation.* PhD thesis, University of Maryland at College Park, 2006.

[158] A. Wallraff, T. Duty, A. Lukashenko, and A. V. Ustinov. Multiphoton transitions between energy levels in a current-biased Josephson tunnel junction. *Phys. Rev. Lett.*, 90:037003, Jan 2003.

[159] N. Grønbech-Jensen, M. G. Castellano, F. Chiarello, M. Cirillo, C. Cosmelli, L. V. Filippenko, R. Russo, and G. Torrioli. Microwave-induced thermal escape in Josephson junctions. *Phys. Rev. Lett.*, 93:107002, Aug 2004.

[160] X. Y. Jin, J. Lisenfeld, Y. Koval, A. Lukashenko, A. V. Ustinov, and P. Müller. Enhanced macroscopic quantum tunneling in $Bi_2Sr_2CaCu_2O_{8+\delta}$ intrinsic Josephson-junction stacks. *Phys. Rev. Lett.*, 96:177003, May 2006.

[161] Floriana Lombardi, Thilo Bauch, Karin Cedergren, Jesper Johansson, Tobias Lindström, Francesco Tafuri, Giacomo Rotoli, Per Delsing, and Tord Claeson. Energy level quantization in a $YBa_2Cu_3O_{7-\delta}$ Josephson junction. *Physica C: Superconductivity and its Applications*, 460 - 462, Part 1:335 – 338, 2007. Proceedings of the 8th International Conference on Materials and Mechanisms of Superconductivity and High Temperature Superconductors M2S-HTSC {VIII}.

[162] Sun Guozhu, Wang Yiwen, Cao Junyu, Chen Jian, Ji Zhengming, Kang Lin, Xu Weiwei, Yu Yang, Han Siyuan, and Wu Peiheng. Microwave-induced phase escape in a Josephson tunnel junction. *Phys. Rev. B*, 77:104531, Mar 2008.

[163] K. Ota, K. Hamada, R. Takemura, M. Ohmaki, T. Machi, K. Tanabe, M. Suzuki, A. Maeda, and H. Kitano. Comparative study of macroscopic quantum tunneling in $Bi_2Sr_2CaCu_2O_y$ intrinsic Josephson junctions with different device structures. *Phys. Rev. B*, 79:134505, Apr 2009.

[164] H F Yu, X B Zhu, J K Ren, Z H Peng, D J Cui, H Deng, W H Cao, Ye Tian, G H Chen, D N Zheng, X N Jing, Li Lu, and S P Zhao. Resonant phase escape in $Bi_2Sr_2CaCu_2O_{8+\delta}$ surface intrinsic Josephson junctions. *New Journal of Physics*, 15(9):095006, 2013.

[165] A. J. Dahm, A. Denenstein, T. F. Finnegan, D. N. Langenberg, and D. J. Scalapino. Study of the Josephson plasma resonance. *Phys. Rev. Lett.*, 20:1020–1020, Apr 1968.

[166] C. K. Bak, B. Kofoed, N. F. Pedersen, and K. Saermark. Parametric excitation of plasma oscillations in a Josephson tunnel junction. *Journal of Applied Physics*, 46(2), 1975.

[167] Claude Cohen-Tannoudji, Bernard Diu, and Frank Laloe. *Quantum Mechanics*, volume 2, pages 1323–1338. Wiley, 1992.

[168] Maria Göppert-Mayer. Über elementarakte mit zwei quantensprüngen. *Annalen der Physik*, 401(3):273–294, 1931.

[169] W. Kaiser and C. G. B. Garrett. Two-photon excitation in $CaF_2$: $Eu^{2+}$. *Phys. Rev. Lett.*, 7:229–231, Sep 1961.

[170] Warren R. Zipfel, Rebecca M. Williams, and Watt W. Webb. Nonlinear magic: multiphoton microscopy in the biosciences. *Nat. Biotech.*, 21:1369 – 1377, Oct 2003.

[171] Yukihiro Ota, Masahiko Machida, and Tomio Koyama. Macroscopic quantum tunneling in multigap superconducting Josephson junctions: Enhancement of escape rate via quantum fluctuations of the Josephson-Leggett mode. *Phys. Rev. B*, 83:060503, Feb 2011.

[172] Hidehiro Asai, Yukihiro Ota, Shiro Kawabata, Masahiko Machida, and Franco Nori. Theory of macroscopic quantum tunneling with Josephson-Leggett collective excitations in multiband superconducting Josephson junctions. *Phys. Rev. B*, 89:224507, Jun 2014.

[173] Hidehiro Asai, Shiro Kawabata, Yukihiro Ota, and Masahiko Machida. Two-dimensional macroscopic quantum tunneling in multi-gap superconductor Josephson junctions. *Journal of Physics: Conference Series*, 568(2):022006, 2014.

[174] Hidehiro Asai, Yukihiro Ota, Shiro Kawabata, and Franco Nori. Inter-band phase fluctuations in macroscopic quantum tunneling of multi-gap superconducting Josephson junctions. *Physica C: Superconductivity*, 504:81 – 83, 2014. Proceedings of the 26th International Symposium on Superconductivity.

[175] Ya.G. Ponomarev, S.A. Kuzmichev, M.G. Mikheev, M.V. Sudakova, S.N. Tchesnokov, N.Z. Timergaleev, A.V. Yarigin, E.G. Maksimov, S.I. Krasnosvobodtsev, A.V. Varlashkin, M.A. Hein, G. Muller, H. Piel, L.G. Sevastyanova, O.V. Kravchenko, K.P. Burdina, and B.M. Bulychev. Evidence for a two-band behavior of $MgB_2$ from point-contact and tunneling spectroscopy. *Solid State Commun.*, 129(2):85 – 89, 2004.

[176] A. Brinkman, S.H.W. van der Ploeg, A.A. Golubov, H. Rogalla, T.H. Kim, and J.S. Moodera. Charge transport in normal metal-magnesiumdiboride junctions. *Journal of Physics and Chemistry of Solids*, 67(1-3):407 – 411, 2006. Spectroscopies in Novel Superconductors 2004.

[177] Stanford Research Systems. *Model SR620 Universal Time Interval Counter*, 2.7 edition, February 2006.

[178] Magnesium oxide (MgO) dielectric constants, optical and photoelectric properties. In O. Madelung, U. Rössler, and M. Schulz, editors, *Landolt-Börnstein - Group III Condensed Matter 41B*, volume II-VI and I-VII Compounds; Semimagnetic Compounds. Springer-Verlag Berlin, 1999.

[179] Boron nitride (BN) dielectric constants. In O. Madelung, U. Rössler, and M. Schulz, editors, *Landolt-Börnstein - Group III Condensed Matter 41A1α*, volume Group IV Elements, IV-IV and III-V Compounds. Part a - Lattice Properties. Springer-Verlag Berlin, 2001.

[180] Michel H. Devoret, John M. Martinis, and John Clarke. Measurements of macroscopic quantum tunneling out of the zero-voltage state of a current-biased Josephson junction. *Phys. Rev. Lett.*, 55:1908–1911, Oct 1985.

[181] P. Szabó, P. Samuely, J. Kačmarčík, T. Klein, J. Marcus, D. Fruchart, S. Miraglia, C. Marcenat, and A. G. M. Jansen. Evidence for two superconducting energy gaps in $MgB_2$ by point-contact spectroscopy. *Phys. Rev. Lett.*, 87:137005, Sep 2001.

[182] R S Gonnelli, D Daghero, G A Ummarino, V A Stepanov, J Jun, S M Kazakov, and J Karpinski. Independent determination of the two gaps by directional point-contact spectroscopy in $MgB_2$ single crystals. *Supercon. Sci. Technol.*, 16(2):171, 2003.

[183] A. Anishchanka, A. F. Volkov, and K. B. Efetov. Collective modes in two-band superconductors in the dirty limit. *Phys. Rev. B*, 76:104504, Sep 2007.

# Vita

## Steven A. Carabello

### Education

- B.S., Physics, 1994, Penn State University, University Park, PA.
- M.S., Physics, 1999, Purdue University, West Lafayette, IN.
- Ph.D., Physics, 2016, Drexel University, Philadelphia, PA.

### Publications

- "Microwave resonant activation in hybrid single-gap/two-gap Josephson tunnel junctions", S. Carabello, J. G. Lambert, J. Mlack, W. Dai, Q. Li, K. Chen, D. Cunnane, X. X. Xi, and R. C. Ramos, 2016.
- "Energy gap substructures in conductance measurements of $MgB_2$-based Josephson junctions: beyond the two-gap model", S. Carabello, J. G. Lambert, J. Mlack, W. Dai, Q. Li, K. Chen, D. Cunnane, C. G. Zhuang, X. X. Xi, and R. C. Ramos, Superconductor Science and Technology 28(5):055015, 2015.
- "Momentum-dependent multiple gaps in magnesium diboride probed by electron tunnelling spectroscopy", K. Chen, W. Dai, C. G. Zhuang, Q. Li, S. Carabello, J. G. Lambert, J. T. Mlack, R. C. Ramos, and X. X. Xi, Nature Communciations 3:619, 2012.
- "Differential conductance measurements of $MgB_2$ -based Josephson junctions below 1 Kelvin", S. Carabello, J. Lambert, J. Mlack, and R. Ramos. IEEE Trans. Appl. Supercond., 21(3):3083-3085, 2011.

### Honors and Awards

- Grant in Aid of Research, Sigma Xi, 2010.
- Graduate Student Research Award (Junior Division), Department of Physics, Drexel University, 2010.
- Best Graduate Poster Presentation: Physical Science and Engineering, Drexel University, 2011.

### Professional Experience

- Instructor of Physics, Penn State Harrisburg, 2003-present.